Final Scientific Report

Federal Agency and Organization: DOE EERE – Geothermal Technologies Program

Recipient Organization: Energy & Geoscience Institute, The University of Utah
DUNS Number: 009095365
Recipient Address: 423 Wakara Way, Suite 300, Salt Lake City, UT 84108

Award Number: DE-EE0002766

Project Title: Development of a Chemical Model to Predict the Interactions between Supercritical CO_2, Fluid and Rock in EGS Reservoirs

Project Period: April 1, 2010 to May 31, 2014

Principal Investigator: Brian McPherson
Professor
b.j.mcpherson@utah.edu
(801) 585-9986

Co-Principal Investigator: Feng Pan
Research Assistant Professor
fpan@egi.utah.edu
(801)587-5898

Project Team Members: Brian McPherson, Feng Pan of the University of Utah (UU); John Kaszuba of the University of Wyoming (UW); Satish Karra of Los Alamos National Laboratory (LANL); Caroline Lo Ré of UW; Chuan Lu of Idaho National Laboratory (INL); Peter Lichtner of LANL; Joe Moore of UU; John Muir, Alan Eastman of GreenFire Energy; Yini Nordin, Joe Iovenitti of AltaRock Energy.

Development of a Chemical Model to Predict the Interactions between Supercritical CO_2, Fluid and Rock in EGS Reservoirs

Final Report

Project: DE-EE0002766

Prepared by

Brian J. McPherson[1], Feng Pan[1], John Kaszuba[2], Satish Karra[3], Caroline Lo Ré[2], Chuan Lu[4], Peter Lichtner[3],

1. Energy & Geoscience Institute, The University of Utah
2. Department of Geology & Geophysics, The University of Wyoming
3. Earth and Environmental Sciences Division, Los Alamos National Laboratory
4. Idaho National Laboratory

Disclaimer

Executive Summary

This report summarizes development of a coupled-process reservoir model for simulating enhanced geothermal systems (EGS) that utilize supercritical carbon dioxide as a working fluid. Specifically, the project team developed an advanced chemical kinetic model for evaluating important processes in EGS reservoirs, such as mineral precipitation and dissolution at elevated temperature and pressure, and for evaluating potential impacts on EGS surface facilities by related chemical processes. We assembled a new database for better-calibrated simulation of water/brine/ rock/CO_2 interactions in EGS reservoirs. This database utilizes existing kinetic and other chemical data, and we updated those data to reflect corrections for elevated temperature and pressure conditions of EGS reservoirs.

The project team designed and deployed an aggressive laboratory experimental/testing program to produce new (original) data for the new database. The experimental data are tailored for an "archetype" granite, representative of a typical host rock of EGS reservoirs, and "archetype" reservoir brines. We compared these new experimental results to the new thermodynamic model results and reviewed both in the context of natural systems and commercial operations.

Finally, to test and verify the new database, we conducted core-scale and EGS-reservoir scale reactive-transport simulations by implementing the database in modified versions of the TOUGHREACT and PFLOTRAN codes. We included batch (no-flow) simulations to mimic the experimental data for calibration of kinetic rate constants and reactive surface area of minerals. We also designed and developed simplified numerical simulations of a "generalized" EGS reservoir (e.g., 2-spot and 5-spot well patterns) to explore the possible effects of scCO_2 interactions with EGS reservoir rocks, which include the investigation of suitable conditions for

CO_2 as a working fluid in EGS reservoirs or $CO_2^{\text{EGS-Working Fluid}}$, optimization of geothermal heat extraction efficiency for $CO_2^{\text{EGS-Working Fluid}}$, and assessment of CO_2 leakage risk and possibility of concurrent carbon sequestration. The larger-scale model simulation analysis required that we develop a dual-continuum feature for fracture flow and reactive transport, which we coded and added to the PFLOTRAN model. For sake of specific commercial applicability analysis, we developed a field-scale model to emulate approximate conditions of St. John's Dome CO_2-EGS research site, including evaluation of the effects of CO_2 as a working fluid on system flow, heat extraction, geochemical processes of CO_2-rock-fluid interaction, and possible carbon sequestration at that field scale. Finally, we conducted a simplified 1-D simulation to investigate mineral and saline precipitation on the production wells and EGS surface facilities.

In sum, this project addressed several critical needs of EGS reservoirs that utilize CO_2 as the primary working fluid. The methods and models developed in this project invoked the most typical chemical reactions, kinetics, risk, and feasibility requirements, including the coupling of EGS with geologic carbon dioxide sequestration.

TABLE OF CONTENTS

LIST OF TABLES

LIST OF FIGURES

1. Motivation

Supercritical CO_2 ($scCO_2$) has been suggested as a heat transmission fluid in Enhanced Geothermal Systems (EGS) to improve energy extraction and CO_2 sequestration (Brown, 2000; Pruess, 2007, 2008). Advantages of CO_2 as a heat transmission fluid include its larger expansivity, lower viscosity, and that it is a poor solvent for rock minerals compared to water (Brown, 2000). Disadvantages of CO_2 as a working fluid include its lower heat capacity (by mass) than water (Brown, 2000; Pruess, 2007). Understanding the properties of supercritical CO_2 and CO_2-brine-rock interactions at high temperatures is particularly important to quantify the relative ability of CO_2 to enhance energy extraction and sequestration in EGS reservoirs.

Much research related to CO_2-EGS systems has been conducted recently, including experiments and numerical simulations of heat extraction, CO_2-brine-rock interactions, geochemical processes of fluid-rock reaction, and CO_2 mineralization or sequestration etc. (André et al., 2007; Newell et al., 2008; Pruess, 2007, 2008; Rosenbauer et al., 2005; Wan et al., 2011; Wigand et al., 2009; Xu et al., 2004, 2008). Pruess (2007, 2008) compared CO_2 and water with respect to heat extraction rate and mass flow rate in EGS reservoirs. Heat extraction and flow rate largely increase with CO_2 as the working fluid instead of water, indicating good potential for CO_2 use in EGS reservoirs. Rosenbauer et al. (2005) experimentally tested CO_2-brine-rock interactions at 120 ^oC and 200-300 bar. Results suggested that solubility of CO_2 may enhance water-rock interaction and CO_2 sequestration in carbonate mineral phases. Wan et al. (2011) and Xu et al. (2008) simulated geochemical processes of fluid-rock interaction with CO_2 as the working fluid under high pressure and temperature, and showed that significant CO_2 may be stored in EGS reservoirs by mineral trapping due to precipitation of carbonate minerals. Xu et

al. (2004) also performed batch geochemical simulations for three different aquifer mineral compositions, to evaluate long term CO_2 disposal in deep aquifers. Results suggested that CO_2 sequestration by mineral trapping varies largely with rock type and mineral composition, and porosity decreased due to precipitation of carbonates. André et al. (2007) conducted numerical modeling of fluid-rock chemical interactions of two CO_2 injection scenarios, CO_2-saturated water and supercritical CO_2, in a deep carbonate aquifer. Their results illustrated that geochemical activity with supercritical CO_2 injection was much lower than simulations of CO_2-saturated water injection.

Although previous studies have been conducted for CO_2 as a working fluid in EGS reservoirs, the chemical interactions of supercritical CO_2 ($scCO_2$) and fractured rocks at high temperature and pressure in EGS reservoirs have yet to be comprehensively investigated. Previously-published thermodynamic databases are limited with respect to range and consistency of applicable temperatures and pressures for EGS reservoirs. In addition, data for kinetic rate constants of mineral reactions are sparse and often inconsistent. Furthermore, the effects of $scCO_2$ as a working fluid and acidization agent on geothermal energy extraction, reservoir stimulation, and carbon sequestration at field scale must be understood.

The purposes of this project were to provide essential tools and advance our knowledge of the interaction of $scCO_2$ and reservoir rocks in EGS reservoirs and to provide crucial information to estimate the feasibility and practical benefits of using $scCO_2$ as a working fluid in EGS reservoirs.

2. Research Scope

The scope of this project is to address the topic of "supercritical carbon dioxide/reservoir rock chemical interactions" by developing a chemical and kinetic model that predicts mineral precipitation and dissolution within the EGS reservoir and in the EGS surface facilities. In order to develop this model, the project team assembled a collection of databases and updated these to include the thermodynamic and kinetic rates for water/brine/rock/CO_2 interactions at high temperature and pressure. In addition to taking advantage of existing literature, extrapolation of existing data and some laboratory experiment work is conducted to verify the database results. Following database creation, a reactive-transport model is developed by modifying existing open source subsurface reactive flow and transport simulators (TOUGHREACT and PFLOTRAN). Besides the implementation of the new database and chemical model, dual and/or multi continuum capability for fracture flow processes is added as well. Simulations using modified codes are conducted to investigate the interaction between injected scCO_2 and EGS reservoir fluids and rocks. The possibilities and suitable conditions of using CO_2 as a working fluid, as an acidization agent and the simultaneous operation of CO_2 geological storage and geothermal energy extraction are explored by numerical simulations as well. Likewise, simplified numerical simulations investigate the mineral and salt precipitation in production wells and surface facilities.

The specific objectives of this project include: 1) to improve thermodynamic databases to include wider temperature and pressure ranges than those currently available in existing simulators for application to geothermal reservoirs; 2) to determine applicable chemical reactions between water, rock, and scCO_2 through thermodynamics analyses; 3) to estimate respective

kinetic rates of chemical reactions; 4) to evaluate water/brine displacement by $scCO_2$, water recharge, geochemical reaction processes and effects on EGS reservoirs by lab- and field-scale numerical simulations; 5) to investigate mineral precipitation in EGS surface facilities; 6) to assess CO_2 leakage risk and the possibility of concurrent geothermal energy extraction and carbon sequestration; 7) to investigate the possibility of using $scCO_2$ as an acidization agent in EGS reservoirs.

3. Improve High Temperature-Pressure Thermodynamic Database

3.1 Extend Current Databases of Chemical Equilibrium Constants to a Wider Temperature and Pressure Range

Since available thermodynamic databases are limited with respect to range and consistency of applicable temperatures and pressures for EGS reservoirs, it is necessary to extend these databases to include chemical equilibrium constants to a wider temperature and pressure range. We selected mineral and aqueous species common to EGS reservoirs listed in Table 3.1, and gathered and compared possible mineral and aqueous reactions from the SUPCRT92 and EQ3/6 databases. The equilibrium constants at elevated temperature and pressure were calculated using SUPCRT92, if the species were included in the SPRON96 and SLOP98 databases (Johnson et al., 1992). For species absent in the SPRON96 and SLOP98 database, we gathered and compared necessary data from other sources, including public literature and databases (e.g., SOLTHERM) to facilitate the evaluations.

Table 3.1 Principle minerals in EGS reservoirs.

Host rocks (assumed to be granite)	Veins
Quartz, plagioclase (use mixture of albite and anorthite in experiments, K-feldspar (microcline), biotite, muscovite	Quartz, calcite, epidote, chlorite/Mg clinochlore, pyrite, potassium-feldspar

Note: Alteration minerals on vein walls may include chlorite, calcite, smectite, kaolinite, epidote, illite, pyrite, dawsonite, analcime, quartz, quartz polymorphs and dolomite/akerrite/siderite/magnesite. The experiment work initially concentrates on four minerals (quartz, calcite, epidote, and chlorite) in veins.

According to Table 3.1, we gathered and compared possible mineral and aqueous reactions in EGS reservoirs, which included 35 minerals and 24 aqueous geochemical reactions. The equilibrium constants of these reactions were calculated with SUPCRT92. Figures 3.1-3.3 show the dissolution reaction constants of calcite, k-feldspar and quartz as functions of pressure and temperature. Figure 3.4 shows the relationship between the constant of aqueous CO_2 and pressure and temperature. The three aqueous redox reactions, related to Fe2+, Fe3+, S2-, $SO_3$2-, $SO_4$2-, were also included into the database. A detailed list of these reactions can be found in Appendix A, in the format of SUPCRT 95 input file (Johnson et al., 1992).

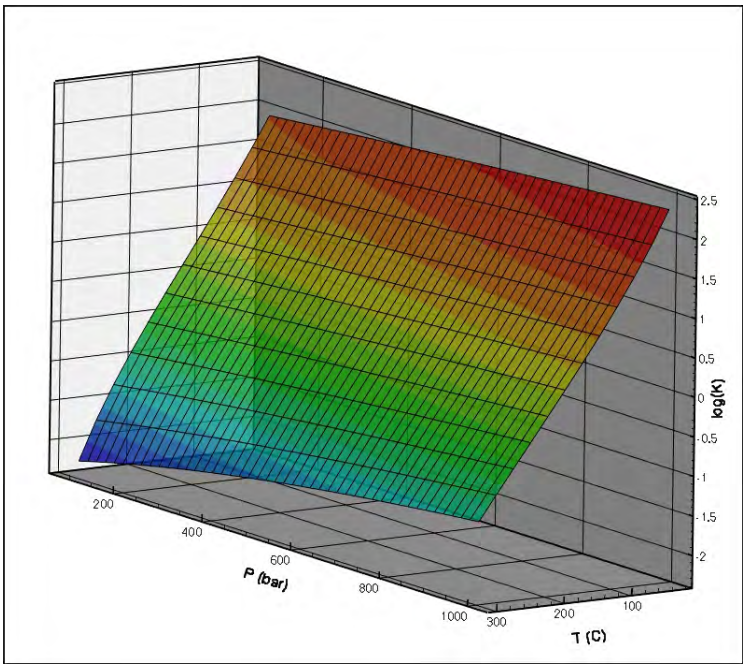

Figure 3.1. Equilibrium constant for the reaction $CaCO_3 + H^+ \leftrightarrow Ca^{2+} + HCO_3^-$ as a function of temperature (25-300°C) and pressure (1-1000 bars) (calcite).

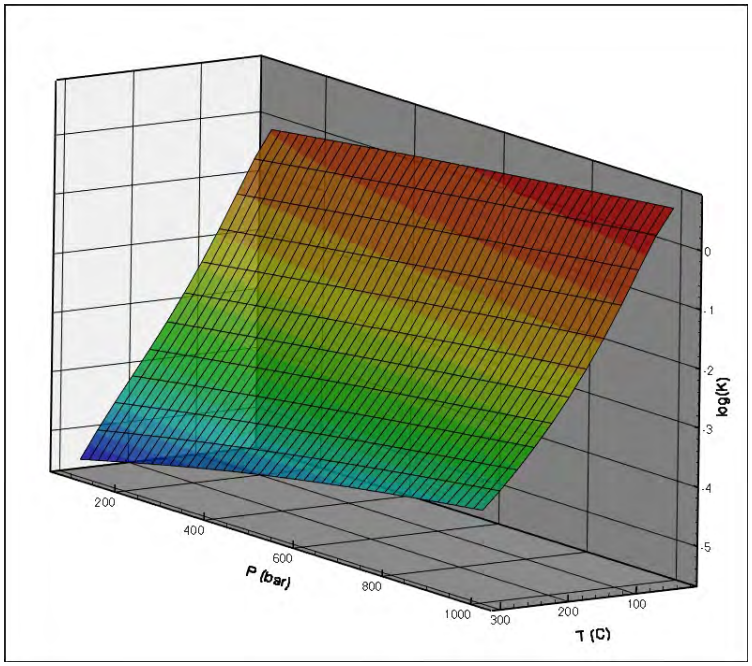

Figure 3.2. Equilibrium constant for the reaction $K(AlSi_3)O_8 + 4H^+ \leftrightarrow Al^{3+} + K^+ + 3SiO_2(aq) + 2H_2O$ as a function of temperature (25-300°C) and temperature (1-1000 bars) (k-feldspar).

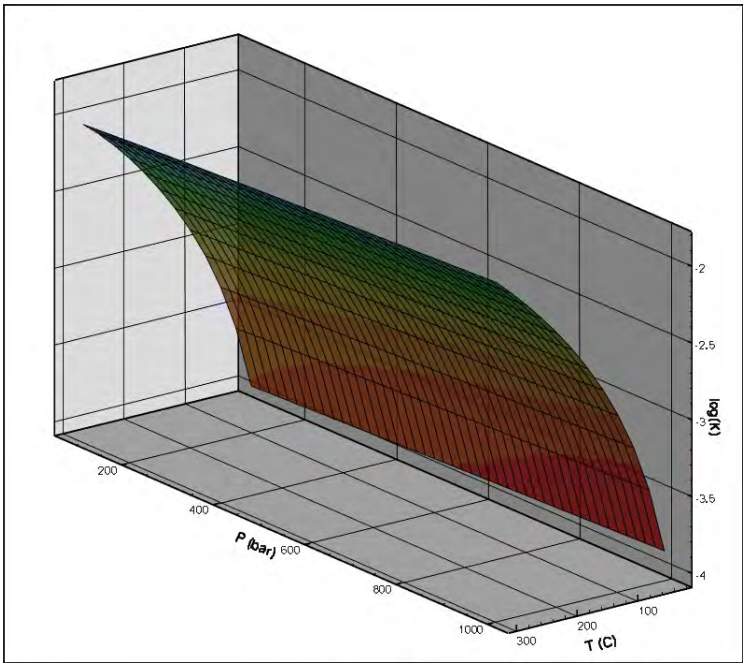

Figure 3.3 Equilibrium constant for the reaction $SiO_2(s) \leftrightarrow SiO_2(aq)$ as a function of temperature (25-300°C) and temperature (1-1000 bars) (quartz).

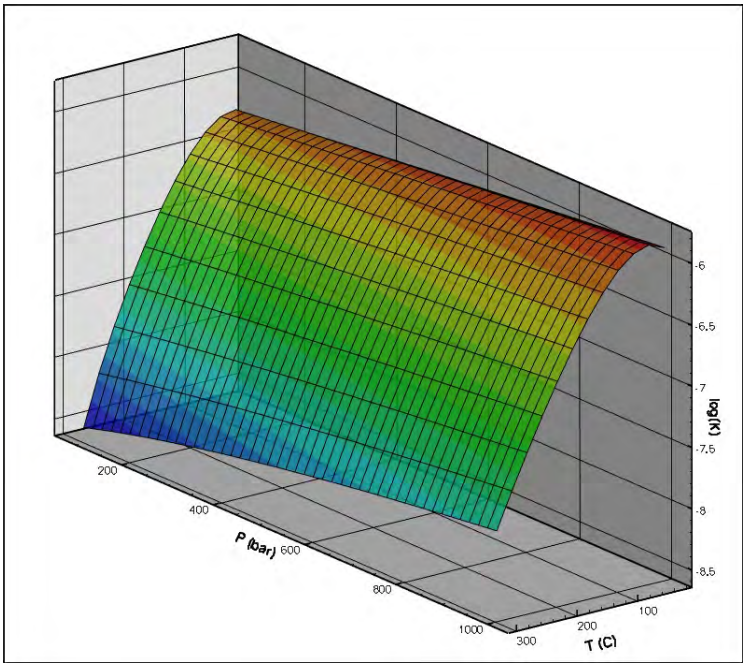

Figure 3.4 Equilibrium constant for the reaction $CO_2(aq) + H_2O \leftrightarrow H^+ + HCO_3^-$ as a function of temperature (25-300°C) and temperature (1-1000 bars) (CO_2(aq)).

The seven gaseous species CO_2, N_2, NO, NO_2, O_2, SO_2 and H_2S were considered and their solubility were evaluated according to Henry's law, instead of the data in SPRON96, to take advantage of recent progress. As an example, the equilibrium constant for reaction $CO_2(aq) \leftrightarrow CO_2(SC)$ can be evaluated with the equation proposed by Duan et.al. (2006) for the calculation of the solubility of carbon dioxide in aqueous solutions containing Na+, K+, Ca2+, Mg2+, Cl-, and $SO_4$2- in a wide temperature–pressure–ionic strength range (273 to 533 K, 0 to 2000 bar, and 0 to 4.5 molality of salts, respectively) with experimental accuracy.

$$\ln m_{CO_2} = \ln y_{CO_2}\varphi_{CO_2}P - \frac{\mu^{(0)}_{CO_2}}{RT} - 2\lambda_{CO_2-Na}(m_{Na} + m_K + 2m_{Mg} + 2m_{Ca}) - \zeta_{CO_2-Na-Cl}m_{Cl}(m_{Na} + m_K + m_{Mg} + m_{Ca}) + 0.07m_{SO_4} \quad (3.1)$$

where: m is the molarity of solvents in the aqueous phase, species are denoted by the subscripts, y and φ are the mole fraction and fugacity coefficients of CO_2 in the gas/SC phase. Details of these gaseous species reactions are also listed in Appendix A.

Within reactive transport simulations, the reaction equilibrium constants need to be calculated in each Newton iteration. It is more effective to represent the pressure and temperature dependence of these reaction equilibrium constants with explicit functions to facilitate the reactive transport simulations. We investigated the following 17-term pressure-temperature (P-T) formulation to calculate the reaction equilibrium constant at elevated pressure and temperature:

$$\begin{aligned}\log K_{eq} = {} & A_1 + A_2 T + A_3 T^{-1} + A_4 \log T + A_5 T^2 + A_6 T^{-2} \\ & + A_7 T^{1/2} + A_8 P + A_9 PT + A_{10} PT^{-1} + A_{11} P \log T + A_{12} P^{-1} \\ & + A_{13} P^{-1} T + A_{14} P^{-1} T^{-1} + A_{15} P^2 + A_{16} P^2 T + A_{17} P^2 T^{-1}\end{aligned} \tag{3.2}$$

where

$$T = \frac{t + 273.15}{273.15}$$

and where t is temperature in °C and P is pressure in units of 100bar. The A_i are parameters obtained by linear regression according to P, T and their functions for all of the mineral, aqueous and redox reactions included in the new database. This formula is applicable within the temperature range 0-300°C, and a pressure range 0.1-100 MPa.

Although the predicted results given by Equation (3.2) are acceptable, its 17-term structure may lead to overwhelming computational requirements. To reduce the computational burden, several new regression formulas are investigated. All of them are based on the observation by Franck (1956) that equilibrium constants at elevated temperature and pressure of many aqueous geochemical reactions exhibit nearly linear behavior while plotted as *logK* vs. *logρ*. This approach has been applied and extended for many studies. Marshall and Franck

(1981) proposed the expression as shown in Equation (3.3):

$$\log K = a + bT + cT^{-2} + dT^{-3} + (e + fT^{-1} + gT^{-2}) \log\rho \quad (3.3)$$

Based on a simplified version of this formula (Equation 3.3), Anderson et al. (1991) only used the terms of a, b, and f in Equation 3.3, and natural logarithms of *K*. It is expressed as:

$$\ln K = p_1 + p_2 T^{-1} + p_3 T^{-1} \ln\rho \quad (3.4)$$

where *p* are constants.

From standard thermodynamic analysis, Equation (3.3) was extended to a density model for estimation of geochemical reaction equilibrium constants at high temperatures and pressures, shown in Equation (3.5):

$$\ln K = \ln K_r - \frac{\Delta H_r^0}{R}\left(\frac{1}{T} - \frac{1}{T_r}\right) + \frac{\Delta a}{R}\left(\ln\frac{T}{T_r} + \frac{T_r}{T} - 1\right) + \frac{\Delta b}{2R}\left(T + \frac{T_r}{T} - 2T_r\right)$$
$$+ \frac{\Delta c}{R}\left(\frac{-T^2 - T_r^2 + 2TT_r}{2T^2T_r^2}\right) + \frac{\Delta C_{pr}^0}{RT_r\left(\partial\alpha/\partial T\right)_{P_r}}\left(\frac{1}{T}\ln\frac{\rho}{\rho_r} - \frac{\alpha_r}{T}(T - T_r)\right) \quad (3.5)$$

where the subscript *r* indicates the reference condition (1bar, 25 °C); the parameters a, b and c are relevant to the heat capacities of aqueous and mineral species; Δ represents the difference in the product and reactant quantities; ΔH_r^0 is the standard enthalpy change of reaction. The term ΔC_{pr}^0 only involves aqueous species; α is the coefficient of thermal expansion of water, defined as:

$$\alpha = \frac{1}{V}\left(\frac{\partial V}{\partial T}\right)_P = -\left(\frac{\partial \ln\rho}{\partial T}\right)_P \quad (3.6)$$

We tested several density oriented formulas based on Equations (3.3) and (3.5), shown as Equation (3.7a-d):

$$\log K = A_1 + A_2 T + A_3 T^{-1} + A_4 \log T + A_5 T^{-2} + A_6 P T^{-1} + A_7 T^{-1} \log\rho \quad (3.7a)$$

$$\log K = A_1 + A_2 T + A_3 T^{-1} + A_4 \log T + A_5 T^{-2} + A_6 P T^{-1} + A_7 T^{-1} \log\rho + A_8 P \quad (3.7b)$$

$$\log K = A_1 + A_2 T + A_3 T^{-1} + A_4 \log T + A_5 T^{-2} + A_6 P T^{-1} + A_7 T^{-1} \log \rho + A_8 (\partial\alpha / \partial T)_{P_r}^{-1} \log \rho + A_9 T^{-1} (\partial\alpha / \partial T)_{P_r}^{-1} \quad (3.7c)$$

$$\log K = A_1 + A_2 T + A_3 T^{-1} + A_4 \log T + A_5 T^{-2} + A_6 P T^{-1} + A_7 T^{-1} \log \rho + A_8 P + A_9 (\partial\alpha / \partial T)_{P_r}^{-1} \log \rho + A_{10} T^{-1} (\partial\alpha / \partial T)_{P_r}^{-1} \quad (3.7d)$$

Among them, Equations (3.7a) and (3.7b) are similar to Equation (3.3), and Equations (3.7c) and (3.7d) are extended from Equation (3.5). It should be noted that the 6th term in Equation (3.7c), the 6th and 8th terms in Equation (3.7d) still have pressure terms; they were added for better regression results.

The equilibrium constants of dissolution reactions of calcite, k-feldspar, quartz and CO_2 were used as testing examples. Regression results from Equations (3.2), and (3.7) are summarized in Table 3.2, where the maximum error is defined as Err = max $\left| \log K^{reg} - \log K^{SUP} \right|$ on all data points, and the superscript *reg* represents the prediction by Equation (3.2), and the superscript *SUP* represents the estimation from SUPCRT92 using the SLOP98 database. All mineral and aqueous reaction equilibrium constants listed in Appendix A have been evaluated. Figure 3.5 shows the comparison of the estimation on reaction equilibrium constant of $CaCO_3 + H^+ \leftrightarrow Ca^{2+} + HCO_3^-$ by a) SUPCRT92; and b) multiple linear regressions from the density model (Equation 3.7d). The data format of the multiple linear regression results is shown in Table 3.3, with dissolution reactions of calcite, k-feldspar, quartz and CO_2 as examples.

Table 3.2. Maximum errors of multiple linear regressions according to Equations (3.2) and (3.7).

Err	calcite	k-feldspar	quartz	CO_2 (aq)
Eqn.1	8.63E-02	3.91E-02	1.01E-02	7.54E-02
Eqn. 6a	4.28E-02	1.05E-01	2.58E-02	1.44E-02
Eqn. 6b	5.58E-02	5.19E-02	1.08E-02	1.19E-02
Eqn. 6c	3.35E-02	1.07E-01	2.69E-02	1.27E-02
Eqn. 6d	3.98E-02	4.51E-02	9.30E-03	1.23E-02

Table 3.3. Coefficients of multiple linear regressions according to Equation (3.7a).

A	calcite	k-feldspar	quartz	CO_2 (aq)
1	3.1129E+01	-9.8747E+01	-5.6646E+01	-5.4958E+00
2	4.2805E+00	-1.1948E+01	-9.8769E+00	-4.0520E+00
3	-4.6060E+01	1.5793E+02	8.8739E+01	8.5297E+00
4	-6.6333E+01	1.7345E+02	1.2191E+02	1.2249E+01
5	1.2862E+01	-4.7271E+01	-2.6800E+01	-5.5897E+00
6	1.5891E-02	-5.3587E-03	-7.0270E-03	1.3146E-02
7	2.8312E+01	2.9038E+01	1.3611E+00	1.8517E+01
8	-7.1965E-03	6.9669E-02	1.8161E-02	4.8281E-03
9	-1.7118E-06	-1.4523E-08	3.5319E-07	-3.6738E-07
10	-1.5400E-07	-5.6539E-07	-9.6262E-08	-1.0634E-07

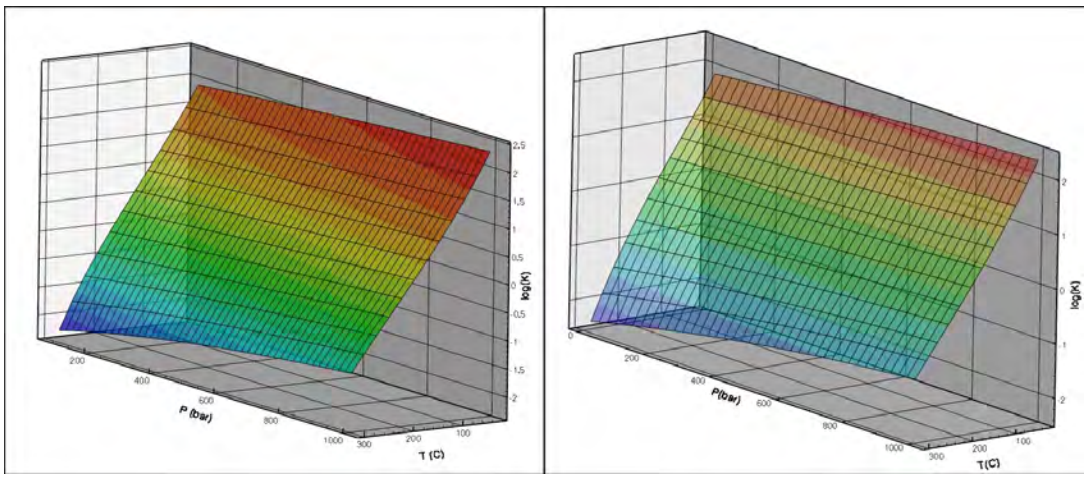

Figure 3.5. Comparison of the estimation on reaction equilibrium constant of CaCO3 + H+ ↔ Ca2+ + HCO_3^- by y a) SUPCRT92 and b) multiple linear regressions from density model: Equation (3.7d).

For mineral reactions, the regression results were obtained from density oriented Equations (3.7a) and (3.7d). Even the modified version of Equation (3.7d) does not offer significant advantages compared to Equation (3.2). This behavior may be partly due to the fact that Equation (3.2) has more fitting parameters. The greater improvement from using density models lies in the regression on aqueous reactions.

Regarding the reaction $CO_2(aq) + H_2O \leftrightarrow H^+ + HCO_3^-$, regression accuracy was increased approximately 5 times by using the density models. Therefore, at the least, application of the density models can reduce the number of terms and computational burden. However, the water density involved in Equation (3.7d) is obtained by the general equation of state for water, which contains several nonlinear terms as well which may increase the computational demand. Therefore, we selected Equations (3.2) to be applied in the code modifications with user-defined options.

3.2 New Thermodynamic Database at a Wider Temperature and Pressure Range

We rearranged and compiled this high pressure and high temperature geochemical dataset in a format compatible with the PFLOTRAN and TOUGHREACT model inputs for geochemical database. A new data file, "geothermal-hpt.dat," was developed from the extension of current "handford.dat' geochemical database to a wider temperature and pressure database for an extensive set of 592 geochemical reactions including aqueous, gas and mineral reactions. The format of the new database read as:

1. **aqueous reactions** ($CO_2(aq)+H_2O=H^+ + HCO_3^-$, for example)

$CO_2(aq)$' 3 -1.0000 'H2O' 1.0000 'H+' 1.0000 'HCO3-'

1.1110E+04 3.1346E+03 2.2143E+03 1.5752E+04 -9.1033E+01 -2.4447E+02 -1.6130E+04 5.7810E-01 1.2769E+00 -1.8024E+00 -7.1284E+00 1.1835E-02 -4.9471E-03 -7.0135E-03 3.5467E-02 -1.2929E-02 -2.4246E-02 3.0 0.0 44.0098

i.e. species name, number of other reactant and production, stoichiometric coefficient followed by species name. Then the 17 parameters are listed. The last 3 parameters are the Debye-Huckel ion size parameter (a0), the ion charge and molar weight.

2. **Mineral reactions** ($K(AlSi_3)O_8 + 4H^+ = Al^{+3} + K^+ + SiO_2(aq) + H_2O$)

'K-Feldspar' 108.8700 5 -4.0000 'H+' 1.0000 'Al+++' 1.0000 'K+' 2.0000 'H2O' 3.0000 'SiO2(aq)' 1.1910E+04 3.0832E+03 3.6830E+03 2.0163E+04 -6.9539E+01 -5.1478E+02 -1.8092E+04 1.3104E+00 2.2292E+00 -3.4312E+00 -1.2880E+01 -2.9052E-02 1.2081E-02 1.7416E-02 6.1892E-02 -2.2504E-02 -4.2950E-02 278.3315

i.e., species name, number of other reactant and production, Stoichiometric coefficient followed by species name. Then the 17 parameters are listed. The last parameter is mineral molar weight.

To check if the fit functions for logKs give reasonable results, we tested by writing a PYTHON code that reads in the 17 coefficients for each reaction and finds the logKs at the 'hanford.dat' temperature values (0,25,60,100,150,200,250,300°C). The pressures used were the corresponding water saturation pressures. As an example, the logKs comparison between the 'supcrt-hpt.dat' database and 'hanford.dat' database for Calcite is shown in Figure 3.6. Excellent match is seen for most of the aqueous, gas and mineral reactions except the ones shown in Table B1 of Appendix B. For this comparison, the min error (%) is calculated as the minimum of (abs(logK_hpt-logK_hanford)/abs(logK_hanford)*100 at each temperature. Table B1 shows the list of species that have this min error (%) greater than 10 and is sorted from largest to smallest. The first set of mineral species highlighted in blue have large error since SUPCRT did not give the correct logKs as the Gibb's free energy for these species was not available in the SUPCRT

slop07.dat database and is set to a large value 99999. Hence, the logKs for these species should not be used from our database supcrit-hpt.dat as well. It is not clear why there is difference in the logKs for the other species.

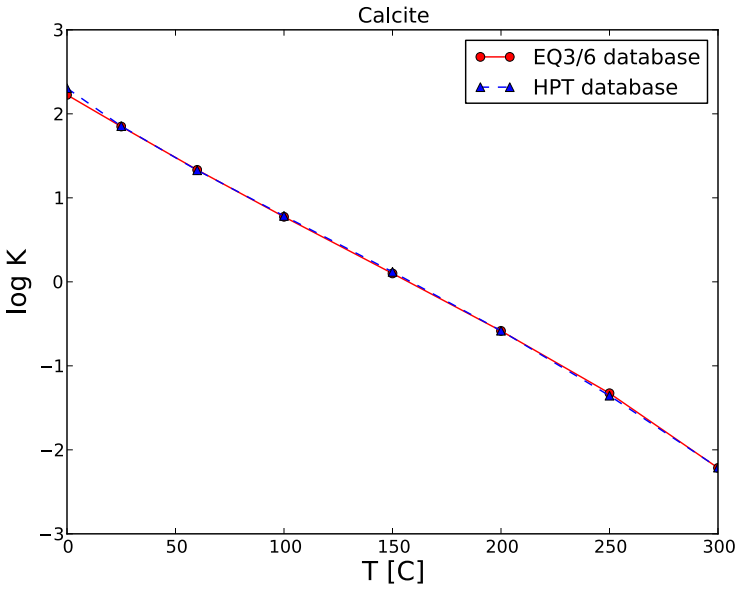

Figure 3.6. Comparison between the HPT database 'supcrt-hpt.dat' and the EQ3/6-based database 'hanford.data' logKs for calcite mineral reaction. The temperatures are at 0, 25, 60, 100, 150, 200, 250, 300 ^{o}C and at corresponding water saturation pressures.

Then, we check if one actually needs a HPT geochemical database. For this logKs from 'hanford.dat' at 0, 25, 60, 100, 150, 200, 250, 300 °C at water saturation pressures is compared with 'supcrt-hpt.dat' calculated logKs at the same temperatures but at 1200 bar. Using another PYTHON code we calculated the error between these logKs and tabulated the max and min errors (%) in Table B2 of Appendix B. The min error (%) is calculated as the minimum of (abs(logK_hpt-logK_hanford)/abs(logK_hanford)*100 at each temperature, and the max error (%) is calculated as the maximum of (abs(logK_hpt-logK_hanford)/abs(logK_hanford)*100 at each temperature. The species are sorted based on the max error (%) from largest to smallest.

The mineral species highlighted in blue should be discounted since the logKs from the supcrt-hpt.dat are not correct as explained above. Otherwise, as can be seen for a majority of species the maximum error exceeds 10% and thus using a HPT geochemical database for these species is important. For example, for Calcite the max error (%) is 454. This significant difference in logKs can be seen in Figure 3.7 where both the cases are plot for Calcite.

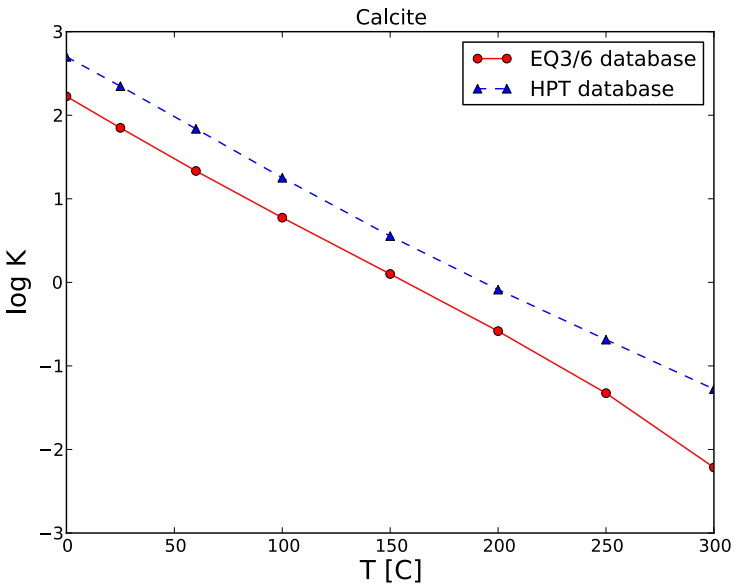

Figure 3.7. Comparison of logKs for calcite between the HPT database at 1200 bar and EQ3/6-based database at water saturation pressures.

The simulators PFLOTRAN and TOUGHREACT were modified accordingly. Originally, the thermodynamic database adopted by both simulators was in the EQ3/6 format, in which eight equilibrium constants at different temperatures (0, 25, 60, 100, 150, 200, 250, 300 ^{o}C) are listed for each reaction included in the database. For example, the data for the mineral reaction ($K(AlSi_3)O_8 + 4H^{+}=Al^{+3} + K^{+} + SiO_2(aq) + H_2O$) is formatted as:

K-Feldspar' 108.8700 5 -4.0000 'H+' 1.0000 'Al+++' 1.0000 'K+' 2.0000 'H2O' 3.0000 'SiO2(aq)' -0.2168 -0.2753 -0.9610 -1.8555 -2.8681 -3.7528 -4.5737 -5.4136 278.3315

The modified PFLOTRAN and TOUGHREACT models can distinguish these two formats according to the number of terms in the data read from file. Then reaction networks are built according to the species name read from input files.

3.3. Update Formulas for Mutual Solubility and Fluid Properties

Currently, CO_2 fluid properties, including density, enthalpy, viscosity etc. are calculated with the Span-Wagner EOS (Span and Wagner, 1996), same as the formula adapted by the National Institute of Standards and Technology, in both PFLOTRAN and TOUGHREACT. Water properties are calculated according to the International Association for the Properties of Water and steam (IAPWS) formula in both simulators (IAPWS, 1998).

PFLOTRAN estimates CO_2 solubility in water according to Duan and Sun (2003), while TOUGHREACT calculates the solubility based on Spycher and Pruess (2003). The comparison of simulation results obtained from these two formulas does not show great discrepancy.

4. Experimental Studies for Supercritical CO_2 in a Granite-hosted Geothermal System

We present experimental data to evaluate aqueous geochemistry and mineralogical relationships in water-granite ± CO_2, water-epidote-granite ± CO_2, water-calcite-granite ± CO_2, water-chlorite-granite ± CO_2, and water-epidote-calcite-chlorite-granite ± CO_2 systems at 250°C and 25-45 MPa. Granite, epidote-granite, chlorite-granite, and calcite-granite experiments provide a baseline understanding for fluid-rock interactions in fresh rock and altered rock, respectively. The epidote-granite, calcite-granite, and chlorite-granite experiments specifically simulate fluid-rock interactions in EGS reservoirs stimulated by fracturing along pre-existing zones of weakness (i.e., epidote and/or calcite veins) and in pervasively altered granitic rocks (i.e., chlorite and/or epidote alteration). We compare results to thermodynamic models and review experimental and theoretical results in the context of natural systems and commercial operations. Of specific interest are 1) the extent of experiment equilibration, 2) the sequence of water-rock reactions, 3) how the water-rock systems respond given 'spontaneous' injection of supercritical CO_2 ($scCO_2$), 4) how natural systems inform us about results and vice versa, 5) what governs smectite formation and how it might affect hydrothermal reservoirs, and 6) how results apply to commercial geothermal operations and carbon sequestration projects.

4.1 Previous Experimental Work in Granitic Systems

Significant experimental efforts have been made over the past 50 years to elucidate hydrothermal fluid-rock interactions for felsic igneous rocks. Early experimental work concluded that observed hydrothermal geochemistry does not necessarily require contribution by magmatic fluids (Ellis and Mahon 1964, 1967) and that fluid-granite reactions can cause the mineralization and alteration typically observed around ore deposits (Ellis, 1968). Driving interests for other fluid-granite experiments include: capacity for metal extraction via fluid

circulation (Baker et al., 1985), fault-seal characterization in seismic zones (Moore et al., 1994; Morrow et al., 2001), CO_2 reactivity in Yellowstone rhyolite as a function of temperature (Bischoff & Rosenbauer, 1996), supercritical fluid solvent strengths (Tsuchiya & Hirano, 2007), permeability as a function of chemo-mechanical processes (Yasuhara et al., 2011), and fundamental dissolution and precipitation of silica polymorphs (Okamoto et al., 2010). Applied fluid-granitoid studies focus on operation of EGS or hot dry rock geothermal systems (e.g., Azaroual & Fouillac, 1997; Baldeyrou et al., 2003; Charles, 1978; Charles & Bayhurst, 1983; Milodowski et al., 1989; Savage et al., 1985, 1987, 1992, 1993), geologic storage of high-level radioactive waste (Bourg et al. 1985; Moore et al., 1983; Morrow et al., 1981; Savage, 1986; Savage and Chapman, 1982), and sequestration of CO_2 in hard rock reservoirs (Lin et al., 2008; Liu et al., 2003; Suto et al., 1997; Ueda et al., 2005).

Appendices C and D outline batch and flow-through studies in granitic systems published in peer-reviewed journals or reports. In addition to granite studies, we also include those using granodiorite, rhyolite, and/or andesite. Temperatures and pressures range between 20-600ºC and 1.4-150 MPa, respectively. Distilled water is most commonly used, followed by dilute Na-Cl, Na-HCO_3-Cl, or Na-Ca-HCO_3-Cl solutions. A few of the more recent studies also use $scCO_2$ at the onset of each experiment. To date, we are unaware of any using both $scCO_2$ *and* a realistic groundwater chemistry. We are also unaware of any that allow a system to approach a steady-state prior to introducing $scCO_2$. Our experiments were designed to explore such conditions, as wanting in the current literature.

Many of the studies in Appendices C and D were designed to answer questions about specific hydrothermal fields, so results vary from study to study and can be difficult to compare. However, we observe two commonalities with respect to dissolution and precipitation reactions.

Specifically, feldspars are the most reactive minerals, and regardless of temperature, common secondary minerals include: smectite, illite, zeolite, and silica with fewer occurrences of kaolinite, anhydrite, calcite, chlorite, albite, and potassium feldspar (K-feldspar). Extreme alteration of feldspars is not unexpected as compared to natural systems. Smectite and mixed smectite/illite occurrences, however, are not commonly seen in nature at temperatures above ~180 and ~220ºC, respectively (e.g., Henley and Ellis, 1983). The common precipitation of smectite in experiments conducted at temperatures >220ºC begs explanation and, to our knowledge, is not discussed in the aforementioned studies. We will review and discuss this observation in the context of experimental, theoretical, and natural systems.

4.2 Approach

4.2.1 Experimental Design

A granitic composition consisting of sub-equal portions of quartz, plagioclase feldspar (oligoclase), and K-feldspar was selected for these experiments based on the composition of the majority of granites (Best, 1995). Biotite was also included to more closely simulate natural granite as well as to provide a source of Fe and Mg in each experiment. Two experiments also include epidote, a common secondary mineral in granitic systems. Trace amounts of pyrite and Fe-oxide inclusions are also present in the K-feldspar. We avoided additional accessory minerals to simplify the analysis of modeling and experimental results. Based on groundwater geochemistry at Roosevelt Hot Springs (Capuano & Cole, 1982), a multi-component, but dominantly Na-Cl water was used in experiments (Section 4.3.3). This composition is typical of many crystalline basement groundwaters (Nicholson, 1993; Bucher and Ingrid, 2000).

The results of five hydrothermal experiments are presented here, including one water-granite experiment (EXP-1), two water-granite-scCO_2 experiments (EXP-2 and EXP-3), one

water-epidote-granite experiment (EXP-4) and one water-epidote-granite-scCO$_2$ experiment (EXP-5). Experiments EXP-2 and EXP-3 are similar with the exception of initial pH, which we varied to observe the effect of pH on the initial water-rock interactions (EXP-2 pH = 5.7; EXP-3 pH = 3.9). Table 4.1 outlines conditions and parameters for each experiment. All experiments included a water-rock stage conducted at 250ºC and 25 MPa that lasted at least 666 hours. The initial water/rock ratio was ~20/1. Two of the experiments (EXP-1 and -4) were terminated when aqueous chemistry approached a steady-state condition. Three of the experiments (EXP-2, -3, and -5) continued for at least another 650 hours after injecting scCO$_2$. The scCO$_2$ portion of these experiments continued at 250ºC with final pressures between 30.7 and 44.8 MPa. Final steady state pressures stabilized over a period of 1-2 days as CO$_2$ dissolved into solution.

Table 4.1 Experimental parameters and mineral compositions.

Experiment	EXP-1	EXP-2	EXP-3	EXP-4	EXP-5
Description	Water + Granite	Water + Granite + scCO$_2$	Low pH Water + Granite + scCO$_2$	Water + Granite + Epidote	Water + Granite + Epidote +
Initial pH, Bench	5.6 ± 0.1	5.7 ± 0.1	3.9 ± 0.1	5.1 ± 0.1	5.2 ± 0.1
Temperature (°C)	250.1 ± 0.8	250.2 ± 1.9	250 ± 2.4	250.1 ± 0.4	249.8 ± 2.0
Pressure (MPa), Pre-scCO$_2$ Injection	25.3 ± 0.7	25.0 ± 1.0	25.2 ± 0.7	24.9 ± 0.8	25.2 ± 0.7
Pressure (MPa), Post-scCO$_2$ Injection	N/A	30.7 ± 0.9	44.8 ± 0.9	N/A	33.9 ± 0.8
Initial Water:Rock Ratio	19.4	20.0	19.0	20.0	20.4
Rock Mass[a]	10.84	12.04	11.08	11.81	9.56
Mineral Proportions (Qtz:Olg:Kfs:Bt:Ep)	32:32:32:4:0	32:32:32:4:0	32:32:32:4:0	16:16:16:2:50	16:16:16:2:50
Water-Rock Reaction Time (hours)	1024	700	674	858	666
Water-Rock-scCO$_2$ Reaction Time (hours)	N/A	1027	1121	N/A	650
Total Reaction Time (hours)	1024	1727	1795	858	1316
Surface Area of Reacted Powders (m^2/g	0.7450 ± 0.0009	0.5765 ± 0.0316	1.0372 ± 0.0062	2.6224 ± 0.0089	3.1251 ± 0.0323

[a] Rock mass input into reaction cell.
DL = below detection limit
N/A = not applicable
sc = supercritical

The amount of CO_2 injected into EXP-2, -3, and -5 ensured $\Sigma CO_2(aq)$ saturation for the duration of each experiment. The Duan & Sun (2003) and/or Duan et al. (2006) equations of state (EOS) for CO_2 were used to calculate the target amounts of injected CO_2. Based on mass balance data, excess $scCO_2$ was present in EXP-2 and EXP-3 for the duration of each experiment. Experiment EXP-5 developed a leak 281 hours after $scCO_2$ injection (363 hours prior to termination). However, we believe $\Sigma CO_2(aq)$ saturation was maintained throughout the experiment because we observed no drastic changes in aqueous chemistry after leak detection. During sample collection before and after leak detection, we also observed a consistent volume of degassed CO_2 from the aqueous phase; this also indicated saturation throughout the experiment.

4.2.2 Geochemical Calculations

Equilibrium modeling was performed using The Geochemist's Workbench® version 8.0.10 (GWB) (Bethke and Yeakel, 2009); the b-dot ion association model; and the resident thermodynamic database, thermo.dat. We use thermo.dat because it is internally consistent and handles Al speciation more adeptly than other readily available databases (e.g., Kaszuba et al., 2011). We used the thermodynamic models to 1) determine initial water compositions; 2) calculate actual in-situ pH conditions, aqueous species concentrations, and mineral stabilities; and 3) predict expected aqueous species concentrations and mineral stabilities.

Availability of thermodynamic data limits accuracy of theoretical calculations and predictions. This is especially so for solid-solution minerals for which only pure end-member thermodynamic data may exist (e.g., feldspars, micas, epidotes, clays, and zeolites). Accordingly, to better represent thermodynamic data for minerals used in our experiments, we adjusted the database to include solid-solution plagioclase and epidote (Section 4.3.3) with

equilibrium constants calculated via ideal solution models. We did not calculate a similar solution model for biotite because 1) it is a minor phase in our experiments, and 2) the mineral stoichiometry is not as well constrained due to notable titanium concentrations and the likely presence of ferric iron. Instead, modeling calculations with biotite assume 44% annite and 56% pholgopite. The K-feldspar is perthitic, meaning the original mineral exsolved to albite and microcline. Since adequate thermodynamic data exist for albite and microcline, K-feldspar is modeled as a mechanical mixture of end-member minerals using 25% albite and 75% microcline. We base above determinations on mineral chemistry, as presented in Table 4.2 and Section 4.3.3.

Table 4.2 Mineral compositions and initial surface area.

Elemental Weight Percent of Mineral Reactants (Wt% oxide)					
Component[a,b]	Quartz (Qtz)	Oligoclase (Olg)	K-Feldspar (Kfs)	Biotite (Bt)	Epidote (Ep)
P2O5	DL	DL/NM	DL	DL/NM	DL
MnO	DL	0.01/DL	0.00	1.03/0.87	0.09
Fe2O3	0.08	0.12/0.04	0.19	22.84b	12.81
FeO	--	--	--	17.65c	--
MgO	DL	DL/DL	DL	13.78/13.82	DL
SiO2	97.79	64.29/61.83	62.48	36.17/38.21	34.70
Al2O3	0.59	24.47/24.25	18.92	11.56/11.33	22.63
CaO	DL	5.23/4.65	0.22	0.10/0.01	23.69
TiO2	0.03	0.02/DL	0.01	2.50/2.12	0.12
Na2O	DL	8.36/8.67	2.35	0.60/0.43	DL
K2O	DL	0.71/0.50	12.60	8.93/9.37	DL
F	NM	NM/DL	NM	NM/2.57	NM
Cl	NM	NM/DL	NM	NM/0.04	NM
Total	98.48	103.37/99.94	96.86	97.50/96.44	94.04
Source	Unknown	Mitchell County, North Carolina	Unknown	Ontario, Canada	Unknown
Surface Area of Unreacted Powders (m^2/g)[c]					
EXP-1	0.3367 ± 0.0028	0.6303 ± 0.0070	0.4408 ± 0.0208	1.5652 ± 0.0420	N/A
EXP-2	0.3367 ± 0.0028	0.6303 ± 0.0070	0.927 ± 0.0385	1.5652 ± 0.0420	N/A
EXP-3	0.3367 ± 0.0028	0.6303 ± 0.0070	0.4408 ± 0.0208	1.5652 ± 0.0420	N/A
EXP-4	0.7124 ± 0.0031	0.6303 ± 0.0070	0.927 ± 0.0385	1.5652 ± 0.0420	0.6327 ± 0.0617
EXP-5	0.7124 ± 0.0031	0.6303 ± 0.0070	0.927 ± 0.0385	1.5652 ± 0.0420	0.6327 ± 0.0617

[a] Component analysis conducted by ICP-OES after acid digestion of mineral.
[b] Component analysis for oligoclase and biotite also conducted by electron microprobe. Microprobe data are the second set of values shown.
[c] Surface areas determined by BET. Powders comprise 75% of mineral reactants with the remaining 25% consisting of mineral chips.
DL = below detection limit
N/A = not applicable
NM = not measured

To determine a water chemistry that would be as close to equilibrium as possible with the minerals, GWB was used. We calculated a different water composition for each set of experiments: one water for the granite experiments (EXP-1, -2, and -3), and another water for the epidote-granite experiments (EXP-4 and -5). This was done to minimize water-rock interaction in the experiments prior to injecting $scCO_2$.

In-situ pH was calculated for each sample using bench pH values, bench $\Sigma CO_2(aq)$ concentrations, and calculated in-situ $\Sigma CO_2(aq)$ concentrations (Sections 4.4.4, 4.4.5) in conjunction with aqueous geochemical data for Na, Cl, Ca, Na, K, $SiO_2(aq)$, SO_4, Al, and Mg (Section 4.4.3.1). Minimal amounts of Fe^{2+} and $O_2(aq)$ were also input into each model because of the presence of redox sensitive, iron-bearing minerals. In-situ pH was calculated for samples in the water-rock portion of each experiment by speciating the fluid at 250ºC. For those experiments injected with $scCO_2$, in-situ pH was calculated for post-injection samples by the method of Newell et al. (2008), with substitution of calculated in-situ $\Sigma CO_2(aq)$ in place of measured in-situ $\Sigma CO_2(aq)$. In-situ pH values can vary depending on whether one allows the aqueous solution to precipitate minerals or not. Therefore, we conducted multiple iterations for each in-situ pH calculation assuming varying degrees of mineral precipitation. Results were routinely similar, and here we only present calculations made assuming no mineral precipitation from the aqueous solution. Aqueous species activities were simultaneously calculated and used on activity-activity diagrams to better define the sequence of water-rock reactions for each experiment (Section 4.5.1).

Results from GWB also predict species concentrations and secondary minerals, pre- and post-$scCO_2$ injection. The input used for each model reflects the fluid-rock proportions and chemistries of each experiment (Tables 4.1, 4.2, and 4.3). During the water-rock portion of each

experiment (i.e., the entirety of EXP-1 and -4 and the first half of EXP-2, -3, and -5), the model speciates the mixture at 250 ºC. For those experiments injected with $scCO_2$ (EXP-2, -3, and -5), an additional reaction path titrates an appropriate amount of $\Sigma CO_2(aq)$ into each system, as calculated using the Duan & Sun EOS (2003) (Section 4.4.4). For these models, we allowed minerals to precipitate from the aqueous solution, but subsequently excluded those that naturally form at higher temperature/pressure conditions (e.g., diopside, andradite, tremolite, etc.). The resulting predicted aqueous concentrations are included in Table 4.3 and on Figure 4.1 in the column labeled 'P' (i.e., 'predicted') on the right side of each graph. Predicted, observed, and typical field alteration mineralogy are outlined in Table 4.4.

Table 4.3. Aqueous geochemistry for all experiments, including analyzed and predicted concentration.

EXP-1: Water chemistry (mmol/kg), water + granite experiment

Time (hours)	pH (STP)[a]	pH (in-situ)[b]	F	Cl	SO_4	Na	K	Ca	Mg	Fe	$SiO_2(aq)$	Al	Mn	ΣCO_2[f], bench	ΣCO_2[g,h], in-situ	Charge Balance[i]
Initial Water[c]	5.6 ± 0.1	6.4	0.01	161	0.81	130	8.8	1.0	0.8	<0.00002	3.4	0.0022	0.00012	0.10	*0.10*	-6.6%
25.1	5.7 ± 0.1	6.6	0.04	161	0.87	135	9.7	1.4	0.3	<0.00002	6.0	0.0063	0.00191	0.10	*0.10*	-4.5%
41.5	5.4 ± 0.1	6.6	0.05	158	0.85	129	9.4	1.5	0.2	<0.00002	6.8	0.0049	0.00080	0.34	*0.34*	-6.0%
113.5	5.6 ± 0.1	6.5	0.05	158	0.78	130	8.3	1.6	0.2	<0.00002	7.4	0.0085	0.00066	0.11	*0.11*	-5.7%
354.0	5.6 ± 0.1	6.5	0.06	157	0.75	130	9.1	1.7	0.2	<0.00002	7.6	0.0091	0.00037	0.16	*0.16*	-5.0%
640.9	5.4 ± 0.4	6.5	0.02	149	0.69	135	8.2	1.5	0.2	<0.00002	8.3	0.0061	0.00076	0.46	*0.46*	-1.5%
1023.6	5.5 ± 0.4	6.4	0.05	161	0.70	128	9.4	4.9	0.3	<0.00002	8.1	0.0066	0.00286	0.27	*0.27*	-4.7%
Quench[d]	5.1 ± 0.1	5.1	0.04	148	0.71	122	8.2	1.8	0.2	<0.00002	7.5	0.0081	0.00378	0.02	*0.02*	-5.5%
Uncertainty ± 1σ	--	--	0.02	10	0.04	4	0.4	0.3	0.1	--	0.5	0.0006	0.00007	±3.0%	--	--
Predicted Equilibrium Value[e]	--	6.2	--	142	0.64	132	10.3	0.1	0.001	0.005	6.2	0.003	--	--	0.1	--

EXP-2: Water chemistry (mmol/kg), moderate pH water + granite + $scCO_2$ experiment

Time (hours)	pH (STP)[a]	pH (in-situ)[b]	F	Cl	SO_4	Na	K	Ca	Mg	Fe	$SiO_2(aq)$	Al	Mn	ΣCO_2[f], bench	ΣCO_2[g,h], in-situ	Charge Balance[i]
Initial Water[c]	5.7 ± 0.1	6.4	0.01	149	0.73	123	8.9	1.4	0.7	<0.00002	3.6	0.0019	0.00013	0.10	*0.10*	-5.3%
22.6	6.0 ± 0.2	6.7	0.01	137	0.62	123	8.1	1.8	0.2	<0.00002	5.8	0.0036	0.00061	0.56	*0.56*	-1.3%
49.9	5.4 ± 0.1	6.5	0.04	140	0.67	127	10.7	2.4	0.2	<0.00002	6.7	0.0038	0.00078	0.65	*0.65*	0.5%
117.9	5.3 ± 0.1	6.5	0.04	137	0.74	132	9.4	1.6	0.1	<0.00002	7.6	0.0057	0.00079	0.49	*0.49*	2.1%
356.7	5.5 ± 0.3	6.5	0.03	136	0.53	130	8.9	1.8	0.2	<0.00002	7.7	0.0044	0.00062	0.57	*0.57*	2.2%
693.0	5.4 ± 0.1	6.5	0.02	137	0.68	131	8.9	1.2	0.2	<0.0004	8.6	0.0064	0.00122	0.36	*0.36*	1.5%
700.3, Inject $scCO_2$																
718.2	5.2 ± 0.2	4.3	0.02	135	0.45	134	9.1	1.1	0.5	<0.0004	9.0	0.0069	0.01281	13.35	**2406**	3.1%
742.3	5.2 ± 0.1	4.4	0.02	137	0.37	131	9.2	0.9	0.6	<0.0004	8.8	0.0033	0.01095	15.44	**2405**	1.3%
814.8	5.2 ± 0.1	4.4	0.02	136	0.39	135	8.9	0.9	0.6	<0.0004	9.3	0.0009	0.00741	15.34	**2406**	3.0%
1053.7	5.3 ± 0.1	4.4	0.02	137	0.28	136	10.7	1.0	0.6	<0.0004	8.7	0.0007	0.00640	14.29	**2404**	3.6%
1318.6	5.6 ± 0.1	4.7	0.02	137	0.30	134	10.3	1.1	0.5	<0.0004	8.2	0.0004	0.00525	17.76	**2405**	2.4%
1726.5	5.3 ± 0.1	4.4	0.02	125	0.19	129	10.6	1.8	0.7	<0.0001	7.5	0.0008	0.00424	19.24	**2414**	6.3%
Quench[d]	6.1 ± 0.3	6.3	0.03	126	0.92	130	9.7	2.5	0.7	<0.0001	7.3	0.0018	0.00861	6.83	--	5.2%
Uncertainty ± 1σ	--	--	0.02	10	0.04	4	0.4	0.3	0.1	--	0.5	0.0006	0.00007	±3.0%	--	--
Predicted Equilibrium Value[e], Pre-Injection	--	6.2	--	136	0.65	126	9.8	0.1	0.001	0.004	6.2	0.003	--	--	0.1	--
Predicted Equilibrium Value[e], Post-Injection	--	5.9	--	136	0.74	186	10.9	0.1	0.007	0.009	6.1	0.002	--	--	2380	--

Table 4.3. (Cont.) Aqueous geochemistry for all experiments, including analyzed and predicted concentration.

EXP-3: Water chemistry (mmol/kg), low pH water + granite + scCO$_2$ experiment

Time (hours)	pH (STP)[a]	pH (in-situ)[b]	F	Cl	SO_4	Na	K	Ca	Mg	Fe	SiO_2(aq)	Al	Mn	ΣCO_2[f], bench	ΣCO_2[g,h], in-situ	Charge Balance[i]
Initial Water[c]	3.9 ± 0.1	6.1	0.00	135	0.72	135	9.4	0.7	0.6	<0.00002	3.6	<0.00001	0.00026	0.10	*0.10*	3.8%
22.4	3.1 ± 0.1	3.9	0.03	134	0.75	132	10.0	1.0	0.2	0.004	6.7	0.0010	0.00086	0.41	*0.41*	3.3%
47.0	3.1 ± 0.1	3.9	0.02	133	0.73	133	6.6	1.0	0.2	<0.00002	7.5	0.0019	0.00062	0.42	*0.42*	2.5%
114.5	3.0 ± 0.1	3.5	<0.001	133	0.73	132	9.1	1.1	0.2	<0.00002	8.1	<0.00001	0.00080	0.61	*0.61*	3.0%
331.6	3.7 ± 0.2	6.0	0.03	139	0.80	131	8.5	3.6	0.3	<0.0003	8.3	0.0041	0.00135	0.30	*0.30*	2.5%
667.9	5.4 ± 0.1	6.5	0.03	137	0.80	129	8.1	1.6	0.3	<0.0003	8.4	0.0048	0.00195	0.41	*0.41*	1.4%
674, Inject scCO$_2$																
696.0	5.7 ± 0.1	3.9	0.04	143	0.61	134	8.5	1.5	0.7	<0.0003	8.8	0.0050	0.01128	0.67	**3364**	0.5%
716.4	5.1 ± 0.1	4.1	0.03	138	0.50	129	8.7	1.3	0.6	<0.0003	8.6	0.0035	0.00755	13.15	**3372**	0.9%
790.8	5.3 ± 0.1	4.3	0.03	135	0.42	136	9.0	1.3	0.7	<0.0003	8.5	0.0009	0.00551	17.15	**3375**	4.0%
1001.7	5.5 ± 0.1	4.4	0.03	133	0.30	123	8.2	1.4	NI	<0.001	8.1	NI	0.04206	16.01	**3378**	4.2%
1794.9	5.7 ± 0.1	4.7	0.02	163	0.31	138	10.0	1.6	0.6	<0.00002	6.8	0.0010	0.00379	23.23	**3371**	-5.3%
Quench[d]	6.1 ± 0.1	6.4	0.02	156	1.06	136	9.2	2.4	0.7	<0.00002	6.7	0.0049	0.01289	5.75	--	-3.1%
Uncertainty ± 1σ	--	--	0.02	10	0.04	4	0.4	0.3	0.1	--	0.5	0.0006	0.00007	±3.0%	--	--
Predicted Equilibrium Value[e], Pre-Injection	--	6.2	--	147	0.63	137	10.6	0.1	0.002	0.005	6.2	0.003	--	--	0.1	--
Predicted Equilibrium Value[e], Post-Injection	--	5.8	--	147	0.73	198	11.4	0.1	0.001	0.01	6.1	0.002	--	--	3330	--

EXP-4: Water chemistry (mmol/kg), water + granite + epidote experiment

Time (hours)	pH (STP)[a]	pH (in-situ)[b]	F	Cl	SO_4	Na	K	Ca	Mg	Fe	SiO_2(aq)	Al	Mn	ΣCO_2[f], bench	ΣCO_2[g,h], in-situ	Charge Balance[i]
Initial Water[c]	5.1 ± 0.1	6.6	<0.001	135	0.66	122	7.9	0.67	0.007	<0.0001	5.5	0.015	0.00006	0.05	*0.05*	-1.9%
22.1	5.8 ± 0.1	--	0.012	141	0.70	NI	NI	NI	0.032	NI	NI	0.063	0.00015	0.34	*0.34*	--
65.8	5.9 ± 0.1	6.8	0.014	140	0.69	123	7.7	1.41	0.002	<0.0001	8.4	0.011	0.00006	0.68	*0.68*	-2.7%
139.3	5.8 ± 0.1	6.7	0.017	141	0.63	126	7.6	1.58	0.005	<0.0001	8.4	0.011	0.00009	0.76	*0.76*	-2.1%
353.7	5.7 ± 0.1	6.7	0.023	138	0.55	122	7.0	1.63	0.006	<0.0001	8.3	0.008	0.00008	0.65	*0.65*	-2.6%
858.2	5.6 ± 0.1	6.6	<0.001	139	0.51	127	7.3	1.56	0.008	<0.0001	8.1	0.009	0.00012	0.62	*0.62*	-1.0%
Quench[d]	6.2 ± 0.2	6.2	0.011	139	0.69	121	7.1	1.87	0.016	<0.0001	7.8	0.010	0.00047	0.19	*0.19*	-3.2%
Uncertainty ± 1σ	--	--	0.005	9	0.05	6	0.4	0.09	0.001	--	0.5	0.003	0.00001	±3.0%	--	--
Predicted Equilibrium Value[e]	--	7.2	--	131	0.67	122	9.5	0.10	2E-05	0.000007	6.3	0.003	--	--	0.05	--

EXP-5: Water chemistry (mmol/kg), water + granite + epidote + scCO$_2$ experiment

Time (hours)	pH (STP)[a]	pH (in-situ)[b]	F	Cl	SO_4	Na	K	Ca	Mg	Fe	SiO_2(aq)	Al	Mn	ΣCO_2[f], bench	ΣCO_2[g,h], in-situ	Charge Balance[i]
Initial Water[c]	5.2 ± 0.1	6.5	0.007	119	0.61	129	7.7	<0.002	0.006	<0.0002	7.0	0.015	0.00004	0.05	*0.05*	6.0%
21.1	6.1 ± 0.2	7.0	0.004	117	0.67	128	8.5	0.83	0.003	<0.0002	7.8	0.026	0.00027	1.03	*1.03*	7.3%
47.8	6.2 ± 0.1	6.7	0.036	119	0.58	127	8.7	1.09	0.001	<0.0002	8.5	0.023	0.00013	0.19	*0.19*	6.8%
115.6	6.1 ± 0.3	6.9	0.038	120	0.61	126	7.3	1.39	0.002	<0.0002	8.7	0.018	0.00016	0.68	*0.68*	5.4%
330.1	5.9 ± 0.3	6.7	0.027	124	0.63	126	7.4	1.65	0.003	<0.0002	8.2	0.020	0.00016	0.49	*0.49*	4.6%
666.4	5.9 ± 0.1	6.7	0.028	120	0.62	129	7.8	1.61	0.029	<0.0002	8.5	0.016	0.00019	0.63	*0.63*	7.3%
672.1, Inject scCO$_2$																
691.4	5.5 ± 0.2	4.5	0.014	121	0.17	129	5.4	2.22	0.187	<0.0002	8.9	0.004	0.00495	15.38	**2650**	5.8%
716.7	5.3 ± 0.1	4.4	0.003	119	0.26	130	7.3	2.64	0.116	<0.0002	8.9	0.001	0.00488	19.60	**2652**	8.1%
787.3	5.8 ± 0.1	4.5	0.008	117	0.20	131	7.1	3.04	0.096	<0.0002	9.0	0.002	0.00293	9.29	**2653**	9.1%
1003.2	5.7 ± 0.1	4.6	0.022	139	0.15	129	7.5	3.19	0.026	<0.0002	8.6	0.001	0.00159	14.13	**2633**	0.0%
1316.0	5.5 ± 0.1	4.5	0.024	135	0.14	130	7.0	3.08	0.017	<0.0002	8.3	0.001	0.00168	17.71	**2637**	2.1%
Quench[d]	6.5 ± 0.1	6.7	0.016	118	0.78	113	6.4	6.52	0.030	0.01	6.8	0.002	0.01147	12.26	--	1.4%
Uncertainty ± 1σ	--	--	0.005	9	0.05	6	0.4	0.09	0.001	--	0.5	0.003	0.00001	±3.0%	--	--
Predicted Equilibrium Value[e], Pre-Injection	--	7.2	--	138	0.62	129	10.0	0.11	2E-05	0.000008	6.3	0.003	--	--	0.1	--
Predicted Equilibrium Value[e], Post-Injection	--	5.5	--	138	0.62	157	2.9	0.34	0.006	0.08	6.1	0.002	--	--	2570	--

[a]Standard conditions temperature (25°C) and pressure (0.1 MPa).
[b]Calculated, see Section 3.2 for explanation.
[c]Unreacted water composition.
[d]Water composition after termination of experiment; In-situ pH calculated at standard conditions.
[e]See Section 3.2 for explanation.
[f] Measured values corresponding to sample collected for bench pH; See Section 5.4 for additional explanation.
[g] (*Italicized*) Pre-injection in-situ values assumed to be same as bench values; See Section 5.4 for additional explanation.
[h] (**Bold**) Post-injection in-situ values calculated; See Sections 3.2 and 5.4 for additional explanation.
[i] Charge balance includes minimal phosphate and bromide values, as well as calculated bicarbonate values (not shown).
NI = not included because data appear anomalous.

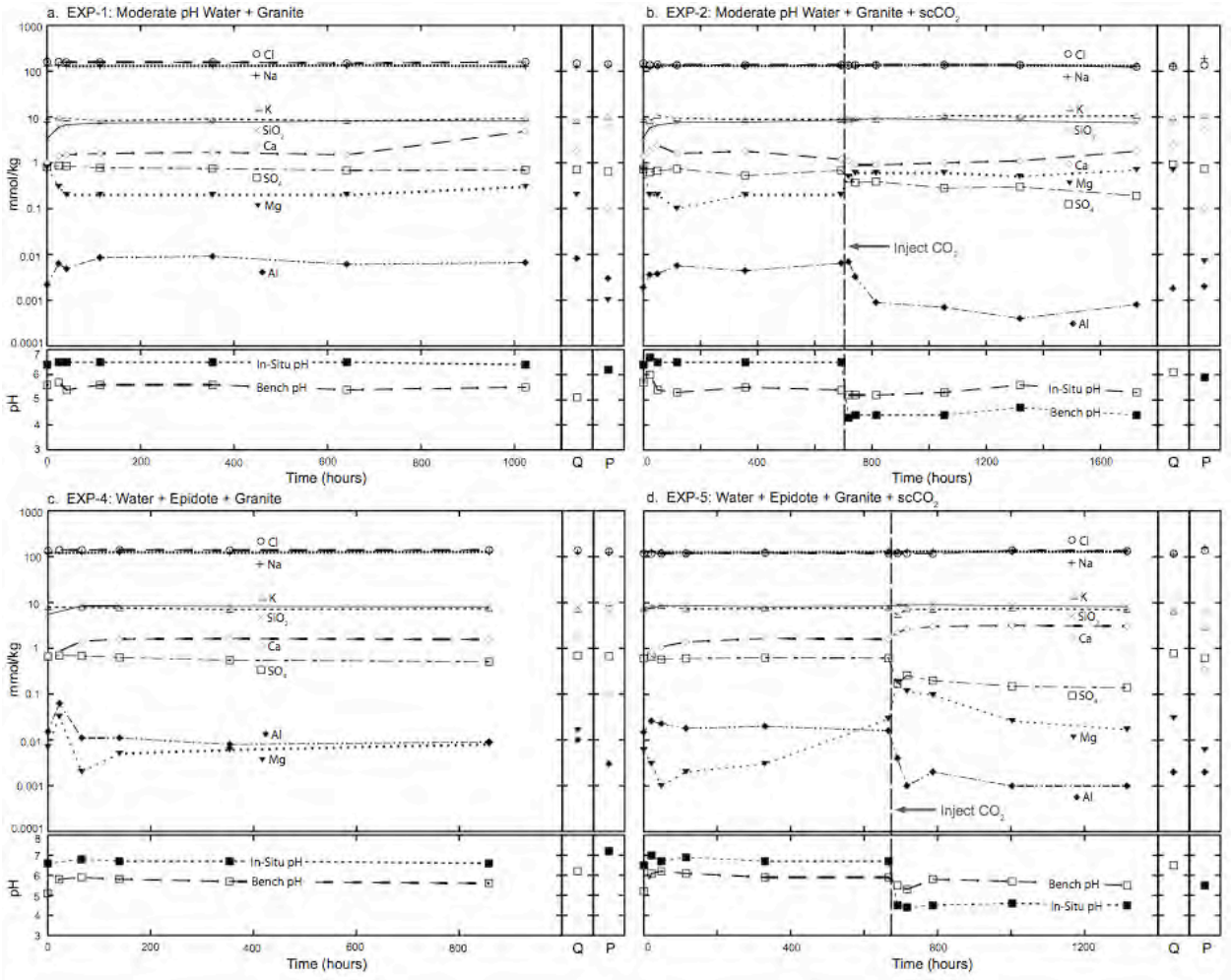

Figure 4.1. Water chemistry as a function of time for (a.) the water-granite experiment, EXP-1, (b.) the moderate pH water-granite-scCO$_2$ experiment, EXP-2, (c.) the water-epidote-granite experiment, EXP-4, and (d.) the water-epidote-granite-scCO$_2$ experiment, EXP-5. Major ion concentrations and pH are plotted for each experiment. On the right of each graph, quench geochemistry (at 25 °C, 0.1 MPa) and predicted equilibrium states (GWB) are also plotted for each experiment in the columns labeled 'Q' and 'P,' respectively. The initial water composition (25 °C, 0.1 MPa) is plotted along the y-axis in each case.

Table 4.4 Comparison of predicted vs. observed secondary minerals at 250 °C.

	EXP-1		EXP-2		EXP-3		EXP-4		EXP-5		Field[b]
Description	Water + Granite		Moderate pH Water + Granite + $scCO_2$		Low pH Water + Granite + $scCO_2$		Water + Epidote + Granite		Water + Epidote + Granite + $scCO_2$		--
	P	O	P	O	P	O	P	O	P	O	
Illite[a]	X	X	X	X	X	X		X	X	X	X
Smectite	X			X		X	X	X	X	X	
Zeolite	X	?		?		?	X	X			X
Carbonate			X		X				X		X
Quartz	X		X		X		X		X		X
Albite	X										X
K-Feldspar	X						X				X
Epidote							X				X
Prehnite							X				X
Fe-Oxide/Sulfide	X		X			X					X

[a] Proxy minerals such as muscovite and phengite are included in this category
[b] Commonly observed alteration minerals observed in hydrothermal fields at 250 ºC (Henley and Ellis, 1983)
P = predicted mineral
O = observed mineral
X = indicates predicted or observed mineral

4.3 Methods and Materials

4.3.1 Experimental Apparatus

Hydrothermal experiments were conducted in rocking autoclaves (rocker bombs) and flexible Au-Ti reaction cells (Dickson cells) using established methods (Seyfried et al., 1987). Each gold cell has a volume of 220-260 cm^3 and is mated with a titanium head and exit tube. The exit tube ports directly to a metered sample valve external to the experimental system. The configuration of the pressure vessel and reaction cell allows for periodic sampling of the liquid, gas, or supercritical phase without perturbing the experiment. Maximum fluctuations for temperature and pressure were approximately ±2.4°C and ±1.0 MPa, respectively (Table 4.1). Aqueous samples were collected approximately every 1, 2, 5, 14, and 28 days for each stage of

an experiment (pre- or post-injection). We also sampled the unreacted water and minerals as well as the very final reacted water and minerals for analysis.

4.3.2 Analytical Methods

We analyzed aqueous samples for major cations and anions, trace metals, and pH. In addition, unreacted and reacted minerals were analyzed for surface area and dissolution/ precipitation features.

Samples were filtered through porous titanium (0.5μm) at the base of a titanium exit tube. Samples of unreacted water and final, reacted water were filtered manually using Millipore 0.45μm filters. Major cation samples were diluted approximately ten times (10X) and acidified with trace-metal-grade nitric acid to a pH of 2. Aqueous samples were refrigerated as soon after sampling as practicably possible.

Major cation and anion concentrations were determined by inductively-coupled plasma optical emission spectroscopy (ICP-OES) and ion chromatography (IC), respectively. Trace metal concentrations were determined by inductively-coupled plasma mass spectrometry (ICP-MS). The pH was measured using an Orion pH meter and Ross microelectrode.

We analyzed minerals and mineral digests using a combination of optical microscopy, X-ray diffraction (XRD) (Cu-Kα), ICP-OES, ICP-MS, IC, electron microprobe, high-resolution field emission scanning electron microscopy (FE-SEM), and energy dispersive spectra (EDS). Surface areas of unreacted and reacted mineral powders were determined using the Braunauer, Emmett and Teller (BET) method (1938). BET data are not discussed further, but are included in Tables 4.1 and 4.2.

4.3.3 Experimental Minerals and Waters

The synthetic granite used in this study consists of powdered (75%, <45 μm) and chipped (0.1-0.7 cm) research-grade minerals. The use of mineral chips allows recovery for post-experimental examination of textures, while use of powder enhances reactivity and kinetic rates. Mineral proportions are included in Table 4.2. Quartz (Qtz), K-feldspar (Kfs), oligoclase (Olg), biotite (Bt), and epidote (Ep) were analyzed for major and minor trace element concentrations after acid digestion by ICP-OES (Table 4.2) and ICP-MS. Oligoclase and biotite chips were also analyzed for major element chemistry by electron microprobe (Table 4.2). Results indicate the plagioclase is oligoclase, An_{23} ($Na_{0.77}Ca_{0.23}(Si_{2.77},Al_{1.23})O_8$) and is not chemically zoned. The K-feldspar is perthitic with approximately 25% albite and 75% K-feldspar lamellae. The epidote composition is $Ca_2(Al_{0.2}Fe_{0.8})Al_2Si_3O_{12}(OH)$, and the biotite composition is approximately $K(Mg_{1.7},Fe_{1.3})(AlSi_3O_{10})(OH)_2$, with notable amounts of Ti, Mn, Cr, and possibly Fe^{3+}.

The synthetic waters (ionic strength (I) ≅ 0.1 molal) were prepared using research-grade salts and solutions. Each contained molal quantities of Na, Cl, and HCO_3 and millimolal quantities of K, SiO_2(aq), SO_4, Ca, Al, and Mg (initial brine compositions, as shown in Table 4.3).

4.4 Experimental and Theoretical Results

4.4.1 Mineral Precipitation

Based on XRD, optical, and SEM analysis; mineral precipitation occurs in all five experiments. Table 4.4 summarizes secondary mineral assemblages observed in each experiment. Whole rock and clay fraction XRD data include results for unreacted and reacted powders. For each experiment, whole rock results exhibit discernible diffractograms for unreacted minerals only (Qtz, Olg, Ksp, Bt, ± Ep). Clay fraction diffractograms and

optical/SEM observation (below), however, do indicate clay precipitation in each experiment (Figure 4.2). Both air-dried and glycolated clay-fraction samples were analyzed, with results showing an appropriate shift in diffraction for swelling clays. Air-dried results are not contained here.

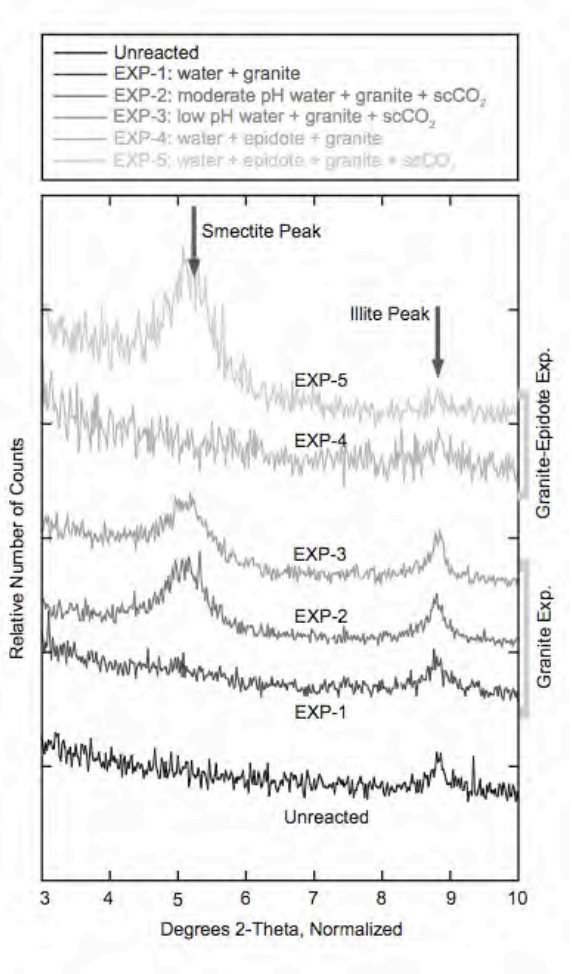

Figure 4.2. Normalized and relative XRD diffraction patterns for glycolated clay-fraction samples from the unreacted granite and from each experiment. Noted peaks include illite peaks on right and smectite peaks on left. Illite peaks are evident in samples from the unreacted granite and from water-granite±scCO$_2$ experiments (EXP-1, -2, and -3). Illite peaks are less defined in the water-epidote-granite±scCO$_2$ experiments (EXP-4 and -5). Smectite peaks are only evident in experiments with CO$_2$, including water-granite-CO$_2$ experiments (EXP-2 and -3) and the water-epidote-granite-CO$_2$ experiment (EXP-5).

The XRD results for unreacted and reacted powders (EXP-1, -2, and -3) indicate the presence of illite. Illite may also be present in the reacted epidote-granite powders (EXP-4 and -5), although the diffraction peaks are not as well defined. Based on optical and SEM observation, there is minimal illite in the unreacted granite as compared to reacted granite suggesting illite precipitated in the experiments. The XRD results indicate the presence of smectite clays in the water-granite-scCO_2 experiments (EXP-2 and -3) and the water-epidote-granite-scCO_2 experiment (EXP-5). There is no XRD evidence for smectite in the water-epidote-granite experiment (EXP-4).

Optical and SEM results also indicate multiple precipitates in each experiment. We observed three precipitates in the granite experiment (EXP-1) including a sparse needle-forming aluminosilicate (interpreted as most likely to be zeolite) with varying amounts of potassium and titanium (Figure 4.3.a), an abundant petal-forming Mg-Fe-rich aluminosilicate (Figure 4.3.b), and one example of hummocky silica. The Mg-Fe-rich aluminosilicate is zoned in reflected light and varies from green to blue. Based on both SEM and XRD data (Figure 4.2), we interpret the Mg-Fe-rich aluminosilicate as an illite (or more technically, probably a fine-grained mica such as celadonite). We believe silica formed during the cooling process (Section 4.4.3.2).

In the water-granite-scCO_2 experiments (EXP-2 and -3), we observed similarly composed illite and zeolite (?) in addition to an Fe-rich, rosette-forming aluminosilicate (Figure 4.3.c). Rosettes also contain significant magnesium and minor calcium, and appear blue-green in reflected light. Together, SEM and XRD data indicate this mineral is a smectite (Figure 4.2). The low pH water-granite-scCO_2 experiment (EXP-3) contains minor amounts of three additional minerals, as identified by EDS: scheelite ($CaWO_4$), magnetite, and gold (Figures 4.3.d, 4.3.e, and 4.3.f).

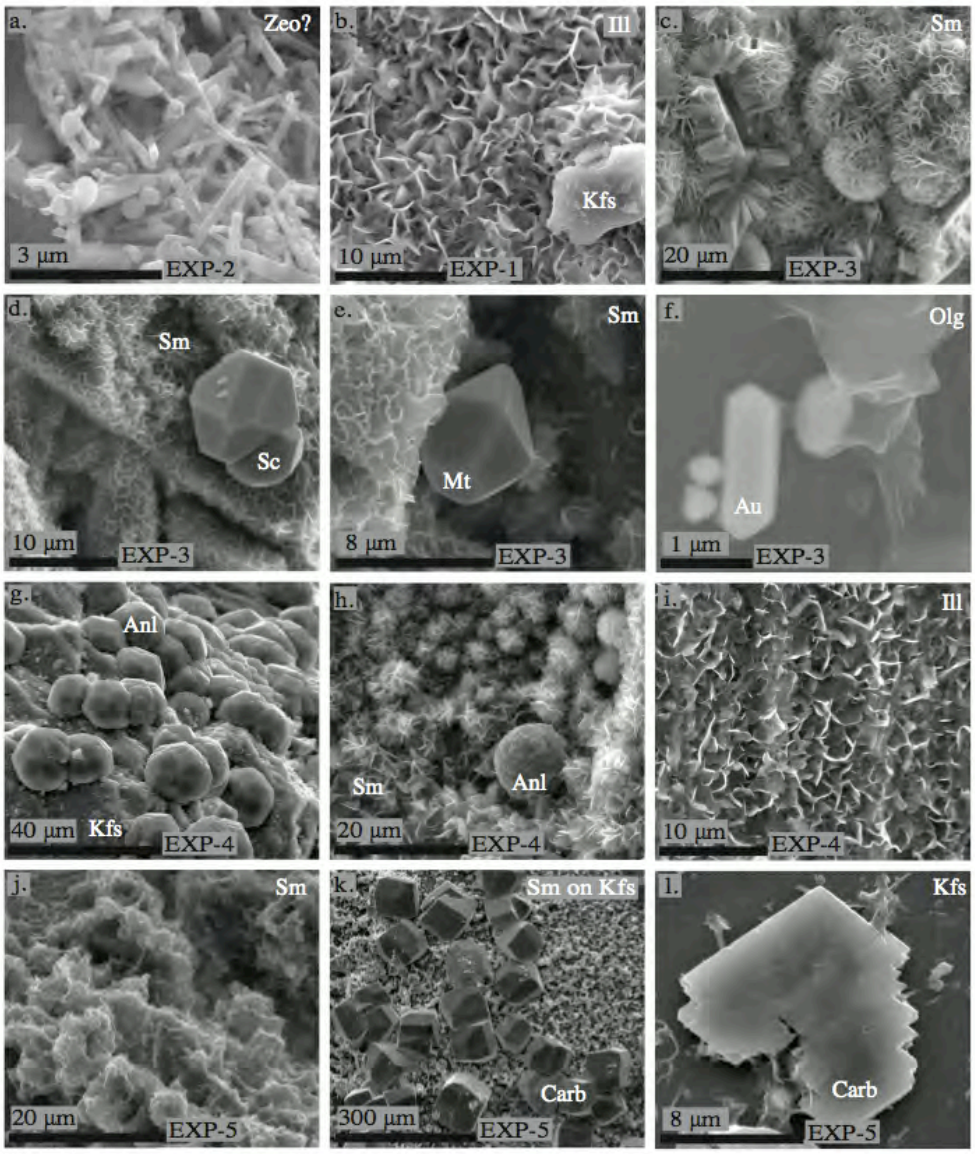

Figure 4.3. FE-SEM micrographs of secondary minerals observed. Each image includes a scale as well as labels for the mineral(s) and associated experiment. Images (a.) and (b.) show typical needle-forming aluminosilicate (zeolite?) and illite petals, respectively, as observed in granite experiments, EXP-1, -2, and -3. (c.) Typical rosette-forming smectite, as observed in $scCO_2$-containing granite experiments, EXP-2 and -3. Images (d.), (e.), and (f.) show scheelite, magnetite, and gold, as observed in the low pH water-granite-$scCO_2$ experiment, EXP-3. (g.) Analcime, as observed in the water-epidote-granite experiment, EXP-4. (h.) Analcime in a bed of rosette-forming smectite, as observed in EXP-4. (i.) Illite, as observed in EXP-4. (j.) Poorly-formed smectite, as observed in $scCO_2$-containing water-epidote-granite experiment, EXP-5. Images (k.) and (i.) show blocky and rhombohedral Ca-carbonates from EXP-5.

We observed a slightly different secondary assemblage in the epidote-granite results. In the epidote-granite experiment (EXP-4), SEM and EDS data indicate the presence of trapezohedral analcime, petal-forming illite (~celadonite, Fe-Ca-rich), and rosette-forming smectite (Fe-Mg-rich) (Figures 4.3.g, 4.3.h, and 4.3.i). Optically, the illite is reddish and the smectite is green. Smectite is a minor phase in EXP-4 since it was observed in only one location during optical and SEM analysis, and is not evident in XRD data.

In the water-epidote-granite-scCO_2 experiment (EXP-5), abundant, poorly-formed smectite (Fe-Ca-rich) (Figure 4.3.j), blocky and rhombohedral Ca-carbonate, (Figure 4.3.k and 4.3.l), and globular silica formed. Based on XRD data, illite is also likely present (Section 4.4.1) but could not be positively identified by SEM. Based on aqueous geochemistry, we believe the silica and carbonate formed during the cooling process (Section 4.4.3.2). Saturation indices (not included) calculated alongside in-situ pH calculations (Section 4.2.2) support this contention.

As an ancillary note, the tungsten source in EXP-3 is likely the high-temperature molybdenum lubrication used on the pressure vessels. Given the possible tungsten contamination in EXP-3, scheelite precipitation is not unprecedented as compared to granitic hydrothermal systems. We attribute gold observations to mobilization from the reaction cell during experimentation; gold crystal morphology contradicts contamination from sample coating or reaction cell abrasion.

4.4.2 Mineral Dissolution

Based on optical and SEM analysis, minerals from the water-rock-scCO_2 experiments (EXP-2, -3, and -5) are more dissolved than minerals in the water-rock experiments (EXP-1 and -4). The feldspars in the water-granite experiments (EXP-1, -2, and -3) exhibit dissolution textures (Figures 4.4.a, 4.4.b, 4.4.c, and 4.4.d), with relatively more dissolution of K-feldspar

than plagioclase. Feldspars in EXP-2 (initial pH = 5.7) are relatively less dissolved than feldspars in EXP-3 (initial pH = 3.9). In the epidote-granite experiments (EXP-4 and -5), epidote (Figures 4.4.e and 4.4.f), oligoclase (Figure 4.4.g), K-feldspar, and quartz (Figure 4.4.h) exhibit dissolution textures, in order of decreasing extent. In all experiments, biotite is not dissolved but exhibits clay mineralization directly on its surface (Figure 4.4.i).

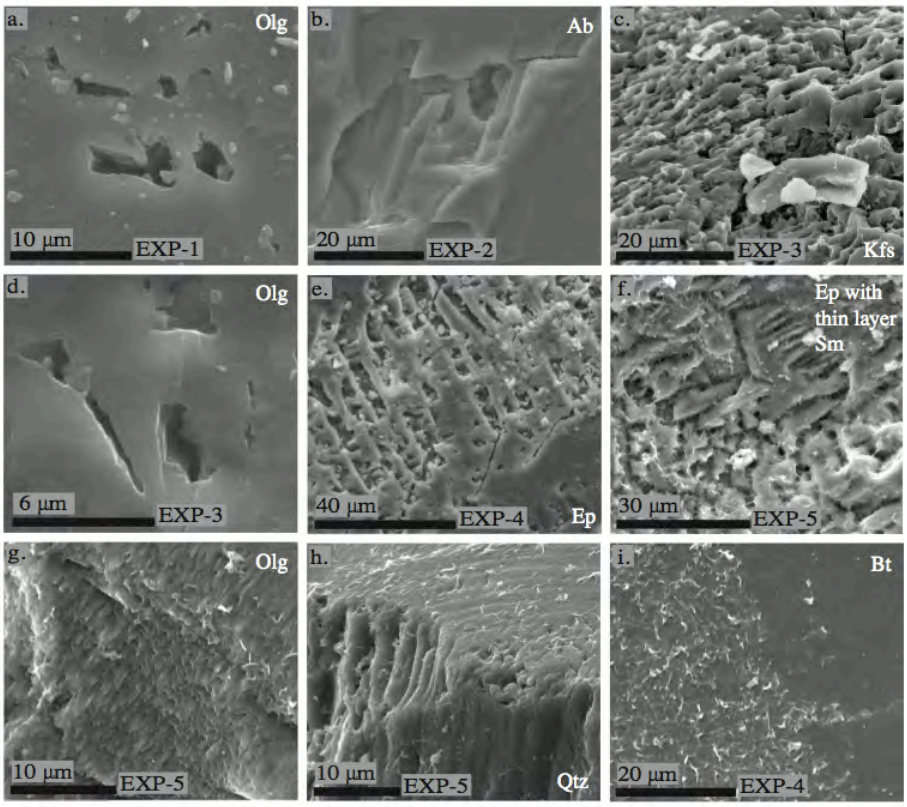

Figure 4.4. FE-SEM micrographs of reactant mineral dissolution textures. Each image includes a scale as well as labels for the mineral(s) and associated experiment. Images (a.), (b.), (c.), and (d.) represent typical dissolution pitting/etching in oligoclase, albite, and K-feldspar in the granite experiments (EXP-1, -2, and -3). Progressively more dissolution is evident in feldspars from $scCO_2$-injected systems (EXP-2 and -3). Images (e.) and (f.) respectively show epidote dissolution in the water-epidote-granite experiment (EXP-4) and the water-epidote-granite-$scCO_2$ (EXP-5). As seen in (f.), epidote surfaces in EXP-5 are often coated with a thin layer of smectite. Images (g.) and (h.) respectively show typical oligoclase and quartz dissolution in EXP-5. As shown in image (i.), biotite does not exhibit dissolution textures, but clay minerals precipitate on biotite surfaces in all experiments.

4.4.3 Major Element Aqueous Geochemistry

Table 4.3 presents aqueous geochemical data for each experiment, and Figure 4.1 shows select geochemical trends for EXP-1, -2, -4, and, -5. The time of $scCO_2$ injection is noted for EXP-2 and -5. Data from EXP-3 are not shown since results are generally similar to those from EXP-2.

4.4.3.1 Experimental Results

Changes in cation and anion concentrations in each experiment over time indicate active fluid-rock interactions. In the water-granite experiment (EXP-1) and the pre-injection portion of the water-granite-$scCO_2$ experiments (EXP-2 and -3), there are relatively constant concentrations of Cl, Na, K, and SO_4; increasing concentrations of SiO_2(aq) and Al; and decreasing concentrations of Mg (Figures 4.1.a and 4.1.b). Concentrations for these analytes approach steady state at termination of EXP-1 and prior to injecting $scCO_2$ into EXP-2 and -3. Calcium concentrations vary irregularly over time, suggesting that steady state was not established between the fluid and calcium-bearing minerals.

Post-injection concentrations of Cl, Na, and K are relatively constant for EXP-2 (Figure 4.1.b) and EXP-3. Concentrations of Ca, SO_4, and Al appear to decrease in both experiments during the first 5 days after $scCO_2$ injection while Mg concentrations increase over the same period of time. Post-injection concentrations of SiO_2(aq) gradually decrease over time. Not all analytes establish a steady-state concentration by the end of these experiments, including SiO_2(aq), Ca, Mg, SO_4, and Al in EXP-2 and SiO_2(aq) and Ca in EXP-3.

In the water-epidote-granite experiment (EXP-4) and the pre-injection portion of the water-epidote-granite-$scCO_2$ experiment (EXP-5), there are relatively constant concentrations of Cl, Na, K, and SO_4 and increasing concentrations of SiO_2(aq) and Ca (Figures 4.1.c and 4.1.d).

Concentrations for these analytes approach steady state at termination of EXP-4 and prior to injecting $scCO_2$ into EXP-5. Concentrations for Al and Mg vary more irregularly over time but also approach a steady-state concentration, with the exception of Mg in EXP-5.

Post-injection concentrations of Cl, Na, and K are relatively constant for EXP-5 (Figure 4.1.d). Concentrations of SiO_2(aq) and Ca appear to increase during the first 5 days after $scCO_2$ injection while SO_4 and Al concentrations decrease over the same period of time. Post-injection concentrations of Mg increase abruptly then gradually decrease over time. With the exception of Mg, these analytes appear to establish a steady-state concentration prior to the end of the experiment.

4.4.3.2 Results for Quench Samples

When an experiment is cooled, depressurized, and the contents processed; samples are collected to identify resulting dissolution or precipitation reactions. We refer to this process as 'quenching' and to the samples as 'quench' samples. Although completed as quickly as possible, the entire process can take up to 24 hours. The quench sample data are included in Table 4.3 and shown on Figure 4.1 in the columns labeled 'Q' (i.e., quench) to the right. Quench samples contain higher concentrations of Ca, SO_4, and Al and lower concentrations of K compared to the samples collected just prior to quenching. In two cases, EXP-1 and EXP-5, concentrations of SiO_2(aq), Na, and Cl also decrease.

Increased Ca and SO_4 suggest possible dissolution of a calcium sulfate during the quench process. We observed no anhydrite or similar mineral during analysis. Decreased SiO_2(aq), Na, Cl, and possibly K suggest potential precipitation of silica and/or halite/sylvite. We observed no salts during analysis, but we identified examples of silica precipitation in both EXP-1 and EXP-

5. Increased concentrations of Al are more difficult to explain, especially with the competing Ca-Na-K-Si reactions already identified.

4.4.4 Total Dissolved Inorganic Carbon (ΣCO_2)

Table 4.3 includes ΣCO_2(aq) 'bench' analyses that correspond to de-gassed and cooled pH samples exposed to atmosphere. Unreacted water started with approximately 0.1 mmol/kg ΣCO_2(aq) and, after exposure to compressed air during reaction cell leak tests, increased to a maximum of 0.8 mmol/kg. We also observe variability in the amounts of ΣCO_2(aq) measured during the water-rock portion of each experiment (0.1-0.8 mmol/kg) and attribute this to reduced instrument precision near the method detection limit. For these samples, contamination and analytical precision pose no problem since ΣCO_2(aq) is significantly undersaturated during the water-rock portion of each experiment and our unreacted minerals exclude carbonates. No issues have been identified with the post-injection ΣCO_2(aq) bench concentrations, which are also reported in Table 4.3.

We exclude results for in-situ ΣCO_2(aq) measurements because of identified sampling and analysis concerns. Specifically, measurements of pre-injection ΣCO_2(aq) are poor because of the combination of atmospheric contamination (from syringe tip) and reduced instrument precision near the detection limit. Measurements of post-injection ΣCO_2(aq) are irregular because of sporadic de-gassing during sample collection. In order to conduct geochemical modeling (Section 4.2.2), therefore, we present calculated ΣCO_2(aq) concentrations (Table 4.3) in place of measured ΣCO_2(aq). We are able to substitute calculated values for measured values because experiments were saturated with respect to post-injection ΣCO_2(aq) (Section 4.2.1). An

executable file available from Duan & Sun, representing their 2003 EOS for CO_2, was used for these calculations (2011, personal communication).

4.4.5 pH

The pH measurements taken in the presence of atmosphere and at standard temperature and pressure conditions (STP) are included as 'bench pH' values in Table 4.3 and shown on Figure 4.1. Granite experiments, EXP-1, -2, and -3, had initial pH values of 5.6, 5.7, and 3.9, respectively. Epidote-granite experiments, EXP-4 and -5, had initial pH values of 5.1 and 5.2, respectively.

In the case of the water-rock portion of each experiment (i.e., no $scCO_2$), bench pH values fluctuate by as much as ±1.0 over the first 48 hours, and then approach steady-state values of 5.4 – 5.5 in EXP-1, -2, and -3 and 5.6 – 5.9 in EXP-4 and -5. After injecting $scCO_2$ into EXP-2, -3, and -5; bench pH values fall within a couple of days and approach a steady-state value of 5.3 – 5.4 in EXP-2 and -3 and 5.5 in EXP-5.

Calculated, in-situ pH values are an average of 1.0 unit higher than bench pH values during the water-rock portion of each experiment. For those experiments also injected with $scCO_2$ (EXP-2, -3, and -5), post-injection in-situ pH values are an average of 1.0 unit lower than bench pH values (Table 4.3 and Figure 4.1).

4.4.6 Geochemical Predictions

In this section, we compare major cation and anion concentrations as predicted by GWB equilibrium calculations (Section 4.2.2) to those measured in the last sample before the quench process. We also compare predicted and observed secondary mineralogy.

4.4.6.1 Predictions for Aqueous Geochemistry

As compared to experimental concentrations, predicted concentrations correspond well for Cl, Na, K, and generally SiO_2(aq) (Table 4.3 and Figure 4.1). However, predictions consistently underestimate Ca and Mg concentrations (all experiments), and overestimate SO_4 in experiments with $scCO_2$ (EXP-1, -3, and -5). Aluminum predictions are an average of ~53% higher than measured concentrations in EXP-2, 3, and -5 and an average of ~61% lower in EXP-1 and -4. In addition, the SiO_2(aq) prediction is ~26% lower than experimental concentrations in EXP-5.

Calculated and predicted in-situ pH values are also included in Table 4.3 and shown on Figure 4.1. Predicted in-situ pH is 0.2 to 0.3 units higher than calculated in the water-rock portion of the granite experiments (EXP-1, -2, and -3) and 0.5 to 0.6 units higher in the water-rock portion of the epidote-granite experiments (EXP-4 and -5). Post-injection, GWB predicts that in-situ pH is 1.1 to 1.4 units lower than calculated for the water-granite-$scCO_2$ experiments (EXP-2 and -3) and 1.0 unit lower in the water-epidote-granite-$scCO_2$ experiment (EXP-5).

4.4.6.2 Predictions for Secondary Mineralogy

Models predict illite as a secondary mineral in all experiments, except the water-epidote-granite experiment (EXP-4); we observed illite in all experiments (Table 4.4). Results of GWB predict smectite as a secondary mineral in the water-granite experiment (EXP-1) as well as both epidote-granite experiments (EXP-4 and -5); we observed abundant smectite in the $scCO_2$ experiments (EXP-2, -3, and -5) and a minimal amount in the epidote-granite experiment (EXP-4). Results of GWB also predict zeolite in experiments without $scCO_2$ (EXP-1 and -4), but we observe it only in the water-epidote-granite experiment, EXP-4. Results of GWB predict quartz formation in all experiments and calcite formation in the water-epidote-granite-$scCO_2$

experiment (EXP-5) and calcite-magnesite-siderite formation in the water-granite-$scCO_2$ experiments (EXP-2 and -3). We observed no quartz or carbonate that formed at experimental conditions. Although sometimes predicted, we also observed no albite, K-feldspar, or epidote in experimental systems.

4.5 Discussion

4.5.1 A Path to Equilibrium: Experimental vs. Theoretical Results

Here, we compare experimental results with equilibrium predictions to determine the extent of system equilibration, the sequence of water-rock reactions, and the water-rock response to $scCO_2$ injection. As noted in Section 4.4.3.1 and shown in Figure 4.1, some major element concentrations reach a steady state over the course of each experiment. Congruence between steady state concentrations and equilibrium predictions (Section 4.4.6.1) indicate local equilibrium. In contrast, some major elements do not reach steady state concentrations, which suggests on-going reaction. This is consistent with the minerals recovered from the experiment (Table 4.4), the continued presence of certain primary minerals and the failure to form specific secondary minerals indicates incomplete reaction progress. Activity diagrams also indicate ongoing reaction, where reaction paths end within stability fields as opposed to being on phase boundaries. We provide two sets of activity diagrams (Figures 4.5 and 4.6) to clarify reaction progress. Each figure plots data from two experiments, the water-granite-$scCO_2$ experiment, EXP-2; and the water-epidote-granite-$scCO_2$ experiment, EXP-5. The other experiments display similar relationships as those shown in Figures 4.5 and 4.6.

Figures 4.5.a and 4.5.b show mineral stability fields, aqueous species activities for each sample, and the final predicted equilibrium state in the CaO-Al_2O_3-SiO_2-H_2O-CO_2 system for EXP-2 and EXP-5, respectively. Two diagrams are shown for each experiment and include

stability fields for experimental conditions just prior to $scCO_2$ injection (on left), and after $scCO_2$ injection and just prior to quenching (on right). Notice the calcite stability field increases significantly with addition of $scCO_2$. (See figure caption for other conventions.) Figures 4.6.a and 4.6.b similarly show mineral stability relationships, aqueous species activities, and the final predicted equilibrium state for the K_2O-Al_2O_3-SiO_2-H_2O-CO_2 system. In Figure 4.6, the stability fields do not shift with addition of $scCO_2$, so pre- and post-injection data are shown on one plot for each experiment. Both Figures 4.5 and 4.6 plot log $(aAl^{3+})/(aH^{+})^3$ against log $aSiO_2(aq)$ (a = activity).

Before discussing each diagram individually, we note and discuss a feature they all share: the illustrated reaction paths all approach or track along the chalcedony stability boundary, indicating saturation with chalcedony and supersaturation with quartz. This trend is best explained by the Ostwald step rule, which relates nucleation kinetics, thermodynamic mineral solubilities, and interfacial tensions (e.g., Stumm and Morgan, 1996). The rule postulates that the least stable phase will precipitate first in a chain of reactions because the nucleation kinetics favor formation of the phase with the lowest fluid-rock interfacial tension (e.g., Rimstidt and Barnes, 1980). Applying this rule to our system (or a natural system), it is not unreasonable to find that silica activity is initially controlled by chalcedony instead of quartz; the Ostwald step rule permits chalcedony precipitation prior to quartz because chalcedony has a higher solubility and lower fluid-rock interfacial tension than quartz.

As also related to the silica trends on the activity diagrams, we note that calculations for the final predicted equilibrium state allowed quartz precipitation (Section 4.2.2); so predictions necessarily lie along the quartz stability boundary. This has introduced a bias towards lower silica activities for the final predicted equilibrium state. If calculations allowed chalcedony

precipitation instead of quartz, the predicted equilibrium states would align with the chalcedony boundary, and therefore, more closely match observed results. In our assessment of reaction path progress for each activity diagram below, we ignore this low bias.

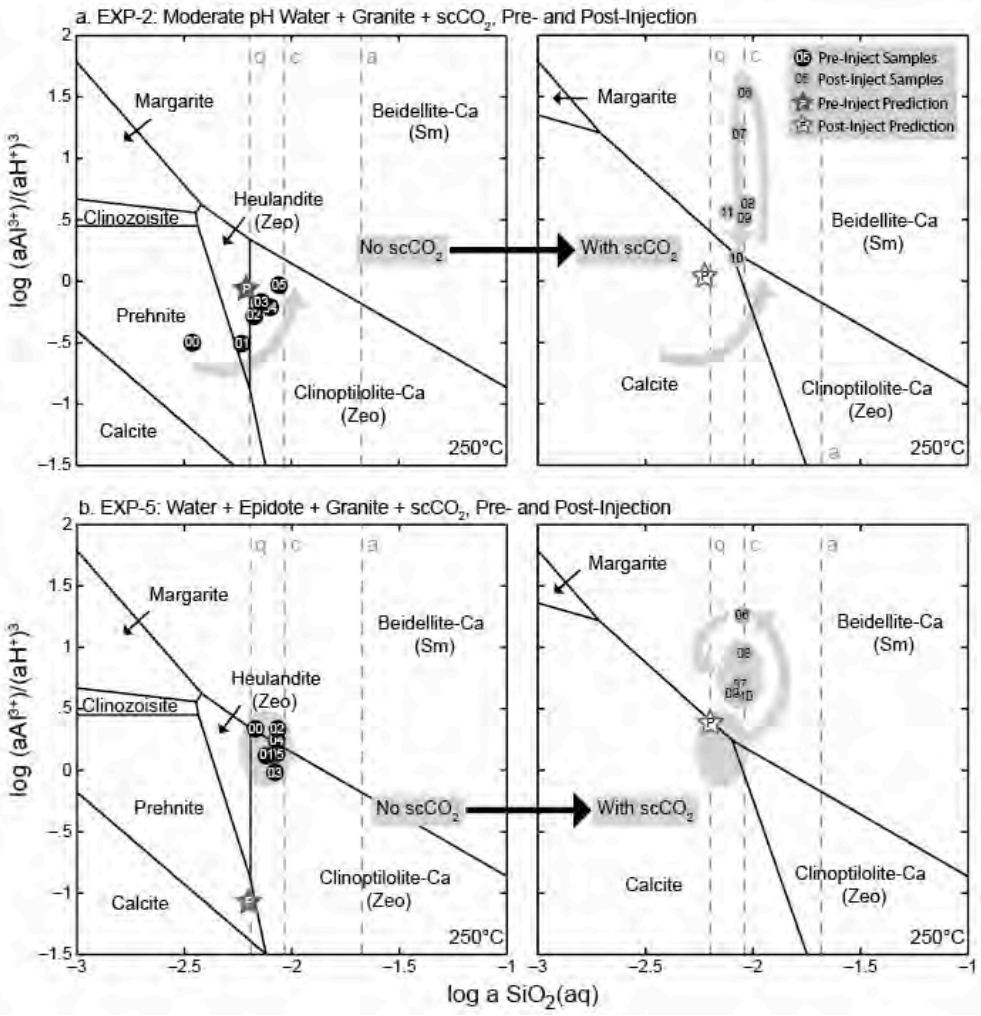

Figure 4.5. Mineral stability relationships, aqueous species activities for individual samples, and predicted equilibrium states in the CaO-Al2O3-SiO2-H2O-CO_2 system for a.) the water-granite-$scCO_2$ expeirment, EXP-2 and b.) the water-epidote-granite-$scCO_2$ experiment, EXP-5. Two diagrams are shown for each experiment and include stability fields for experimental conditions just prior to $scCO_2$ injection (on left) and after $scCO_2$ injection and just prior to the quench (on right). Silica stability fields for quartz ('q'), chalcedony ('c'), and amorphous silica ('a') are also outlined on each diagram with dashed, vertical lines. Activities for sequential, pre-injection samples are on the left side; activities for post-injection samples are on the right side. Wide,

gray arrows indicate the general path to equilibrium during experiment evolution. Predicted pre- and post-injection equilibrium states are shown using dark and light-colored stars, respectively.

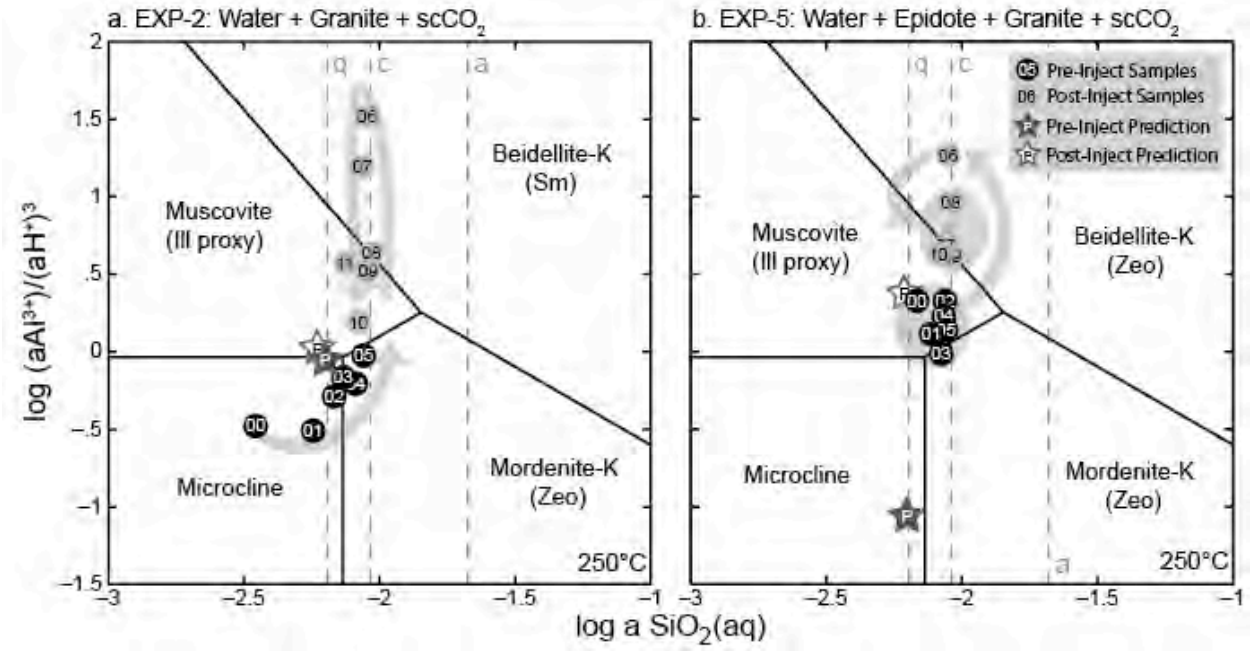

Figure 4.6. Mineral stability relationships, aqueous activities for individual samples, and predicted equilibrium states in the K2O-Al2O3-SiO2-H2O-CO_2 system for a.) the water-granite-scCO_2 experiment, EXP-2 and b.) the water-epidote-granite-scCO_2 experiment, EXP-5. Pre- and post-injection stability fields do not shift with changes in CO_2, so there is only one diagram for each experiment. Silica stability fields for quartz ('q'), chalcedony ('c'), and amorphous silica ('a') are outlined on each diagram with dashed, vertical lines. Activities for sequential, pre-injection samples are shown with dark-colored circles; activities for post-injection samples are shown with light-colored circles. Wide, gray arrows indicate the general path to equilibrium during experiment evolution. Predicted pre- and post-injection equilibrium states are shown using dark and light-colored stars, respectively.

In the water-granite-scCO_2 (EXP-2) diagram, species activities for pre-injection samples define a reaction path that moves from microcline to zeolite stability (Figure 4.6.a) and from prehnite to zeolite stability (Figure 4.5.a). The reaction paths terminate near the predicted equilibrium state within the zeolite stability field (Figure 4.5.a) or on the zeolite-illite stability boundary (Figure 4.6.a). These predicted theoretical minerals correspond to minerals precipitated in the experiments (Table 4.4); observations indicate near-equilibration in the pre-injection portion of EXP-2.

The post-injection reaction path for EXP-2 shows an abrupt swing into the smectite stability field (Figure 4.5.a and 4.6.a), then decreases towards the predicted equilibrium state within the carbonate stability field (Figure 4.5.a) and along the illite-microcline stability boundary (Figure 4.6.a). The reaction path falls just short of achieving the predicted equilibrium state, indicating incomplete reaction progress. Given additional time, the experiment may have achieved equilibrium. The theoretical minerals predicted by the position of the final aqueous activities, smectite (Figure 4.5.a) and illite (Figure 4.6.a), correspond to minerals observed in the post-injection portion of EXP-2 (Table 4.4). In addition, the final aqueous activities of the reaction path in Figure 4.5.a agree with the absence of carbonate in this experiment.

With respect to the water-epidote-granite-scCO_2 (EXP-5) diagrams, species activities for pre-injection samples cluster in the zeolite, smectite (Figure 4.5.b), and illite (Figure 4.6.b) stability fields. The reaction paths terminate far from the predicted equilibrium state, indicating the system was far from equilibrium prior to injecting scCO_2. The theoretical minerals predicted by the position of the final aqueous activities correspond to minerals that precipitated, including illite and zeolite (Table 4.4).

The post-injection reaction path for EXP-5 also shows an abrupt swing into the smectite stability field. The reaction path then moves towards the predicted equilibrium state along the carbonate-smectite stability boundary (Figure 4.5.b) and within the illite stability field (Figure 4.6.b). Like results for EXP-2, the reaction paths do not achieve the predicted equilibrium state, indicating incomplete reaction progress. Theoretical mineral predictions agree with the presence of illite and smectite in EXP-5 (Table 4.4). Results also agree with the absence of carbonate, as attributable to in-situ formation.

The relatively circuitous path to equilibrium in the post-injection portion of these activity diagrams merits comment. The abrupt increase in log $(aAl^{3+})/(aH^{+})^3$ drives the reaction pathways away from the predicted equilibrium states. This swing into the smectite field after $scCO_2$ injection may seem counterintuitive since carbon speciation leads to an increase in H^+ activity which could lower log $(aAl^{3+})/(aH^{+})^3$ activity. In this case, however, activities for H^+ and Al^{3+} of individual samples (taken just prior to and just after $scCO_2$ injection) increase by two and eight orders of magnitude, respectively. Accordingly, the Al^{3+} activity temporarily overpowers H^+ activity causing the observed 'swing.' Over time, Al^{3+} activity gradually decreases driving the reaction pathways back towards predicted equilibrium.

Although we exclude activity diagrams for the low pH water-granite-$scCO_2$ experiment, EXP-3, it is informative to say something about the behavior of this system. The activity diagrams for this experiment are similar to those shown for EXP-2 (Figures 4.5.a and 4.6.a) with one significant difference: The '00' and '03' sample activities for log $(aAl^{3+})/(aH^{+})^3$ activities for EXP-3 are an order of magnitude lower than those for the moderate pH experiment, EXP-2. This difference reflects the abundance of hydrogen ions in EXP-3 and is noteworthy because, with continued reaction, the system achieves similar pH and aqueous species concentrations as EXP-2. This observation highlights the buffering capacity of the primary granite on the fluid composition. (See also Section 4.5.2.2)

In general, the activity diagrams indicate the path to equilibrium is: 1) well defined, 2) may be circuitous, and 3) approaches but does not achieve the predicted equilibrium state. The diagrams confirm observed water-rock response including illite and zeolite precipitation during the water-rock portion of each experiment, smectite precipitation after injection of $scCO_2$, and the lack of carbonate precipitation after injection $scCO_2$. Kinetics control experimental reaction

progress, and additional time would likely be required for each experiment to achieve equilibrium. In addition, the Ostwald step rule results in high silica activities, with control by chalcedony instead of quartz.

4.5.2 Results in the Context of Natural Systems

Natural geothermal systems where aqueous surface features exceed 100 °C are often associated with felsic volcanic systems (e.g., Ellis, 1979). Since our experiments were designed to mimic this kind of natural system (i.e., Roosevelt Hot Springs), our experimental and/or theoretical results may provide insight into such systems or vice versa. As an empirical guide, we first compare secondary mineralogy at 250 °C to help understand experimental, theoretical, and natural systems. We then discuss how study results may inform us more directly about other types of natural systems.

4.5.2.1 Comparison of Secondary Mineralogy

Figure 4.7 shows 1) secondary mineralogy for our experiments, 2) generalized secondary mineralogy found in natural systems between 100 and 300 ºC (Henley and Ellis, 1983), and 3) secondary mineralogy from a deep-seated well in the Roosevelt Hot Springs geothermal field (Capuano and Cole, 1982). The most conspicuous disparity between secondary mineralogy at 250 °C is the occurrence of smectite in experiments and the lack of smectite in natural systems. This is an interesting observation, discussed more completely in Section 4.5.3. Figure 4.7 also indicates the presence of illite and zeolite in many natural systems at 250 °C, and this validates observed experimental illite and zeolite. Illite exists in the Roosevelt field, and illite and zeolite both exist in geothermal fields similar to Roosevelt, such as Ohaki-Broadlands, New Zealand (Browne and Ellis, 1970) and Wairakei, New Zealand (Steiner, 1968). Occurrences of these minerals corroborate metasomatic processes found in natural hydrothermal systems and vice

versa; illite and zeolite occurrences indicate potassium and sodium-magnesium-calcium metasomatism, respectively (e.g., Giggenbach, 1984).

The morphology of experimental clay minerals (illite and smectite) may also elucidate processes in natural systems. Hydrothermal clay formation is thought by some to mimic that of diagenetic clay formation whereby smectite is a precursor to illite, with the conversion taking place due to increasing temperature (e.g., Inoue et al., 1992). To others, hydrothermal clay formation proceeds via direct precipitation from solution (e.g., Bethke et al., 1986; Wang and Xu, 2006). This debate also ties into field observations that associate smectite and interlayerd illite/smectite with lower temperature regimes (<~200 °C) and illite with higher temperature regimes (starting at ~200 °C) (Inoue, 1995; Henley and Ellis, 1983). When illite and smectite coexist in natural hydrothermal rocks, they are present as interlayered illite/smectite (i.e., mixed clays) (Inoue, 1995). As demonstrated in some hydrothermal fields, however, illite and smectite can also coexist without interlayering and possibly precipitate directly from solution (e.g., Browne and Ellis, 1970). We conducted experiments at a steady temperature of 250 °C and observed coexisting illite and smectite with no textural evidence for interlayering or prograde reactions. In addition, smectite precipitation occurred only after major perturbation to the system ($scCO_2$ injection), and smectite has morphology suggestive of euhedral growth in open space. In the context of the debate regarding hydrothermal clay formation, therefore, experimental results validate that 1) temperature may not always dictate clay stability (see also Section 4.5.3), 2) smectite and illite can coexist without interlayering, and 3) clays can precipitate directly from solution.

Mixed clays, epidote, calcite, chlorite, quartz, K-feldspar, and albite also commonly occur in natural systems, but these minerals were not observed in the experiments as secondary

minerals (Figure 4.7). This is not unexpected since not all minerals coexist and/or form contemporaneously. Many parameters affect mineral stability in hydrothermal systems, including temperature, host rock, permeability, fluid composition, reaction time, kinetics, pressure (with respect to governing the depth of boiling), water/rock ratio, etc. (e.g., Browne 1978; Ellis, 1979; Rose & Burt, 1979; Henley and Ellis, 1983). Related hydrothermal processes such as boiling, mixing, and conductive cooling also greatly affect local equilibrium conditions. That being said, it is beyond the scope of this study to evaluate all explanations for these differences, although a few examples follow. For instance, calcite is stable in CO_2-rich systems such as Roosevelt (Capuano and Cole, 1982) and Ohaki-Broadlands (Browne and Ellis, 1970), whereas epidote is more commonly stable in CO_2-poor systems such as Wairakei (Steiner, 1968). These field observations validate our predicted results for carbonate stability in the CO_2-rich experiments (EXP-2, and -5) (Figures 4.5 and 4.6) as well as the predicted and observed results regarding epidote dissolution in the water-epidote-granite-CO_2 experiment, EXP-5 (Figure 4.4).

Silica stability in natural systems also informs us about our theoretical and experimental results. As demonstrated by Fournier and Rowe (1966) and Mahon (1966), natural geothermal waters above 180 °C are often in equilibrium with quartz. Thermodynamic calculations also indicate quartz should be the silica mineral controlling silica saturation at 250 °C. However, in some natural systems, metastable amorphous or crystalline silica can exist up to 300 °C (Ellis, 1979), including some areas of the Roosevelt field (Capuano and Cole, 1982). As discussed in Section 4.5.1, tendency towards metastable silica phases can be attributed to the Ostwald step rule. Although we do not observe secondary silica attributable to formation at 250 °C, our calculated silica activities do indicate oversaturation with quartz and saturation with chalcedony. Silica geothermometry (using experimental aqueous silica concentrations and the method of

Fournier and Potter, 1982) corroborates these results by overestimating the experimental temperatures by an average of 20 °C. Therefore, natural system processes and experimental results again validate one another and indicate incomplete reaction progress in experiments with respect to establishing local equilibrium with quartz.

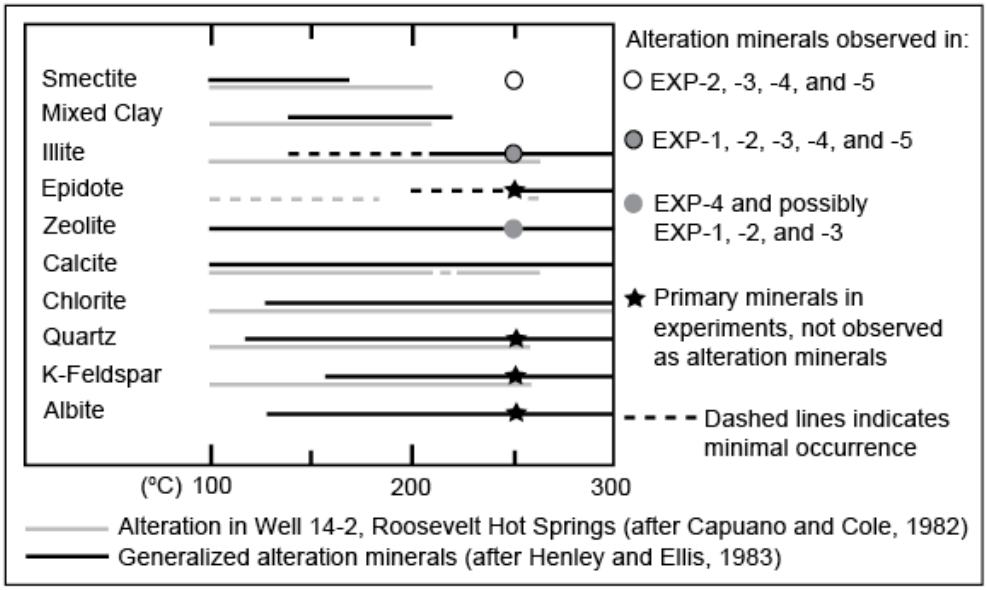

Figure 4.7. A comparison between secondary mineralogy in experiments, generalized secondary mineralogy found in natural systems, and secondary mineralogy from a deep-seated well in the Roosevelt Hot Springs geothermal field.

4.5.2.2 Direct Application of Results to Other Systems

Our experimental and theoretical results also apply to other systems, geochemically similar to the system studied here. In this project, we consider acid alteration in felsic rocks, vein zonation in granitic rocks, and tungsten ore formation. During pluton emplacement and cooling, magmatic volatiles such as CO_2, SO_2, HCl, and H_2O escape outwards and mix with local meteoric groundwater. As warm, acidic fluids ascend, they react with country rock and become progressively more neutral because of the buffering capacity of the wall rock. This

progression has implications for the evolution of ore fluids and is commonly observed in epithermal and porphyry copper deposits (e.g., Reed, 1997 and references therein). Our experimental work simulates this type of process. Specifically, the pre-injection half of the low pH water-granite-scCO_2 experiment, EXP-3, shows how HCl-rich fluids might interact with wall rock; over a period of 28 days, the pH of this system increases from 3.9 to 6.5 (Table 4.3) exhibiting the capacity of the granite to buffer the fluid composition. This validates and explains the neutral pH conditions of many geothermal systems (Ellis, 1979; Reed, 1997) even for those systems with initially acidic fluids.

The post-injection portions of the water-rock-scCO_2 experiments also show how CO_2-rich, acidic fluids might interact with fresh wall-rock (EXP-2 and EXP-3) or epidote-granite rocks (EXP-5). With a magmatic pulse of CO_2, the fluid-rock interactions may proceed through a series of metastable reactions such as those described by Figures 4.5 and 4.6, until achieving the predicted, stable assemblage. On the other hand, it is also possible that our experimental reaction paths imitate development of the zoned, close-proximity alteration fronts typical of veins in granitic systems whereby sericitic (illite-rich), argillic (smectite-rich), and propylitic assemblages are observed from the vein inwards. Thermodynamic equilibrium relationships do not readily explain why the argillic assemblage is found between sericitic and propyllitic assemblages (Reed, 1997). The observed progression, therefore, calls on the formation and persistence of metastable and/or unstable smectites that form as a result of kinetics and changing availability of constituents as fluids diffuse into the rock (Reed, 1997; Rose and Burt, 1979 and references therein). It is plausible that our post-scCO_2 injection mineral assemblages roughly correspond to this natural progression from illite-rich to smectite-rich assemblages because of kinetics and changing constituent availability (particularly silica; see also Section 4.5.3.) Note

that the persistence of metastable and/or unstable smectite, a swelling clay, may prevent replacement by stable minerals due to reduction in permeability and subsequent availability for fluid-rock interaction (Reed, 1997).

Due to scheelite precipitation, the experimental results for the low pH water-granite-$scCO_2$ experiment (EXP-3) may also provide some insight into tungsten ore formation. Although we believe the tungsten was a contaminant from the high-temperature lubrication used on the pressure vessel (Section 4.4.1), it is appropriate to explore possible mechanisms for scheelite formation since it is found naturally in granitic hydrothermal systems. Homogenization temperatures of fluid inclusions in scheelite range from 200-400 °C, with the most occurrences ranging from 200-300 °C (Naumov et al., 2011). Compiled data also indicate an increased occurrence of scheelite with CO_2-rich fluids (Naumov et al., 2011). Temperature and CO_2 contents, therefore, appear to be in line with the given experimental system and validate available fluid inclusion data for natural systems. Although not explored in depth, we believe the specific fluid chemistry in the experiment also influenced scheelite formation since we observed magnetite formation and gold mobilization in the low-pH experiment (EXP-3) and not in the moderate-pH experiment (EXP-2).

4.5.3 The Smectite Problem: Stability at 250 °C

There is one conspicuous difference among our experimental results, other published experimental results (Appendices C and D), our theoretical results, and natural systems: experiments commonly contain high-temperature smectite as a secondary mineral, but it is rarely observed in natural systems at similar temperature conditions (250 ºC, in our case) (Sections 4.1 and 4.5.2, Figure 4.7). As noted in Section 4.5.2, our experimental illite observations correlate with generalized natural system mineralogy, but the experimental smectite occurrences do not.

This result compares to other water-granite±CO_2 experiments that precipitate smectite at temperatures even higher than 250 ºC (up to 500 ºC) (Appendix C). There are many possible factors responsible for this difference, including kinetics, extent of thermodynamic equilibrium, reliance on incomplete thermodynamic data, water:rock ratio, and silica activity.

4.5.3.1 Smectite Occurrence as Function of Kinetics and/or Equilibrium Thermodynamics

In this discussion, we assume most natural systems achieve local thermodynamic equilibrium and do not support smectite or mixed clays at temperatures greater than 180-220 ºC. With respect to smectite in our experiments, secondary smectite may reflect metastable mineralogy achieved on the path to equilibrium (e.g., EXP-2 and -3) (Section 4.5.1) or stable mineralogy as predicted by thermodynamics (e.g., EXP-4 and -5) (Table 4.4). Smectite can also be theoretically predicted, but not observed in an experimental system (e.g., EXP-1). When smectite is a metastable mineral, kinetics is the logical factor driving smectite formation. When smectite is thermodynamically stable, however, its theoretical prediction poses a problem as compared to secondary mineralogy in natural systems at temperatures greater than 180-220 ºC. The difference between theoretical and natural data begs further consideration.

A common explanation for this type of difference is our reliance on incomplete thermodynamic data (e.g., Langmuir, 1997). This is especially relevant for systems containing smectites, illites, micas, and zeolites with poorly constrained thermodynamic data. It is, of course, valid to call on this explanation for the majority of thermodynamic modeling of multi-phase, solid-solution systems. Below, we discuss other possible explanations for smectite occurrences at temperatures >250 °C.

4.5.3.2 Smectite Occurrences as a Function of Water/Rock Ratio

As recognized by others, the fluid/rock ratio may also account for major variations between theoretical, experimental, and natural systems (e.g., Giggenbach, 1984; Savage et al., 1987; Seyfried & Bischoff, 1977). The fluid/rock or water/rock ratio, by mass, describes proportions of system constituents and empirically defines the character of fluid-rock interactions, including secondary mineral assemblages. At temperatures above 250 ºC, the theoretical composition for an altered granite in a rock-dominated system (i.e., low water/rock ratio) consists of K-feldspar, K-mica, albite, biotite, quartz, and epidote, wairakite, or prehnite (Giggenbach, 1984). In a fluid-dominated granite system (i.e., high water:rock ratio), the assemblage will shift to reflect the type of metasomatism active. With respect to our experiments, occurrences of illite, smectite, and zeolite correlate with potassium, hydrogen, and sodium-magnesium-calcium metasomatism types, respectively (Giggenbach, 1984). These observations confirm our experiments behave as fluid-dominated systems and that smectite precipitation may result from using a high water/rock ratio.

We conducted our experiments with an initial water/rock ratio of approximately 20/1, by mass, or 2.6-3.2, by atom % oxygen (for granite and epidote+granite experiments, respectively). As determined theoretically by Taylor (1979), water/rock ratios by atom % oxygen in hydrothermal systems range between 0.1 and 4. Our results, therefore, may better approximate natural systems with relatively higher water/rock ratios. To further evaluate the effect of water/rock ratio on our systems, we provide results from two sets of theoretical models to determine the effect of 1) changing water/rock ratio on our experiments and 2) the effect of increasingly smaller water/rock ratios on clay precipitation in a theoretical system.

Over the course of the experiments, water/rock ratios decreased from approximately 20/1 to a minimum of 11/1 in the water-rock experiments (EXP-1 and -4) and a minimum of 10/1 in the water-rock-scCO$_2$ experiments (EXP-2, -3, and -5). Theoretical prediction models (not shown) for water/rock ratios of 20/1 and 10/1 for each experiment indicate no significant shift in secondary mineralogy or species activities. Accordingly, we do not believe that the decrease in water/rock ratio during each experiment greatly influenced observed results.

To evaluate the possible effect of water/rock ratio on smectite and illite stability, we also modeled the evolution of the water-epidote-granite-scCO$_2$ experiment, EXP-5, using increasingly smaller water/rock ratios (by mass): 20, 15, 1, and 0.25. (We used this experiment for the simulation because smectite was both predicted and observed in this system.) For the post-injection phase of the experiment, when smectite is a predicted secondary mineral, we find that the amount of smectite decreases and the amount of illite increases with decreasing water/rock ratio. Although this result is not well-defined, it does suggest a possible link between clay stability and water/rock ratio. Since the constraint on thermodynamic data is poor, it is notable that other's research also documents the link between clay stability and water/rock ratio.

Whitney (1990) directly explored illitization of smectite as a function of water/rock ratio. He conducted batch hydrothermal experiments (250-400 °C, 1-60 days, 100 MPa) for water/rock ratios between 1/1 and 1/20 (by mass) and found that low ratios retard illitization, especially at lower temperatures. Experimental work by Vidal et al. (2012) indicates smectite can be stable at temperatures as high as 300 °C given the system is fluid-rich, silica-rich, and potassium-poor. Efforts such as these suggest smectite stability is possible at our experimental conditions and validates the theoretical and observed results for smectite in the water-epidote-granite ± scCO$_2$ experiments, EXP-4 and EXP-5. In summary, although uncommon for most natural systems,

smectite stability may be possible in fluid-rich systems at temperatures > 250 °C (as possibly observed by Gianelli et al., 1998). Whether any natural high-temperature smectite occurrences are thermodynamically stable is still debated (Vidal et al., 2012 and references therein).

4.5.3.3 Smectite Occurrence as Function of Silica Activity

Another possible explanation for the difference between experimental and natural smectite occurrences may hinge on silica stability and metastability. At temperatures of 250 ºC, quartz is the stable silica mineral in natural systems (e.g., Henley and Ellis, 1983). In our experimental work, however, chalcedony governs silica saturation as a metastable phase (Section 4.5.1). Theoretically predicted, secondary mineralization shifts with differences in silica saturation, so it follows that mineralization in a natural system buffered by quartz vrsus minerals in an experimental system buffered by chalcedony will not be the same. We propose, therefore, that high silica activity contributed to smectite formation in our experiments. Other studies validate smectite formation as a function of silica activity (e.g., Abercrombie et al., 1994; Hutcheon et al., 1994; Vidal et al., 2012;).

4.5.4 Implications for Commercial Geothermal Fields and Carbon Sequestration

There is renewed interest in tapping both traditional and non-traditional geothermal reservoirs for energy extraction (MIT, 2006) as well as sequestering carbon dioxide to mitigate increasing concentrations of atmospheric carbon (Benson and Cook, 2005). Traditional geothermal operations use water to extract heat from relatively shallow, naturally permeable reservoirs. Non-traditional geothermal operations may use $scCO_2$ as the working fluid instead of water. For example, EGS reservoirs which require stimulation of a deep reservoir by fracturing, could either circulate water or $scCO_2$ as a working fluid. CO_2-plume geothermal systems (CPG) (Randolph and Saar, 2011) would also circulate $scCO_2$ but would utilize reservoirs that are

naturally porous and permeable. In either case, CO_2-based geothermal systems may also promote carbon sequestration (Brown, 2000; Preuss, 2006) via mineral and/or dissolution trapping mechanisms (Benson & Cook, 2005). Our results apply to these systems as well as to arkosic reservoirs targeted for carbon sequestration. We review our study in the context of such systems to help constrain processes that may impact their functionality and success, including clay and carbonate formation.

Based on our results and the results of others (Appendix C), clays form when foreign fluids circulate through a fresh or altered granite reservoir. Our experiments specifically indicate water-rock systems (i.e., no $scCO_2$) precipitate illite and that water-rock-$scCO_2$ systems precipitate smectite. This generalization applies to both water-granite±$scCO_2$ and water-epidote-granite±$scCO_2$ systems. Therefore, traditional water-based and non-traditional CO_2-based geothermal operations should anticipate illite and smectite precipitation within production pathways, respectively. Regardless of clay stability, they will affect reservoir porosity and permeability and must be considered. This may be especially important in the case of smectite, a swelling clay. Clay formation, including smectite, is not uncommon in currently operating geothermal facilities (e.g., Beaufort et al., 1995; McLin et. al, 2012), and is generally overcome with scale inhibitor. Similar treatment would likely be required for water or CO_2-based EGS where fluid-flow is focused along discrete, fractured pathways. Clay formation may not impact CPG systems as significantly because reservoirs have higher overall porosity/permeability (Randolph and Saar, 2011); however, over time, reduced porosity/permeability will still reduce system functionality, especially if clay formation shields against continued fluid-rock interaction (e.g., Reed, 1997). (Clay formation may similarly affect deep, arkosic aquifers targeted for carbon sequestration projects.) Since clay type and abundance depend on factors such as

temperature, water/rock ratio, and silica activity; operators could adjust injection and/or production parameters to try and further reduce the incidence of clay formation. Based on the results described for our low-pH water+granite+$scCO_2$ experiment (EXP-3) (Section 4.4), we also note the possibility that use of scale inhibitors (i.e., acids) may result in further dissolution of reservoir wall-rock and additional clay precipitation. We acknowledge the need to balance use of scale inhibitors with respect to maintaining open production pathways and possibly deteriorating the fluid-flow channels by further fluid-rock interaction.

Our experimental results also contribute to research addressing possible carbon sequestration in granite-hosted reservoirs (e.g., Lin et al., 2008; Liu et al., 2003; Suto et al., 1997; Ueda et al., 2005) and arkosic reservoirs (e.g., Rosenbauer et al., 2005). With respect to mineral trapping, whereby carbon is sequestered by solid phases, our equilibrium models do predict carbonate formation after injection of $scCO_2$ into experimental systems (EXP-2, -3, and, -5). However, we do not observe carbonates as secondary minerals at experimental conditions. Failure to form carbonates likely reflects incomplete reaction progress (Section 4.5.1); if more time were allotted, experiments with $scCO_2$ may have achieved carbonate saturation. It is possible that carbonate formation will result in the field given sufficient time to overcome the kinetic constraints faced in the laboratory. Based on increased bicarbonate activities in samples from the post-injection portion of EXP-2, -3, and -5; dissolution trapping of carbon does appear to be a viable sequestration mechanism. Depending on where carbonates form (i.e., proximal or distal to injection point), we acknowledge that injection and/or production pathways may require treatment to remove secondary carbonates.

4.6 Carbon Dioxide-Water-Rock Interactions in Altered Granite: Insights from Hydrothermal Experiments and Field Geochemistry

In Sections 4.1-4.5, we present the experimental data to evaluate aqueous geochemistry and mineralogical relationships in water-granite ± CO_2 and water-epidote-granite ± CO_2 systems at 250°C and 25-45 MPa. Alteration mineral experiments were conducted to provide understanding for fluid-rock interactions in altered rock, complementary to Sections 4.1-4.5. Three alteration minerals (epidote, chlorite, and calcite) were included within one pair of experiments. A total of additional seven experiments were conducted at 250°C and 25-45 MPa, including water-granite-chlorite ± CO_2, water-granite-calcite ± CO_2, and water-granite-chlorite-calcite-epidote ± CO_2. Each of these experiments simulates fluid-rock interactions in EGS reservoirs stimulated by fracturing along pre-existing zones of weakness (i.e., epidote and/or calcite veins) and in pervasively altered granitic rocks (i.e., chlorite and/or epidote alteration). We also construct thermodynamic models and compare calculations/ predictions to our experimental results, and then compare our experimental and model data to natural systems.

The experimental design and setup, analytical methods, and manner in which the geochemical calculations were conducted are the same as described in Section 4.3. Seven hydrothermal experiments were conducted: water-granite-chlorite (two total, EXP-6 and EXP-7), water-granite-chlorite-scCO_2 (EXP-8), water-granite-calcite (EXP-9), water-granite-calcite-scCO_2 (EXP-10), water-granite-calcite-epidote-chlorite (EXP-11), and water-granite-calcite-epidote-chlorite-scCO_2 (EXP-12). EXP-6 and EXP-7 were conducted for different times (1053 and 2544 hours, respectively) to evaluate assumptions regarding steady state behavior in the hydrothermal experiments. Table 4.5 outlines conditions and parameters for each experiment. Following the methods of Kacandes and Grandstaff (1989), we evaluate our experimental results

in the context of geothermal waters sampled for the Roosevelt Geothermal System (Capuano and Cole, 1982) and for other geothermal wells in the surrounding area.

Table 4.5. Experimental parameters and mineral compositions for experiments EXP-6 to EXP-12.

Experiment	EXP-6	EXP-7	EXP-8	EXP-9	EXP-10	EXP-11	EXP-12
Description	Water, Granite and Chlorite	Water, Granite and Chlorite	Water, Granite, Chlorite and ssCO2	Water, Granite and Calcite	Water, Granite, Calcite and ssCO2	Water, Granite, Calcite, Chlorite, and Epidote	Water, Granite, Calcite, Chlorite, Epidote and ssCO2
Initial pH	5.1	4.9	5.3	5.3	5.3	4.8	4.7
Temperature (°C)	250.0	250.0	250.0	250.0	250.0	250.0	250.0
Pressure (MPa), Pre-$scCO_2$ Injection	250.0	250.0	250.0	250.0	252.0	250.0	249.0
Pressure (MPa), Post-$scCO_2$ Injection	N/A	N/A	360.0	NA	490.0	NA	339.0
Initial Water:Rock Ratio	20.07	20.34	20.00	20.00	20.00	19.99	19.98
Rock Mass[a]	7.03	8.17	8.02	8.20	10.26	524.76	8.01
Mineral Proportions (Qu:Ol:Pe:Bi:Ch)	16:16:16:2:50	16:16:16:2:50	16:16:16:2:50	NA	670.9	NA	NA
Mineral Proportions (Qu:Ol:Pe:Bi:Ca)	NA	NA	NA	16:16:16:2:50	16:16:16:2:50	NA	NA
Mineral Proportions (Qu:Ol:Pe:Bi:Ca:Ch:Ep)	NA	NA	NA	NA	NA	16:16:16:2:16.7:16.7:16.7	16:16:16:2:16.7:16.7:16.7:16.7
Water-Rock Reaction Time (hours)	1053.3	2495.2	668	707	707	821.4	525
Water-Rock-$scCO_2$ Reaction Time (hours)	N/A	N/A	718	NA	630	NA	387
Total Reaction Time (hours)	1053.3	2495.2	1386	707	1336	821.4	912

[a] Rock mass input into reaction cell.
$scCO_2$ = supercritical CO_2
N/A = not applicable
Ep= Epidote

Qu = Quartz
Ol = Oligoclase
Pe= Perthite
Bi = Biotite
Ch= Chlorite
Ca= Calcite

Table 4.6 presents aqueous geochemical data for each experiment. The changes in cation and anion concentrations in each experiment over time indicate active fluid-rock interactions, analogous to those described in Section 4.4. Figures 4.8 to 4.10 present cation/proton activity ratios of waters sampled from our experiments. Also plotted are fluids from Roosevelt Geothermal wells, nearby geothermal wells, and other geothermal fields and experiments as listed in Kacandes and Grandstaff (1989).

Table 4.6. Aqueous major and minor element geochemistry for EXP-6 to EXP-12, including analyzed and predicted concentrations.

Exp 6: Water, Granite and Chlorite

				Cations (mmol/Kg)								Anions (mmol/Kg)				Minor Cations (µM/Kg)									
Time (hours)	Sample	pH (STP)[a]	pH (in-situ)[b]	Si	Mn	Fe	Mg	Ca	Al	Na	K	F	Cl	PO4	SO4	Al	Ba	Fe	Mg	Mn	Rb	Sr	ΣCO2 [e,f], in-situ	ΣCO2 [d], bench	charge imbalance
0	0	5.04		5.40	BDL	BDL	BDL	0.38	BDL	119.65	7.41	0.02	120.24	BDL	0.68	20.60	0.70	BDL	10.24	3.81	0.16	0.05		0.08	2.48
22.0	1	4.61		7.37	BDL	BDL	0.06	0.70	BDL	118.18	7.43	0.04	122.91	0.03	0.75	12.61	1.18	BDL	86.34	5.76	1.43	1.34	1.34	0.19	1.05
49.5	2	3.63		7.78	BDL	BDL	BDL	0.60	BDL	130.22	7.53	0.04	123.17	0.02	0.74	2.52	0.53	BDL	48.07	1.26	1.09	1.27	1.26	0.28	5.38
117.3	3	3.54		7.86	BDL	BDL	BDL	0.65	BDL	124.56	7.31	0.04	128.57	0.10	0.71	1.96	0.98	BDL	47.07	0.22	1.06	1.24	1.84	0.23	1.11
334.0	4	3.69		7.99	BDL	BDL	0.05	0.71	BDL	125.90	7.65	0.05	125.90	0.03	0.76	2.73	0.37	BDL	51.24	0.36	1.04	1.25	1.25	0.22	2.88
Detection Limit				0.03	0.02	0.01	0.01	0.02	0.01	0.08	0.07	0.02	0.02	0.20	0.20	0.02	0.00	37.38	0.04	0.03	0.01	0.00			
1052.1	5	3.41		8.02	BDL	BDL	0.10	0.89	BDL	129.60	8.43	0.07	129.58	0.00	0.86	4.25	0.86	5.77	60.88	0.36	1.10	1.40	0.99	1.89	3.18
1053.3	Q	5.50		7.70	BDL	BDL	0.12	0.86	BDL	120.33	7.32	0.06	121.11	0.00	0.77	8.62	0.67	2.98	101.60	0.10	1.01	1.53		0.03	2.73
Detection Limit				0.04	0.00	0.01	0.02	0.03	0.02	0.02	0.17	0.02	0.02	0.20	0.20	0.33	0.01	1.72	0.01	0.04	0.00	0.00			

Uncertainty ± 1σ

Predicted Equilibrium Value[e]

Exp 7: Water, Granite and Chlorite

				Cations (mmol/Kg)								Anions (mmol/Kg)				Minor Cations (µM/Kg)									
Time (hours)	Sample	pH (STP)[a]	pH (in-situ)[b]	Si	Mn	Fe	Mg	Ca	Al	Na	K	F	Cl	PO4	SO4	Al	Ba	Fe	Mg	Mn	Rb	Sr	ΣCO2 [e,f], in-situ	ΣCO2 [d], bench	charge imbalance
0	0	5.19		5.49	BDL	BDL	0.00	0.35	BDL	122.63	7.44	BDL	122.10	BDL	0.71	13.21	0.75	1.22	6.51	0.09	0.11	0.04		2.42	2.85
20.8	1	4.72		7.38	BDL	BDL	0.00	0.62	BDL	121.33	7.39	0.04	122.00	BDL	0.74	0.98	0.85	6.40	45.88	0.36	0.96	1.01	1.83	1.28	2.53
41.9	2	4.47		7.49	BDL	BDL	0.00	0.55	BDL	124.76	7.93	0.05	121.70	BDL	0.74	1.78	1.07	14.74	36.34	0.42	0.99	1.12	1.74	0.80	4.11
115.1	3	4.49		7.83	BDL	BDL	0.10	0.61	BDL	116.39	7.54	0.06	125.08	BDL	0.79	1.75	1.26	9.08	41.89	0.34	0.98	1.17	1.34	1.26	-0.54
428.1	4	5.24		8.06	BDL	BDL	0.10	0.73	BDL	126.99	7.15	0.08	122.65	BDL	0.76	1.38	0.82	5.16	45.91	0.35	1.02	1.30	1.97	0.96	4.44
689.8	5	4.72		8.23	BDL	BDL	0.00	0.71	BDL	115.40	6.89	0.06	122.46	BDL	0.73	2.22	0.68	4.16	46.57	0.28	1.03	1.41	1.57	0.89	-0.11
977.7	6	4.92		8.11	BDL	BDL	0.00	0.82	BDL	118.97	7.17	0.07	124.74	BDL	0.78	3.63	1.00	4.44	43.38	0.42	1.04	1.50	2.05	0.90	0.56
Detection Limit				0.04	0.00	0.01	0.02	0.03	0.02	0.02	0.17	0.020	0.020	0.200	0.200	0.33	0.01	1.72	0.01	0.04	0.00	0.00			
2490.3	7	5.37		8.12	0.00	0.00	0.00	0.66	0.00	114.74	7.29	0.09	134.86	0.00	0.80	4.18	0.66	7.51	36.64	0.34	1.01	1.51	1.29	1.19	-5.08
2495.2	Q	4.85		7.37	0.00	0.00	0.15	0.69	0.00	123.84	7.30	0.09	131.15	0.00	0.73	7.49	0.30	6.59	129.75	1.63	0.94	1.76		1.25	0.05
Detection Limit				0.05	0.00	0.00	0.01	0.01	0.01	0.02	0.16	0.02	0.02	0.20	0.20	0.02	0.01	16.33	0.10	0.07	0.01	0.01			

Uncertainty ± 1σ

Predicted Equilibrium Value[e]

Exp 8: Water, Granite, Chlorite and ssCO2

				Cations (mmol/Kg)								Anions (mmol/Kg)				Minor Cations (µM/Kg)									
Time (hours)	Sample	pH (STP)[a]	pH (in-situ)[b]	Si	Mn	Fe	Mg	Ca	Al	Na	K	F	Cl	PO4	SO4	Al	Ba	Fe	Mg	Mn	Rb	Sr	ΣCO2 [e,f], in-situ	ΣCO2 [d], bench	charge imbalance
0	0	4.55		5.11	BDL	BDL	BDL	0.29	BDL	120.83	7.66	BDL	128.48	0.01	0.70	13.25	0.38	BDL	7.35	0.03	0.10	0.04		0.88	-0.32
15.75	1	7.57		7.37	BDL	BDL	0.08	0.86	BDL	120.60	8.16	BDL	135.74	BDL	0.79	7.80	1.99	11.95	122.25	0.43	0.84	1.62	2.29	1.30	-2.49
39.07	2	4.26		7.48	BDL	BDL	BDL	0.59	BDL	120.36	8.28	0.06	131.80	0.01	0.75	6.21	1.39	6.09	48.90	0.05	0.83	1.50	3.27	0.65	-1.35
107.8	3	4.35		7.86	BDL	BDL	BDL	0.64	BDL	124.96	8.25	0.06	132.92	0.01	0.76	3.52	0.75	5.30	59.34	0.05	0.87	1.51	2.83	1.04	-0.01
663.4	4	4.41		7.79	BDL	BDL	BDL	0.65	BDL	128.14	7.76	0.07	131.12	0.01	0.75	2.72	0.16	8.24	48.46	0.09	0.86	1.43	2.08	0.20	1.67
684.6	5	5.08		8.43	BDL	BDL	0.67	0.75	BDL	121.41	7.89	0.06	133.57	0.00	0.79	1.66	1.16	7.57	605.01	0.13	0.95	2.00	1274.59	13.67	-1.16
708.9	6	5.19		8.37	BDL	BDL	0.79	0.80	BDL	125.57	8.02	0.05	130.50	0.01	0.76	2.11	1.66	10.10	682.47	0.23	0.97	2.28	1414.82	22.93	1.73
788.0	7	5.43		8.38	BDL	0.07	0.71	0.76	BDL	122.60	8.24	0.05	132.04	0.00	0.69	1.53	2.85	86.45	663.84	2.05	1.03	2.61	1861.23	28.66	0.16
1004.5	8	5.31		8.02	0.00	0.08	0.63	0.77	BDL	124.66	8.37	0.04	130.24	BDL	0.58	0.89	2.59	93.78	581.12	2.15	1.09	3.15	906.41	23.45	1.70
1335.1	9	5.43		7.46	0.00	0.16	0.33	0.92	BDL	120.68	8.75	0.03	129.39	0.01	0.51	0.83	2.37	182.32	429.27	3.44	1.15	3.48	797.34	41.11	0.68
1390.1	Q	5.43		7.28	BDL	0.01	0.86	1.18	BDL	122.53	8.04	0.07	129.06	0.01	0.76	11.78	2.85	10.43	744.68	0.04	1.07	4.33		39.70	1.51
Detection Limit				0.05	0.00	0.00	0.01	0.01	0.01	0.02	0.16	0.02	0.02	0.20	0.20	0.02	0.01	16.33	0.10	0.07	0.01	0.01			
2342.2	QF	6.86		5.89	0.00	0.00	0.82	1.13	0.00	122.32	7.71	0.07	130.04	0.00	0.77	3.38	2.84	5.35	657.92	0.00	0.94	4.07		4.97	0.86
Detection Limit				0.04	0.00	0.01	0.01	0.03	0.01	0.02	0.22	0.02	0.02	0.05	0.02	1.26	0.92	3.90	0.34	0.08	0.01	0.05			

Uncertainty ± 1σ

Predicted Equilibrium Value[e]

Table 4.6. (cont.) Aqueous major and minor element geochemistry for EXP-6 to EXP-12, including analyzed and predicted concentrations.

Exp 9: Water, Granite and Calcite

				Cations (mmol/Kg)								Anions (mmol/Kg)				Minor Cations (µM/Kg)									
Time (hours)	Sample	pH (STP)[a]	pH (in-situ)[b]	Si	Mn	Fe	Mg	Ca	Al	Na	K	F	Cl	PO4	SO4	Al	Ba	Fe	Mg	Mn	Rb	Sr	ΣCO2 [e,f], in-situ	ΣCO2 [d], bench	charge imbalance
0	0	5.74		2.47	BDL	BDL	8.25	0.12	BDL	305.63	8.93	BDL	312.38	0.00	0.72	0.83	0.10	3.43	6784.65	0.03	0.13	0.03		0.62	2.71
27.43	1	4.64		5.00	0.00	0.02	0.73	7.44	BDL	296.21	9.49	BDL	310.87	BDL	0.69	0.62	1.19	70.62	681.62	1.44	1.21	4.46	5.62	2.69	1.55
47.37	2	3.99		5.98	BDL	0.01	0.15	7.92	BDL	297.61	9.29	0.02	310.35	0.00	0.69	0.60	0.91	63.74	181.02	0.73	1.27	5.04	5.34	3.74	1.78
126.4	3	4.37		7.42	BDL	BDL	BDL	8.05	BDL	295.60	10.13	0.02	311.03	0.00	0.64	0.89	0.73	54.02	26.04	0.21	1.28	5.69	7.76	8.07	1.50
342.9	4	4.81		8.02	BDL	BDL	BDL	8.52	BDL	300.34	9.83	0.03	311.33	0.00	0.57	0.97	0.71	57.48	15.79	0.14	1.33	6.42	6.81	5.84	2.30
675.2	5	4.75		8.22	BDL	BDL	BDL	8.66	BDL	312.44	9.95	0.03	306.49	0.01	0.52	1.02	1.03	57.93	18.24	0.14	1.41	7.23	6.97	7.09	4.96
706.7	Q	5.60		7.99	BDL	BDL	0.08	9.59	BDL	299.27	10.00	0.03	312.64	0.00	0.71	3.31	1.12	64.31	107.28	0.52	1.38	7.64		7.64	2.26
Detection Limit				0.05	0.00	0.00	0.01	0.01	0.01	0.02	0.16	0.02	0.02	0.20	0.20	0.02	0.01	16.33	0.10	0.07	0.01	0.01			
1679.2	QF	6.60		4.53	BDL	BDL	0.26	8.89	BDL	271.16	8.25	0.03	293.77	0.00	0.72	1.42	1.12	25.03	242.24	0.47	1.14	6.78		3.85	0.42
Detection Limit				0.04	0.00	0.01	0.01	0.03	0.01	0.02	0.22	0.02	0.02	0.05	0.02	1.26	0.92	3.90	0.34	0.08	0.01	0.05			

Uncertainty ± 1σ

Predicted Equilibrium Value[e]

Exp 10: Water, Granite, Calcite and ssCO2

				Cations (mmol/Kg)								Anions (mmol/Kg)				Minor Cations (µM/Kg)									
Time (hours)	Sample	pH (STP)[a]	pH (in-situ)[b]	Si	Mn	Fe	Mg	Ca	Al	Na	K	F	Cl	PO4	SO4	Al	Ba	Fe	Mg	Mn	Rb	Sr	ΣCO2 [e,f], in-situ	ΣCO2 [d], bench	charge imbalance
0	0	5.74		2.51	BDL	BDL	8.21	0.14	BDL	301.97	8.96	0.00	313.29	BDL	0.73	0.81	0.10	4.79	6906.47	0.03	0.13	0.04		0.24	2.01
41.0	1	5.05		5.15	0.01	0.01	BDL	7.99	BDL	298.90	10.05	0.04	314.11	0.00	0.68	2.56	1.48	72.00	93.40	8.10	1.43	5.08	4.91	2.58	1.48
66.1	2	4.89		6.16	BDL	0.01	BDL	8.16	BDL	296.97	9.66	0.03	312.03	0.00	0.69	6.56	1.14	59.85	48.41	0.63	1.44	5.36	7.31	3.41	1.50
119.9	3	5.05		7.21	BDL	0.00	BDL	8.38	BDL	295.77	9.75	0.03	313.13	0.01	0.69	5.84	0.93	57.76	34.12	0.27	1.36	5.14	7.17	6.48	1.21
668.4	4	4.95		8.25	BDL	0.01	BDL	8.60	BDL	306.02	9.90	0.03	312.54	0.01	0.55	2.76	1.41	60.76	29.42	0.30	1.53	6.12	10.58	3.09	3.01
687.4	5	5.33		10.09	BDL	0.01	2.09	8.46	BDL	300.55	9.86	0.03	305.03	0.01	0.28	2.36	2.72	68.25	1729.54	4.11	1.53	6.35	1011.57	22.30	4.06
710.6	6	5.79		10.24	0.01	0.05	2.45	8.80	BDL	297.47	9.83	0.04	312.95	0.01	0.38	2.05	2.18	102.47	2024.47	5.81	1.55	6.34	845.07	62.43	2.51
781.0	7	5.43		10.25	BDL	0.03	2.63	8.18	BDL	298.90	10.28	0.04	304.47	BDL	0.28	1.18	2.68	93.71	2130.64	3.58	1.55	6.25	2658.09	20.72	4.06
Detection Limit				0.05	0.00	0.00	0.01	0.01	0.01	0.02	0.16	0.02	0.02	0.20	0.20	0.02	0.01	16.33	0.10	0.07	0.01	0.01			
999.4	8	5.3		9.63	BDL	0.05	2.24	7.04	BDL	272.49	9.11	0.02	304.69	BDL	0.26	0.00	3.47	68.94	1708.26	1.58	1.41	6.45	2413.61	26.75	-0.82
1334.5	9	5.48		10.95	BDL	0.04	1.77	7.22	BDL	277.98	8.81	0.04	309.87	BDL	0.24	0.99	3.68	60.17	1377.91	0.96	1.43	7.44	1261.75	32.25	-0.90
1341.7	Q	6.09		10.59	0.01	0.04	3.25	17.64	0.11	268.11	9.58	0.00	303.78	BDL	0.64	74.35	2.12	86.69	2481.09	3.00	1.47	10.28		38.16	2.37
1671.6	QF	7.67		8.48	BDL	0.02	3.15	14.93	BDL	275.96	8.84	0.01	302.72	BDL	0.68	2.43	1.97	47.59	2469.99	0.40	1.36	9.80		19.87	2.70
Detection Limit				0.04	0.00	0.01	0.01	0.03	0.01	0.02	0.22	0.02	0.02	0.05	0.02	1.26	0.92	3.90	0.34	0.08	0.01	0.05			

Uncertainty ± 1σ

Predicted Equilibrium Value[e]

Exp 11: Water, Granite, Calcite, Chlorite, and Epidote

				Cations (mmol/Kg)								Anions (mmol/Kg)				Minor Cations (µM/Kg)									
Time (hours)	Sample	pH (STP)[a]	pH (in-situ)[b]	Si	Mn	Fe	Mg	Ca	Al	Na	K	F	Cl	PO4	SO4	Al	Ba	Fe	Mg	Mn	Rb	Sr	ΣCO2 [e,f], in-situ	ΣCO2 [d], bench	charge imbalance
0	0	5.01		5.04	BDL	BDL	BDL	0.17	BDL	272.52	4.43	BDL	287.16	BDL	0.58	7.62	0.07	2.28	15.49	0.04	0.06	0.02		8.70	-1.95
22.9	1	5.26		7.68	BDL	BDL	BDL	0.88	BDL	278.85	4.78	0.07	284.55	BDL	0.57	9.91	0.19	7.46	4.72	0.12	0.81	1.31	12.64	8.28	-0.06
46.0	2	5.14		7.49	BDL	BDL	BDL	1.08	BDL	275.44	4.79	0.07	280.83	BDL	0.55	11.43	0.19	5.14	4.07	0.09	0.83	1.49	13.57	8.77	0.06
116.8	3	4.99		7.85	BDL	BDL	BDL	1.33	BDL	282.78	5.33	0.07	282.28	BDL	0.56	10.75	0.34	5.81	4.57	0.11	0.91	1.76	12.51	7.64	1.28
307.6	4	5.15		8.13	BDL	BDL	BDL	1.50	BDL	272.10	4.86	0.08	283.82	BDL	0.57	10.95	0.79	5.79	5.85	0.12	1.13	2.31	13.20	8.59	-0.90
811.9	5	5.13		8.02	BDL	BDL	BDL	1.51	BDL	271.01	5.95	0.10	287.26	0.01	0.57	7.92	1.25	4.79	4.50	0.11	1.37	2.83	13.15	9.27	-1.50
821.4	Q	6.26		7.62	BDL	BDL	0.13	5.11	BDL	276.72	5.11	0.09	289.77	0.00	0.60	3.72	1.96	13.59	96.62	1.61	1.36	3.61		11.56	0.22
Detection Limit				0.04	0.00	0.01	0.01	0.03	0.01	0.02	0.22	0.02	0.02	0.05	0.02	1.26	0.92	3.90	0.34	0.08	0.01	0.05			

Uncertainty ± 1σ

Predicted Equilibrium Value[e]

Exp 12: Water, Granite, Calcite, Chlorite, Epidote and ssCO2

				Cations (mmol/Kg)								Anions (mmol/Kg)				Minor Cations (µM/Kg)									
Time (hours)	Sample	pH (STP)[a]	pH (in-situ)[b]	Si	Mn	Fe	Mg	Ca	Al	Na	K	F	Cl	PO4	SO4	Al	Ba	Fe	Mg	Mn	Rb	Sr	ΣCO2 [e,f], in-situ	ΣCO2 [d], bench	charge imbalance
0	0	4.85		5.10	BDL	BDL	BDL	0.19	BDL	265.36	7.23	BDL	293.70	BDL	0.59	8.48	0.08	2.25	17.81	0.22	0.14	0.02		0.65	-3.86
19.1	1	6.44		7.27	BDL	BDL	BDL	1.12	BDL	264.44	7.58	0.06	291.13	BDL	0.58	17.32	0.36	6.70	7.38	0.85	0.86	1.37	1.30	0.95	-3.19
42.1	2	5.89		7.47	BDL	BDL	0.06	1.32	BDL	265.22	6.98	0.08	292.16	0.01	0.59	16.19	0.25	4.90	5.80	0.06	0.85	1.60	2.96	1.69	-3.25
111.2	3	5.83		7.87	BDL	BDL	BDL	1.64	BDL	268.12	7.29	0.07	295.99	BDL	0.60	7.49	0.42	7.56	2.30	0.38	0.93	2.05	1.98	2.41	-3.23
524.4	4	5.77		8.03	BDL	BDL	BDL	1.90	BDL	268.41	7.64	0.08	295.39	0.00	0.60	5.32	0.90	9.24	2.81	0.74	1.07	2.94	0.29	2.70	-2.92
552.6	5	5.46		8.49	0.01	BDL	0.53	3.68	BDL	271.66	7.78	0.07	296.59	BDL	0.41	7.76	2.44	17.02	580.83	6.33	1.07	4.30	1740.11	21.80	-1.64
566.2	6	5.83		8.58	0.01	0.02	0.74	4.09	BDL	264.14	7.67	0.06	292.53	BDL	0.39	41.49	3.29	22.63	621.83	7.09	1.06	4.41	2737.30	26.44	-2.06
642.4	7	5.70		7.90	0.01	0.02	0.65	3.74	BDL	263.29	7.67	0.06	294.27	BDL	0.36	6.33	2.78	17.60	683.80	7.20	1.06	5.44	1096.09	34.45	-2.66
912.0	8	5.64		7.36	0.01	0.01	0.53	3.78	BDL	269.06	8.31	0.06	290.93	BDL	0.36	5.47	2.74	17.69	529.43	5.92	1.16	8.54	922.20	21.71	-0.98
Detection Limit				0.041	0.003	0.008	0.013	0.029	0.015	0.016	0.220	0.02	0.02	0.05	0.02	1.263	0.918	3.903	0.344	0.079	0.015	0.048			
	Q			ND	ND	ND	ND	ND	ND	ND	ND	ND	ND	ND	ND	ND	ND	ND	ND	ND	ND	ND			ND

Uncertainty ± 1σ

Predicted Equilibrium Value[e]

As discussed in Kacandes and Grandstaff (1989), the offsets observed between samples from geothermal fields and from hydrothermal experiments reacting fresh rock may be explained in one of two ways: formation of metastable minerals in experiments and problems associated with calculating deep fluid compositions from gas-charged field samples. Results from our experiments suggest that including alteration minerals in the experiments changes some of the fluid parameters, but by itself this cannot explain all the observed offsets. Introduction of CO_2

into the experiments produces chemistries that more closely duplicate fluid chemistries of high-temperature geothermal fields (Figures 4.8 to 4.10). Also, the activity relationships for waters sampled from the granite-water experiment (EXP-1 in Section 4.4), waters from the Beaver City wells, and waters from the Roosevelt Geothermal field are consistent with control of calcium/proton and magnesium/proton activity by metastable smectities, as opposed to chlorite (Figure 4.10). In our granite-water experiments, however, calcium/proton and magnesium/proton activity appear to be controlled by the primary mineral assemblage. Our granite-water-scCO_2-alteration mineral experiments yield water chemistries consistent with geochemistries of geothermal fields (lower left of Figures 4.8 to 4.10). Within the broad area depicted for waters sampled from geothermal fields, however, calcium/proton and magnesium/proton activity in our experiments appear to be controlled by metastable smectities as opposed to chlorite. This relationship suggests that aspects of field geochemistry (for example, calcium/proton and magnesium/proton activity) in geothermal and hydrothermal systems are controlled by alteration minerals assemblages as opposed to primary granite minerals.

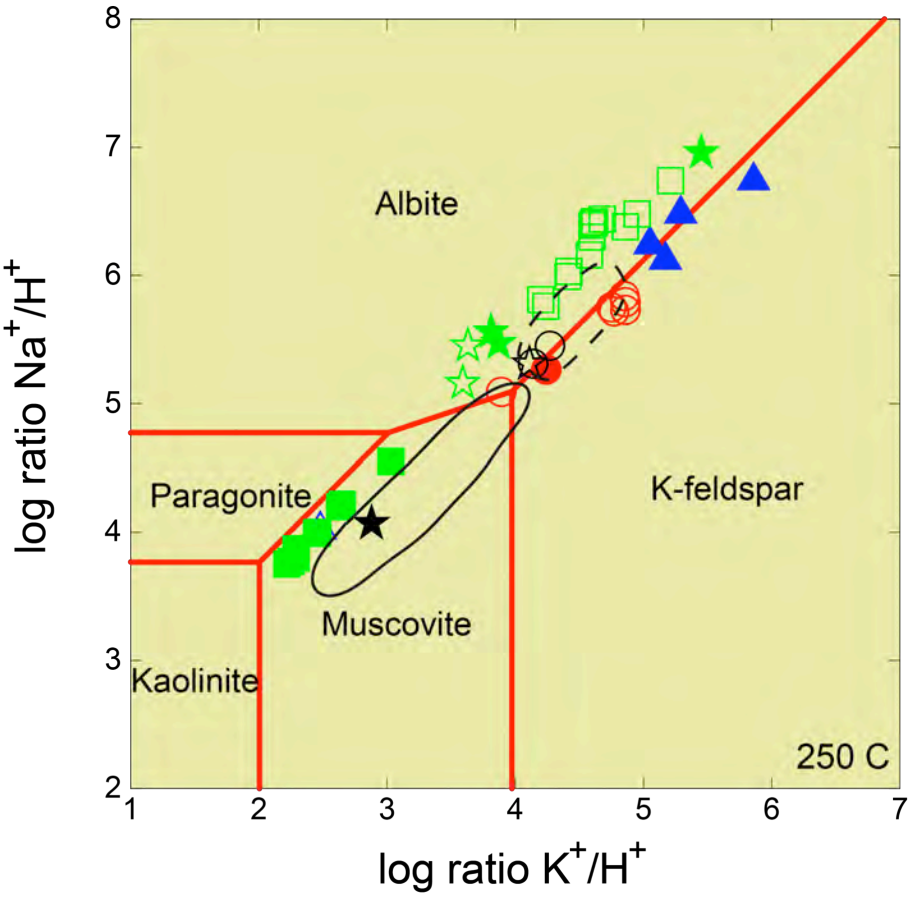

Figure 4.8. Sodium/proton vs potassium/proton activity ratios produced during experiments and comparisons with fluids from Roosevelt Geothermal wells, nearby geothermal wells, and other geothermal fields and experiments as listed in Kacandes and Grandstaff (1989). Equilibrium boundaries for end-member mineral phases, shown for reference, were calculated for quartz saturation and 250°C. Key to symbols: red circles are waters sampled from Roosevelt wells (Capuano and Cole, 1982); filled red circle is water sample with restored gas chemistry for Roosevelt well #14-2 (Capuano and Cole, 1982); blue triangles are Beaver City wells; black star is starting water composition for granite-water experiment of this study (EXP-1 in Section 4.4); black circles are waters sampled from the granite-water experiment (EXP-1) of this study; filled black star is waters sampled from terminated (quenched) granite-water experiment (EXP-1) of this study; green stars are starting water compositions for granite-water ± $scCO_2$ ± calcite ± epidote ± chlorite experiments of this study; green squares are waters sampled from granite-water ± calcite ± epidote ± chlorite experiments of this study; filled green squares are waters sampled from granite-water-$scCO_2$ ± calcite ± epidote ± chlorite experiments of this study; filled green stars are waters sampled from terminated (quenched) granite-water ± $scCO_2$ ± calcite ± epidote ± chlorite experiments of this study. Solid line bounds waters sampled from geothermal fields as described by Kacandes and Grandstaff (1989). Dashed line bounds waters produced in hydrothermal experiments as described by Kacandes and Grandstaff (1989); these hydrothermal experiments reacted fresh rock (no alteration minerals) with formation waters containing little/no dissolved carbon dioxide.

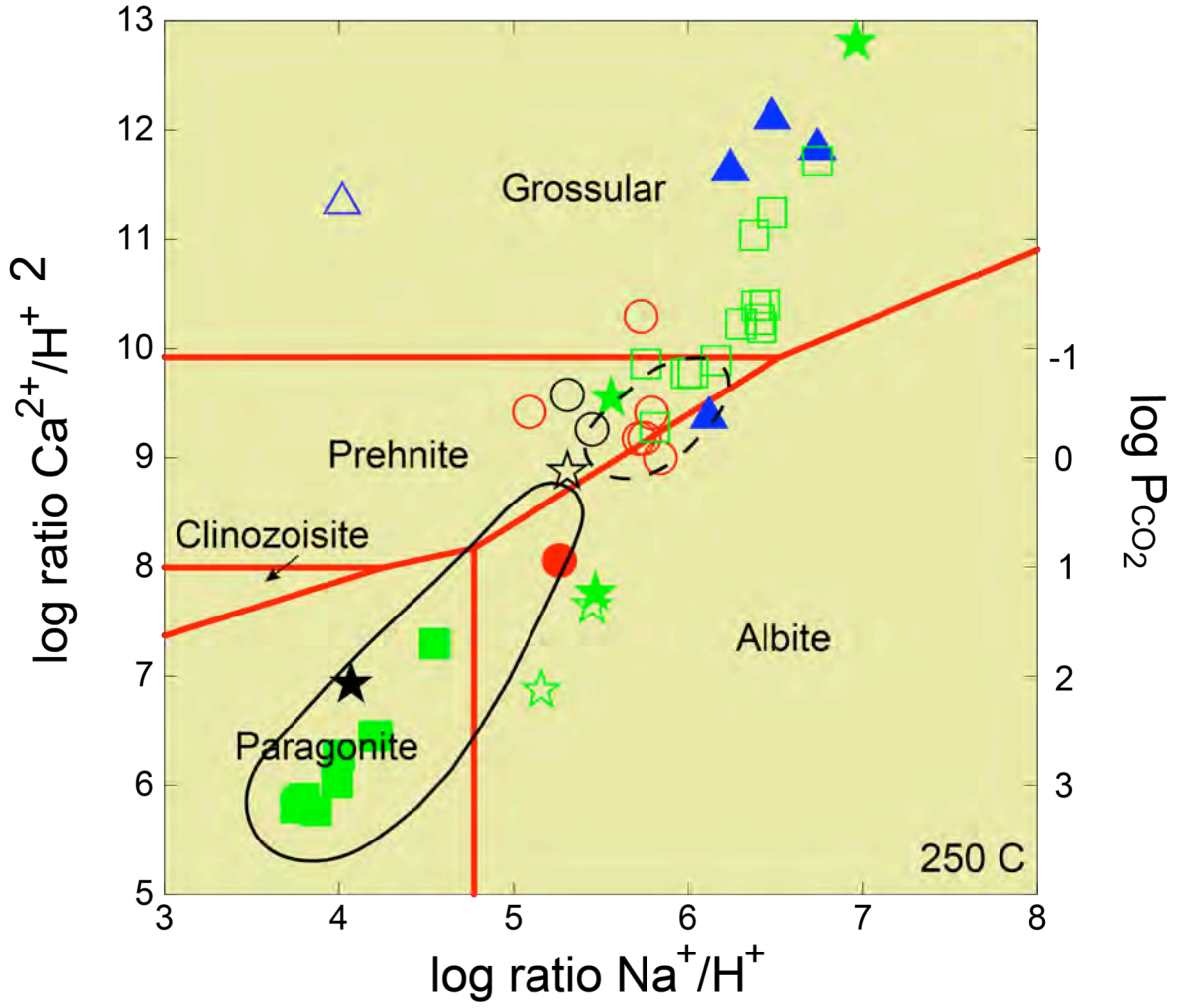

Figure 4.9. Calcium/proton vs sodium/proton activity ratios produced during experiments and comparisons with fluids from Roosevelt Geothermal wells, nearby geothermal wells, and other geothermal fields as listed in Kacandes and Grandstaff (1989). Equilibrium boundaries for end-member mineral phases, shown for reference, were calculated for quartz saturation and 250°C. Symbols and areas defined by solid and dashed lines are the same as described for Figure 4.8.

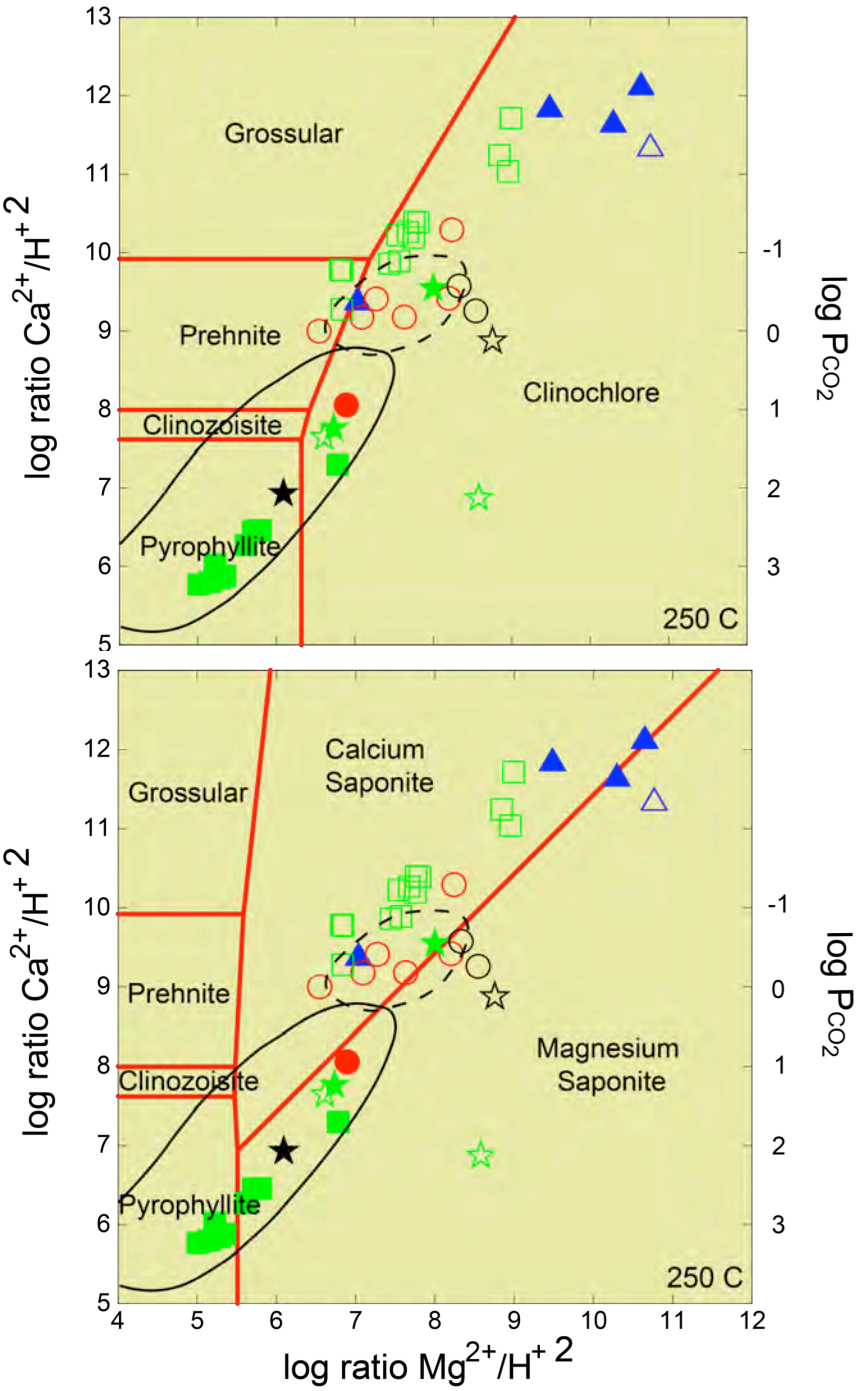

Figure 4.10. Calcium/proton vs magnesium/proton activity ratios produced during experiments and comparisons with fluids from Roosevelt Geothermal wells, nearby geothermal wells, and other geothermal fields as listed in Kacandes and Grandstaff (1989). Equilibrium boundaries for end-member mineral phases, shown for reference, were calculated for quartz saturation and 250°C. the upper figure provides the stability field for chlorite (clinochlore) and the lower figure provides the stability fields for metastable smectites. Symbols and areas defined by solid and dashed lines are the same as described for Figure 4.8.

5. Modification of Existing Simulators and Execution of Numerical Simulations

In this section, we describe the new developed database (Section 3) into the PFLOTRAN and TOUGHREACT models. We also modified the PFLOTRAN code to include dual-continuum fracture flow. In addition, we conducted batch simulations to mimic the 12 batch experiments (Section 4) for calibration of kinetic rate constants and reactive surface area of minerals; this calibration utilized the iTOUGH2-PEST parameter estimation tool with the TOUGHREACT model. Finally, we designed 2-D and 3-D conceptual models with generic 2-well patterns to simulate the flow, heat, and geochemical processes of CO_2-rock-fluid interactions and investigate the effects of using CO_2 as a working fluid on the energy extraction, carbon sequestration, and risk of CO_2 leakage.

5.1 Modification of Existing Simulators

In this section, we describe: 1) massively parallel implementation of multiple-continuum feature into PFLOTRAN model for heat transfer and reactive transport in fractured porous medium; 2) testing of the implementation with a set of benchmark problems; 3) implementation of the new database (Section 3) into PFLOTRAN and TOUGHREACT models; 4) comparison of flow and heat simulations for single- and dual-continuum models between PFLOTRAN and TOUGH2; 5) Grid refinement; 6) Parallel dual-continuum model implementation for reactive transport in PFLOTRAN.

5.1.1 Implementation of a Multiple-continuum Feature in PFLOTRAN Model for Reactive Transport in Fractured Porous Medium

We consider a single component tracer diffusion problem. Assuming that the porous medium is made of fractures (also referred to as primary continuum) and matrix (or secondary

continuum), we assume that the volume fraction of the REV occupied by the fracture is ϵ_f. The mass balance equations for the primary and secondary equations are:

$$\frac{\partial}{\partial t}\left(\epsilon_f \varphi_f C_f\right) + \boldsymbol{\nabla} \cdot \left(\boldsymbol{q}C - \epsilon_f \varphi_f \tau_f D_f \boldsymbol{\nabla} C_f\right) = -A_{fm}\Gamma_{fm}, \tag{5.1}$$

where φ_f, τ_f, D_f are the porosity, tortuosity and diffusion coefficient in the primary continuum, respectively, and C_f is the concentration of the tracer in the fracture. The term in the right hand side represents the coupling between the primary and the secondary continua, with A_{fm} being the interfacial area between the two continua, and Γ_{fm} being the mass flux between the two continua.

At each primary continuum node in the discretized system, we assume that there is a secondary continuum space which is primarily unidirectional. With this assumption for the secondary continuum, the mass balance equation is (with the assumption that the flow is small in the matrix and so advection is negligible compared to diffusion process)

$$\frac{\partial}{\partial t}\left(\varphi_m C_m\right) - \frac{\partial}{\partial \xi}\left(\varphi_m \tau_m D_m \frac{\partial C_m}{\partial \xi}\right) = 0, \tag{5.2}$$

φ_m, τ_m, D_m are the porosity, tortuosity and diffusion coefficient of the secondary continuum, respectively, and C_m is the concentration in the secondary continuum. The variable ξ is the spatial direction in the secondary continuum space.

In addition to the general initial and boundary conditions needed to solve (5.1), a set of initial and boundary conditions are required for the secondary equations (5.2). These are given as

$$\begin{aligned} C_m(\xi, t=0; \boldsymbol{r}) &= C_m^{\text{init}}, \\ \frac{\partial C_m}{\partial \xi}(\xi = 0, t; \boldsymbol{r}) &= 0, \\ C_m(\xi = L, t; \boldsymbol{r}) &= C_f(\boldsymbol{r}, t), \end{aligned} \tag{5.3}$$

where r is the position vector of primary continuum point in primary continuum space, L is the

distance between the secondary continuum node closest to the primary node and secondary node farthest from the primary continuum node.

The second equation of Eqn. (5.3) implies that the gradient is zero at one end of the secondary continuum (which is away from the primary continuum) and the third equation of Eqn. (5.3) assumes that the concentration of the secondary continuum node close to the primary continuum has the same value as the primary concentration.

Next, the flux term between the primary and secondary continua Γ_{fm} is given by

$$\Gamma_{fm} = -\varphi_m \tau_m D_m \frac{\partial C_m}{\partial \xi}(\xi = L, t; \boldsymbol{r}) \quad . \tag{5.4}$$

The primary and secondary continuum balance equations are discretized in their respective spaces during each time step, while the primary continuum equations are solved using a Newton-Raphson scheme. During each N-R iteration for primary continuum equation, the update on primary continuum concentration is used to solve the secondary continuum equations in (5.2). The secondary continuum equations reduce to a tri-diagonal system of linear equations, which can be efficiently solved using Thomas algorithm. The results from these equations give the secondary continuum concentrations, which are used along with the primary continuum concentration to calculate the coupling term in that iteration. The coupling term is then used to update the residual and the Jacobian of the primary continuum N-R iteration scheme. This process is continued till convergence is achieved and then stepped in time. Since the Thomas algorithm used to solve the secondary continuum equations does not require concentrations from other primary continuum nodes, this process is *embarrassingly parallel* (meaning no communication of one processor with other processors is required, and the calculations on each processor can be done independent of others).

Note that this is the same algorithm used for solving the heat conduction problem with multiple continua. The parallel performance of this algorithm for the heat conduction problem is given by a scalability study (Figure 5.1). As can be seen from Figure 5.1, there is almost no computational overhead when 10 secondary continuum nodes are used. There is an increase in computational time when 100 secondary continuum nodes are used, however, at around 1.5 times higher.

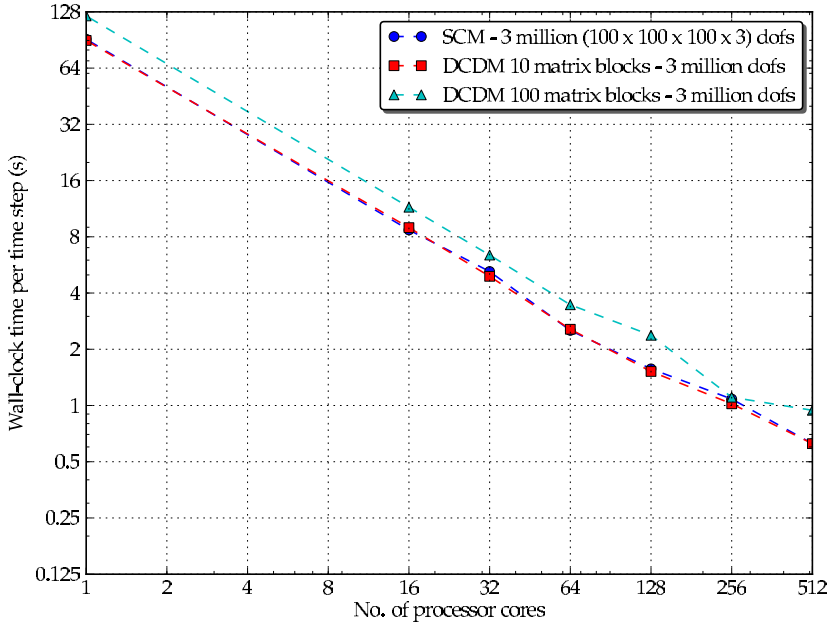

Figure 5.1. Parallel scalability of the multiple continuum algorithm in comparison with single continuum model using Jaguar XK6 at Oakridge National Laboratory (without I/O).

5.1.2. Single-component Reactive Transport

The aforementioned algorithm is then extended to single component reactive transport with linear mineral kinetics. In such a case, the governing equations for the primary and the secondary continua are

$$\frac{\partial}{\partial t}\left(\epsilon_f \varphi_f C_f\right) + \boldsymbol{\nabla}\cdot\left(\boldsymbol{q}C - \epsilon_f \varphi_f \tau_f D_f \boldsymbol{\nabla} C_f\right) = -A_{fm}\Gamma_{fm} - \epsilon_f I_f,$$
$$\frac{\partial \phi_f}{\partial t} = I_f \widehat{V}, \tag{5.5}$$

where Eqn. (5.5) is the evolution equation for the primary solid concentration. For the secondary continuum, the equations are

$$\frac{\partial}{\partial t}\left(\varphi_m C_m\right) - \frac{\partial}{\partial \xi}\left(\varphi_m \tau_m D_m \frac{\partial C_m}{\partial \xi}\right) = -I_m,$$
$$\frac{\partial \phi_m}{\partial t} = I_m \widehat{V}. \tag{5.6}$$

where $\varphi_{f,m}$, $I_{f,m}$ represent the volume fraction of the solid and the reaction rate in primary (f) and secondary continuua (m) respectively, and $\widehat{V}$ is the molar volume of the mineral.

Assuming linear kinetics, the rate of reaction $I_{m,f}$, is given by

$$I_{m,f} = k a_{m,f}\left(C_{m,f} - C_{eq}\right)\zeta_{m,f}, \tag{5.7}$$

where k is the equilibrium constant which is calculated from the database, $a_{m,f}$ is the mineral surface area in the matrix/fracture and the factor $\zeta_{m,f}$ is calculated using the following relation:

$$\zeta_{m,f} = \begin{cases} 1, & I_{m,f} > 0 \quad \text{or} \quad \phi_{m,f} > 0, \\ 0, & \text{otherwise.} \end{cases} \tag{5.8}$$

5.1.3 Benchmark Problems

The following problems (taken from Lichtner and Kang (2007)) were used to test the results from the above-described algorithm for the dual continuum model. The parameters used in the benchmark problems are listed in Table 5.1.

5.1.3.1 Tracer Diffusion Problem

A horizontal one-dimensional domain is considered with initial tracer concentrations of 0.1 mol/L in the primary and secondary continua. Fluid is injected from the left with zero tracer

concentration. Other parameters used in this problem are given in Table 5.1. Figure 5.2 shows the long tail in breakthrough curve due to leaching of tracer. These results compare well with Figure 6 of Lichtner and Kang (2007).

Table 5.1 Parameters used in the benchmark problems.

parameter	units	fracture	matrix
domain length	cm	4	-
domain width	cm	1.2	-
matrix block size	mm	-	3.5
channel width	mm	-	0.5
channel length	mm	-	9.0
primary vol. fraction	-	0.4167	-
porosity	-	1	0.4464
diffusion coeff.	m^2/s	10^{-9}	8×10^{-9}
specific mineral surface area	1/cm	2.917	17.857
Darcy velocity	m/yr	14.4	0

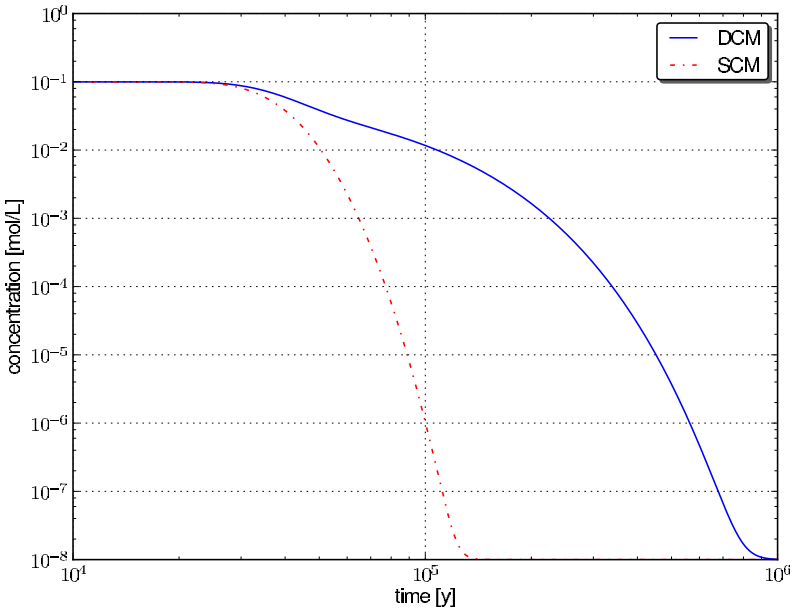

Figure 5.2 Comparison between the single (SCM) and dual continuum (DCM) results for the tracer example. The results shown are for the right end of the domain.

5.1.3.2. Reaction with Linear Kinetics Problem

Next, the same domain with parameters as the tracer problem is used with single component mineral reactions assuming linear kinetics. Two rates of $10^{-10}\ \mathrm{mol\ cm^{-2}s^{-1}}$ and $10^{-7}\ \mathrm{mol\ cm^{-2}s^{-1}}$ are considered. Figure 5.3 shows the transient as well as steady state results for the slower rate dual continuum and is compared with the single continuum steady solution. For the single continuum solution, a surface area of $2.87\ \mathrm{cm^{-1}}$ is used, as explained by Lichtner and Kang (2007). The steady state solution for dual continuum with faster rates is also shown. All these results compare well with Figures 7 and 8 from Lichtner and Kang (2007).

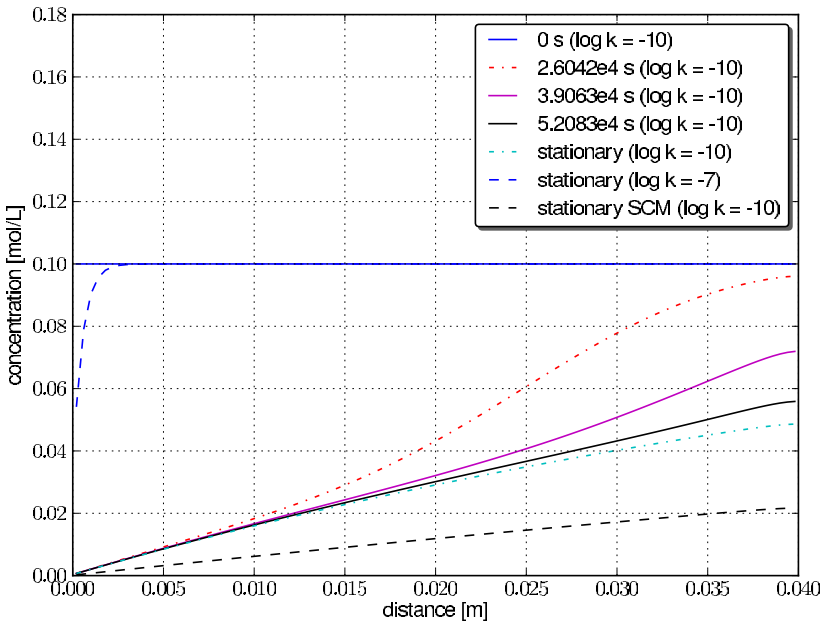

Figure 5.3. Transient and steady dual continuum results along with steady state single continuum solution. The parameters used are in Table 5.1.

5.1.4 Extension of Multiple Continuum Formulation to Multicomponent Reactive Transport

The implementation for single component reactive transport was extended to multiple component reactive transport with independent reactions involving linear kinetics. In such cases

the resulting partial differential equations are linear in nature. This framework has been extended to more general geochemistry with nonlinear kinetics and secondary species.

The algorithm discussed in Section 5.1.1 for solving single component reactive transport system was extended to multiple component systems with linear cases. The resulting algebraic system upon discretization for the secondary continuum becomes a block tridiagonal system instead of a tridiagonal system. A block tridiagonal solver is used to perform the forward-solution, for which the coupling terms between the primary and secondary continua are evaluated. Once the Newton-Raphson calculation for the primary continuum equations converges at the end of each time-step, the secondary continuum concentrations are updated using back-solve of the block tridiagonal solver.

Two example cases were chosen to test the multicomponent reactive transport implementation. Both cases involve a 1-D horizontal porous channel and a fluid (without a tracer) being injected. In the first problem, the fluid channel was assumed to contain two tracers with two different initial concentrations. The breakthrough curves for both tracers are shown in Figure 5.4 using single and dual continuum formulation at 2.6×10^4 s. Both tracers exhibit a long tail in the curves for the dual continuum case, which is expected.

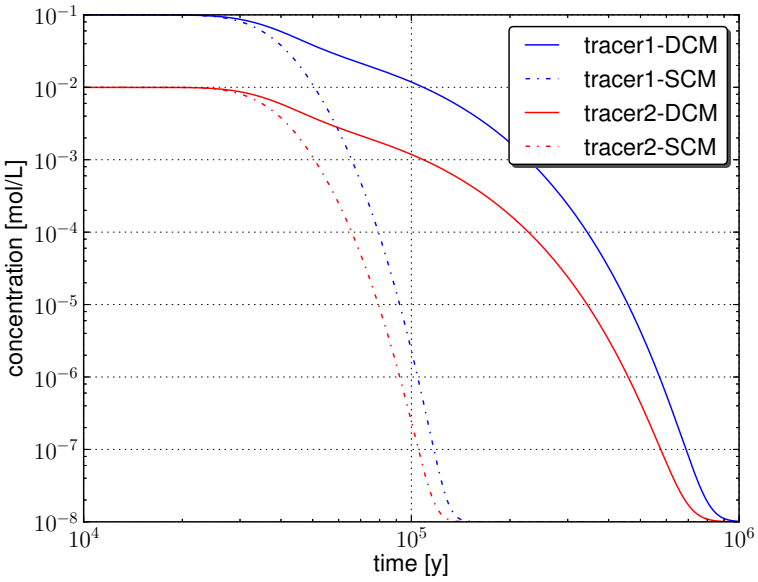

Figure 5.4. Breakthrough curves for two tracers in the domain with different initial conditions. The single continuum results are also shown.

The second example involves linear kinetics with two independent minerals (e.g., A and B), which have two different equilibrium concentrations. Both minerals are assumed to be in equilibrium with their aqueous counterparts initially, and fluid is injected from the left as discussed in the first problem. Both the minerals were assumed to have the same parameters in Table 5.1 except equilibrium concentrations. Figure 5.5 shows the concentration profile with distance at various times for both the minerals, which was expected.

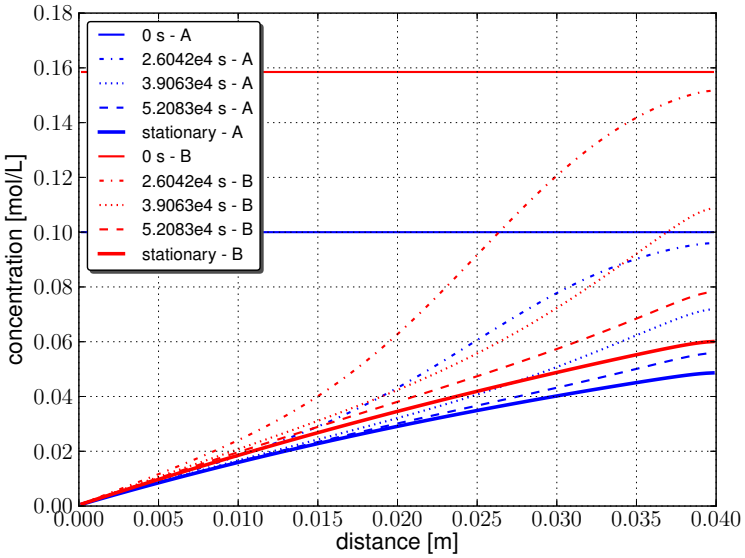

Figure 5.5. Concentration profiles at various times for two minerals from two simultaneous reactions that follow linear kinetics with different equilibrium concentrations.

5.1.5. Implementation of a New Database in PFLOTRAN and TOUGHREACT Models

The new database was implemented in the PFLOTRAN and TOUGHREACT simulators with utilization of high P/T reaction equilibrium constants. Additional capability to read the new format of the HPT database with the 17 coefficients has been implemented in PFLOTRAN and TOUGHREACT simulators.

A radial 1-D conceptual model was designed as a simple case to verify the implementation of the new database in the TOUGHREACT model. The results using new database implementation were also compared with results corresponding to the original database for theTOUGHREACT model. The model domain is 10,000 m long and 100 m thick. The injection well with radius of 0.3 m is placed in the center of model domain. The production well is located 50 m far from the injection well. The boundary conditions are set as impermeable. The injection and production rate are 0.03 kg/s for 50 years. The pressure is set to 200 bar corresponding to 2,000 m depth from surface. The temperature is 75 ^{o}C, inferred from a

temperature gradient of 30 ^{o}C/km at a depth of 2000 m, and with the ground surface temperature of 15 ^{o}C. The temperature of injected CO_2 is 20 ^{o}C. Summary details of hydrologic parameters are listed in Table 5.2.

A typical sandstone reservoir was selected as the verification example. The initial mineralogical composition and possible secondary minerals are listed in Table 5.3. The modified TOUGHREACT code adopts the new thermodynamics database with the Equation (3.2). For the original TOUGHREACT code, the EQ3/6 thermodynamics database was adopted. A batch simulation was first conducted to obtain the initial aqueous solutions that would be in equilibrium with the primary minerals. The initial aqueous solutions are listed in Table 5.4.

Table 5.2. Hydrologic parameters used for the new database verification case for the TOUGHREACT model.

Parameters	Reservoir
Temperature (°C)	75.0
Pressure (bar)	200.0
Rock grain density (kg/m^3)	2600.0
Porosity	0.30
Kz, vertical absolute permeability (m^2)	1.0×10^{-13}
Relative permeability parameters for van Genuchten-Mualem function: $k_{rl}=\sqrt{S^*}\left\{1-\left(1-\left[S^*\right]^{1/\lambda}\right)^{\lambda}\right\}^2$, here $S^*=(S_l-S_{lr})/(S_{ls}-S_{lr})$	
λ	0.457
S_{lr}	0.30
S_{ls}	1.0
S_{gr}	0.05
Capillary pressure parameters for van Genuchten function: $P_{cap}=-P_0\left(\left[S^*\right]^{-1/\lambda}-1\right)^{1-\lambda}$, here $S^*=(S_l-S_{lr})/(S_{ls}-S_{lr})$	
λ	0.457
S_{lr}	0.0
S_{ls}	0.999
P_{max}(Pa)	1.0×10^{7}
$1/P_0$(Pa)	5.1×10^{-5}

Table 5.3. Chemical composition and initial volume fractions of primary and secondary minerals for the case.

Minerals	Chemical formula	Volume Fraction (%)
Primary		
Calcite	$CaCO_3$	1.93
Quartz	SiO_2	57.89
Illite	$K_{0.6}Mg_{0.25}Al_{1.8}(Al_{0.5}Si_{3.5}O_{10})(OH)_2$	0.95
Na-smectite	$Na_{0.29}Mg_{0.26}Al_{1.77}Si_{3.97}O_{10}(OH)_2$	3.90
Kaolinite	$Al_2Si_2O_5(OH)_4$	2.02
K-feldspar	$KAlSi_3O_8$	8.18
Oligoclase	$CaNa_4Al_6Si_{14}O_{40}$	19.80
Secondary		
Albite	$NaAlSi_3O_8$	
Ca-smectite	$Ca_{0.145}Mg_{0.26}Al_{1.77}Si_{3.97}O_{10}(OH)_2$	
Magnesite	$MgCO_3$	
Dolomite	$CaMg(CO_3)_2$	
Dawsonite	$NaAlCO_3(OH)_2$	

Table 5.4. The initial aqueous concentrations (mol/kg H2O) for the geochemical simulations.

Concentrations	Reservoir
T（℃）	75.0
pH	7.26
Components	C_{TOT}(mol/kg H_2O)
Ca^{2+}	0.4737E-02
Mg^{2+}	0.2669E-04
Na^{+}	0.9905E+00
K^{+}	0.5980E-02
SiO_2(aq)	0.1034E-02
HCO_3^{-}	0.4562E-01
SO_4^{2-}	0.1324E-08
AlO_2^{-}	0.1361E-07
Cl^{-}	0.1001E+01

The geochemical simulations were conducted for 50 years using the original and modified TOUGHREACT models, respectively. Figure 5.6 plots the simulated saturation and temperature at the injection and production wells with CO_2 continuous injection of 50 years using the original "old" and new database with TOUGHREACT code. Figure 5.7 does the same for pH values. One can see from Figures 5.6 and 5.7, there are significant differences of simulated saturation, temperature and pH values between the results using the old and new database. Figure 5.8 descripts the concentration of aqueous species (Ca++, Na+, Cl-, and HCO3-) at the injection and production wells for 50 years. Figure 5.9 plots the same for the change of abundance of minerals quartz, oligoclase, calcite, and albite. It was also observed that there are significant aqueous concentration changes and mineral abundance changes between the results using the old and new databases. The results indicate that the newly implemented thermodynamics database could produce significantly different mineral dissolution and precipitation compared to the old database.

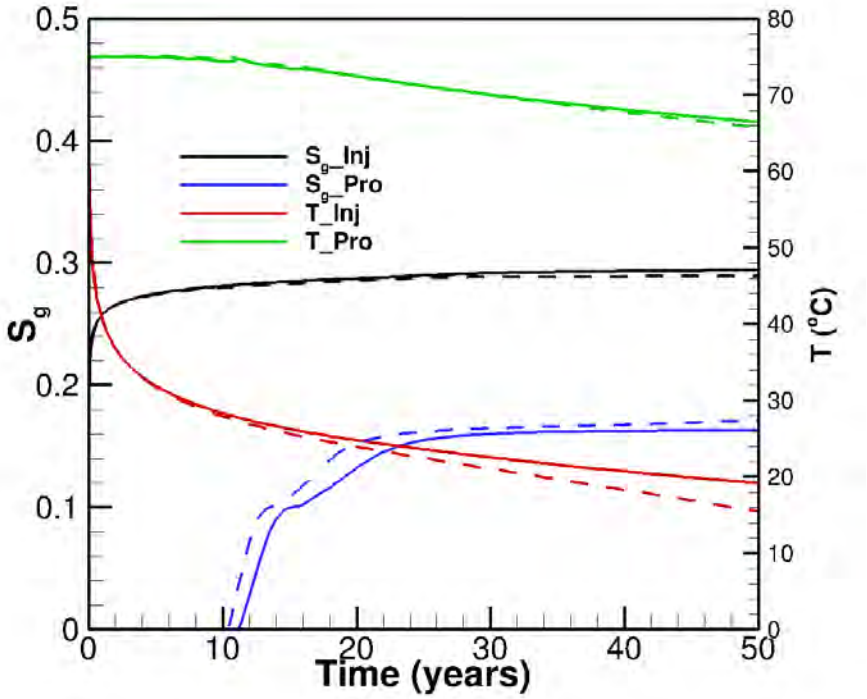

Figure 5.6. The simulated saturation and temperature at the production and injection wells for 50 years of continuous CO_2 injection with old (solid line) and new (dash line) thermodynamics database using TOUGHREACT model.

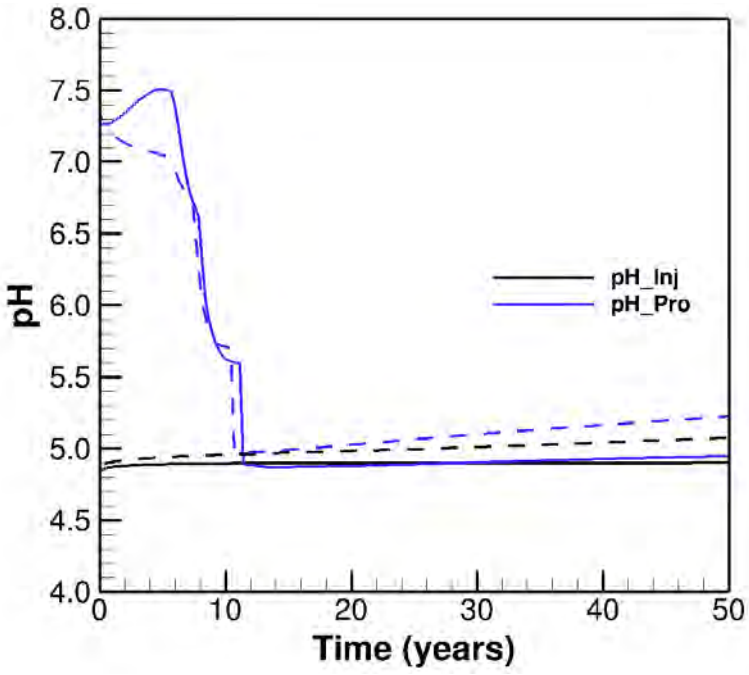

Figure 5.7. The simulated pH values at the production and injection wells for 50 years of continuous CO_2 injection with old (solid line) and new (dash line) thermodynamics database using TOUGHREACT model.

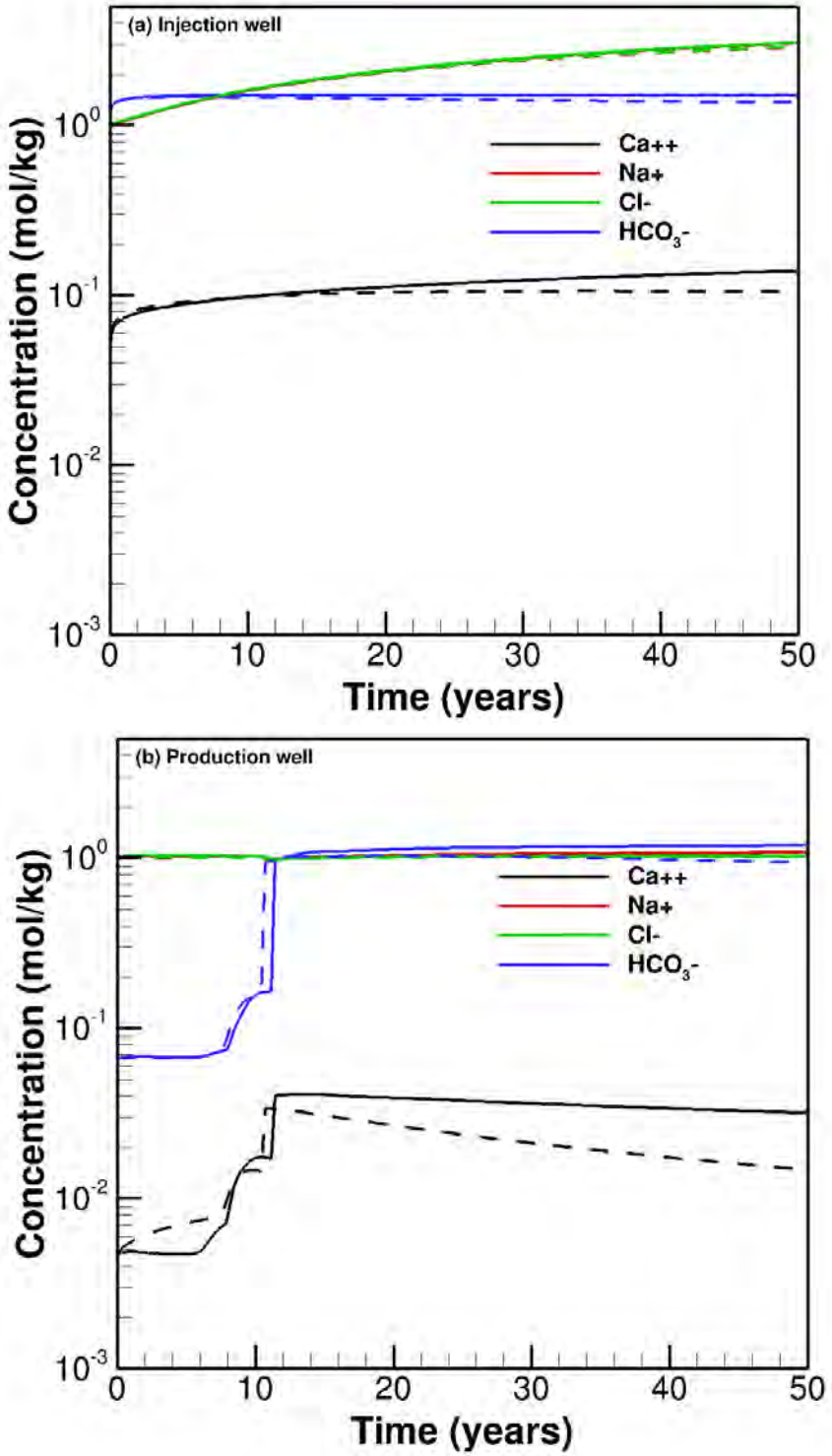

Figure 5.8. The simulated aqueous concentrations of species (Ca++, Na+, Cl-, and HCO3-) at the injection and production wells for 50 years of continuous CO_2 injection with old (solid line) and new (dash line) thermodynamics database using TOUGHREACT model.

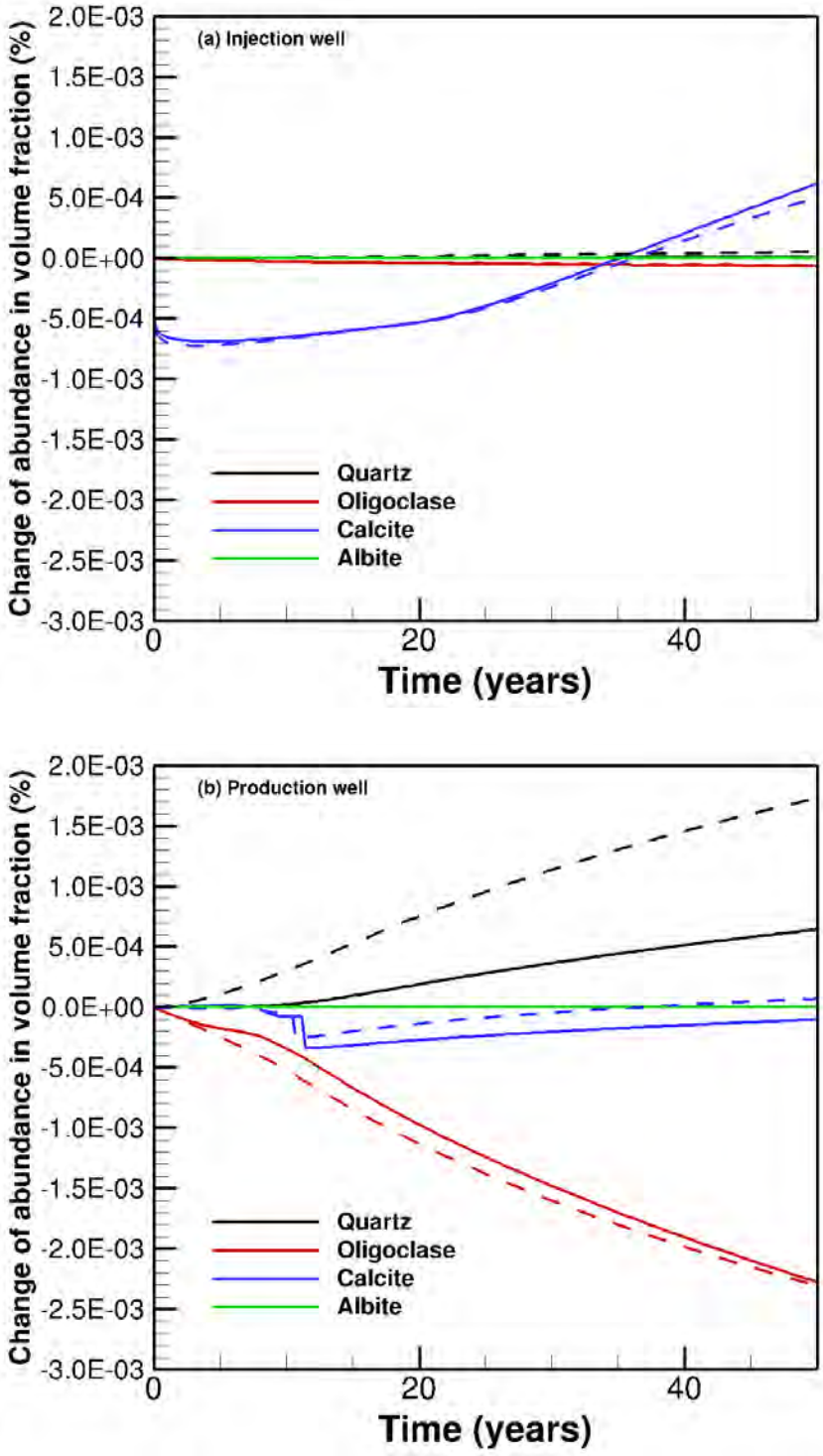

Figure 5.9. The simulated changes of abundance in volume fraction (%) for minerals (quartz, oligoclase, calcite, and albite) at the injection and production wells for 50 years of continuous CO_2 injection with old (solid line) and new (dash line) thermodynamics database using TOUGHREACT model.

5.1.6 Comparison of Flow and Heat Simulations for Single- and Dual-continuum Models between PFLOTRAN and TOUGH2

We first compared the single continuum results between PFLOTRAN and TOUGH2 (Figure 5.10). For the single-continuum domain, an inner fractured zone was assumed with a higher permeability of 10^{-13} m^2. Table 5.5 lists the model domain design and parameter setup for the comparisons of flow and heat simulations for single- and dual-continuum models between PFLOTRAN and TOUGH2. Excellent agreement can be seen between the results for single continuum model using PFLOTRAN and TOUGH2.

Next, the results for dual-continuum models between PFLOTRAN and TOUGH2 are plotted in Figure 5.11. Generally good agreement is exhibited between the results, although minor disparities are observed in the initial time steps. One must note that these differences are expected due to the difference in the dual continuum formulation between PFLOTRAN and TOUGH2 as follows: the boundary conditions are implemented for the matrix in the dual continuum formulation is different. PFLOTRAN uses a Dirichlet boundary condition at the matrix-fracture interface and assumes that the temperature at the interface is the fracture node temperature. On the other hand, in TOUGHREACT, a flux boundary condition is used at the interface between the fracture and matrix block.

Table 5.5 Hydrologic parameters, initial, and production/injection conditions used for comparisons of single- and dual-continuum models between PFLOTRAN and TOUGH2.

domain size	1800 m × 500 m × 500 m
number of cells	18 × 10 × 10
injection well location	(350, 275, 275)
production well location	(1350, 275, 275)
Dual-continuum number of nested blocks	10
fracture volume	2 %
fracture spacing	50 m
fracture permeability	10^{-13} m^2
fracture porosity	0.05
fracture tortuosity	1.0
fracture van Genuchten λ	0.444
fracture van Genuchten α	2.4×10^{-4}
matrix permeability	10^{-15} m^2
matrix porosity	0.05
matrix tortuosity	0.1
matrix van Genuchten λ	0.444
matrix van Genuchten α	1.485×10^{-6}
thermal conductivity (matrix and fracture)	2.51 W/m/^{o}C
rock specific heat (matrix and fracture)	1000 J/kg/^{o}C
rock density (matrix and fracture)	2650 kg/m^3
initial temperature	200^{o}C
initial pressure	200 bar
injection rate	50 kg/s
bottom hole pressure (production)	175 bar
well facture	1×10^{-11}
initial fluid in domain	water

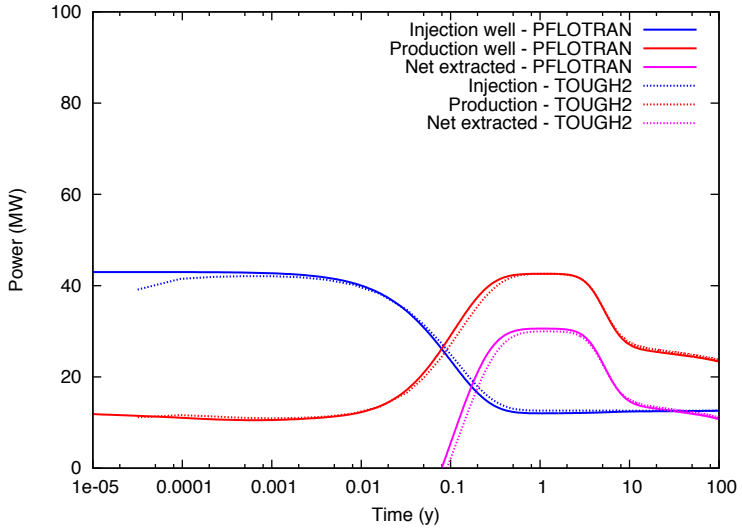

(a) Power generated

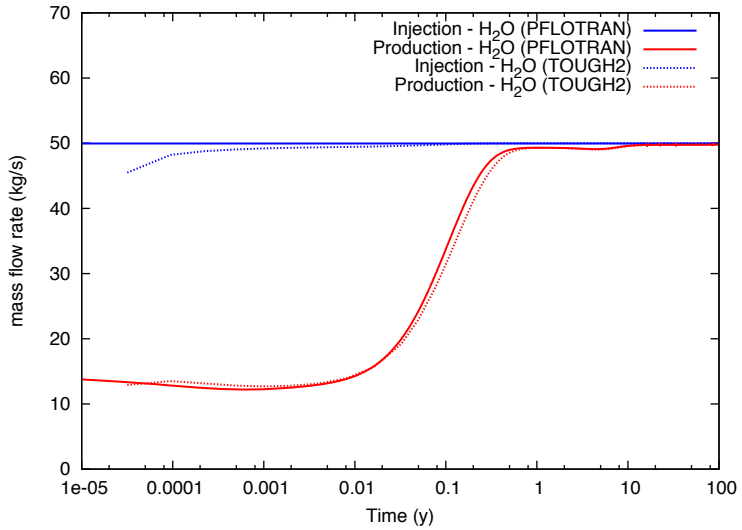

(b) Mass flow rate

Figure 5.10. Comparison of net power generated, mass flow rates, pressure, and temperature between PFLOTRAN and TOUGH2 using the single continuum model.

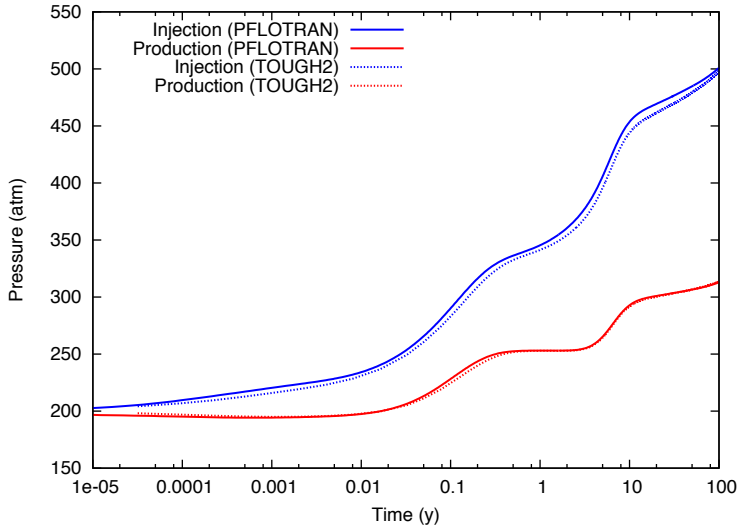

(c) Pressure

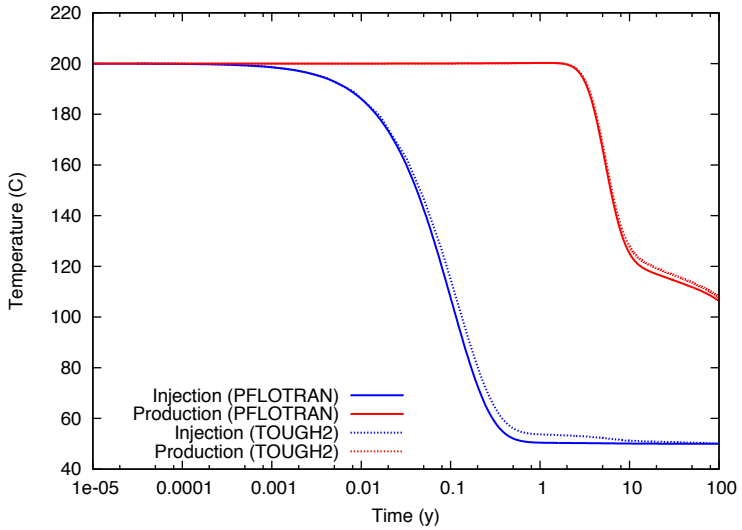

(d) Temperature

Figure 5.10. (Cont.) Comparison of net power generated, mass flow rates, pressure and temperature between PFLOTRAN and TOUGH2 using the single continuum model.

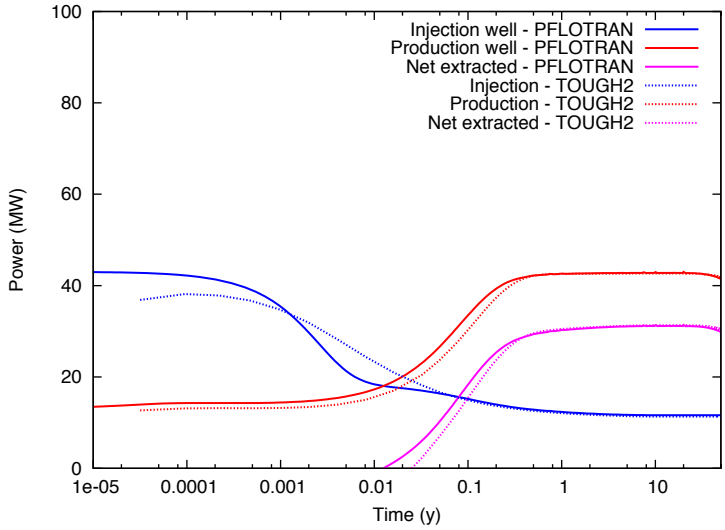

(a) Power generated

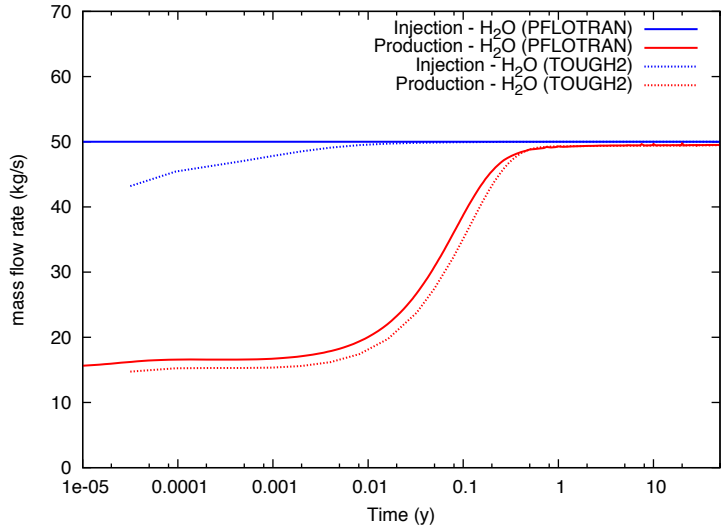

(b) Mass flow rate

Figure 5.11. Comparison of net power generated, mass flow rates, pressre, and temperature between PFLOTRAN and TOUGH2 using the dual continuum model.

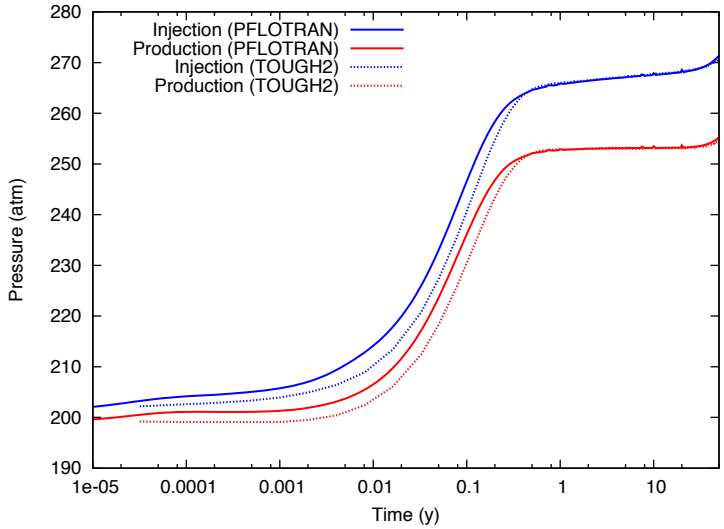

(c) Pressure

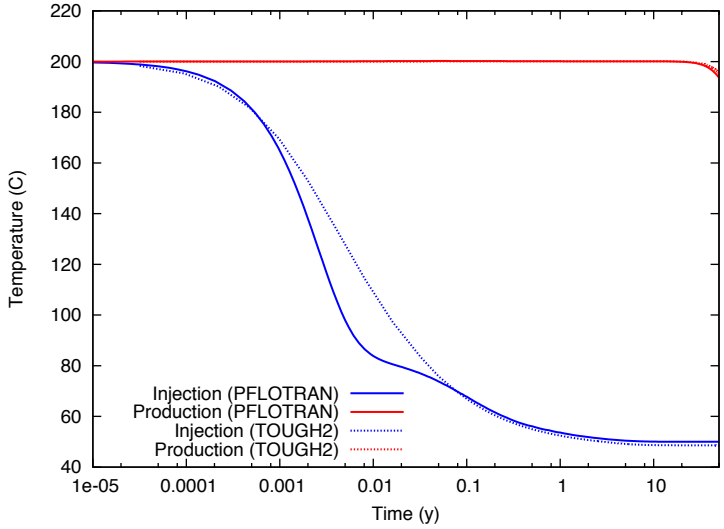

(d) Temperature

Figure 5.11. (Cont.) Comparison of net power generated, mass flow rates, pressure and temperature between PFLOTRAN and TOUGH2 using the dual continuum model.

5.1.7 Grid Refinement Study

To investigate the effect of grid refinement on the results, a study was performed with 90x25x25, 180x50x50 and 360x100x100 grid cells using the PFLOTRAN single-continuum model. Results corresponded to grid spacings of 5 m, 10 m and 20 m. Water was used as the

working fluid and the domain was the same as described in the previous section. Approximately 1080 processor cores for the 360x100x100 case, 144 processor cores for the 180x50x50 case and 16 processor cores for the 90xx25x25 case were used to run the simulation for 100-year time period. Times taken were 14 min, 33.76 min, 144.44 min, respectively, for the simulations to complete. The comparison between the results from these three cases is shown in Figure 5.12.

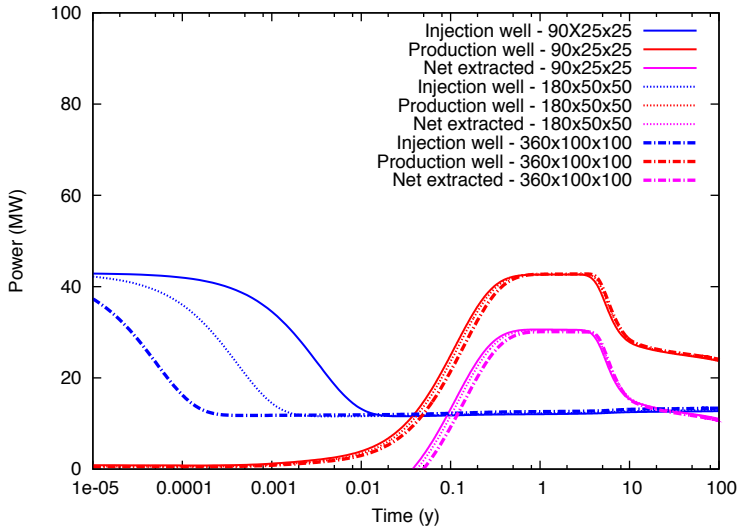

(a) Power generated

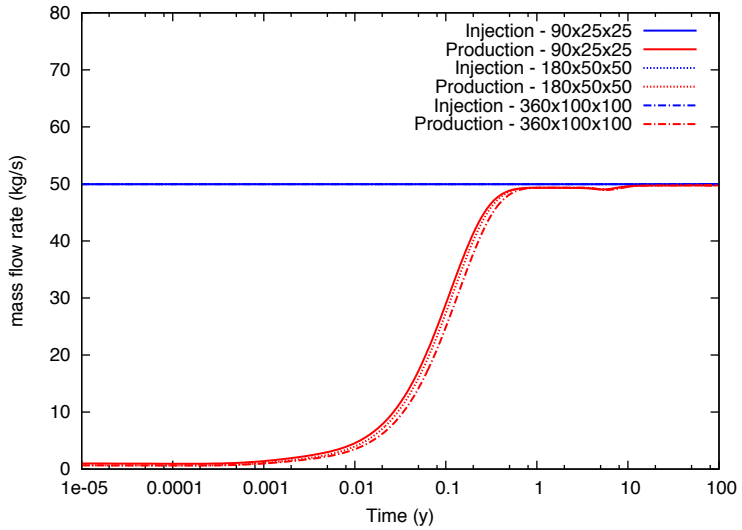

(b) Mass flow rate

Figure 5.12. Comparison of net power generated, mass flow rates, pressure and temperature for various grid sizes using PFLOTRAN single-continuum model with water as a working fluid.

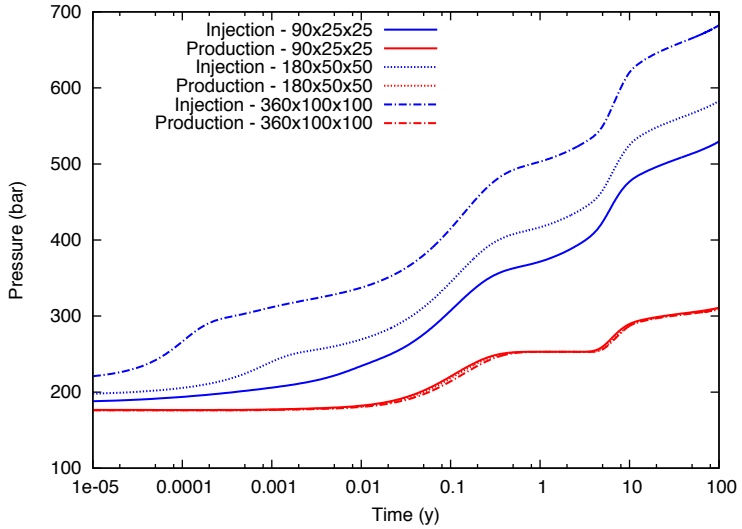

(c) Pressure

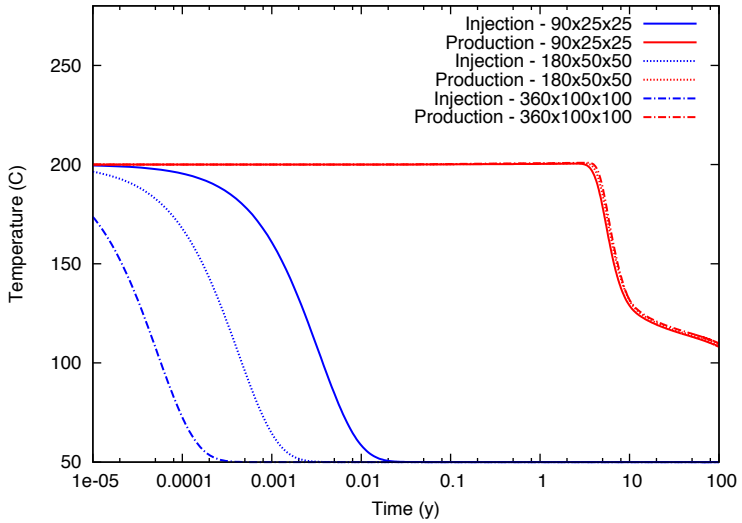

(d) Temperature

Figure 5.12. (Cont.) Comparison of net power generated, mass flow rates, pressure and temperature for various grid sizes using PFLOTRAN single-continuum model with water as a working fluid.

The mass flow rates, production temperature and production power exhibit similar values for all three cases. Differences in injection temperature and hence injection power can be found only at initial time periods (less than 0.1 years), and they reach the same values asymptotically. Minor differences are observed in the production pressure. However, the injection pressure

seems to depend substantially on the grid spacing and attains higher values for smaller grid spacing. Thus, for estimating the power production in a geothermal reservoir it seems like one can work with a coarse grid, provided chemical interactions are not considered which very likely will require a finer grid in comparison to solving the flow equations. On the other hand, this could affect the pressure predictions at the injection well, which could therefore affect the design of the injection well.

5.1.8 Parallel Performance

The presence of a secondary continuum can tremendously increase the number of degrees of freedom (or the unknowns to be solved for) in the given problem. The degrees of freedom to be solved for with the multi-continuum formulation are $N_{\text{cells}}^{\text{pri}} \times N_{\text{dof}}^{\text{pri}} + N_{\text{cells}}^{\text{pri}} \times N_{\text{cells}}^{\text{sec}} \times N_{\text{dof}}^{\text{sec}}$, which $N_{\text{cells}}^{\text{pri}}$ is the number of cells in the primary continuum, $N_{\text{dof}}^{\text{pri}}$ is the number of degrees of freedom per cell in the primary continuum, $N_{\text{cells}}^{\text{sec}}$ is the number of secondary cells at each primary cell, $N_{\text{dof}}^{\text{sec}}$ is the number of degrees of freedom per secondary cell. Thus, the ratio of the multi-continuum approach degrees of freedom to that of a single continuum for the same domain is

$$N_r = 1 + \frac{N_{\text{cells}}^{\text{sec}} \times N_{\text{dof}}^{\text{sec}}}{N_{\text{dof}}^{\text{pri}}}. \tag{5.9}$$

The parallel performance with reactive transport for a single component system is first considered.

A comparison of actual (clock) simulation times required using the Thomas algorithm versus the block tridiagonal solver is shown in Figure 5.13. A million primary cells are considered, with $N_{\text{dof}}^{\text{prim}}$ and $N_{\text{dof}}^{\text{sec}}$ both being equal to 1. The total number of degrees of freedom

for using 10 and 100 secondary cells are 11 million and 101 million, respectively. The single continuum case scales linearly up to 48 processor cores. The Thomas algorithm with 10 cells scales up to 192 processor cores and surprisingly takes almost the same time as single continuum for the cases with 384, 768 and 1,536 processor cores. Note the difference from the heat transport case where the single continuum and multiple continuum with 10 cells had almost the same CPU times for all processor cores. This is because the primary continuum had 3 degrees of freedom in the heat transport whereas the primary continuum had only one with reactive transport.

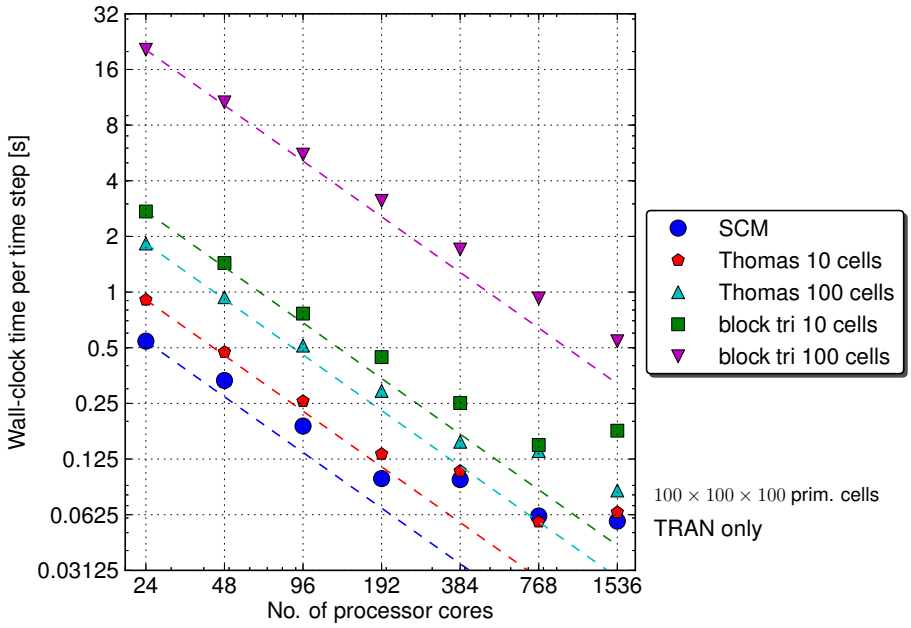

Figure 5.13. Parallel scalability comparison between the Thomas algorithm and the tridiagonal solver for the multiple continuum formulation using Mustang supercomputer at Los Alamos National Laboratory (without I/O). Only transport is considered with 1 degree of freedom per grid cell for both primary and secondary continua. The dashed line shows ideal scaling based on the wall clock time per time step for 24 cores.

With 100 cells, Thomas algorithm scales up to 384 processor cores. As expected, the Thomas algorithm scales better with an increase in the number of secondary cells since more

work is done. Also, in the linear scaling regime wall-clock time with the 100 cells case is only about twice that of 10 cells. The block tridiagonal solver takes a wall-clock time of about 3 times for 10 cells and about 12 times for 100 cells compared to Thomas algorithm. In addition, the block tridiagonal solver scales up to 384 and 1536 cores with 10 and 100 cells respectively. Thus the block tridiagonal solver is slower than Thomas algorithm but scales better since it does more amount of work. Furthermore, as the number of secondary cells increase the ratio of the wall-clock times between the block tridiagonal solver and the Thomas algorithm also increases.

A comparison between the computational times for single component and multicomponent scenarios is considered. For the multicomponent cases, 10 and 20 components are used essentially using tracers. 1 million primary grid cells are considered with 10 and 20 secondary cells for the mutlicontinuum case. Table 5.6 shows the degrees of freedom involved for the different scenarios with single and multiple components for the single and multi-continuum formulation. Looking at the parallel scalability study in Fig. 5.14, the following conclusions can be drawn: (1) an increase in the number of secondary cells for fixed number of components increases the parallel scalability, and (2) an increase in the number of components for fixed number of secondary cells increases the parallel scalability as well. This is expected since more work needs to be done by the processor cores in both scenarios.

Table 5.6. Number of degrees of freedom based on number of components and number of secondary continuum grid cells for 1 million primary grid cells.

	1 comp	10 comp	20 comp
SCM	1 million	10 million	20 million
10 secondary cells	11 million	110 million	220 million
20 secondary cells	21 million	210 million	420 million

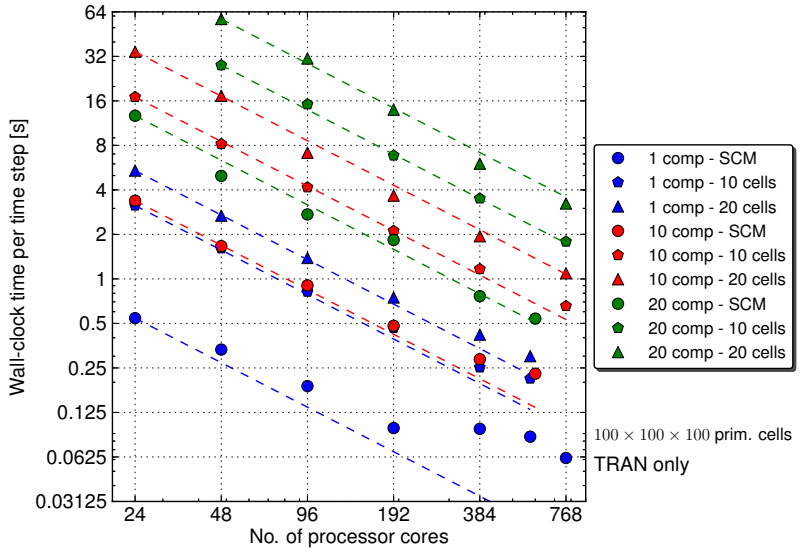

Figure 5.14. Parallel scalability comparison for different number of components with the multiple continuum formulation using Mustang supercomputer at Los Alamos National Laboratory (without I/O). Only transport is considered with 1, 10, 20 degree of freedom per grid cell for primary as well as secondary continua. Block tridiagonal solver is used in the multiple continuum algorithm. The dashed line shows ideal scaling. Ideal scaling is calculated based on wall- clock time per time step using 24/48 cores.

Figure 5.15 shows the ratio of wall-clock times for a given number of components to corresponding single continuum wall-clock time as a function of number secondary continuum grid cells. Note that the ratio of the number of degrees of freedom for a multi-continuum with multiple components case to the one for a single continuum case with same number multiple components ends up being N_r (and for transport N_r is the number of secondary cells plus one). Ideally, one would expect that the four cases in Figure 5.15 to be matched on the same curve. The 5-component and 1-component cases match up to 20 secondary cells case while the 10-component case matched with 1, 5-component cases up to 10 secondary cells. Difference is observed with larger number of secondary continuum grid cells. Also, none of the 20-

components cases match with other components cases. One explanation for the deviation from ideal behavior is that the increase in the computational time was taken to solve the secondary continuum linear system of equations with an increase in the number of components as well as the number of secondary grid cells. This could perhaps be reduced by using a parallel solver for this aspect.

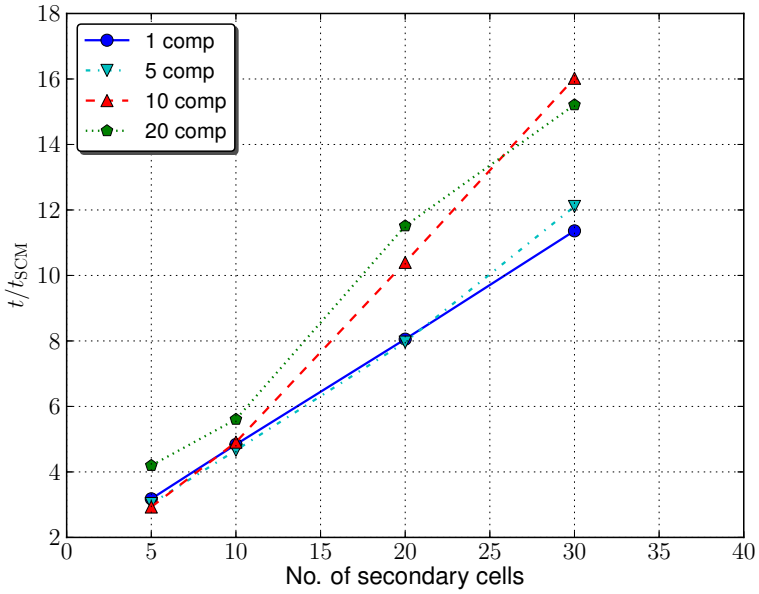

Figure 5.15. Ratio of multiple continuum times to single continuum time corresponding to the same number of components as a function of ratio of degrees of freedom to that of single continuum for fixed number of components. The times chosen for the 1 million primary cells case are based on wall-clock time per step using 48 cores.

5.1.9 Effect of Secondary Continuum Grid Spacing

The effect of spacing between nodes in the discretized secondary continuum on the solution convergence is discussed in this section. A horizontal one-dimensional column with flow from left to right is considered. A tracer is assumed to be present initially in the domain. The initial, left boundary and right boundary concentrations are set to 10^{-8}, while the initial

concentration in the secondary continuum is set to 1. In such a scenario, one would expect that the tracer to leach out from the secondary continuum to the primary continuum increasing the concentration in the primary continuum. The tracer then leaves the domain through the boundary due to flow, which will decrease the primary concentration. Figure 5.16 shows the concentration at the node closet the right boundary as a function of time for various grid spacing in the secondary continuum with cube geometry. The curves in blue represent the results with equal grid spacing. Note that when equal grid spacing is used, even with 250 grid cells in the secondary continuum, a convergence in the solution is not reached. This is because the accuracy of the primary continuum solution depends on the accuracy of the coupling flux term, which in turn depends on the gradient between the primary node and the secondary node closest to the primary node. The smaller the distance between these two nodes, the more accurate is the gradient. If one resorts to equal grid spacing, then a large number of nodes is needed to get a small distance. Alternatively, one could use fewer number of grid cells with variable grid spacing such that the smallest spacing is the one between the primary node and the secondary node closest to the primary. One approach is using grid spacings that follow geometric series. This requires specification of the smallest grid spacing which is between the primary node and the secondary node closest to it, the number of secondary nodes and the sum of the grid spacings which is the matrix block size (or side of the cube), i.e.,

$$\frac{L}{2} = (\Delta\xi)_1 \left[\frac{r^n - 1}{r - 1}\right] \tag{5.10}$$

where: L is the side of the cube, n is the number of secondary grid cells, $(\Delta\xi)_1$ is the smallest grid spacing, r is the geometric ratio. From the above equation, the value of r can be evaluated, then the remaining grid spacings can be computed. Using this variable grid spacing, the problem

discussed above is solved and the results are shown with red curves in Figure 5.16. Note that with just 10 grid cells convergence in the solution is achieved. The smallest grid spacing used was 10^{-4} m for this problem. Other parameters used are shown in Table 5.7.

Table 5.7. Parameters to study the effect of secondary grid spacing.

parameter	units	fracture	matrix
domain length	m	10	-
domain width	m	1	-
matrix block size	m	-	50
primary vol. fraction	-	0.002	-
porosity	-	0.02	0.5
diffusion coeff.	m^2/s	10^{-9}	10^{-9}
Darcy velocity	m/yr	1	0
primary grid cells	-	100	-

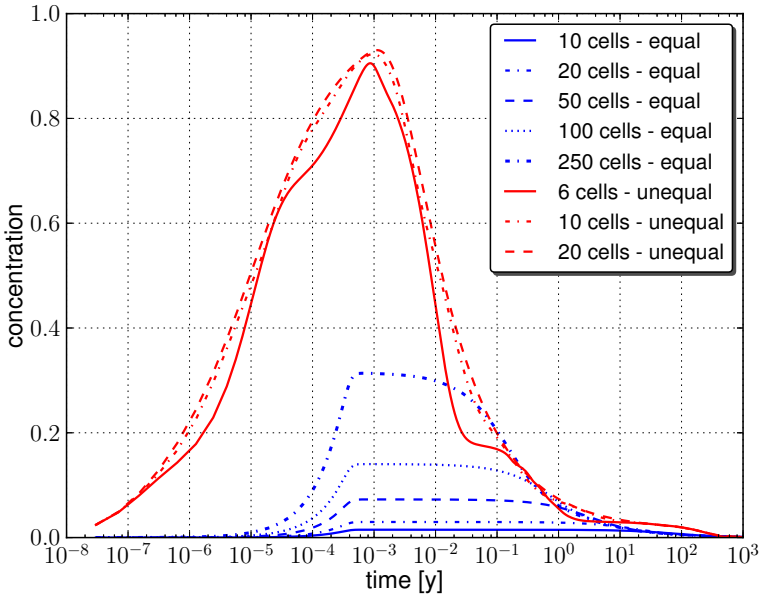

Figure 5.16. Primary continuum concentration profiles close to the right boundary for different grid cells in the secondary continuum. The blue curves use equal grid spacing while the red curves are based on geometric progressive grid spacing with the smallest being closest to the primary-secondary continua interface.

5.2. Conduct Laboratory-scale Simulations, Calibrate and Evaluate Kinetic Rates

5.2.1 Calibration of Kinetic Rate Constants and Reactive Surface area of Minerals for Batch Experiments EXP-1 to EXP-5

The five batch experiments with water-granite ± epidote ± CO_2 experiments (EXP-1 to EXP-5) were conducted and analyzed, as described in Section 4. The five experiments are moderate pH water + granite experiment, moderate pH water + granite + $scCO_2$ experiment, moderate pH water + granite + $scCO_2$ experiment, moderate pH water + granite + epidote experiment, and moderate pH water + granite + epidote + $scCO_2$ experiment, respectively. In this section, we coupled a parameter estimation tool (iTOUGH2-PEST) with the TOUGHREACT model to mimic the batch experiments, for sake of calibration of kinetic rate constants and reactive surface area of minerals against major cation concentrations.

Simulations of the batch experiments were conducted using the TOUGHREACT code, but without flow, to mimic the batch conditions. The TOUGHREACT code was run with a single grid cell to represent a reactor vessel. Input to TOUGHREACT requires specifying the initial volume fractions and surface areas of the primary mineral assemblage together with the initial fluid composition. The thermodynamic database used for the batch simulations was taken from EQ3/6 database (Wolery, 1992). The possible secondary mineral assemblage was selected based on initial equilibrium batch modeling, with associated procedures discussed below. Firstly, CO_2 is added to the initial formation brine in contact with the primary mineral assemblage, and the saturation indices of all minerals present in the database are calculated and analyzed. Minerals that become supersaturated and have the potential to form under the given conditions are included in the secondary mineral composition. Then, batch models are re-executed with the new (resulting) mineral assemblage until an equilibrium aqueous solution is reached. In addition,

the carbonate-bearing minerals are also considered as a possible secondary mineral assemblage because of expected reactions following CO_2 injection. For the five batch experiments water + granite ± $scCO_2$ (EXP-1 to EXP-3), the primary minerals, possible secondary minerals and their chemical compositions and initial volume fractions based on the batch experiment data are listed in Table 5.8. With the addition of epidote for experiments EXP-4 and EXP-5, the possible secondary mineral assemblage was re-selected based on initial equilibrium batch modeling. The corresponding primary and possible minerals assemblages are also listed in Table 5.8. The kinetic properties (rate constant, activation energy, and power term) of multiple mechanisms (neutral, acid and base) for the primary and secondary minerals are listed in Table 5.9.

Simulation periods were assigned to be 2000 hours, based on the original experimental work. Supercritical CO_2 was injected at 674.4 hours at a rate of 5.7611×10^{-6} kg/s for experiment EXP-2, at 700.4 hours with a rate of 5.4600×10^{-6} kg/s for experiment EXP-3, and at 672.1 hours with a rate of 5.7×10^{-6} kg/s for experiment EXP-5 for an hour, respectively. At the same time as CO_2 injection, brine was extracted with an equal and opposite rate for the three experiments EXP-2, EXP-3, and EXP-5, respectively, to match experimental conditions.

Table 5.8. Chemical composition and initial volume fractions of primary and secondary minerals for five batch experiments used with the TOUGHREACT simulation model.

Mineral	Chemical composition	Initial volume fraction of minerals				
		EXP-1	EXP-2	EXP-3	EXP-4	EXP-5
Primary:						
Quartz	SiO_2	0.3184	0.3189	0.3178	0.1805	0.1805
Oligoclase-uwy[a]	$Na_{0.77}Ca_{0.23}Al_{1.23}Si_{2.77}O_8$	0.3184	0.3189	0.3187	0.1805	0.1805
Albite	$NaAlSi_3O_8$	0.0805	0.0804	0.0806	0.0456	0.0456
K-Feldspar	$KAlSi_3O_8$	0.2472	0.2469	0.2474	0.1401	0.1401
Annite	$KFe_3AlSi_3O_{10}(OH)_2$	0.0145	0.0143	0.0145	0.0082	0.0084
Phlogopite	$KAlMg_3Si_3O_{10}(OH)_2$	0.0209	0.0206	0.0209	0.0119	0.0121
Epidote	$Ca_2Al_2(Fe^{3+},Al)(SiO_4)(Si_2O_7)O(OH)$	--	--	--	0.4331	0.4327
Porosity	-	0.9814	0.9815	0.9813	0.9877	0.9835
Calcite	$CaCO_3$	0.0	0.0	0.0	0.0	0.0
Magnesite	$MgCO_3$	0.0	0.0	0.0	0.0	0.0
Illite	$(K,H_3O)(Al,Mg,Fe)_2(Si,Al)_4O_{10}[(OH)_2,(H_2O)]$	0.0	0.0	0.0	0.0	0.0
Smectite	$K_{0.04}Ca_{0.5}(Al_{2.8}Fe_{0.53}Mg_{0.7})(Si_{7.65}Al_{0.35})O_{20}(OH)_4$	0.0	0.0	0.0	0.0	0.0
Kaolinite	$Al_2Si_2O_5(OH)_4$	0.0	0.0	0.0	0.0	0.0
Chlorite	$Mg_{2.5}Fe_{2.5}Al_2Si_3O_{10}(OH)_8$	0.0	0.0	0.0	0.0	0.0
Muscovite	$KAl_3Si_3O_{10}(OH)_2$	0.0	0.0	0.0	0.0	0.0
Hematite	Fe_2O_3	0.0	0.0	0.0	0.0	0.0
Dolomite	$CaMg(CO_3)_2$	0.0	0.0	0.0	0.0	0.0
Ankerite	$CaMg_{0.3}Fe_{0.7}(CO_3)_2$	0.0	0.0	0.0	0.0	0.0
Dawsonite	$NaAlCO_3(OH)_2$	0.0	0.0	0.0	0.0	0.0
Siderite	$FeCO_3$	0.0	0.0	0.0	0.0	0.0

a) Oligoclase at specific ratio used for batch experiment by University of Wyoming.

Table 5.9 Kinetic rate parameters of primary and secondary minerals, reactive surface area for geochemical simulations using the TOUGHREACT code.

Mineral	Neutral Mechanism		Acid Mechanism			Base mechanism		
	logk [a]	E_a [b]	logk [a]	E_a [b]	n [c]	logk [a]	E_a [b]	n [c]
Primary:								
Quartz	-13.99	87.7	-	-	-	-	-	-
Oligoclase	-11.84	69.8	-9.67	65.0	0.457	-	-	-
Albite	-12.56	69.8	-10.16	65.0	0.457	-15.6	71.0	-0.572
K-Feldspar	-12.41	38.0	-10.06	51.7	0.500	-21.2	94.1	-0.823
Annite [d]	-12.55	22.0	-9.84	22.0	0.525	-	-	-
Phlogopite	-12.40	29.0	-	-	-	-	-	-
Epidote	-11.99	70.7	-10.60	71.1	0.338	-17.33	79.1	-0.556
Chlorite	-12.52	88.0	-11.11	88.0	0.500	-	-	-
Calcite	-5.81	23.5	-0.30	14.4	1.000	-	-	-
Secondary:								
Calcite	-5.81	23.5	-0.30	14.4	1.000	-	-	-
Magnesite	-9.34	23.5	-6.38	14.4	1.000	-	-	-
Illite[e]	-13.55	22.0	-11.85	22.0	0.370	-14.55	22.0	-0.200
Smectite	-12.78	35.0	-10.98	23.6	0.340	-16.52	58.9	-0.400
Kaolinite	-13.16	22.2	-11.31	65.9	0.777	-17.05	17.9	-0.472
Chlorite	-12.52	88.0	-11.11	88.0	0.500	-	-	-
Muscovite	-13.55	22.0	-11.85	22.0	0.370	-14.55	22.0	-0.220
Hematite	-14.60	66.2	-9.39	66.2	1.000	-	-	-
Dolomite	-7.53	52.2	-3.19	36.1	0.500	-5.11	34.8	0.500
Ankerite[f]	-7.53	52.2	-3.19	36.1	0.500	-5.11	34.8	0.500
Dawsonite	-7.00	62.8	-	-	-	-	-	-
Siderite	-8.90	62.8	-3.19	36.1	0.500	-	-	-

Note: Kinetic rate parameters from Palandri and Kharaka (2004);
a) logk: kinetic rate constant k at 25 ^oC ($mol/m^2/s$);
b) E_a: activation energy (KJ/mol);
c) n: power term with respect to H^+;
d) set to Biotite; e) set to Muscovite; f) set to Dolomite

The measured aqueous concentration of Na+ was selected to calibrate the kinetic rate constant (*k*) at 25 ^oC and the reactive surface area of minerals Albite and Oligoclase for the experiments EXP-1 through EXP-5. The kinetic rate constants and reactive surface area of mineral K-feldspar were calibrated against measured K+ concentrations. The Ca2+ concentration was used to calibrate epidote for the experiments EXP-4 and EXP-5. The model setup for all

chemical related inputs is identical to the batch simulations. The kinetic rate constants and reactive surface areas of Albite, Oligoclase, K-Feldspar, and Epidote were calibrated using iTOUGH2-PEST with the TOUGHREACT model, against measured Na+, Na+, K+, and Ca2+ concentrations, respectively.

The results of calibrated kinetic rate constants for the five batch experiments are listed in Table 5.10. Table 5.11 lists results for calibrated reactive surface areas of the minerals. Figure 5.17 plots the measured and simulated Na+ concentrations over time for the five batch experiments as a result of the kinetic rate constants and reactive surface area calibration for Oligoclase. Figure 5.18 plots measured and simulated concentrations relevant to Albite. Figures 5.19 and 5.20 plots K+ and Ca2+ concentrations for calibrations of K-feldspar and epidote, respectively. Measured and simulated pH values over time for the five batch experiments are compared in Figure 5.21. The simulated Na+ concentrations shown in Figure 5.17 reflect good agreements with measured values for the experiments EXP-1 and EXP-4 without CO_2 injection. The simulations of Na+ concentrations agree well with the measured values for the experiment EXP-3 and are smaller than the measured values for EXP-2 and EXP-5. However, the simulations can capture the trend of the measurements for the experiments; specifically, the Na+ concentration sharply decreases right after CO_2 injection and then gradually increases. The calibrated kinetic rate constants of Oligoclase (Tables 5.10) for the experiments exhibit small differences compared to literature values. The differences between the calibrated and BET measured surface reactive surface area for Oligoclase are also very little (Table 5.11). Similar results were obtained for the calibration for Albite against the Na+ concentrations (Figure 5.18 and Tables 5.10 and 5.11). A possible explanation for this outcome is incomplete reaction progress for the batch experiments.

Results of simulated K+ concentrations indicate a relatively good fit to measured values for experiments EXP-1 through EXP-5 (Figure 5.19). Ccalibrated kinetic rate constants for Ki-feldspar via the five experiments are about 5 to 180 times larger than previously published values (Table 5.10). The calibrated reactive surface areas are also 2 to 5 times larger than the BET measured values for K-feldspar (Table 5.11), probably due to the mineral surface area measurements being based on unreacted powders by BET after the experiments completed. Therefore, a longer reaction period may be necessary for the batch experiments to facilitate more effective calibration of mineral reactive surface areas and kinetic parameters.

Simulated pH values associated with kinetic parameter calibration analyses generally capture the trends of measured values (Figure 5.21). The pH values dramatically drop right after CO_2 injection for experiments EXP-2, EXP-3 and EXP-5, and then gradually increase to the original level. For experiments EXP-1 and EXP-4 without CO_2 injection, the pH values slightly increase at the beginning and then remain constant through the remainder of experiments.

Table 5.10. Calibrated kinetic rate constants of minerals Albite, Oliogclase, K-Feldspar, and Epidote for EXP-1 to EXP-5.

Minerals	K_{25} (mol/m²/s)	Calibrated K_{25} (mol/m²/s)				
		EXP-1	EXP-2	EXP-3	EXP-4	EXP-5
Oligoclase	0.145e-12	0.100e-12	0.100e-12	0.100e-12	0.100e-12	0.100e-12
Albite	0.275e-12	0.300e-12	0.300e-12	0.300e-12	0.300e-12	0.300e-12
K-Feldspar	0.389e-12	0.700e-10	0.300e-10	0.200e-10	0.220e-11	0.200e-11
Epidote	0.102e-11	--	--	--	0.100e-11	0.260e-10

Table 5.11. Calibrated reactive surface area of minerals Albite, Oliogclase, K-Feldspar, and Epidote for EXP-1 to EXP-5.

Minerals	Measured Surface area (cm^2/g)	Calibrated surface area (cm^2/g)				
		EXP-1	EXP-2	EXP-3	EXP-4	EXP-5
Oligoclase	6,303	6,000	6,000	6,000	6,000	5,670
Albite	9,270 (EXP-2, 4, 5) 4,408 (EXP-1,3)	4,500	9,300	4,500	9,300	9,300
K-Feldspar	9,270 (EXP-2, 4, 5) 4,408 (EXP-1,3)	10,000	50,000	9,000	14,000	22,000
Epidote	6,327	--	--	--	6,400	5,600

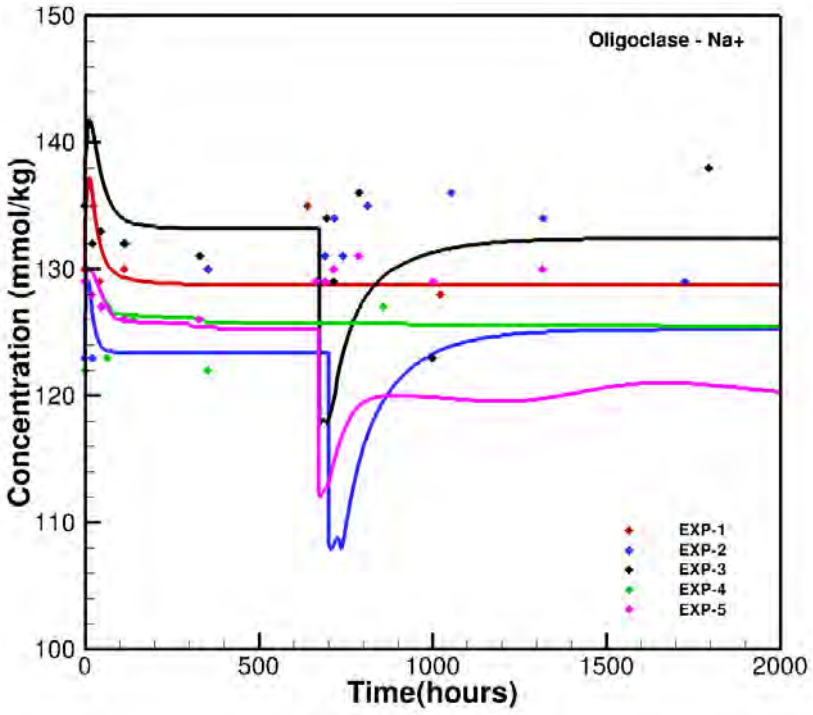

Figure 5.17. The measured and simulated Na+ concentration over time as a result of kinetic rate constants and reactive surface area calibration of Oligoclase using iTOUGH2-PEST with TOUGHREACT model for the batch experiments EXP-1 through EXP-5. The diamond symbols represent measured data, and solid lines represent simulated data

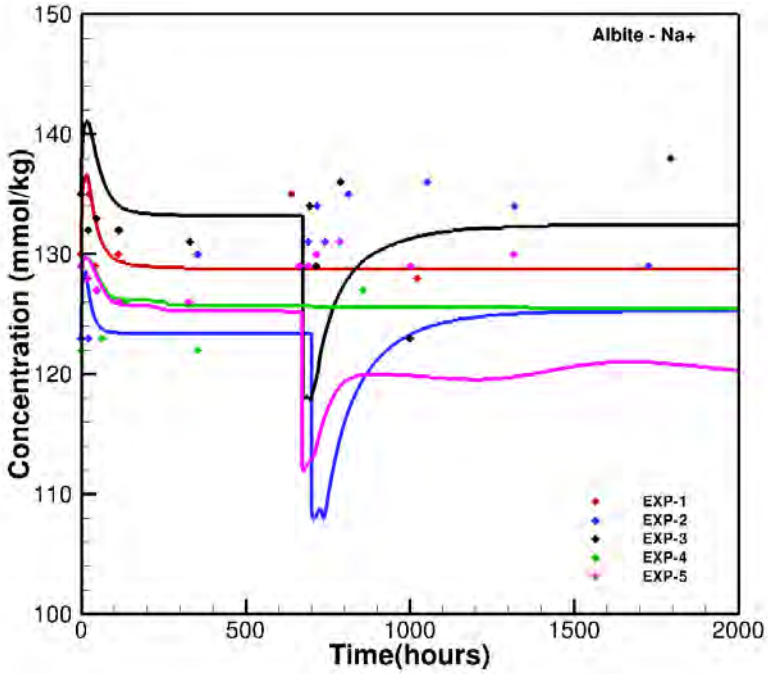

Figure 5.18. Measured and simulated Na+ concentration over time associated with calibration of kinetic rate constants and reactive surface area for Albite using iTOUGH2-PEST with the TOUGHREACT model of batch experiments EXP-1 through EXP-5. The diamond symbols represent measured data, and solid lines represent simulated data.

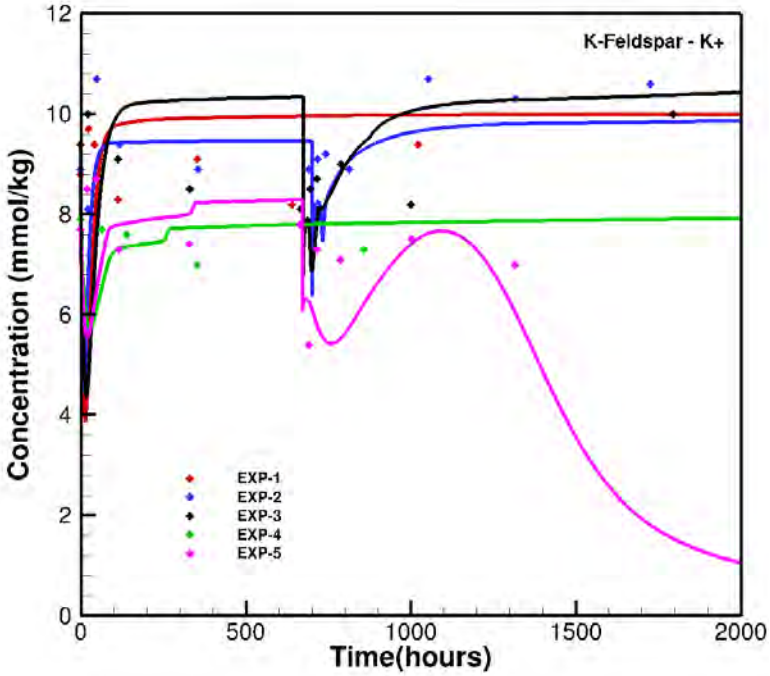

Figure 5.19. Measured and simulated K+ concentration over time as a result of calibration of kinetic rate constants and reactive surface area of K-feldspar using iTOUGH2-PEST with the TOUGHREACT model for batch experiments EXP-1 through EXP-5. The diamond symbols represent measured data, and solid lines represent simulated data.

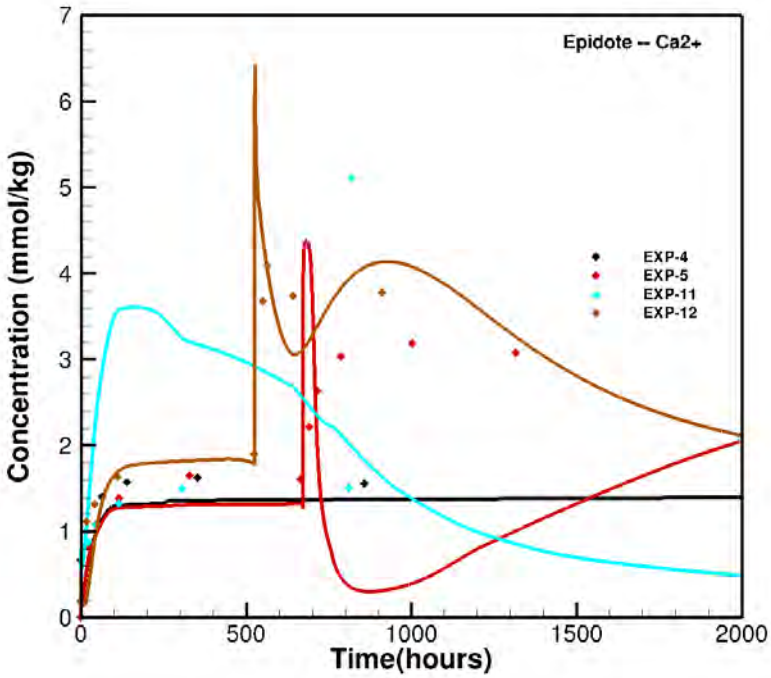

Figure 5.20. Measured and simulated Ca2+ concentration over time associated with calibration of kinetic rate constants and reactive surface area for epidote using iTOUGH2-PEST with the TOUGHREACT model of batch experiments EXP-4, EXP-5, EXP-11, and EXP-12. The diamond symbols represent measured data, and solid lines represent simulated data.

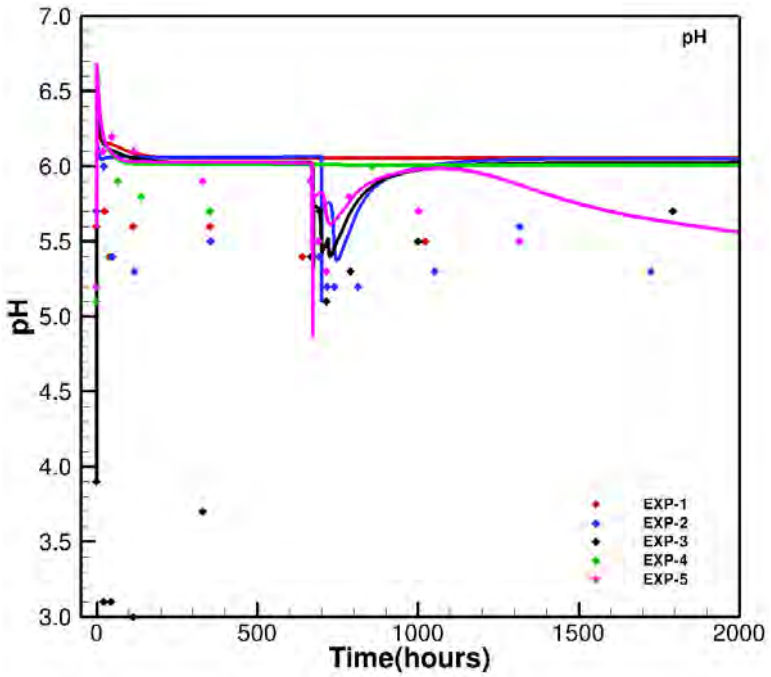

Figure 5.21. Measured and simulated pH values over time as a result of calibration of kinetic rate constants and reactive surface areas using iTOUGH2-PEST with the TOUGHREACT model for batch experiments EXP-1 through EXP-5. The diamond symbols represent measured data, and solid lines represent simulated data.

5.2.2 Calibration of Kinetic Rate Constants and Reactive Surface area of Minerals for Batch Experiments EXP-7 to EXP-12

As discussed in Section 4, the batch experiments (EXP-6 to EXP-12) were conducted with the addition of vein minerals chlorite, calcite and epidote. We evaluated results of the batch experiments (EXP-7 to EXP-12) and calibrated the kinetic rate constants and reactive surface areas of the minerals using iTOUGH2-PEST-TOUGHREACT. We adopted the same secondary mineral assemblage for the experiments (EXP-7 to EXP-12) as those of EXP-5. Since no measured BET surface areas of the minerals are available for these experiments, the areas for EXP-5 were adopted for the experiments EXP-7 to EXP-12. The initial volume fractions of primary and possible secondary minerals for the experiments EXP-7 to EXP-12 are listed in Table 5.12.

The setup of batch simulations is the same as those detailed in Section 5.2.1. The batch simulations for EXP-7 to EXP-12 were also conducted for 2,000 hours. The supercritical CO_2 was injected at 668.1, 670.9, and 526.1 hours for experiments EXP-8, EXP-10, and EXP-12 for an hour, respectively. Concurrently with CO_2 injection, brine was extracted with an equal and opposite rate. The kinetic rate constants and reactive surface area of the minerals Oligoclase, Albite, K-Feldspar, Chlorite, Calcite, and Epidote were calibrated against measured Na+, Na+, K+, Mg2+, Ca2+, and Ca2+ concentrations, respectively. The results of calibrated kinetic rate constants of the minerals are listed in Table 5.13. Table 5.14 lists resulting values for calibrated reactive surface areas of the minerals. Figures 5.22 -5.25 plot measured vs. simulated Na+, K+, Ca2+, and Mg2+ concentrations over time as a result calibration of Oligoclase, K-feldspar, Calcite, and Chlorite for EXP-7 to EXP-12, respectively. Figure 5.26 shows the measured and simulated pH values for these experiments.

Table 5.12. Chemical composition and initial volume fractions of primary and secondary minerals for the experiments EGS-007 to EGS-012.

Mineral	Chemical composition	Initial volume fraction of minerals					
		EGS-007	EGS-008	EGS-009	EGS-010	EGS-011	EGS-012
Primary:							
Quartz	SiO_2	0.1580	0.1587	0.1611	0.1612	0.1656	0.1689
Oligoclase-uwy[a]	$Na_{0.77}Ca_{0.23}Al_{1.23}Si_{2.77}O_8$	0.1580	0.1587	0.1598	0.1612	0.1682	0.1442
Albite	$NaAlSi_3O_8$	0.0396	0.0401	0.0410	0.0407	0.0419	0.0431
K-Feldspar	$KAlSi_3O_8$	0.1217	0.1232	0.1260	0.1251	0.1286	0.1322
Annite	$Kfe_3AlSi_3O_{10}(OH)_2$	0.0067	0.0073	0.0059	0.0058	0.0071	0.0076
Phlogopite	$KalMg_3Si_3O_{10}(OH)_2$	0.0097	0.0105	0.0085	0.0083	0.0102	0.0110
Chlorite	$(Mg,Fe^{2+})_5Al(AlSi_3O_{10})(OH)_8$	0.5062	0.5014	--	--	0.1734	0.1808
Calcite	$CaCO_3$	--	--	0.4977	0.4977	0.1720	0.1754
Epidote	$Ca_2Al_2(Fe^{3+},Al)(SiO_4)(Si_2O_7)O(OH)$	--	--		--	0.1330	0.1368
Porosity	-	0.9864	0.9860	0.9864	0.9863	0.9867	0.9869
Secondary							
Calcite	$CaCO_3$	0.0	0.0	--	--	--	--
Magnesite	$MgCO_3$	0.0	0.0	0.0	0.0	0.0	0.0
Illite	$(K,H_3O)(Al,Mg,Fe)_2(Si,Al)_4O_{10}[(OH)_2,(H_2O)]$	0.0	0.0	0.0	0.0	0.0	0.0
Smectite	$K_{0.04}Ca_{0.5}(Al_{2.8}Fe_{0.53}Mg_{0.7})(Si_{7.65}Al_{0.35})O_{20}(OH)_4$	0.0	0.0	0.0	0.0	0.0	0.0
Kaolinite	$Al_2Si_2O_5(OH)_4$	0.0	0.0	0.0	0.0	0.0	0.0
Chlorite	$Mg_{2.5}Fe_{2.5}Al_2Si_3O_{10}(OH)_8$	--	--	0.0	0.0	--	--
Muscovite	$KAl_3Si_3O_{10}(OH)_2$	0.0	0.0	0.0	0.0	0.0	0.0
Hematite	Fe_2O_3	0.0	0.0	0.0	0.0	0.0	0.0
Dolomite	$CaMg(CO_3)_2$	0.0	0.0	0.0	0.0	0.0	0.0
Ankerite	$CaMg_{0.3}Fe_{0.7}(CO_3)_2$	0.0	0.0	0.0	0.0	0.0	0.0
Dawsonite	$NaAlCO_3(OH)_2$	0.0	0.0	0.0	0.0	0.0	0.0
Siderite	$FeCO_3$	0.0	0.0	0.0	0.0	0.0	0.0

a) Oligoclase at specific ratio used for batch experiment by University of Wyoming.

The simulated Na+ concentrations shown in Figure 5.22 appear to be consistent with the measured values by batch experiments EXP-7, EXP-8, EXP-10, EXP-11, and EXP-12. The simulations also reflect the general trend of measured values before and after the CO_2 injection. The calibrated kinetic rate constants of Oligoclase for EXP-7 to EXP-12 (Table 5.13) vary from

3 times less to 1.5 less than literature values. The calibrated reactive surface areas of Oligoclase range from 2413 to 6300 cm^2/g compared to the original value of 6303 cm^2/g. Measured and simulated K+ concentration (Figure 5.23) qualitatively agree for experiments EXP-7, EXP-8, and EXP-9. However, EXP-10, EXP-11, and EXP-12 (Figure 5.23) reflect poor consistency between measured and simulated values. The simulated Ca2+ and Mg2+ concentrations (Figures 5.24 and 5.25) seem consistent with measured batch experiment values (those without CO_2 injection). Simulated Ca2+ and Mg2+ concentrations (Figures 5.24 and 5.25) generally follow the trend of measured values for the batch experiments with CO_2 injection. The calibrated kinetic rate constants at 25 ^oC for the minerals (Table 5.12) are close or within one order of magnitude to values from literature. The calibrated reactive surface areas of the minerals are close or within one order of magnitude to the original reactive surface areas (Table 5.13). The simulated pH values with the kinetic parameter calibration of the minerals generally show good agreement with measured values (Figure 5.26). These results suggest that such calibration of kinetic rate constants and reactive surface areas of minerals will improve batch simulations for high pressure and temperature conditions, and calibrated data can also be used for related geochemical simulations of EGS reservoirs with elevated temperature.

Table 5.13. Calibrated kinetic rate constants of minerals Albite, Oliogclase, K-Feldspar, Chlorite, Calcite, and Epidote for EXP-7 to EXP-12.

Minerals	K_{25} (mol/m^2/s)	Calibrated K_{25} (mol/m^2/s)					
		EGS-007	EGS-008	EGS-009	EGS-010	EGS-011	EGS-012
Oligoclase	0.145e-12	0.100e-12	0.500e-13	0.140e-12	0.900e-13	0.100e-12	0.100e-12
Albite	0.275e-12	0.300e-12	0.300e-12	0.400e-11	0.300e-12	0.300e-12	0.300e-12
K-Feldspar	0.389e-12	0.300e-12	0.190e-10	0.94e-12	0.200e-11	0.390e-12	0.200e-12
Chlorite	0.302e-12	0.300e-12	0.300e-12	--	--	0.300e-12	0.500e-11
Calcite	0.155e-8	--	--	0.200e-8	0.300e-9	0.220e-8	0.800e-8
Epidote	0.102e-11	--	--	--	--	0.100e-11	0.140e-10

Table 5.14. Calibrated reactive surface area of minerals Albite, Oliogclase, K-Feldspar, Chlorite, Calcite, and Epidote for EXP-7 to EXP-12.

Minerals	Surface area (cm^2/g)	Calibrated surface area (cm^2/g)					
		EGS-007	EGS-008	EGS-009	EGS-010	EGS-011	EGS-012
Oligoclase	6,303	3,981	2,413	6,000	3,375	6,303	6,300
Albite	9,270	9,270	9,270	6,000	9,300	9,270	9,270
K-Feldspar	9,270	364	36,000	15,000	32,000	9,300	8,800
Chlorite	6,327	6,000	6,000	--	--	6,327	10,000
Calcite	6,327	--	--	6,000	40,000	9,900	6,000
Epidote	6,327	--	--	--	--	6,000	6,000

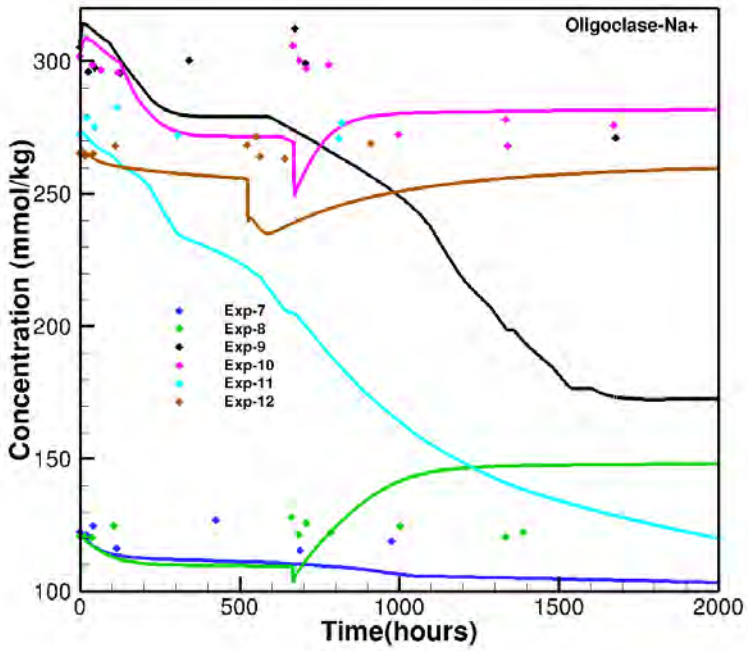

Figure 5.22. Measured and simulated Na+ concentration over time as a result of calibration of kinetic rate constants and reactive surface area for Oligoclase using iTOUGH2-PEST-TOUGHREACT for batch experiments EXP-7 through EXP-12. The diamond symbols represent measured data, and solid lines represent simulated data.

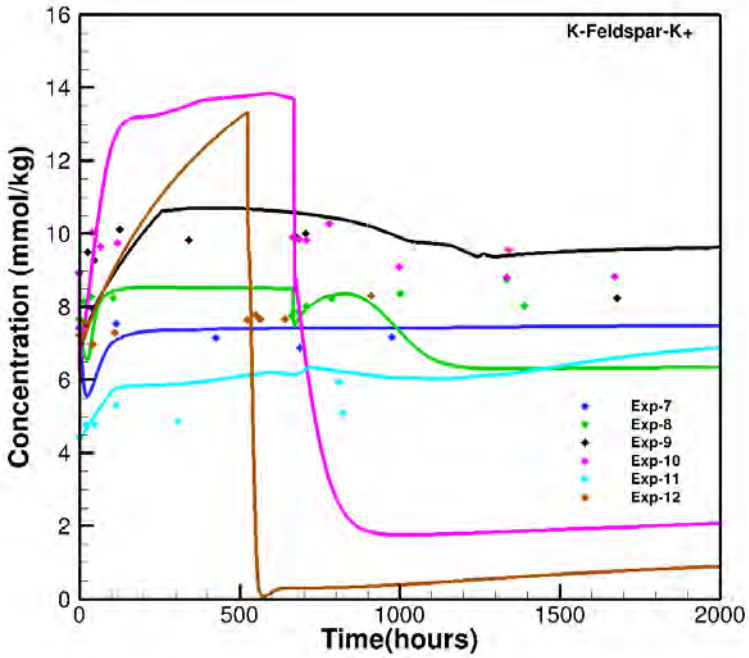

Figure 5.23. Measured and simulated K+ concentration over time as a result of calibration of kinetic rate constants and reactive surface area calibration of K-feldspar for batch experiments EXP-7 through EXP-12. The diamond symbols represent measured data, and solid lines represent simulated data.

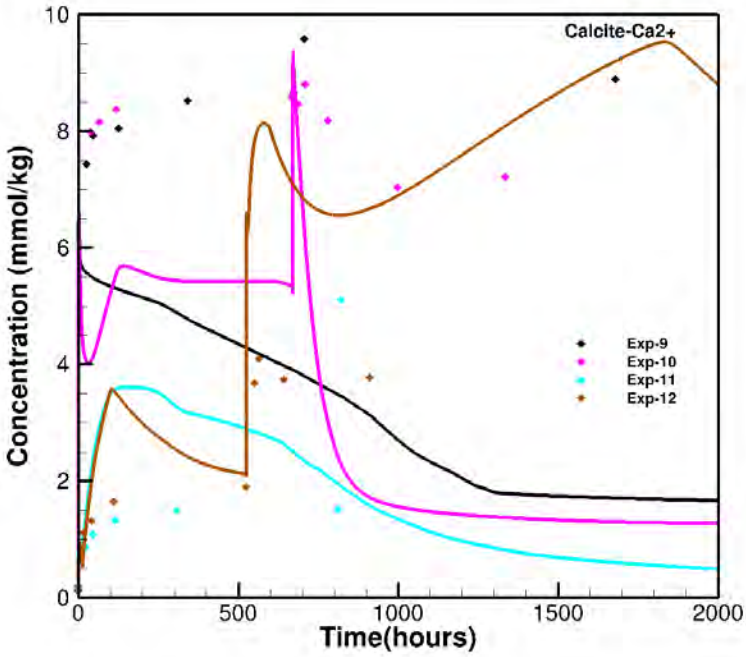

Figure 5.24. Measured and simulated Ca2+ concentration over time as a result of calibration of kinetic rate constants and reactive surface area for Calcite associated with batch experiments EXP-9, EXP-10, EXP-11, and EXP-12. The diamond symbols represent measured data, and solid lines represent simulated data.

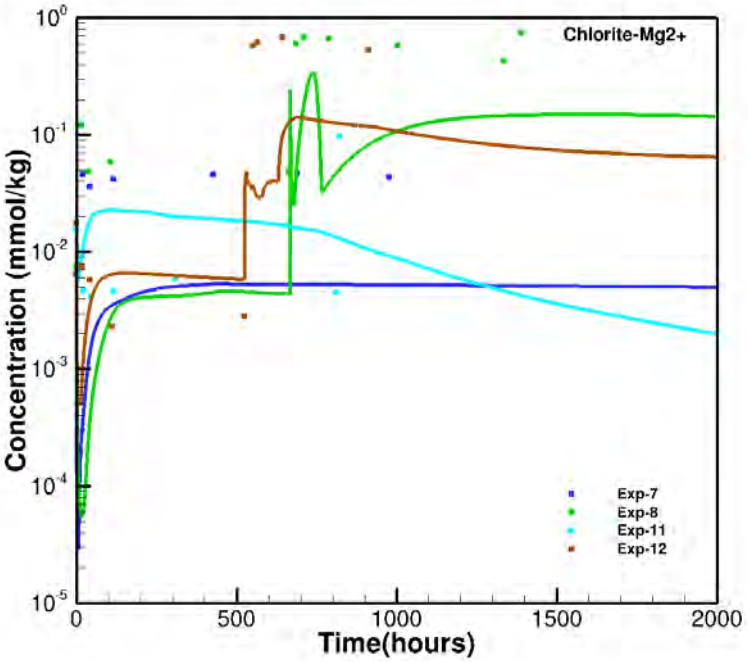

Figure 5.25. Measured and simulated Mg2+ concentration over time as a result of calibration of kinetic rate constants and reactive surface area for Chlorite associated with batch experiments EXP-7, EXP-8, EXP-11, and EXP-12. The diamond symbols represent measured data, and solid lines represent simulated data.

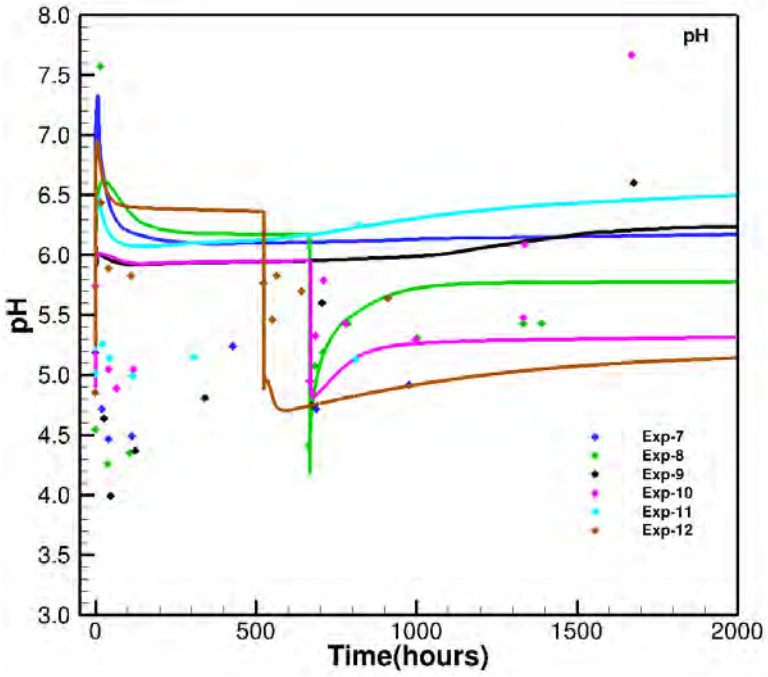

Figure 5.26. Measured and simulated pH values over time as a result of calibration of kinetic rate constants and reactive surface area for batch experiments EXP-7 through EXP-12. The diamond symbols represent measured data, and solid lines represent simulated data.

5.3 Conduct Simulations to Explore the Possible Effects of $scCO_2$ Interactions with EGS Reservoir Rock

In this section, we describe results of 2-D and 3-D simulation models for a generic 2-well pattern to evaluate flow, heat, and geochemical processes of CO_2-rock-fluid interactions, and we also analyze effects of using CO_2 as a working fluid on the energy extraction, carbon sequestration, and risk of CO_2 leakage. We also explored the possible effects of boundary conditions, pressure drops between injection and production, initial salinity, and injection temperature on the performance of energy extraction.

5.3.1 Two-dimensional Dual-continuum Flow and Heat Simulations with 2-well Pattern for $scCO_2$ as a Working Fluid using TOUGH2 Model

5.3.1.1 Model Setup

A generalized 2-D domain (Figure 5.27) was designed to evaluate mass flow and heat extraction rates associated with $CO_2^{\text{EGS-Working Fluid}}$ using the ECO2H module and TOUGH2. The 2-D EGS model domain is 1100m × 500m horizontally, with a thickness of 100m; the total number of model grid nodes is 11×5×1 = 55. We also employed a dual-continuum approach to simulate the fracture-matrix heat flow transfer, with fracture spacing of 50m and a fracture volume fraction of 2%. The distance between injection and production wells was 1000m with a defined pressure drop of 25 bar. A Dirichlet condition with constant pressure was set at the boundaries of injection and production sides and a Neumann condition (no flow) was assigned on all other sides. Initial conditions included temperature of 200 ^{o}C and pressure of 200 bar within the EGS reservoir. Details of hydrological properties, initial condition, and injection/production conditions are listed in Table 5.15.

The ECO2H equation-of-state (EOS) algorithm was designed for applications to geologic sequestration of CO_2 in saline aquifers at high temperature and pressure (Pruess, 2005; Spycher and Pruess, 2010). This EOS can provide an appropriate description of thermodynamics and thermophysical properties of water-brine-CO_2 mixtures under conditions of temperature up to 243 ^{o}C and pressure up to 676 bar (Borgia et al., 2012).

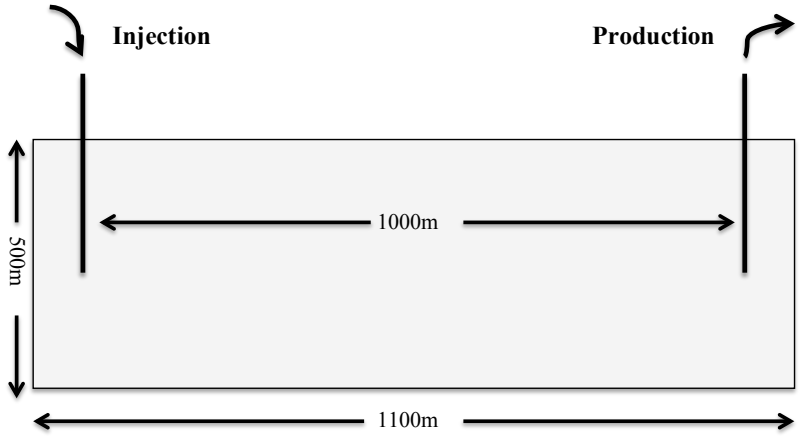

Figure 5.27. Geometry of 2-D general EGS model domain developed in the TOUGH2 model.

Table 5.15 Hydrologic parameters, initial, and production/injection conditions.

Properties	
Fractured rock permeability	10^{-13} m^2
High Granite permeability:	10^{-17} m^2
Fracture spacing	50 m
Fracture volume fraction	2%
Fracture Porosity:	0.50
Fracture Tortuosity:	1.0
Thermal conductivity:	2.51 W/m ^{o}C
Rock specific heat:	1000 J/kg ^{o}C
Rock grain density	2650 kg/ m^3
Initial Condition	
Reservoir fluid	all water
Initial temperature:	200°C
Initial pressure	200 bar
Production/Injection condition	
Injection/production well distance	1000 m
Injection pressure	200 bar
Injection temperature	50°C
Production pressure	175 bar

5.3.1.2 Flow and Heat Simulation Results

Figure 5.28 shows resulting simulated mass flow rate, net heat extraction, temperature, and gas saturation for CO_2 as a working fluid in the generalized 2-D EGS model. Similar results

for water as the working fluid are plotted in Figure 5.28. For CO_2 as a working fluid, the flow containing water only is produced with the rate of 40 kg/s at the initial stage of simulation. After 0.1 year, the water flow rate sharply decreases with the increase of CO_2 flow rate, demonstrating how the mixture of water and CO_2 is produced when CO_2 flow has reached the production well. With continuous CO_2 injection and increase of gas saturation close to the production well, CO_2 flow rate significantly increases with no more water flow production. The oscillations of CO_2 and water flow rate are an artificial numerical response of the constant pressure boundary conditions at injection and production wells; specifically, the flow velocities must oscillate to ensure that pressure is maintained constant. This phenomenon is an artifact of the simulation approach (absolutely fixed pressure, which cannot occur in nature but is a standard analysis approach) and only occurs in grid cells immediately adjacent to the injection and production wells.

The net heat extraction is around 28 MW in the initial stage of simulation and decreases to 10 MW after 0.1 years, which is similar in trend to water flow rate. With increases of CO_2 flow rate, the next heat extraction increases to 24 MW after 4 years of CO_2 injection. After 4 years with full saturation of CO_2 at the production well, the net extraction decreases to 10 MW after 50 years of CO_2 injection. This is due to more rapid thermal depletion of CO_2 compared to water. This can be observed from the rapid decrease of simulated temperature after CO_2 is at full saturation, close to the production well (Figure 5.28b). The temperature next to the injection well decreases from the initial temperature of 200 ^oC to the injection temperature of 50 ^oC. The CO_2 saturation next to the injection well becomes fully saturated after 0.4 years of CO_2 injection.

The mass flow rates next to the injection and production wells remains almost constant at 20 kg/s with water as the working fluid, which is much smaller than the 40 kg/s of water flow

rate at the initial stage and the variable 40-70 kg/s of CO_2 flow rate after full CO_2 saturation is reached in the $CO_2^{\text{EGS-Working Fluid}}$ simulation. The net heat extraction for water as the working fluid is almost constant at 12 MW before 10 years and decreases to 8 MW at 50 years of water injection. Compared to simulation results for $CO_2^{\text{EGS-Working Fluid}}$, the net extraction rate for water as the working fluid is much smaller at the initial stage of simulation and after 1 year of injection for water, indicating that $CO_2^{\text{EGS-Working Fluid}}$ may enhance heat extraction compared to water as the working fluid. However, such differences of net heat extraction decrease with time after 4 years at full CO_2 saturation. This may be explained by more rapid thermal depletion using CO_2 than water, which is also verified by the relatively larger drop of temperature for $CO_2^{\text{EGS-Working Fluid}}$ compared to water (Figure 5.28b). We also infer that the net heat extraction rate for CO_2 as a working fluid is slightly smaller than the rate for water as a working fluid between 0.1 and 1 years of injection (Figure 5.28a). This is attributed to a relatively lower CO_2-water mixture production flow rate when CO_2 has reached the production well, which maintains a lower gas saturation.

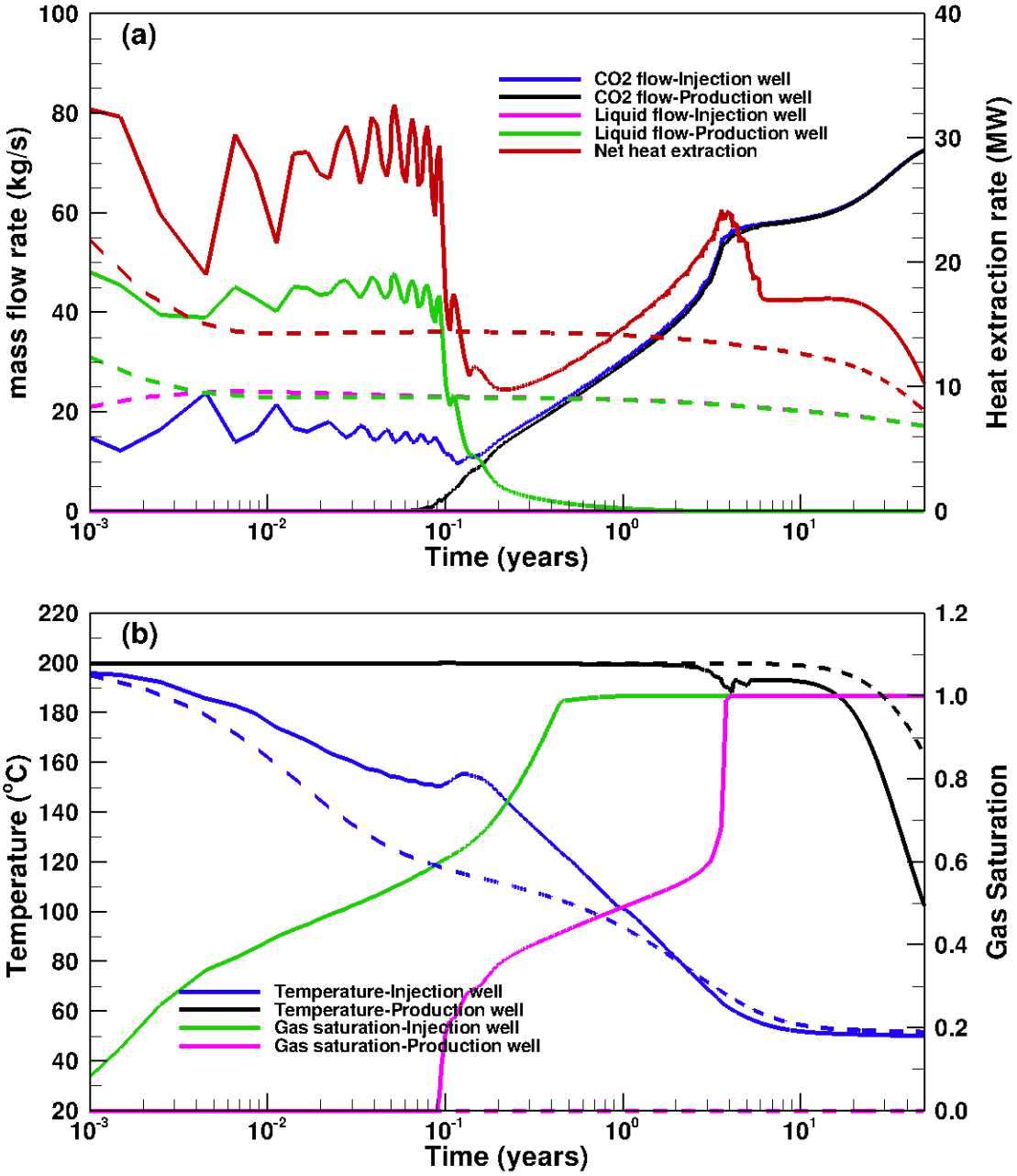

Figure 5.28. Comparison of net heat extraction, mass flow rate, temperature, and gas saturation for CO_2 (solid line) and water (dash line) as working fluids.

5.3.1.3 Effects of Injection/production Pressure Drop, Injection Temperature, and Initial Salinity on Energy Extraction

This section describes results of analysis of effects of injection/production pressure drop, injection temperature, and initial salinity on heat extraction rate with $scCO_2$ as a working fluid using a general 2-D EGS model with a 2-well pattern (Figure 5.27).

Figure 5.29 plots simulated net heat extraction rate, mass flow rate, temperature, and gas saturation for CO_2 working fluid at injection/ production pressure drops of 10, 25, 50, and 100 bar, respectively. The mass flow rates of water and CO_2 production show similar trends for different pressure drops, but their values are significantly different. For example, the water flow production rate in the initial stage of simulation are around 230, 100, 40, and 20 kg/s for pressure drop of 100, 50, 25, and 10 bar, respectively. The CO_2 flow rates close to the production well also significantly increase with pressure drop from 10, 25, 50 to 100 bar after full CO_2 saturation is reached. This is driven by the large pressure gradient leading to a larger mass flow rate. The net heat extraction rates for different pressure drops also exhibit similar trends. However, after full CO_2 saturation is reached, the gradient of net heat extraction rate for a higher pressure drop is much larger than the rate for a smaller pressure drop, which is similar to trends of simulated temperature profiles (Figure 5.29b). These trends may be explained by the large pressure gradient causing a large mass flow rate and rapid temperature drop. Thus, the relatively smaller temperature differences of CO_2 between injection and production wells generate smaller density differences and less buoyancy that could reduce the power consumption at production well (Pruess, 2007). After 50 years of CO_2 injection, the net heat extraction is 10 MW for a pressure drop of 25 bar and 5-7 MW for pressure drops of 10, 50, and 100 bar, indicating that a pressure drop of 25 bar may be suitable for sufficient heat extraction in EGS reservoirs. Full CO_2

saturation next to the production well is reached much faster with a large pressure drop than for a small pressure drop (Figure 5.29b). This may also be explained by the large CO_2 flow rate driven by the large pressure gradient.

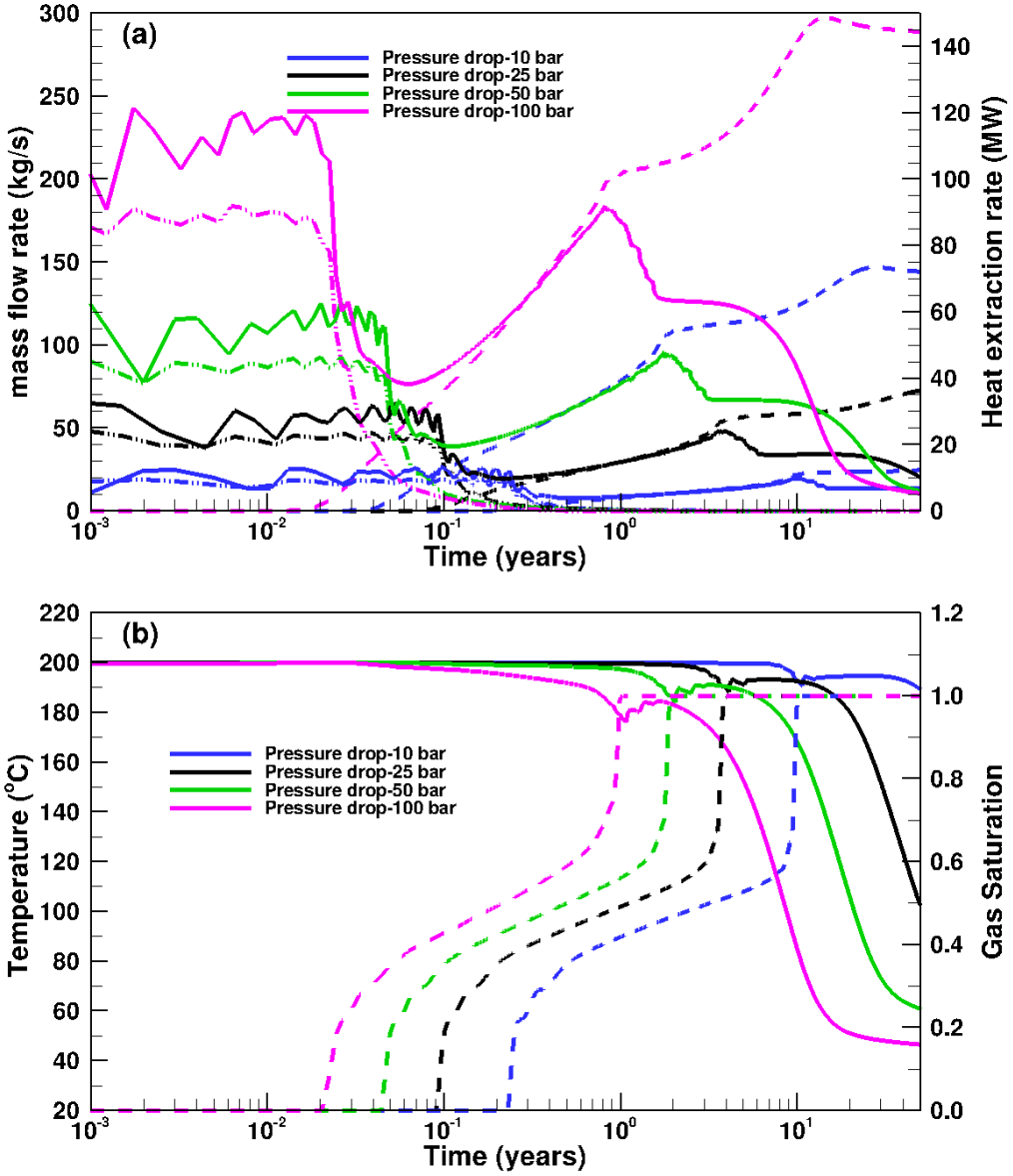

Figure 5.29. Simulated net heat extraction (solid line in (a)), mass flow rate (dash dotdot line in (a) for water flow; dash line for CO_2 flow), temperature (solid line in (b)), and gas saturation (dash line) with injection/production pressure drops at 10, 25, 50, and 100 bar for CO_2 as a working fluid.

Figure 5.30 plots simulated net heat extraction rate, mass flow rate, temperature, and gas saturation for supercritical CO_2 as a working fluid for injection temperatures of 35^oC, 50^oC, and 70^oC. Comparisons of simulated results show the mass flow rates, net heat extraction rates, and temperature profile at the production well are almost the same for different injection temperatures except for slight differences at the latest stage of the simulation. The gas saturation profiles are also similar for the three cases. The temperature next to the injection well (Figure 5.30b) exhibits a trend from 200^oC of initial temperature gradually decreasing to the injection temperature over time. Therefore, the larger the injection temperature, the smaller the temperature differences between injection and production wells. This leads to reduced buoyancy and larger pressure gradients at the production well for higher injection temperatures. This may explain why the mass flow rate for higher injection temperatures is slightly larger than rates for lower injection temperatures. However, the net heat extraction has similar characteristics with higher net heat extraction rate for lower injection temperature. This results from the larger heat consumption at injection well and smaller buoyancy forces at the production well for higher injection temperatures.

Figure 5.31 depicts simulated net heat extraction rate, mass flow rate, temperature, and gas saturation for CO_2 as a working fluid under different initial salinity values. At the early stages of simulation, water production rates are around 40, 35, 27, and 25 kg/s for initial brine at 0%, 10%, 30%, and 50%, respectively. Correspondingly, the net heat extraction also decreases from 30 MW with 0% initial brine to 12 MW with 50% initial brine. The differences among CO_2 flow production rates under different initial salinity become smaller with continuous injection of CO_2. They are almost the same after 4 years of CO_2 injection. The net heat extraction also shows a similar trend as CO_2 mass flow rate. Such may suggest that the initial

salinity has a significant effect on heat extraction at the early stages of simulation. The temperature profiles are almost the same with different initial salinity values (Figure 5.30b). The gas saturation next to the production well increases from 0.78 to 1.0 for initial brine from 50%, 30%, 10% to 0% after 50 years of CO_2 injection, demonstrating that brine cannot be fully extracted from the production well.

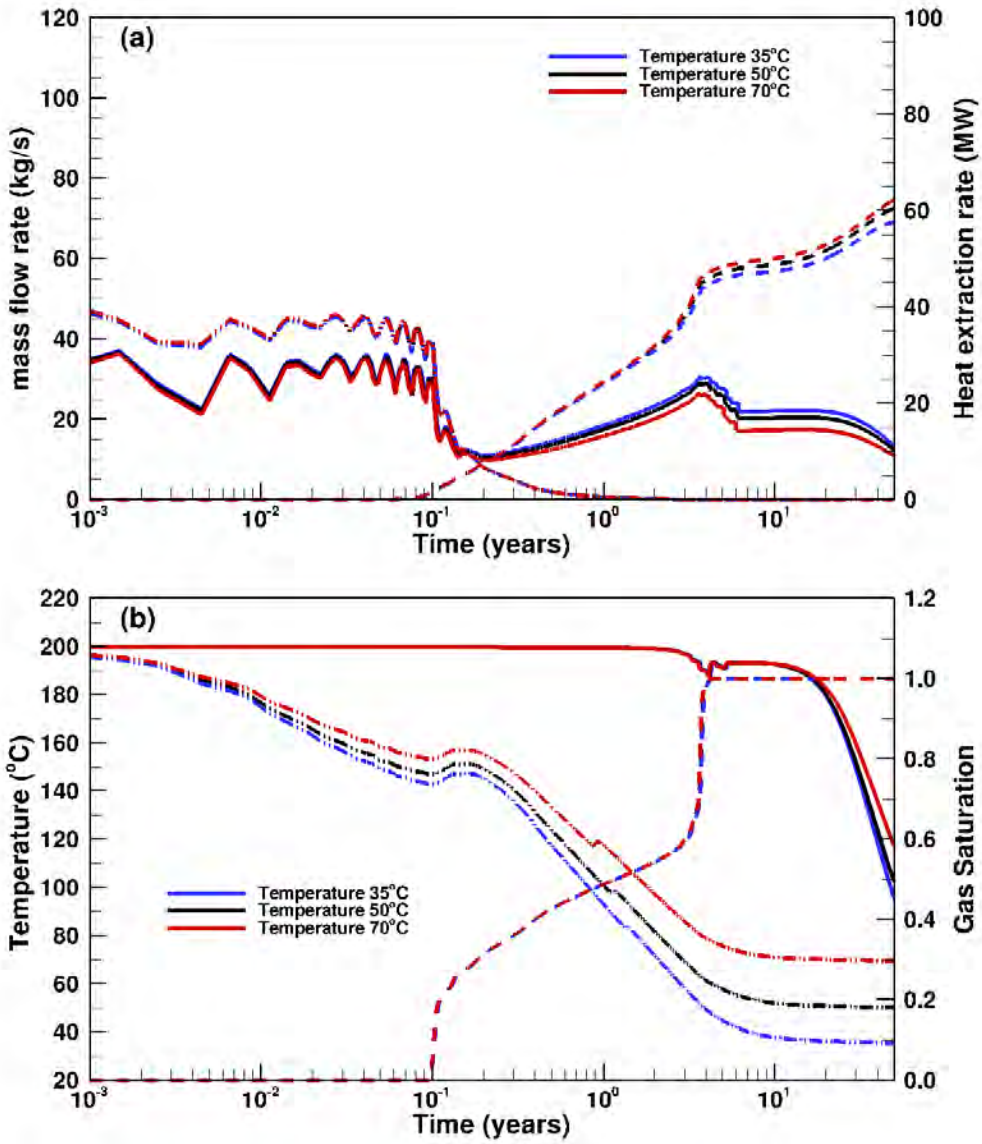

Figure 5.30. Simulated net heat extraction (solid line in (a)), mass flow rate (dash dotdot line (a) for water flow; dash line for CO_2 flow), temperature at production well (solid line in (b)), temperature at injection well (dash dotdot line), and gas saturation (dash line in (b)) with injection temperature at 35°C, 50°C, and 70°C at injection well for CO_2 as a working fluid.

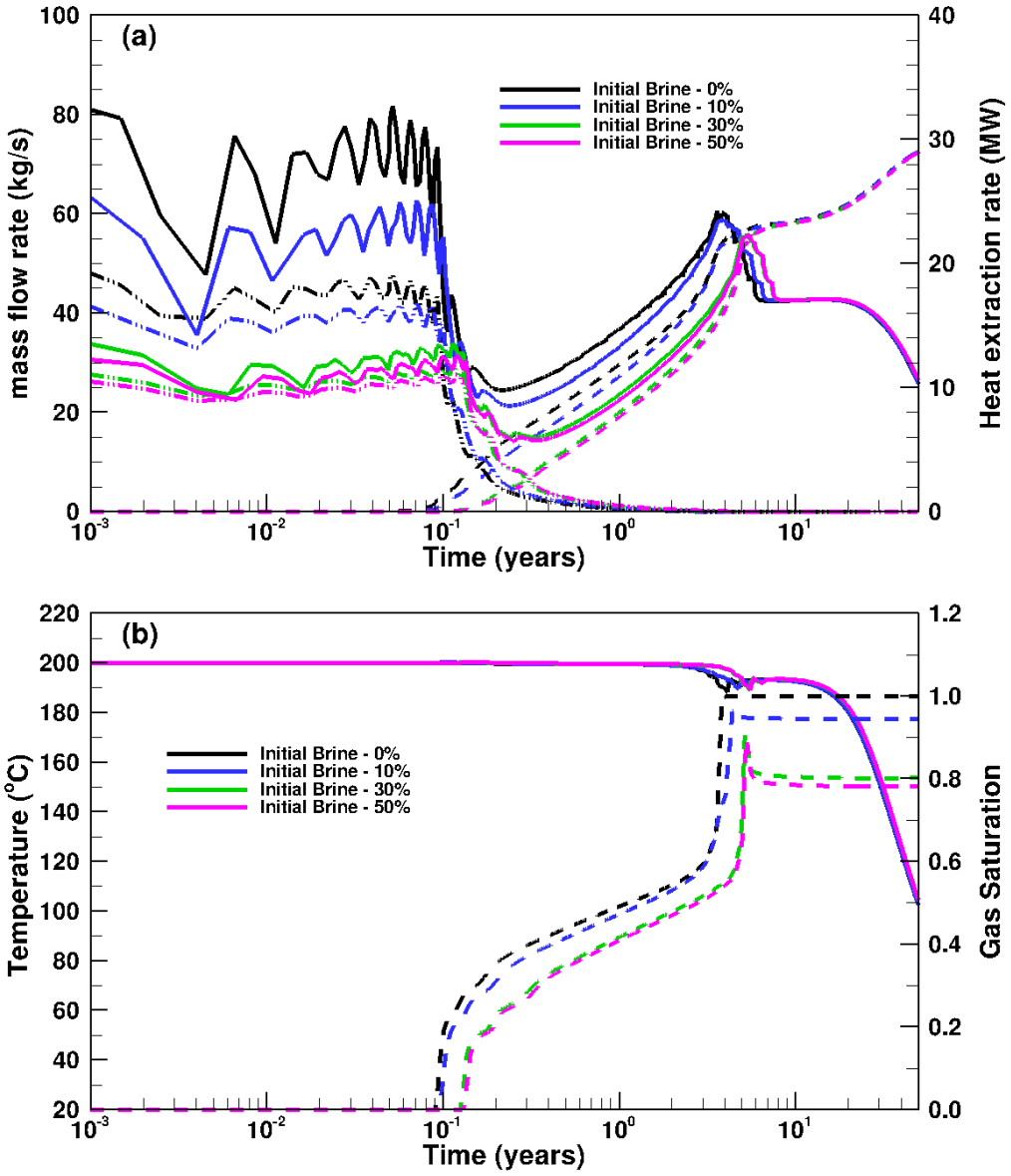

Figure 5.31. Simulated net heat extraction (solid line in (a)), mass flow rate (dash dotdot line for water flow; dash line in (a) for CO_2 flow), temperature (solid line in (b)), and gas saturation (dash line) with initial brine of 0%, 10%, 30%, and 50%.

5.3.1.4 Effects of Boundary Conditions on Energy Extraction

As discussed in Section 5.3.1.1, the boundary conditions for simulations with CO_2 as a working fluid were set to constant pressure at the injection and production wells. This section describes a comparison of simulation results for the different boundary conditions. Figure 5.32

depicts the simulated heat extraction rate, mass flow rate, temperature and gas saturation with CO_2 as a working fluid for the constant pressure of 200 bar and the constant flux of 50kg/s at the injection well. Different from the constant pressure condition, the CO_2 flow rate next to production well remains constant to the same amount of injection flux at 50kg/s after 0.2 years for the constant flux condition. The liquid flow rate next to the production well exhibits similar trends for both cases, but the values for a constant flux condition are much larger than those for constant pressure conditions at the early stages of simulation, leading to the larger net heat extraction rates for a constant flux condition. The CO_2 flow rate for a constant flux condition is much larger than that for a constant pressure condition at the early stages of simulation. This results in a larger pressure gradient and mass flow rate at the production well for a constant flux condition. The net heat extraction rate for a constant flux condition is larger than that for a constant pressure, until 2 years after CO_2 injection and slightly smaller after that. This may be because of the larger CO_2 flow rate at the production well for a constant pressure condition after 2 years (Figure 5.32a). The gas saturation at the production well for a constant flux condition reaches full saturation faster than that for a constant pressure condition (Figure 5.32b). This may be explained by the larger CO_2 injection flow rate for a constant flux condition.

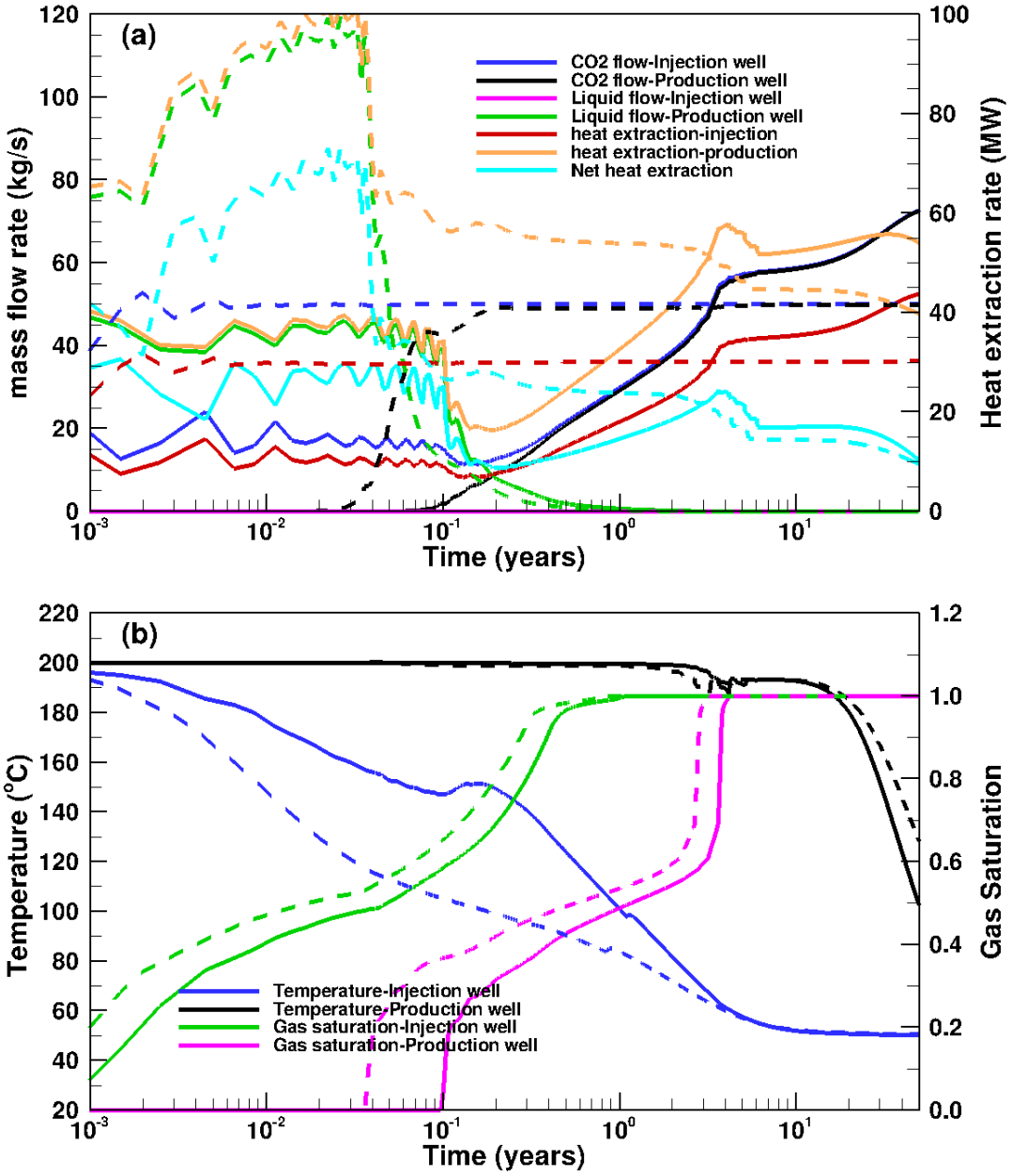

Figure 5.32. Simulated net heat extraction, mass flow rate, temperature, and gas saturation with CO_2 as a working fluid for constant pressure of 200 bar (solid line) and constant flux of 50kg/s (dash line) at the injection well.

5.3.2 3-D Study on the Placement of the Production Well using PFLOTRAN model with $scCO_2$ as a Working Fluid

Three-dimensional simulations were conducted using supercritical CO_2 as the working fluid with an injection rate of 50 kg/s at a temperature of 50◦C and a pressure of 200 bar with the production well placed at a higher elevation compared to the injection well. For this domain (Figure 5.33), the number of nodes chosen were Nx = 50, Ny = 20, Nz = 20, in the x, y, z directions respectively. The system was assumed to contain water initially. All boundary conditions are no flow. Flow parameters used in the simulation are listed in Table 5.16. A comparison between results for cases when the wells are at the same depth and when the production well is placed at a higher elevation (with supercritical CO_2 as working fluid) is shown in Figure 5.34.

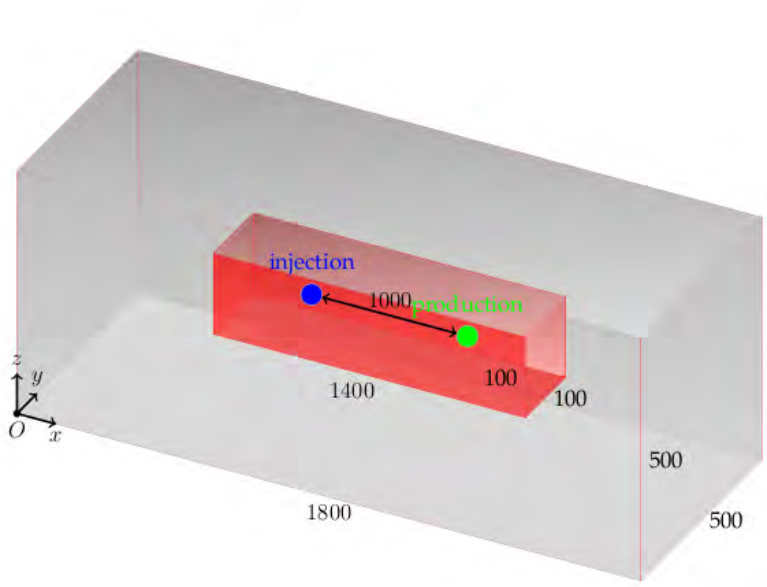

Figure 5.33. The three-dimensional domain used in the production well location analysis. The gray zone corresponds to the unfractured granite and the red zone represents the fractured volume. All the dimensions shown are in meters. The positions of the injection and the production wells are at (400, 250, 250) m and (1400, 250, 250) m, respectively. For the case when the production well is placed at the higher elevation compared to the injection well, the coordinate of the production well is (1400, 250, 450) m.

Table 5.16 Model parameters.

Fractured rock permeability:	$k_h = 10^{-12}$, $k_v = 10^{-13}$ m^2
High Granite permeability:	$k_h = 10^{-14}$, $k_v = 10^{-15}$ m^2
Porosity:	0.05
Tortuosity:	0.1
Thermal conductivity:	2.51 W/m°C
Rock specific heat:	1000 J/kg°C
Injection rate (3D):	50 kg/s for 50 y
Productivity index:	10^{-12} m^3
Bottom-well pressure:	5 MPa
Initial temperature:	200°C
Injection temperature:	50°C
Initial pressure:	200 bar

The net power generated for the case when the production well is at a higher elevation compared to injection well is greater. We interpret this higher net power generation to be because injection power for both cases is the same inasmuch as the fluid is injected at the same depth. However, the production power is higher for the case when the production well is at a higher elevation because the temperature and pressure at the production well is higher (Figures 5.34d, and 5.34c), rendering the enthalpy at the production well to be higher.

In order to assess the parallel performance of PFLOTRAN for the EGS problem with supercritical CO_2 as the working fluid, parallel scalability studies were performed. These studies were performed on the Jaguar Cray XT5 supercomputer at Oakridge National Laboratory. First, a domain with 100 × 50 × 50 cells was chosen for which the number of degrees of freedom are 750, 000 (100 × 50 × 50 × 3) and we observed that the code scales well up to 160 processor cores. Then, the number of cells were increased to 100 × 100 × 100 with 3 million degrees of freedom and the code scaled well up to 960 processor cores. The results from this exercise are detailed in Figure 5.35.

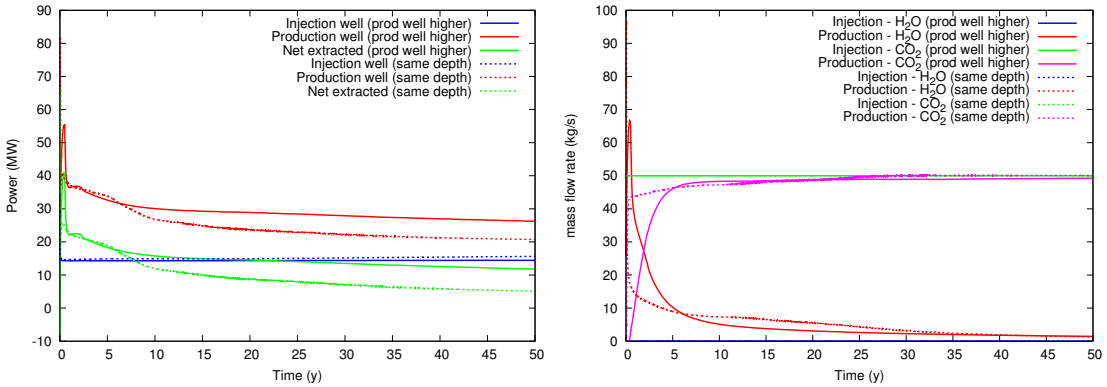

(a) Power generated

(b) Mass flow rate

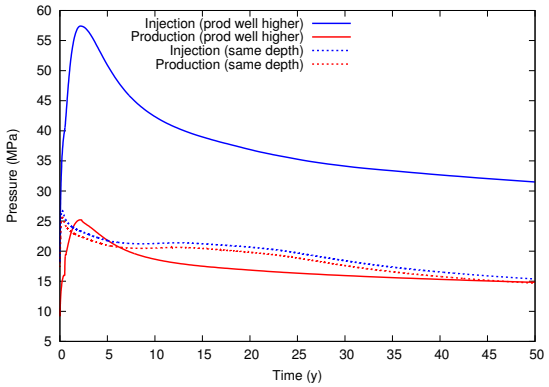

(c) Pressure

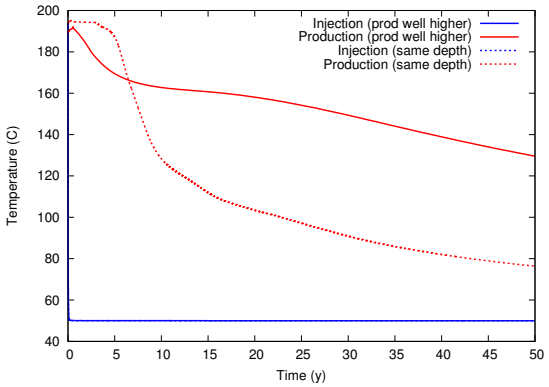

(d) Temperature

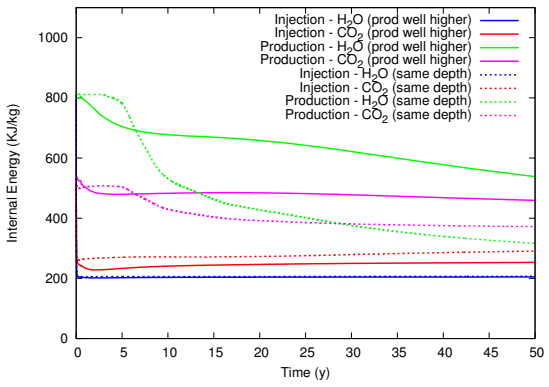

(e) Specific internal energy

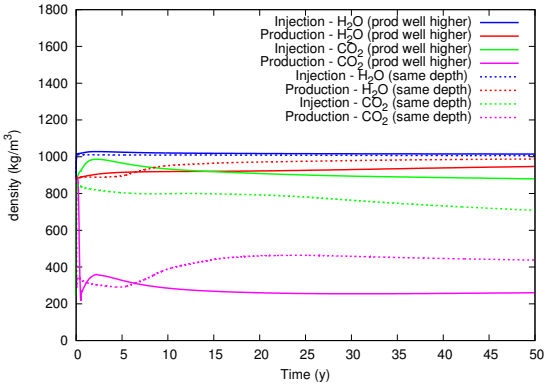

(f) Density

Figure 5.34. Comparison of PFLOTRAN results for the case when the wells are at the same depth versus that for the production well located at a higher elevation (by 200 m). The working fluid is supercritical CO_2 and the system is assumed to have water present initially. A grid size of 50×20×20 was used for 3D the simulations.

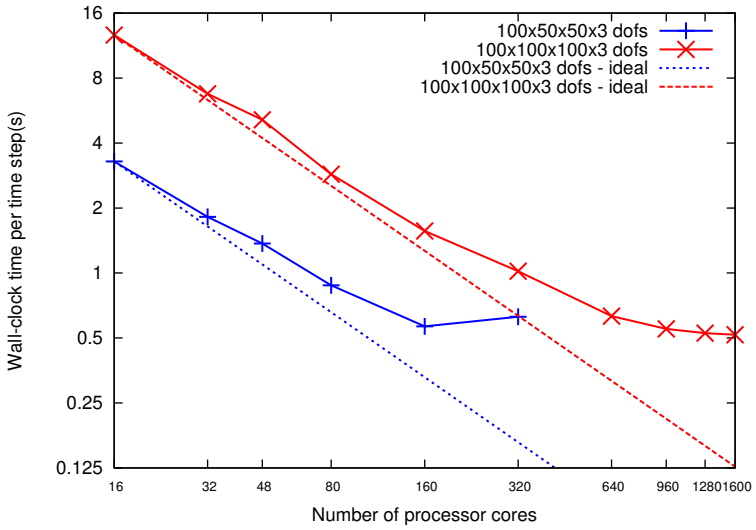

Figure 5.35. Strong parallel scaling with PFLOTRAN's MPHASE mode exhibited for the 3D EGS problem using Jaguar Cray XT5 supercomputer at ORNL.

5.3.3 Application of PFLOTRAN with New Multi-continuum Single-component Reactive Transport Feature to Enhanced Geothermal System

In this section, we describe how we implemented a multiple continuum formulation in PFLOTRAN for a single component reactive system applied to an EGS reservoir. A single-component system with silica dissolution and precipitation assuming linear kinetics in a generic EGS domain is shown in Figure 5.33. The parameters used for the flow in the domain are listed in Table 5.17. Water was assigned as the working fluid. The system was assumed to be in equilibrium with quartz initially. Two cases were considered: the first included injection of water in equilibrium with quartz and the second included injection of water in equilibrium with amorphous silica. The second scenario is intended to mimic the recycling of water, which is supersaturated with quartz. In the reaction, the rate constant at 25°C was chosen to be 14.4 $mol/m^2/s$. The rate constant at a temperature T was calculated using the relation

$$k(T) = k_0 \exp\left[\frac{E_a}{R}\left(\frac{1}{T_0 + 273.15} - \frac{1}{T + 273.15}\right)\right], \tag{5.11}$$

where: E_a is the activation energy chosen to be 89 KJ/mol, T_0 = 25°C, R is the ideal gas constant. Note that for the range of temperatures of interest in an EGS between 50°C and 200°C, the Arrhenius factor (k/k_0) varies from 16 to 584,693. The volume fractions of quartz were chosen to be 0.5 for fracture and 0.95 for matrix. Quartz surface area was set to 100 m^{-1} in the fracture and 6000 m^{-1} in the matrix roughly corresponding to a 1-mm grain size.

Table 5.17. Model parameters used for the new multicontinuum PFLOTRAN EGS model.

parameter	units	value
Fracture permeability	m^2	$k_h = 10^{-12}$, $k_v = 10^{-13}$
Matrix permeability	m^2	$k_h = 10^{-14}$, $k_v = 10^{-15}$
Fracture porosity	-	0.5
Matrix porosity	-	0.05
Tortuosity	-	0.1
Thermal conductivity	W/m/K	2.51
Rock specific heat	J/kg/K	1000
Injection rate	kg/s	50
Well productivity factor	m^3	10^{-12}
Bottom-well pressure	bars	175
Initial temperature	°C	200
Injection temperature	°C	50
Initial pressure	bar	200
Fracture aperture	cm	1
Fracture spacing	m	50

The simulated temperature profiles at the injection and the production wells are shown in Figure 5.36. The results for the concentration and porosity at the production well for the first case are shown in Figures 5.37 and 5.38, respectively. The corresponding trends for the second case are shown in Figures 5.39 and 5.40.

In the first case, the fluid is saturated or under-saturated with respect to quartz and so the primary porosity increases due to dissolution. In addition, the secondary porosity also increases as quartz also dissolves in the matrix. The single continuum result shows that the fluid remains saturated and the porosity does not change much. In the second case, the fluid is supersaturated with respect to quartz and hence quartz precipitates, in turn decreasing the primary porosity as well as the secondary porosity. The secondary porosity becomes artificially negative, reflecting precipitation and associated clogged matrix pores. Negative porosities are not physical but represent precipitation and associated feedback to fluid flow. In the case of a single continuum, the porosity starts to decrease at later times than the dual continuum case. This is when the injected fluid reaches the production well. On the other hand, in the dual continuum case due to matrix diffusion the precipitation starts earlier. In both the scenarios, $90 \times 25 \times 25$ grid cells were chosen for the primary continuum and 10 secondary grid cells per primary continuum grid cell was chosen for solving both flow and reactive transport. This leads to about $3\times90\times25\times25+2\times10\times90\times25\times25 = 23\times90\times25\times25 \sim 1.3$ million degrees of freedom to be solved. A typical simulation takes about 30 minutes to solve on 12 processor cores on a desktop computer.

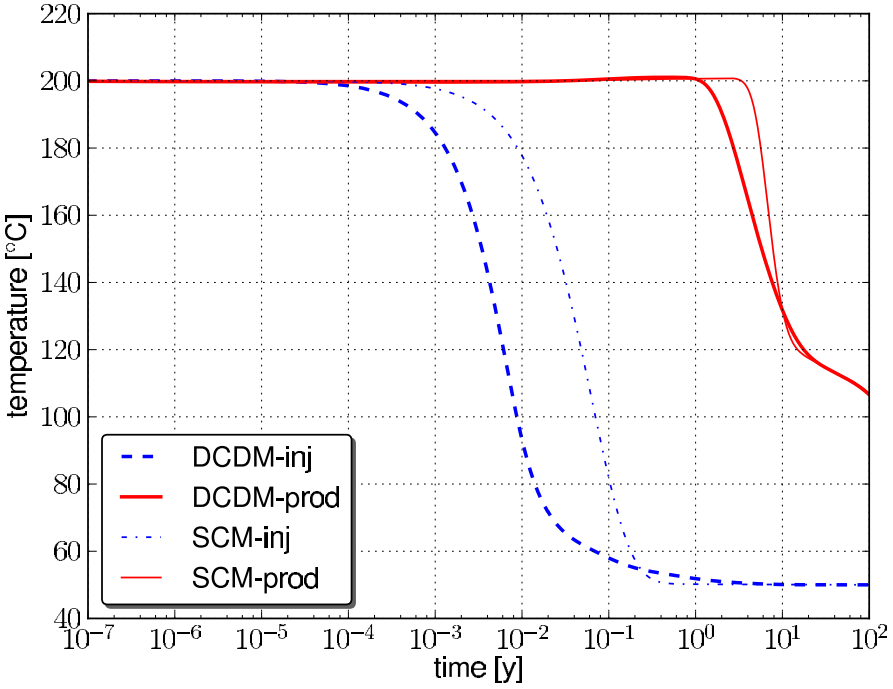

Figure 5.36. Comparison of simulated temperature between single and dual continuum formulations at the injection and production wells.

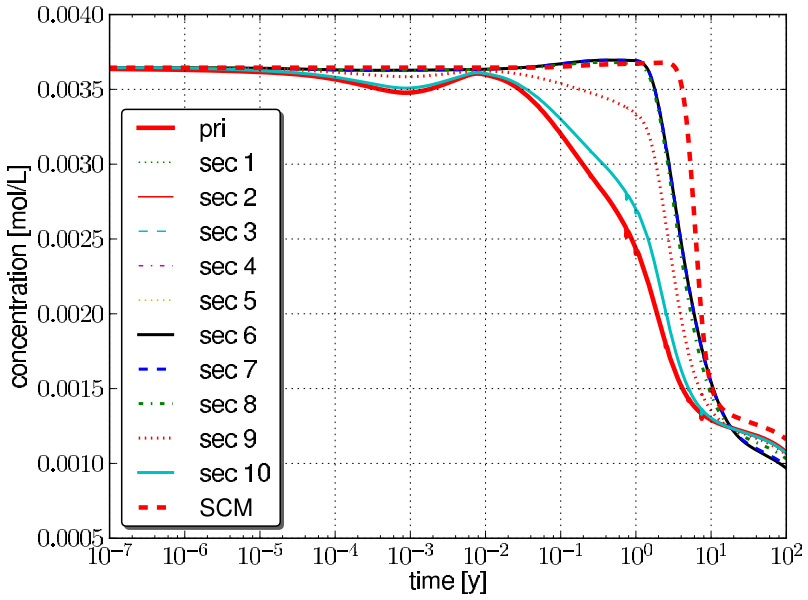

Figure 5.37. Concentrations of the primary and secondary continua at the production well. The fluid injected was assumed to be in equilibrium with quartz. The single continuum results are also shown.

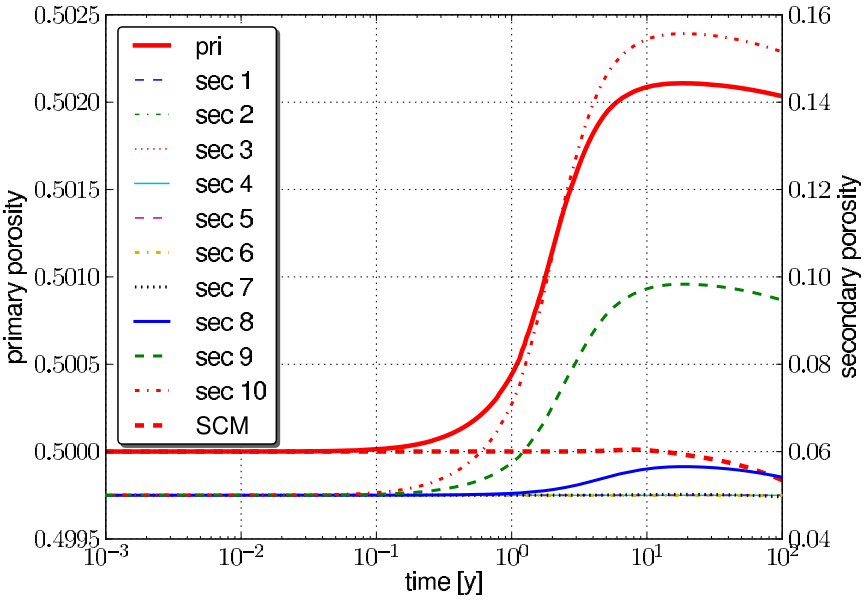

Figure 5.38. Simulated porosity of the primary and secondary continua at the production well. The fluid injected was assumed to be in equilibrium with quartz. The single continuum results are also shown.

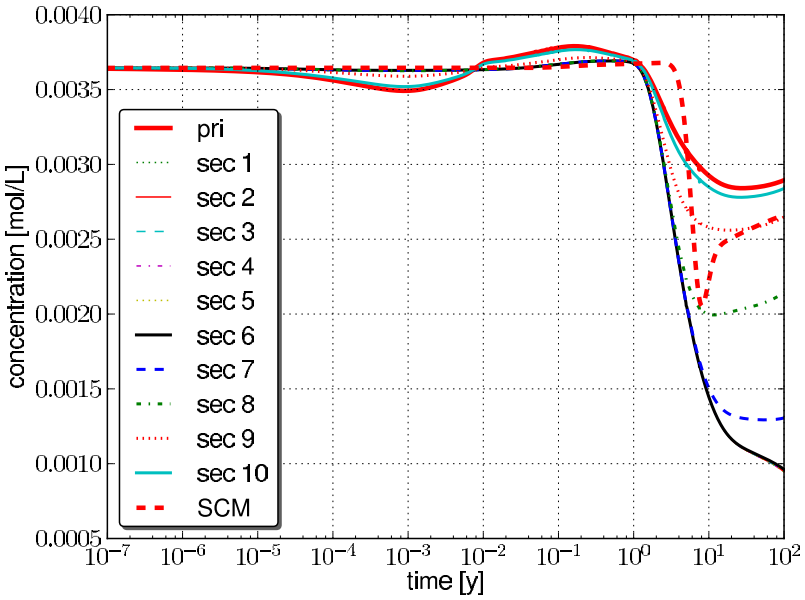

Figure 5.39. Simulated concentrations of the primary and secondary continua at the production well. The fluid injected was assumed to be in equilibrium with amorphous silica. The single continuum results are also shown.

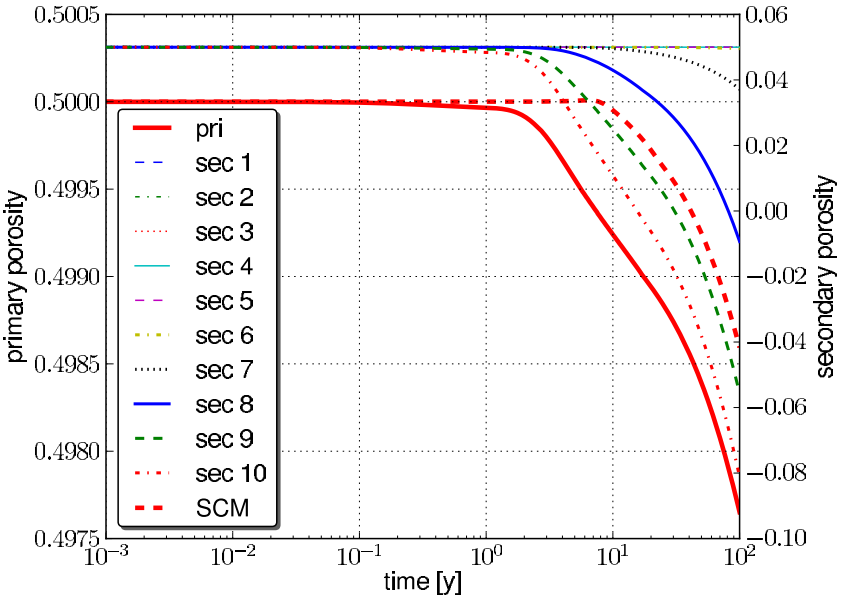

Figure 5.40. Simulated porosity of the primary and secondary continua at the production well. The fluid injected was assumed to be in equilibrium with amorphous silica. The single continuum results are also shown.

6. Conduct Field-scale Numerical Simulations

We collected basic information of geology, geophysics, seismic data, and injection/production well placement etc. at a CO_2-EGS research site, St. John's Dome, Arizona. We set up a field-scale model to emulate the conditions at the St. John's Dome CO_2-EGS research site, to simulate flow and associated heat extraction efficacy with CO_2 as a working fluid along with an acidization agent, and to investigate the potential of concurrent carbon sequestration and as well as the risk of CO_2 leakage.

6.1. St. John's Dome CO_2-EGS Research Site

The St. John's Dome is a geologic structure located along the boundary between Arizona and New Mexico, about half way between the Four Corners area and the Mexican Border. It extends across approximately 1,800 km^2 (700 $miles^2$). The dome consists of a broad, asymmetric anticline that trends northwest with an axis that plunges to the northwest and the southeast (Rauzi, 1999, and Rauzi, personal communication, 2013). The St. John's Dome is part of the Colorado Plateau. Basement rock consists of Precambrian granite. Sedimentary rocks present at the site range in age from Permian through Quaternary. An unconformity is present between rocks of Triassic and Late-Cretaceous age. The depth to basement rock ranges from 2,300 feet to 4,600 feet below ground surface.

The dome is notable for hosting a natural gas field consisting of almost pure CO_2. It is one of five such large CO_2 domes in the U.S. The CO_2 reserves are hosted primarily in the Fort Apache, Big A Butte and Amos Wash members of the Supai Formation (Permian) and also in the faulted and weathered material at the top of the basement rock. Caprock bounding the top of the CO_2-rich zones consists of anhydrites and mudstones (Coblentz, 2011).

Exploration and research of the geothermal potential of the St. John's Dome extends back at least into the 1970s. Interest in this area is based on (1) the presence of moderate to high chemical geothermometers, (2) the proximity of the Springerville Volcanic Field, and (3) the intersection of prominent regional lineaments (Stone, 1979). More than 40 wells have been drilled at the dome to help determine the gas reserves. The deepest of these extends a short distance into the basement granites. Bottom-hole temperature measurements have been taken in seven of these wells. These measurements suggest that temperature gradients appear to be highest in the south-central portion of the dome and the temperature at a depth of 3 km in the south-central portion of the dome is 150° C or greater. Based on identified geothermal resources and larger volume reserves of CO_2, the St. John's Dome is uniquely suitable for developing CO_2-EGS because it greatly reduces the risk and cost of testing and developing the technology.

6.2. Conduct Simulations to Identify Suitable Conditions for Using CO_2 as a Working Fluid for Geothermal Energy Extraction

6.2.1 3-D Field-scale Flow and Heat Simulation for scCO_2 as a Working Fluid using PFLOTRAN

We set up a field-scale model using geological data from the St. John's Dome site near Springerville, Arizona. Structure-contour data of the Fort Apache member (from Figure 4 of Rauzi (1999)) was digitized. These digitized data were then converted and used for aquifer depth in the model. Figure 6.1 shows the region of study, northeast of the system's primary fault. The model domain is from 23 km to 60 km in X direction, from 0 km to 65 km in Y direction, and from 650m to 2000m in Z direction. Figure 6.2 shows the aquifer height above sea level (extracted from Rauzi (1999)) and the smoothened interpolated contour data of the study site, which was used for mesh generation and aquifer delineation in the mesh. Based on the data

shown in Figure 6.2, the mesh was generated with an assumption of aquifer thickness of 100 m in the entire domain. Figure 6.3 plots two cross-sections of the model domain at y = 0 and y = 37.5 km, respectively. The system's primary fault is located in the left of the domain with a length of 500m in X direction through the entire vertical profile. The aquifer is embedded in the caprock on the top and baserock at the bottom (Figure 6.3). We adopted a uniform mesh of 100x100x200. The material data of the study site in Figure 6.3 were used to generate a HDF5 file using Python scripts, which can be read by the PFLOTRAN model to identify the material regions in the simulation.

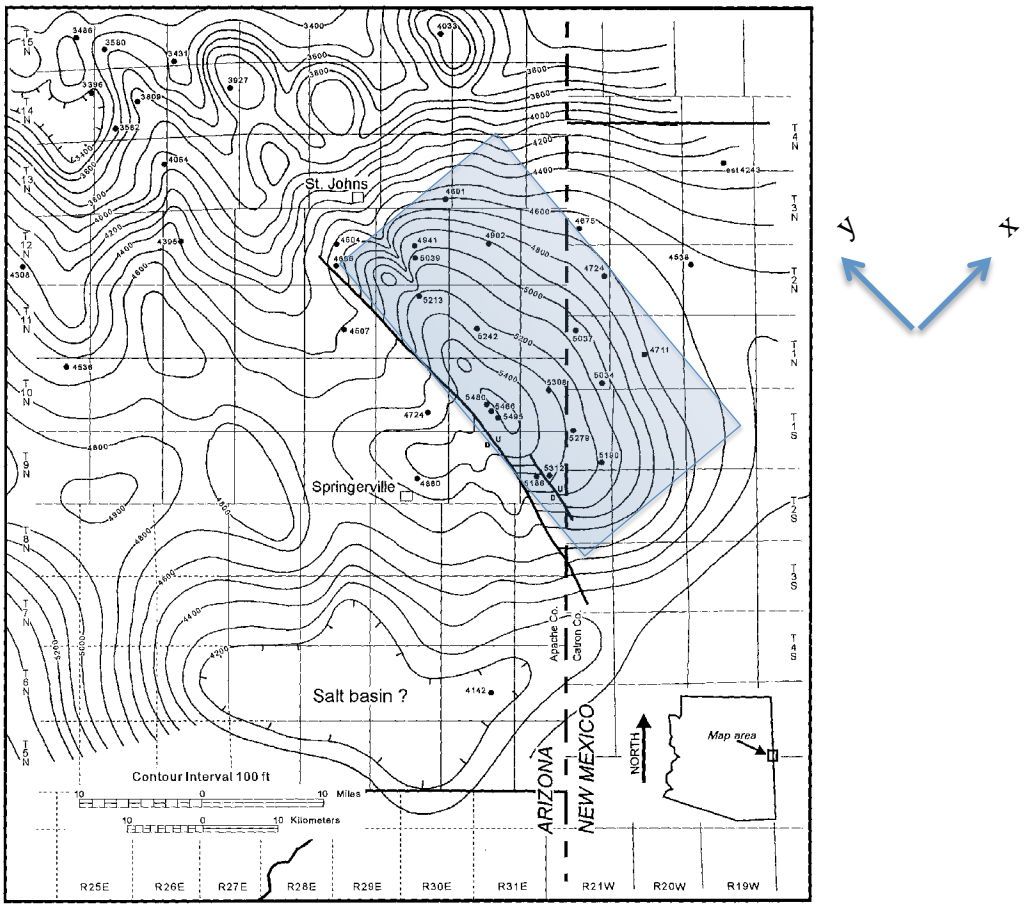

Figure 6.1. Fort Apache regional structure base contour at Springerville-St. John's CO_2 site (from Rauzi (1999)). The region of study was chosen to be the area northeast of the fault shown in color.

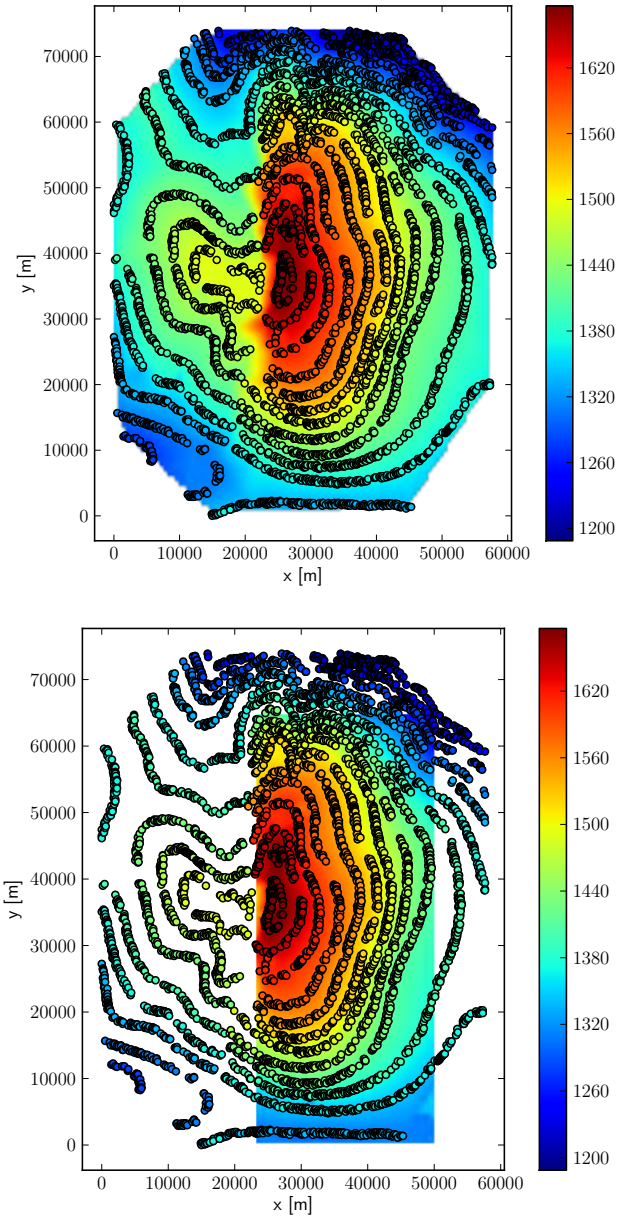

Figure 6.2. Scatter plot of the aquifer height measured above sea level (extracted from Rauzi (1999)) (top); and smoothed, interpolated data for the region of interest in Figure 6.1 (below).

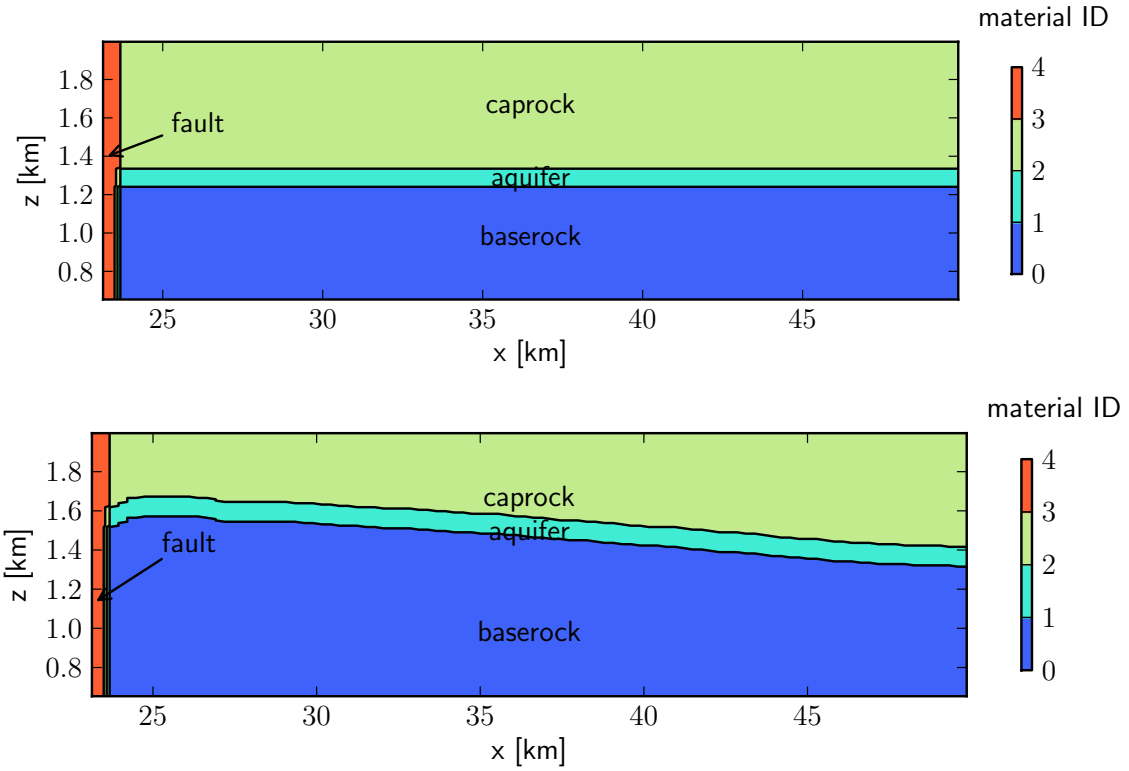

Figure 6.3. Cross-section of the domain at y = 0 (top) and y = 37.5 km (bottom). Shown here in color is the material ID. This cross section information is used to generate the mesh for simulating flow and reactive transport; *z* is measured in terms of height above sea level.

Preliminary set-up for flow and heat simulation is performed using the PFLOTRAN model. Figure 6.4 shows a snap-shot of the output from PFLOTRAN at time = 0. A three-dimensional rendering also shows the topography of the aquifer varying with x, y and z directions (Figure 6.4). Also, note that the z direction is scaled 25 times for visualization. A flow simulation was performed using the domain and mesh information shown Figure 6.4.

The injection and production wells were placed at (30000m, 30000m) and (30000m, 31000m) within the aquifer. The material properties used in the domain are listed in Table 6.1. A grid of 100x100x100 was used for the simulation. The total simulation time was 100 years with CO_2 injection at a temperature of 50 ^{o}C for 50 years. The initial temperature in the domain was set to 20 ^{o}C. All the boundaries of the domain were assumed closed and an initial pressure of 200 bar

at the top of the domain with a hydrostatic profile was set. CO_2 injection rate was set to 50 kg/s. The simulation was run on 400 processors of the Los Alamos National Laboratory supercomputer Wolf for about 6 hours. The total number of flow degrees of freedom solved were 3 million.

Figure 6.5 shows simulated temperature and pressure profiles at the injection and production wells over time. Figure 6.6 descripts the contours of simulated CO_2 saturation for the plane y=30,000m at simulation times of 0.1, 10, 25, 50, 75, and 100 years, respectively. The temperature at the production well remains fairly close to the initial temperature of 200 ^oC. It can be seen from Figure 6.6 that CO_2 rises to the top of the domain through the caprock after 25 years. The CO_2 also travels towards the fault and rises through the fault as well. We found that all CO_2 remained in the domain during the simulation time and very little amount of CO_2 was recovered. Therefore, the geothermal energy power production was very poor. Since the domain is very large, the recovered CO_2 would be small unless the extent of CO_2 is restricted, resulting in the small energy extraction. Extent of CO_2 can be restricted by closing up the boundaries to the size of the model domain in Section 5.3 and Section 5.1, but how this could be accomplished in an actual field setting would be site-specific. A net positive energy extraction is observed in these simulations. The amount of CO_2 sequestered with this particular model domain will be evaluated in Section 6.4.

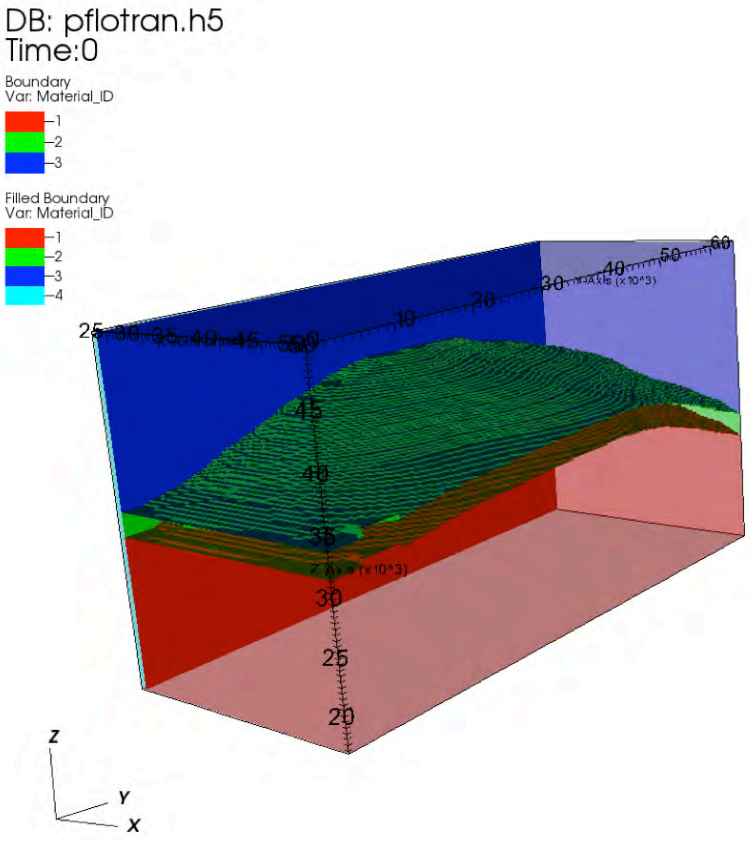

Figure 6.4. A 3-D rendering of the St. John's Dome model domain with different material IDs shown in color. (baserock in red; caprock in blue; aquifer in green; fault in cyan; the z direction is scaled (increased) 25 times for visualization purposes).

Table 6.1. Material properties assigned to the 3-D Springerville-St. John's CO_2-EGS field-scale simulation.

Material	Baserock	Aquifer	Fault	Caprock
Material ID	1	2	3	4
Porosity	0.05	0.05	0.05	0.05
Permeability	1.e-15 (m^2)	1.e-13 (m^2)	1.e-12 (m^2)	1.e-15 (m^2)
Rock density	2650 (kg/m^3)	2650 (kg/m^3)	2650 (kg/m^3)	2650 (kg/m^3)
Specific heat	1000 (J/kg/C)	1000 (J/kg/C)	1000 (J/kg/C)	1000 (J/kg/C)
Thermal conductivity	2.51 (W/m/C)	2.51 (W/m/C)	2.51 (W/m/C)	2.51 (W/m/C)
Tortuosity	0.1	0.1	0.1	0.1
Van Genuchten alpha	2.4e-4 (Pa^{-1})	1.48e-6 (Pa^{-1})	1.48e-6 (Pa^{-1})	1.48e-6 (Pa^{-1})
Van Genuchten lambda	0.444	0.444	0.444	0.444
Residual liquid saturation	0.1	0.1	0.1	0.1
Residual gas saturation	0	0	0	0

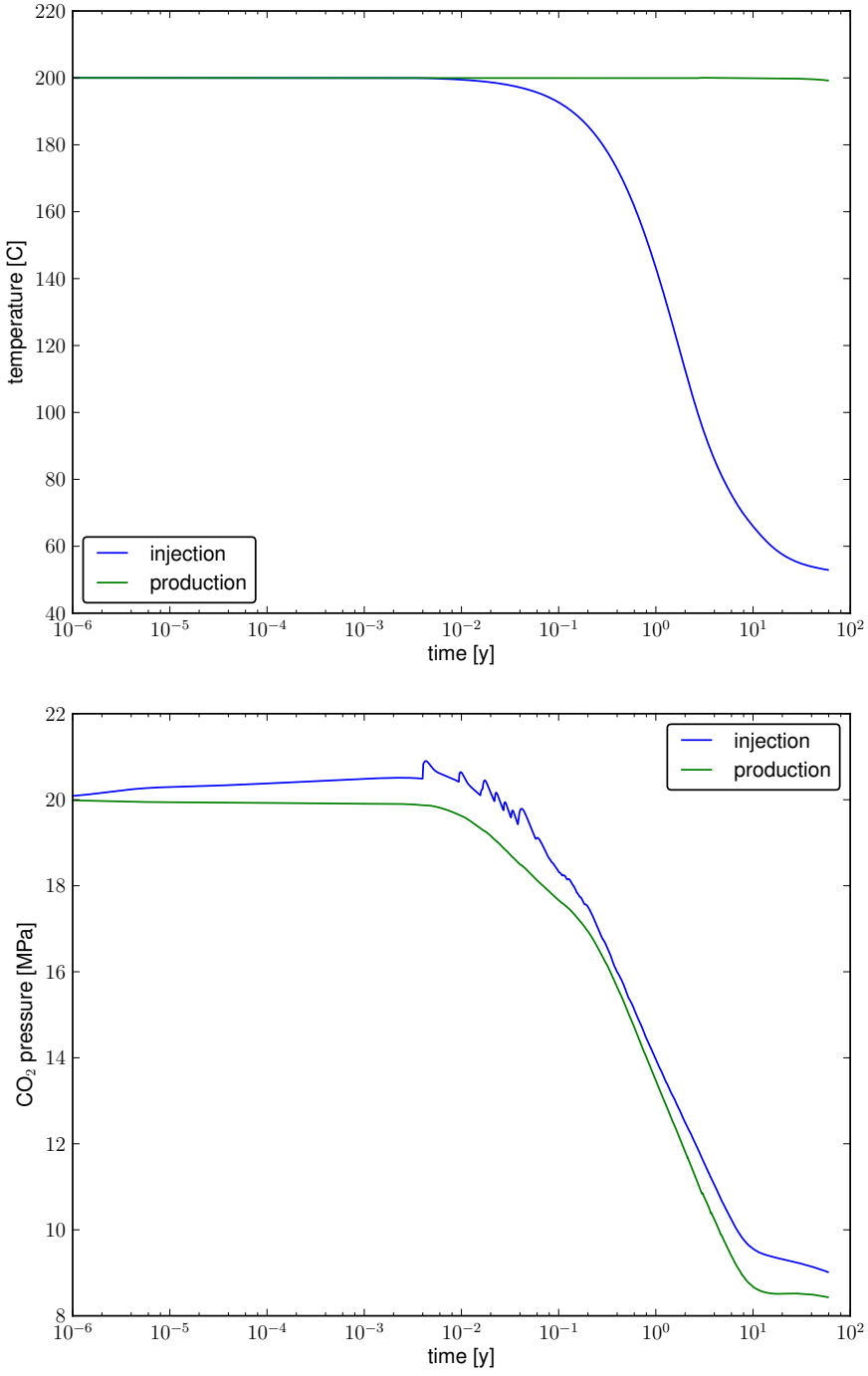

Figure 6.5. Simulated temperature (top) and pressure (bottom) profiles at the injection and production wells as a function of time.

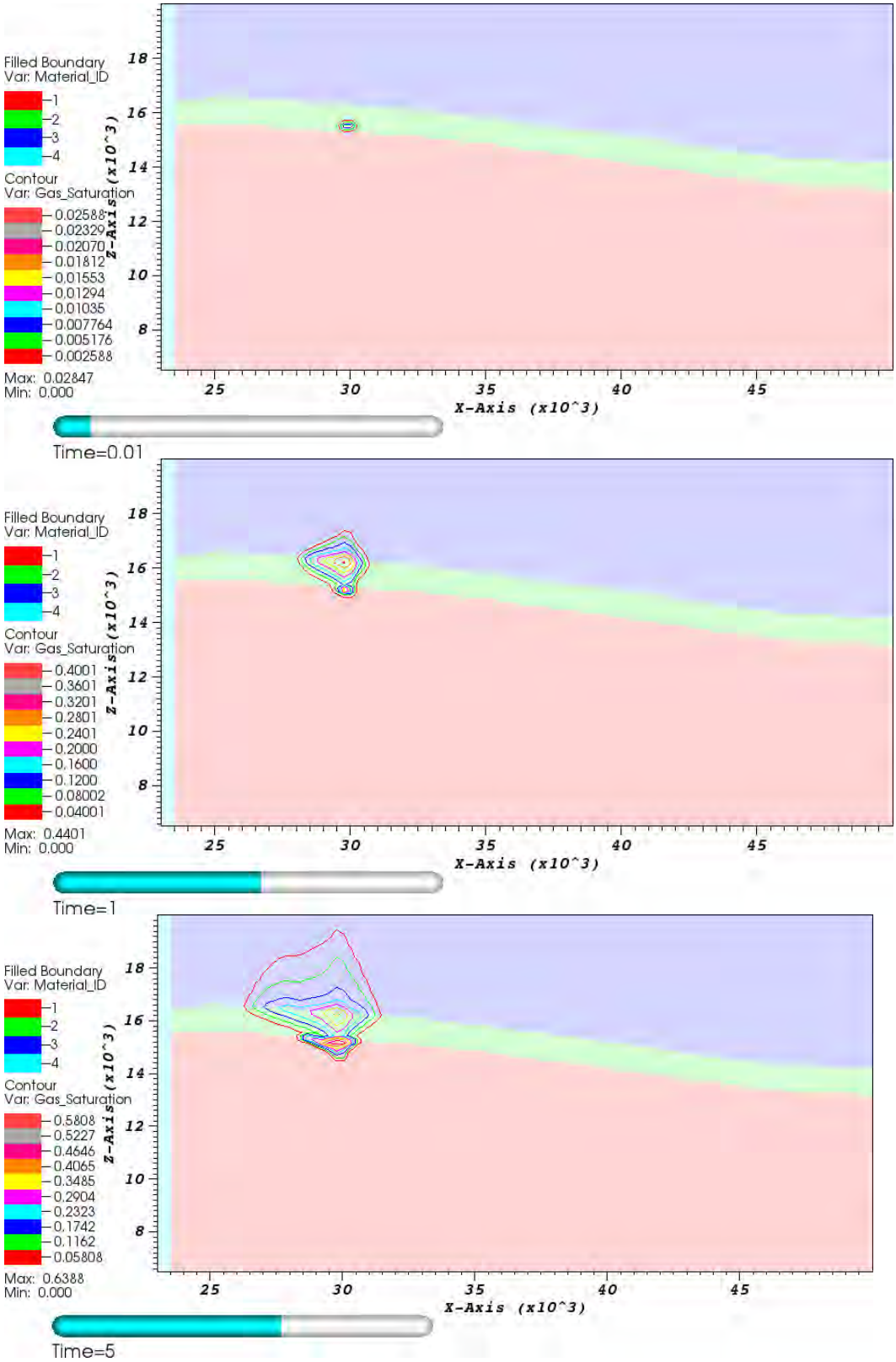

Figure 6.6. Simulated CO_2 saturation profiles after 0.01, 1, 5, 10, 25, and 50 years.

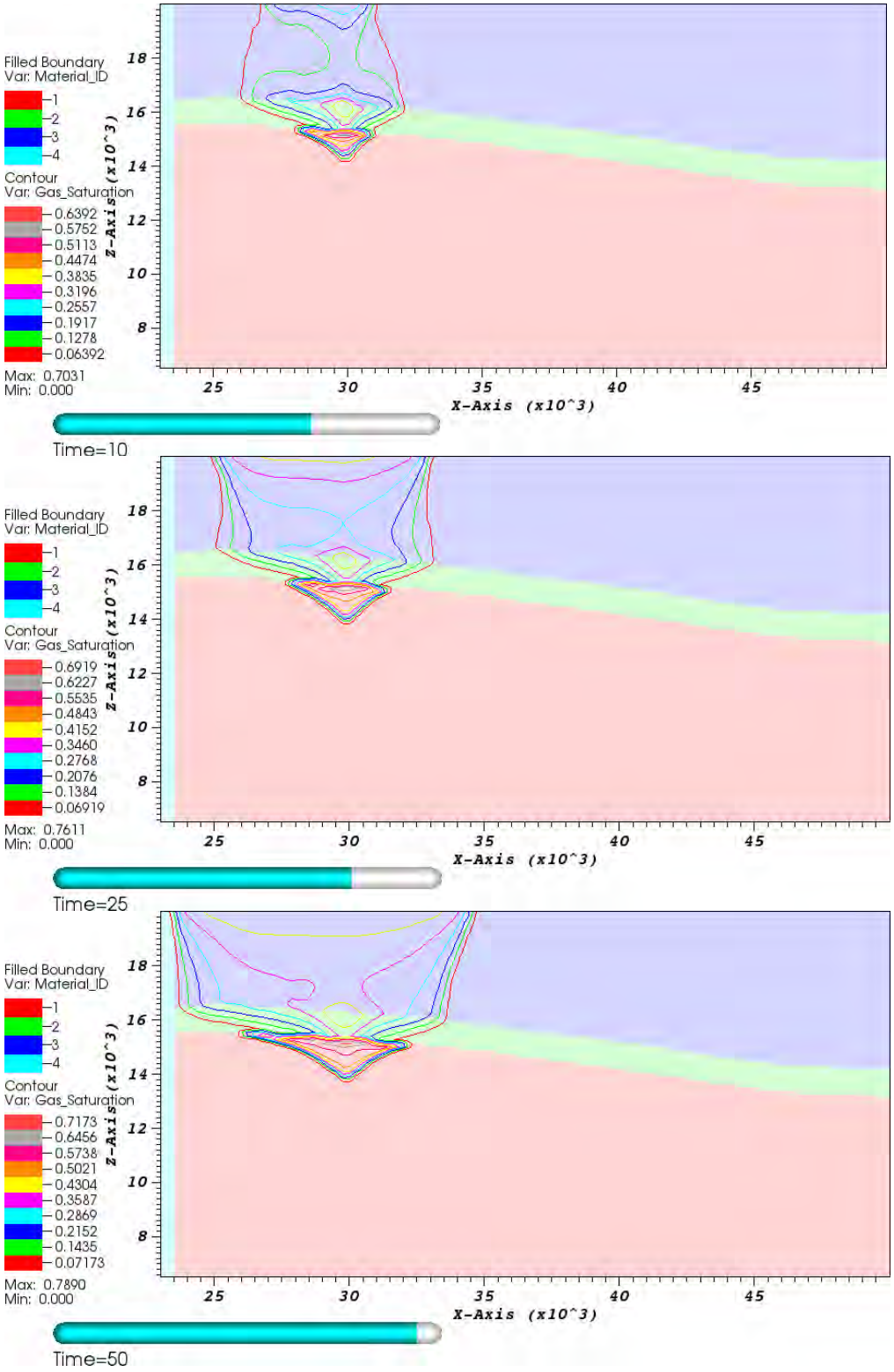

Figure 6.6. (Cont.) Simulated CO_2 saturation profiles after 0.01, 1, 5, 10, 25, and 50 years.

6.2.2 3-D Flow and Heat Simulation with 5-spot Well Pattern for scCO$_2$ as a Working Fluid using TOUGH2 model

As discussed in the previous section of this report, we set up a 3-D PFLOTRAN model to evaluate different EGS scenarios at the St. John's Dome CO_2-EGS research site in Arizona. We simulated flow and heat transport with CO_2 as a working fluid. In this section, we describe results of a 3-D simulation model including a generic 5-spot well pattern, calibrated with physical properties of the CO_2-EGS site in St. John's Dome. We evaluated system performance with respect to energy extraction, geochemical reactions, geological CO_2 sequestration, and risk of CO_2 leakage.

6.2.2.1 Problem Setup

We elected to adopt a 5-spot well pattern because of its wide application in oil fields and geothermal reservoirs (Pruess, 2006, 2008; Spycher and Pruess, 2010, Wan et al., 2011; Borgia et al., 2012; Randolph and Saar, 2011). The resulting 3-D model domain with its 5-spot well pattern is illustrated in Figure 6.7. Due to the symmetry of the 5-spot well pattern, we employed a 1/8 symmetry domain (of the 5-spot pattern) for all simulations (Figure 6.7), but results are shown on a full-well basis (similar to the approach of Pruess, 2006). The thickness of the domain is 500 m with a layered geological setting, including 100m-thick fractured rock at the center and 200m-thick granite at the top and bottom of the model domain (Figure 6.7). The grid cell size is uniform at 70.7m horizontally (X and Y directions), and 50m vertically (Z direction). We also implemented a dual-continuum approach at the 100m-thick center of the model domain to represent a typical fractured EGS reservoir.

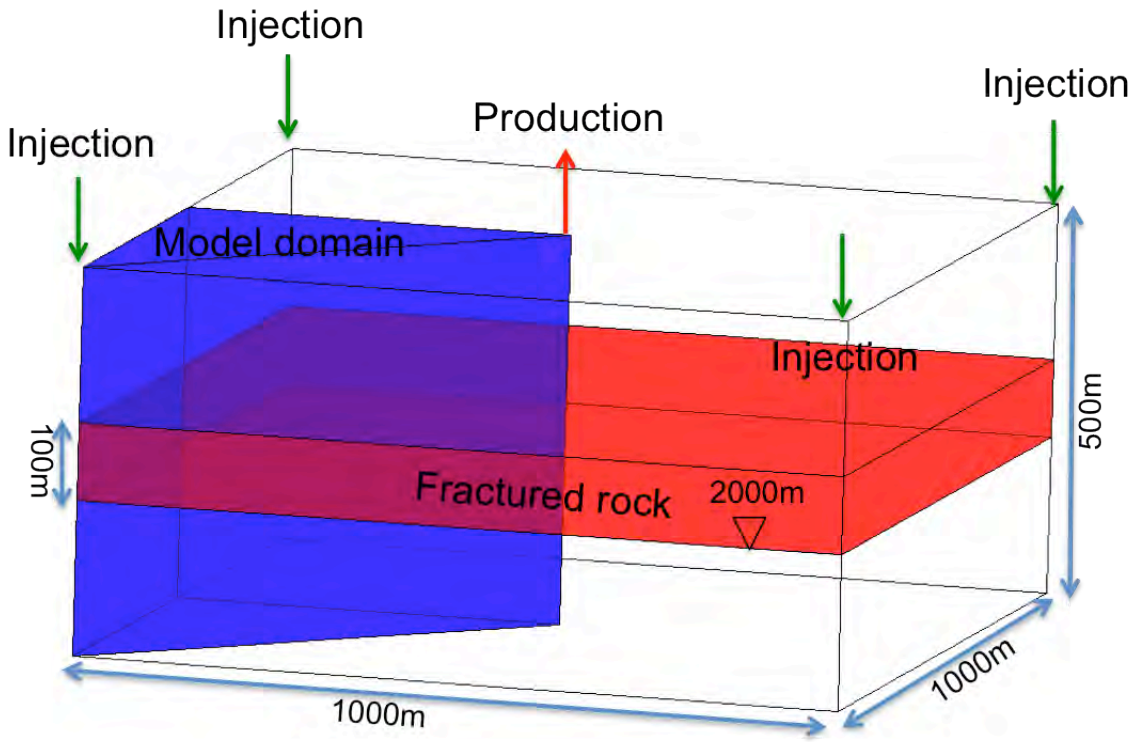

Figure 6.7. Schematic of the 3-D numerical model domain with a 5-spot well pattern (1/8 system domain used for all simulations).

We collected all publicly-available of hydrologic data for wells near the St. John's Dome, primarily from files of the Arizona Geological Survey. The mean value of measured permeability (0.25 mD) was assigned to all fractured aspects of the model. The MINC (multiple interacting continua) of TOUGH2 code (Pruess et al., 1999; Pruess, 2005) is used to represent matrix-fracture heat transfer with a fracture spacing of 50m and fracture volume fraction of 2%. Injection and production wells are placed at the bottom of the fractured rock layer with a depth of 275 m from the top of domain, and 2000 m from the surface (Figure 6.7). Assigned initial conditions include hydrostatic pressure and conductive heat flow (temperature gradient 40^{o}C/km), with 200 bars and 200 ^{o}C at 275 m depth from the top of the domain. A Dirichlet boundary condition (constant pressure) is assigned to boundaries of injection and production,

with a pressure drop of 25 bars between the injection and production wells. For wells, constant pressure is assigned as initial plus 12.5 bar at the injection well, and initial minus 12.5 bar at the production well. A Neumann condition (no flow) is assigned on all other sides. Details of parameter settings are summarized in Table 6.2. The ECO2H module of TOUGH2 code is employed to conduct the flow and heat simulations for 50 years with $scCO_2$ as a working fluid.

Table 6.2. Hydrologic parameters, initial, and injection/production boundary conditions used for 3-D simulations of a 5-spot well pattern.

Properties	
Fractured rock permeability	0.25 mD
High Granite permeability:	0.01 mD
Fracture spacing	50 m
Fracture volume fraction	2%
Fracture Porosity:	0.50
Granite porosity	0.08
Fracture Tortuosity:	1.0
Thermal conductivity:	2.51 W/m ^{o}C
Rock specific heat:	1000 J/kg ^{o}C
Rock grain density	2650 kg/ m^3
Initial Condition	
Reservoir fluid	all water
Initial temperature:	200°C at the layer of production well with 40 ^{o}C/km geothermal gradient
Initial pressure	Hydrostatic pressure with 200 bar at the layer of production well
Production/Injection condition	
Injection/production well distance	707 m
Injection pressure	Initial + 12.5 bar
Injection temperature	50°C
Production pressure	Initial -12.5 bar

6.2.2.2 Flow and Heat Simulation Results

Figure 6.8 plots the net heat extraction rate, mass flow rate, temperature and gas saturation at the gridblock next to the injection and production wells for the model with $scCO_2$ as

the working fluid. Results for water as a working fluid are also plotted in Figure 6.8. For the case of CO_2 as a working fluid, flow containing water only is produced at a rate of ~180 kg/s during the initial stages of simulation. After 0.05 years, the produced water flow rate sharply decreases with the increase of produced CO_2 flow rate, demonstrating the mixture of water and CO_2 produced when CO_2 has reached the production well. With continuous CO_2 injection and increases in gas saturation at the production well, the produced CO_2 flow rate significantly increases with no water production. The oscillation in mass flow and heat extraction rate at the early stages of simulation (Figure 6.8) is a simulation artifact. Specifically, as explained for other simulations in previous sections, this minor oscillation is a numerical response to maintain constant pressure at the wellbore; an absolute constant pressure in a wellbore cannot exist in nature, and to force such in a simulation translates to some oscillatory variability in flows. We adopted fixed wellbore pressure at depth, despite the minor oscillation artifact, because it is a common approach of analysis. The net heat extraction rate is around 120 MW in the initial stage of simulation and decreases to 60 MW after 0.1 year, which is a similar trend to the produced water flow rate. With increases of produced CO_2 flow rate, the net heat extraction increases to its maximum of 80 MW after 5-year CO_2 injection. With continuous increase of CO_2 gas saturation at the production well, the net heat extraction decreases to 12 MW after 50 years of CO_2 injection. This is due to more rapid thermal depletion of CO_2 compared to water, associated with the rapid decrease of simulated temperature (Figure 6.8). The CO_2 saturation next to the injection well becomes 100% after 0.2 years of CO_2 injection. The CO_2 flow breaks through to the production well after 0.06 years of injection and gas saturation continues increasing to 1.0 after 10 years of CO_2 injection. However, the gas saturation decreases from 1.0 to 0.6 at the production well after 20 years of CO_2 injection, demonstrating possible CO_2 leakage to upper-

lying layers (Figure 6.9). The temperature next to the injection well decreases from the initial temperature of 200 ^{o}C to the injection temperature of 50 ^{o}C. The temperature next to the production well remains constant at the initial temperature of 200 ^{o}C until around 2 years CO_2 injection, and then drops to 65 ^{o}C after 50 years of CO_2 injection.

Figure 6.9 plots simulated 3-D profiles of gas saturation and temperature after 30 years of $scCO_2$ injection (as a working fluid), respectively. The gas saturation at the layer of injection/production well decreases from 1.0 to 0.5 toward the production well after 30 years. The gas saturation varies from 0.2 to 0.5 in the area of upper-lying layers after 30 years, demonstrating simulated CO_2 leakage occurs. The gas saturation is around 0.5 in the layer just below the injection/production well (Figure 6.9). The 3-D temperature profile exhibits a similar trend as the gas saturation profile, which increases from 50 ^{o}C at the injection well to 80 ^{o}C at the production well (Figure 6.9), similar to the results in Figure 6.8. The temperature drop also occurs in the layers just above and below the injection/ production layer, associated with large gas saturation in that area.

For water as a working fluid, the mass flow rate next to the production well decreases from 100 kg/s at the initial stage of simulation to 53 kg/s after 50 years of water injection (Figure 6.8), which is less than the 180kg/s initial rate and less than the 150 to 250 kg/s of the produced CO_2 flow rate at the late stage of simulations with $scCO_2$ as a working fluid. A possible explanation is lower viscosity of CO_2 compared to water. The net heat extraction for water as a working fluid has similar trends for the produced water flow rate, which also decreases from 80 MW at the initial stage to 10 MW after 50 years (Figure 6.8). The net heat extraction rate for CO_2 as a working fluid varies from 12 to 180 MW during the simulation period and is much

larger than the rate for water as a working fluid, indicating that $scCO_2$ as a working fluid could enhance heat extraction compared to water, at least for a generic 5-spot well pattern.

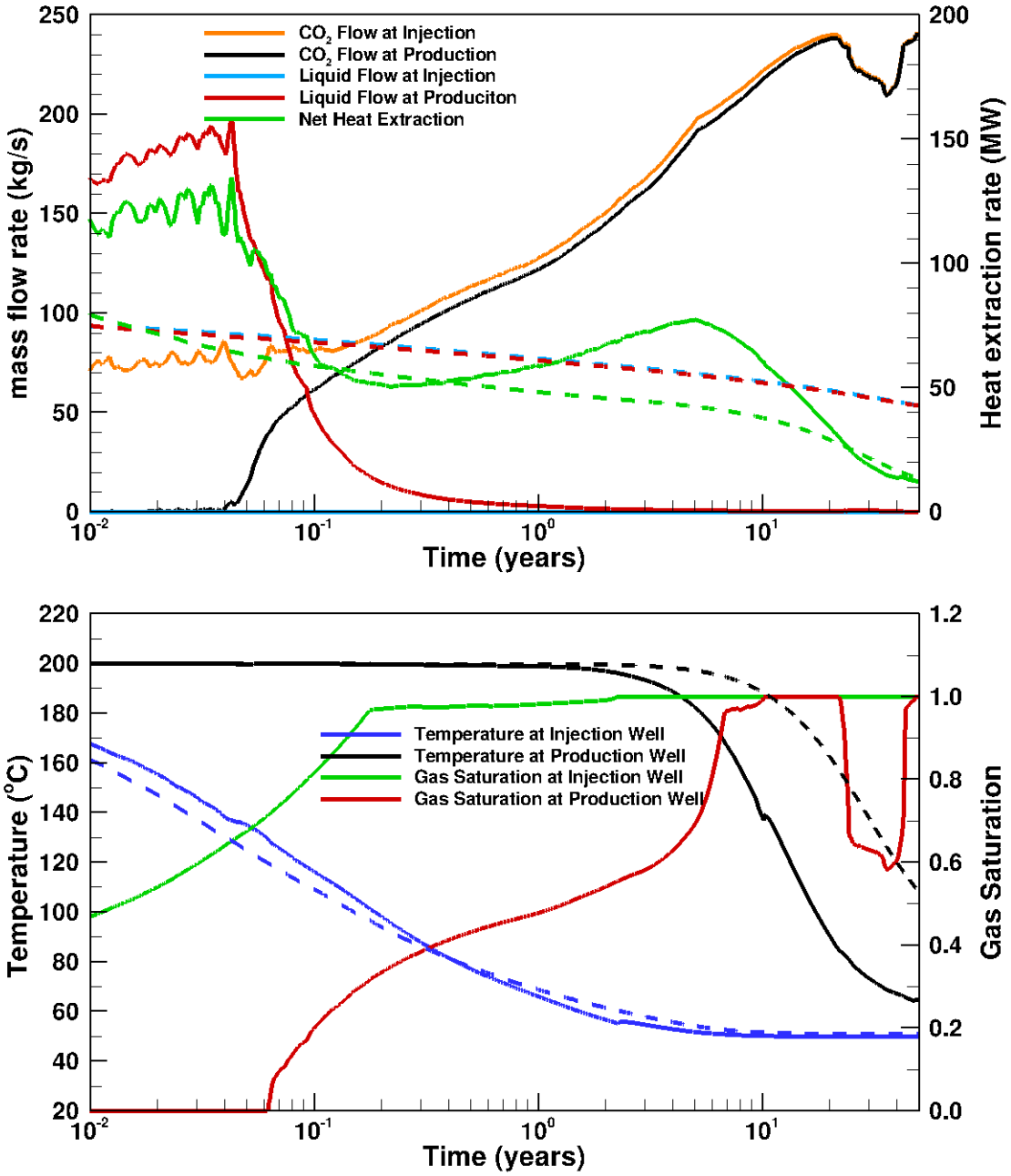

Figure 6.8. Simulated heat extraction rate, mass flow rate, temperature, and gas saturation next to production well for $scCO_2$ (solid line), and water (dash line) as working fluids, respectively.

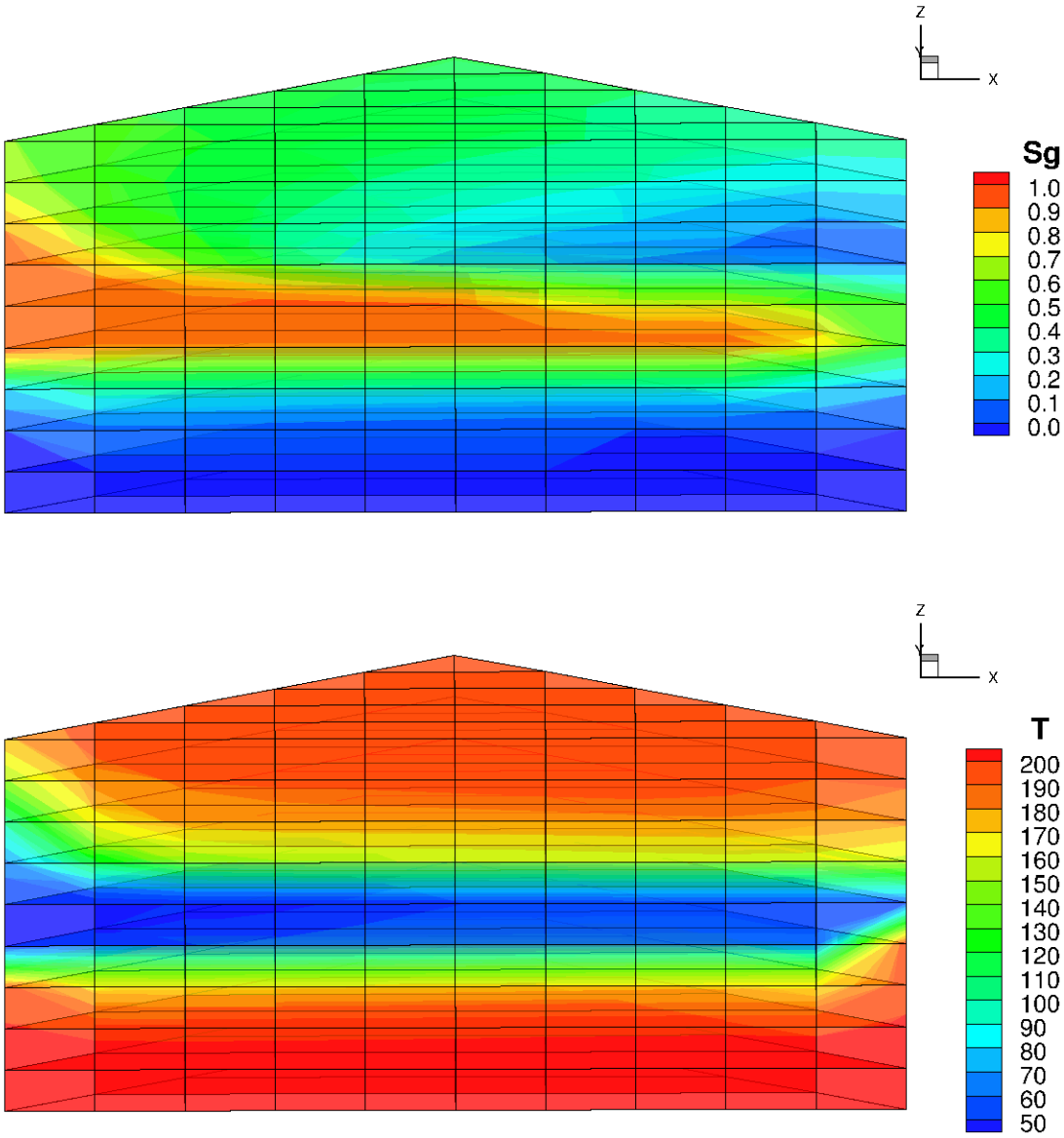

Figure 6.9. Simulated 3-D profiles of gas saturation and temperature after 30 years injection of $scCO_2$ as a working fluid.

6.3. Conduct Simulations to Assess Geochemical Processes of CO_2-rock fluid Interaction and Concurrent Carbon Sequestration

6.3.1 Mineralogical Assemblages in Springerville-St. John's CO_2 Field Site

Two core samples of the Precambrian granite from one of the Arizona wells (22-1X state) at Springerville-St. John's CO_2 research site were analyzed using X-ray diffraction (XRD) at the Energy & Geoscience Institute, University of Utah. The Arizona well 22-1X state is located near the northern boundary of the St. John's CO_2 field (Figure 6.10) with an elevation of 6,393 ft at the ground level, and consisting of Permian Supai formation at a depth from 640 ft to 2060 ft below the surface, and Precambrian granite below that (Rauzi, 1999). The two core samples for Precambrian granite were collected at depths of 2,102.5 ft and 2,124 ft. The mineralogical assemblages of the two samples by XRD are listed in Table 6.3. The Precambrian granite mainly consists of quartz (45-50%), plagioclase (26- 30%), and K-feldspar (19-21%) (Table 6.3).

Table 6.3 Mineral assemblages of core samples from Precambrian granite in Arizona well 22-1X State in the St. John's CO_2 field.

Minerals	Minerals composition (Sample 1 at 2102.5 ft)	Minerals composition (Sample 2 at 2124 ft)
Quartz	50%	45%
Plagiclase	26%	30%
K-feldspar	21%	19%
Biotite	1%	2%
Muscovite	2%	3%
Total	100%	99%

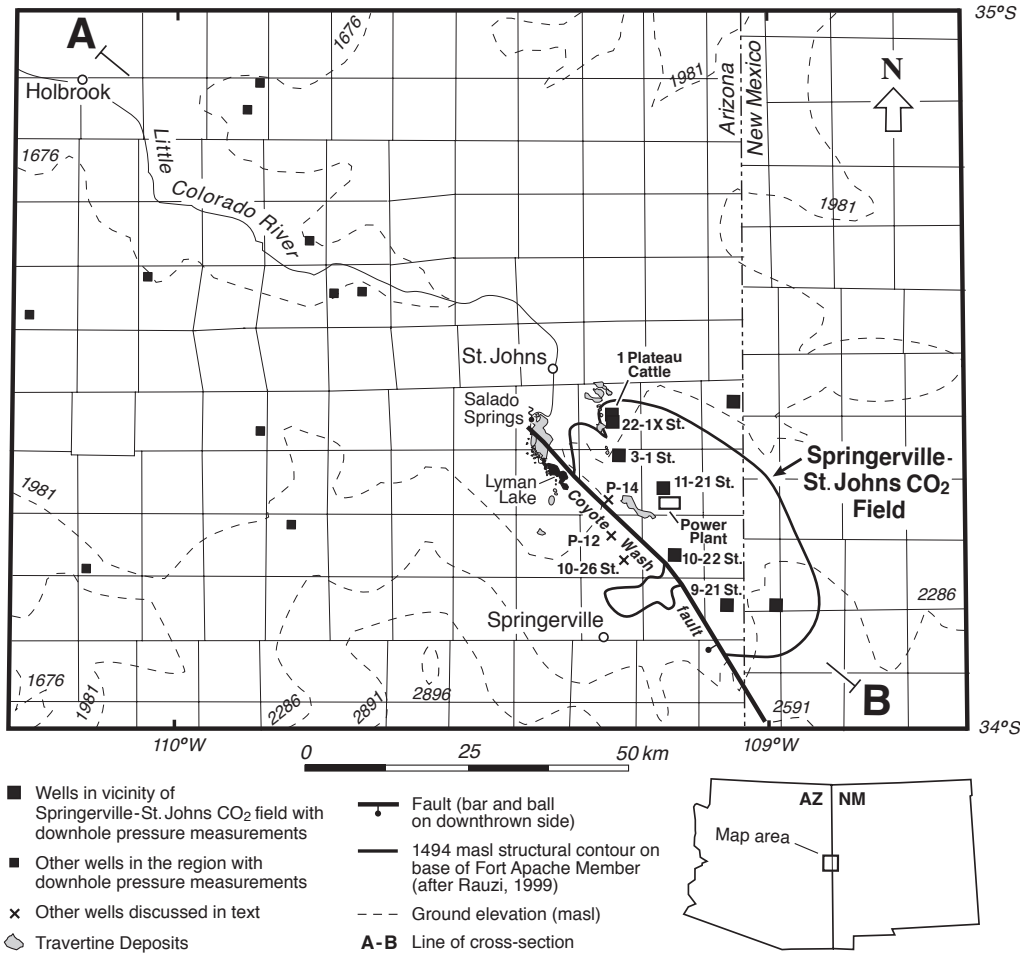

Figure 6.10. Map and well locations of the St. John's CO_2 field (adopted form Moore et al., 2005).

6.3.2 3-D Geochemical Simulation with 5-spot Well Pattern for $scCO_2$ as a Working Fluid using TOUGH2 model

6.3.2.1 Mineralogical Composition and Reaction Kinetics

As discussed in Section 6.3.1, the mineralogical assemblages of two samples in the study area were obtained by XRD analysis. The Precambrian granite mainly consists of quartz (45-50%), plagioclase (26- 30%), and K-feldspar (19-21%). We expressed average percentage of the mineralogical assemblages of the two samples and assigned these as parameters for simulations.

The possible secondary mineral assemblage was selected based on equilibrium batch modeling, described in Section 5.2.1. The primary and secondary mineral assemblages are listed in Table 6.4. The kinetic properties (rate constant, activation energy, and power term) of multiple mechanisms (neutral, acid and base) for the primary and possible secondary minerals are listed in Table 6.5. The reactive surface areas of some minerals (e.g., quartz, oligoclase, albite, k-feldspar, calcite, magnesite, kaolinite, siderite, illite, and smectitie) are taken from Xu et al. (2004). Values for other minerals are assumed as 9.8 cm^2/g (Table 6.5). All geochemical simulations utilize the EQ3/6 thermodynamics database (Wolery, 1992), and all flow aspects are simulated (for 50 years simulation time) using the TOUGHREACT/ECO2H model (Xu et al., 2006, 2011). A set of batch simulations were conducted first, to obtain initial aqueous solutions that would be in equilibrium with the primary minerals.

6.3.2.2 Geochemical Simulation Results

Figure 6.11 plots simulated 3-D profiles of aqueous CO_2 mass fraction and pH values after 30 years, respectively. Figures 6.12 and 6.13 illustrate simulated 3-D profiles of changes of mineral abundances (in volume fraction) for primary minerals (oligoclase and quartz) and secondary minerals (calcite and illite). From the beginning of $scCO_2$ injection, $scCO_2$ dissolution in water results in increased dissolved CO_2 concentration and lower pH values (compared to the initial pH value of 5.4) (Figure 6.11). The dissolved CO_2 and lowered pH values induce dissolution of primary minerals and precipitation of secondary minerals. Aqueous CO_2 is observed at the upper- and lower-lying layers (Figure 6.11), which exhibits larger dissolved CO_2 mass fractions than values at the injection/production layer after 30 years. A reverse trend is associated with the gas saturation distribution (Figure 6.9), indicating that more CO_2 dissolves in the aqueous phase with lower gas saturation in upper- and lower-lying layers. The pH values in

the injection/production layer are smaller than the initial pH value of 5.4, and increase toward to the production well (Figure 6.11), which is similar to the pattern of gas saturation (Figure 6.9). The higher the gas saturation, the lower pH values, in general.

Table 6.4. Chemical composition and initial volume fractions of primary and secondary minerals for geochemical simulations of the St. John's CO_2 field site.

Mineral	Chemical composition	Initial volume fraction of minerals
Primary:		
Quartz	SiO_2	0.475
Oligoclase	$Na_{0.77}Ca_{0.23}Al_{1.23}Si_{2.77}O_8$	0.280
K-Feldspar	$KAlSi_3O_8$	0.200
Annite[a]	$KFe_3AlSi_3O_{10}(OH)_2$	0.0075
Phlogopite[a]	$KAlMg_3Si_3O_{10}(OH)_2$	0.0075
Muscovite	$KAl_3Si_3O_{10}(OH)_2$	0.025
Secondary:		
Calcite	$CaCO_3$	0.0
Magnesite	$MgCO_3$	0.0
Illite	$(K,H_3O)(Al,Mg,Fe)_2(Si,Al)_4O_{10}[(OH)_2,(H_2O)]$	0.0
Smectite	$K_{0.04}Ca_{0.5}(Al_{2.8}Fe_{0.53}Mg_{0.7})(Si_{7.65}Al_{0.35})O_{20}(OH)_4$	0.0
Kaolinite	$Al_2Si_2O_5(OH)_4$	0.0
Chlorite	$Mg_{2.5}Fe_{2.5}Al_2Si_3O_{10}(OH)_8$	0.0
Albite	$NaAlSi_3O_8$	0.0
Hematite	Fe_2O_3	0.0
Dolomite	$CaMg(CO_3)_2$	0.0
Ankerite	$CaMg_{0.3}Fe_{0.7}(CO_3)_2$	0.0
Dawsonite	$NaAlCO_3(OH)_2$	0.0
Siderite	$FeCO_3$	0.0

a) Biotite is assumed as 50% of Annite and 50% of Phlogopite.

Table 6.5 Kinetic rate parameters of primary and secondary minerals, reactive surface area for the geochemical simulations of the St. John;s CO_2 research site.

Mineral	Neutral Mechanism		Acid Mechanism			Base mechanism			Reactive surface area (cm^2/g)
	logk [a]	E_a [b]	logk [a]	E_a [b]	n [c]	logk [a]	E_a [b]	n [c]	
Primary:									
Quartz	-13.99	87.7	-	-	-	-	-	-	9.8
Oligoclase	-11.84	69.8	-9.67	65.0	0.457	-	-	-	9.8
K-Feldspar	-12.41	38.0	-10.06	51.7	0.500	-21.2	94.1	-0.823	9.8
Annite [d]	-12.55	22.0	-9.84	22.0	0.525	-	-	-	9.8
Phlogopite	-12.40	29.0	-	-	-	-	-	-	9.8
Muscovite	-13.55	22.0	-11.85	22.0	0.370	-14.55	22.0	-0.220	151.6
Secondary:									
Calcite	-5.81	23.5	-0.30	14.4	1.000	-	-	-	9.8
Magnesite	-9.34	23.5	-6.38	14.4	1.000	-	-	-	9.8
Illite[e]	-13.55	22.0	-11.85	22.0	0.370	-14.55	22.0	-0.200	151.6
Smectite	-12.78	35.0	-10.98	23.6	0.340	-16.52	58.9	-0.400	151.6
Kaolinite	-13.16	22.2	-11.31	65.9	0.777	-17.05	17.9	-0.472	151.6
Chlorite	-12.52	88.0	-11.11	88.0	0.500	-	-	-	9.8
Albite	-12.56	69.8	-10.16	65.0	0.457	-15.6	71.0	-0.572	9.8
Hematite	-14.60	66.2	-9.39	66.2	1.000	-	-	-	9.8
Dolomite	-7.53	52.2	-3.19	36.1	0.500	-5.11	34.8	0.500	9.8
Ankerite[f]	-7.53	52.2	-3.19	36.1	0.500	-5.11	34.8	0.500	9.8
Dawsonite	-7.00	62.8	-	-	-	-	-	-	9.8
Siderite	-8.90	62.8	-3.19	36.1	0.500	-	-	-	9.8

Note: Kinetic rate parameters from Palandri and Kharaka (2004);
a) logk: kinetic rate constant k at 25 ^oC ($mol/m^2/s$);
b) E_a: activation energy (KJ/mol);
c) n: power term with respect to H^+;
d) set to Biotite; e) set to Muscovite; f) set to Dolomite

The primary mineral (oligoclase) dissolves from the beginning of CO_2 injection. As indicated by Figure 6.12, simulations results show a general trend of more dissolution in the upper-lying layers and the layer just below the injection/production layer after 30 years CO_2 injection. We infer this to be because water is removed gradually from the layer of injection/production wells and no chemical reactions occur between CO_2 in gas phase (non-aqueous CO_2) and rock minerals. The primary mineral, quartz, may precipitate or dissolve after 30 years (Figure 6.12). The quartz slightly dissolves in water-dominated areas and precipitates in

CO_2-laden areas (Figure 6.12). We infer this to be because the lower pH values in areas reached by CO_2 result in precipitation of quartz; pH values approaching 5.4 in the water-dominated area lead to dissolution of the primary mineral quartz. The distribution of quartz precipitation has similar patterns and characteristics to the mineral oligoclase. The more precipitation of quartz occurs within the upper-lying layers and the layer just below injection/production layer (Figure 6.12).

The mineral calcite precipitates after 1 year CO_2 injection (figure not shown). The calcite precipitation distribution also shows similar patterns to the mineral oligoclase dissolution profile after 30 years. More calcite is precipitated in the upper lying layers and the layer just below injection/production layer (Figure 6.13), tracking the distribution of dissolved CO_2 in aqueous phase. Relatively large illite precipitation also occurs in the same areas with large calicite precipitation, also tracking the dissolved CO_2 in aqueous phase. The characteristics and distributions of dissolution or precipitation for other minerals (e.g., Albite, K-feldspar, Siderite etc.) are similar to trends for oligoclase, calcite, and illite (figures not shown).

Figure 6.14 describes the cumulative CO_2 sequestered by carbonate mineral precipitation for $scCO_2$ as a working fluid after 30 years. The total CO_2 sequestered by carbonate precipitation varies around 1.5-3.0 kg/m^3 in the upper-lying layers, which is much larger than the value of 0.2 kg/m^3 at the injection/production layer. The 3-D distribution of total CO_2 sequestration is identical to the amount consumed by calcite precipitation (Figure 6.13) and to the dissolved aqueous CO_2 amount (Figure 6.13) after 30 years of CO_2 injection. This is consistent with $scCO_2$ in the gas phase mainly occupying the layer of injection/production wells (Figure 6.9) and the two phases of water-gas mixtures exist in the area of the upper-lying layers after 30 years,

resulting in more dissolved CO_2 mass fraction in these area (Figure 6.11). Therefore, more dissolution and precipitation occurs in the upper-lying layers.

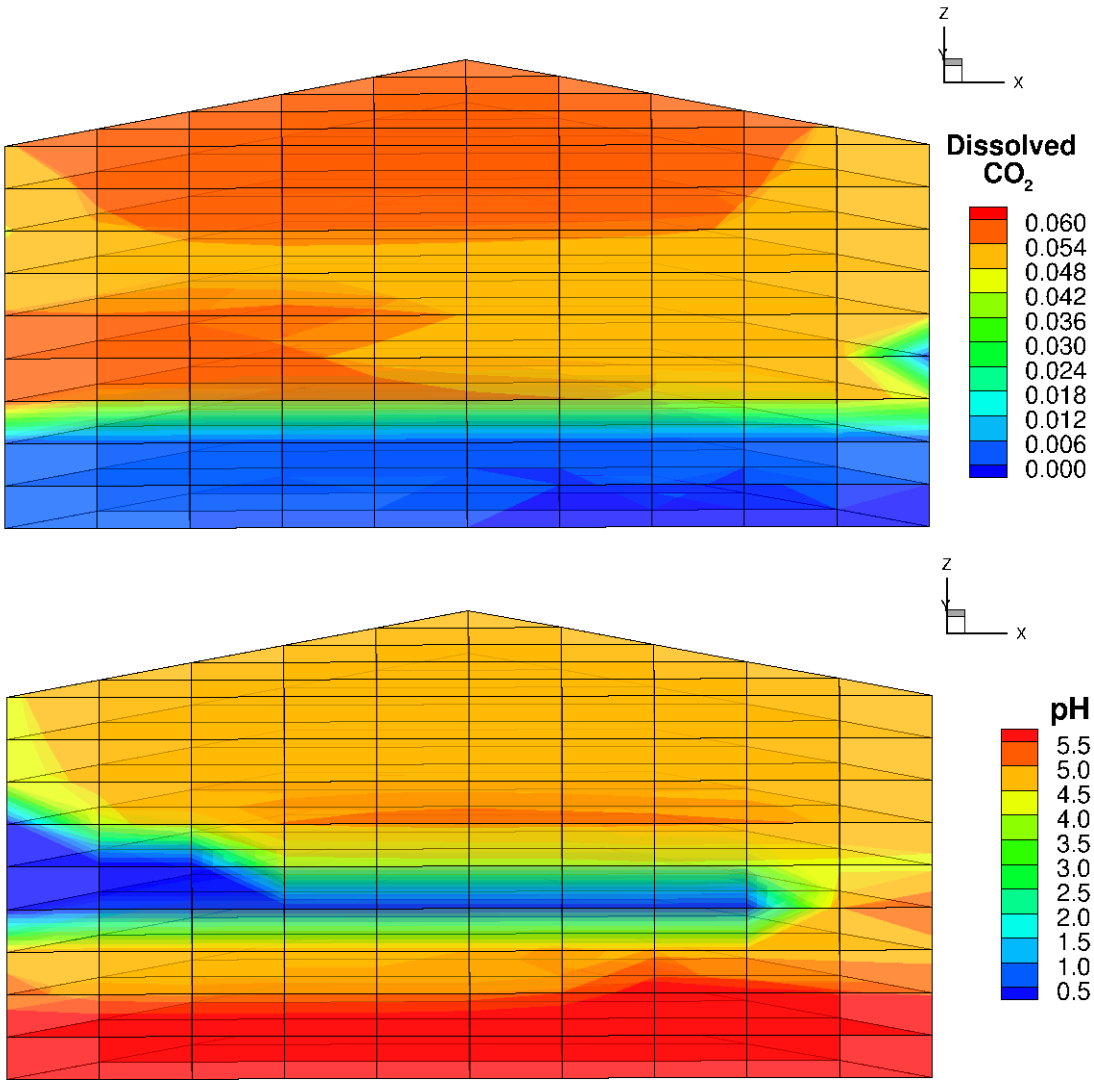

Figure 6.11. Simulated 3-D profiles of dissolved CO_2 mass fraction in aqueous phase and pH values after 30 years injection of $scCO_2$ as a working fluid.

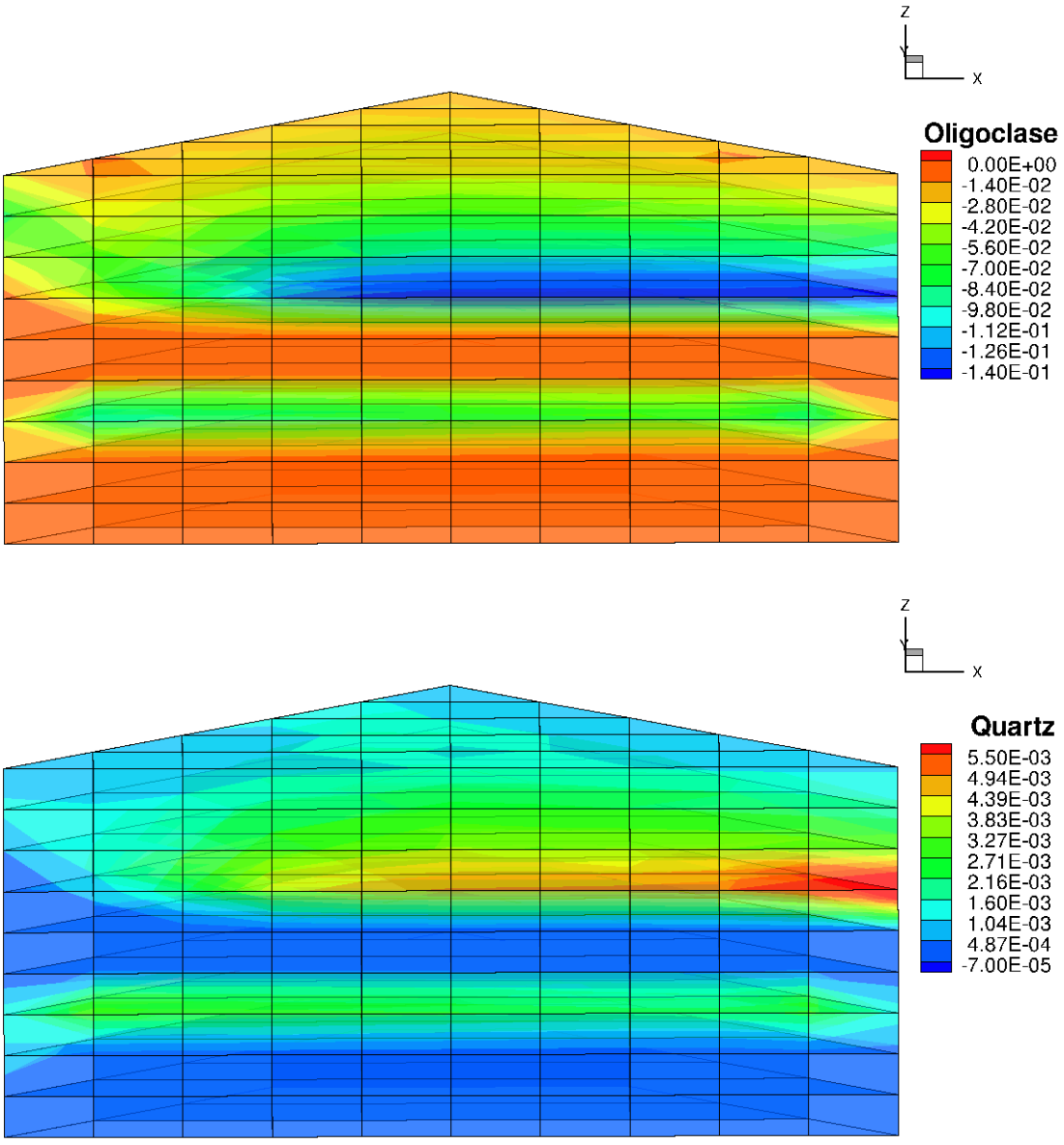

Figure 6.12. Simulated 3-D profiles of changes of mineral abundance (in volume fraction) for primary minerals (Oligoclase and quartz) after 30 years injection of $scCO_2$ as a working fluid.

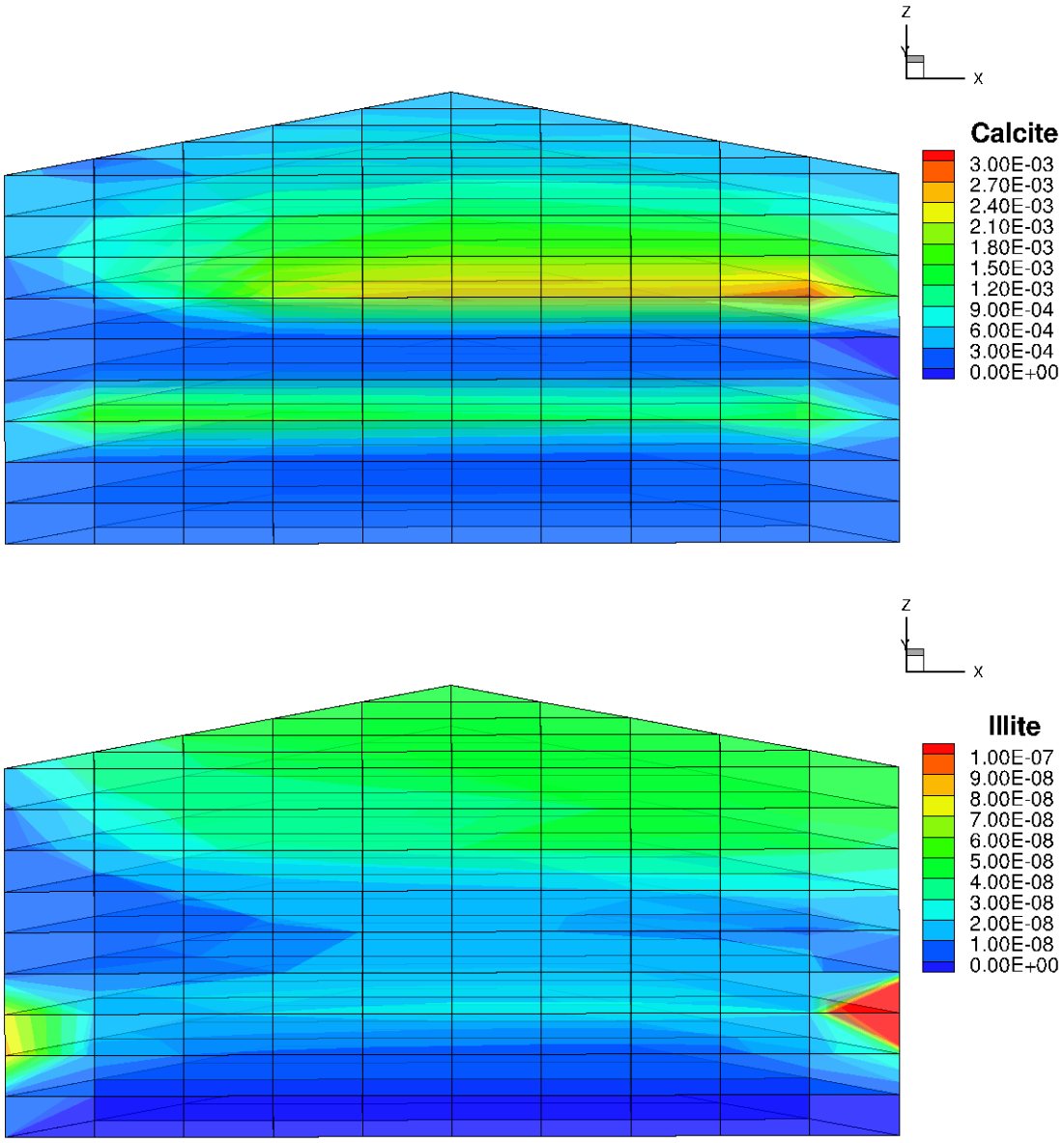

Figure 6.13. Simulated 3-D profiles of changes of mineral abundance (in volume fraction) for secondary minerals (Calcite and Illite) after 30 years injection of $scCO_2$ as a working fluid.

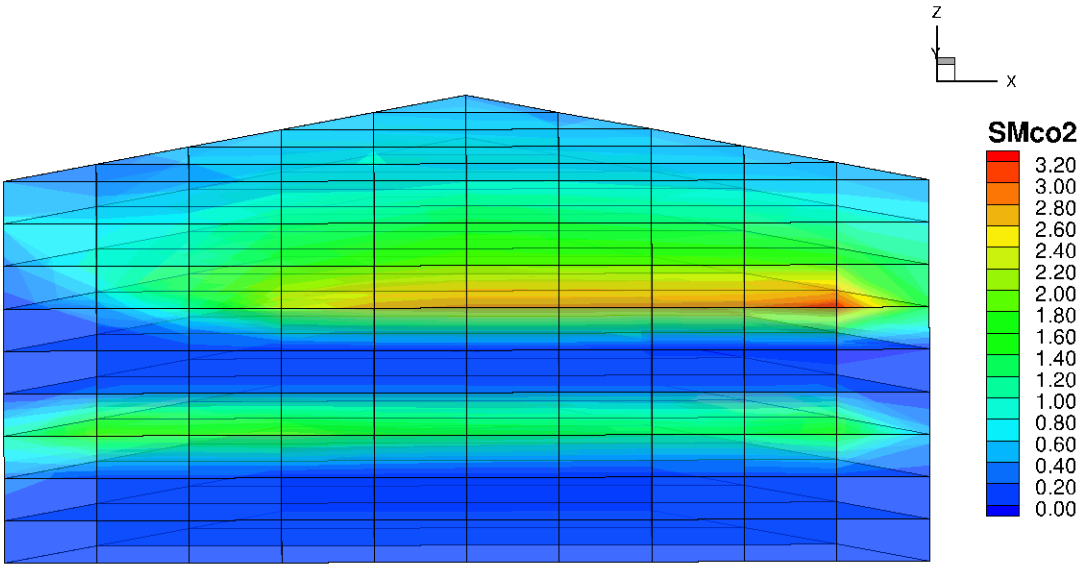

Figure 6.14. Simulated 3-D profile of cumulative CO_2 sequestered (kg/m^3) by carbonate mineral precipitation after 30 years injection of $scCO_2$ as a working fluid.

6.3.3 3-D Geochemical Simulation for $scCO_2$ as a Working Fluid using PFLOTRAN Simulator

Using the model domain described in Section 5.3, we performed a simulation to evaluate geochemical interactions of CO_2 with rock. The flow properties used for the simulation are detailed in Table 5.16, except that porosity was set to a uniform value of 0.15. The simulation was run for 50 years with 18x10x10 grid cells on 4 processors. CO_2 was injected at the rate of 50 kg/s. No-flow boundary conditions were applied at all boundaries. The chemical composition involved the primary species: Al+++, Na+, Ca++, Mg++, H+, K+, CO_2(aq), SiO_2(aq), Cl-, SO_4--. The mixture density for CO_2 dissolved in NaCl is taken from Duan et al. (2008), using the Span-Wagner equation of state for $ScCO_2$ (Span and Wagner 1996). The mineral composition included Quartz, K-Feldspar, Calcite, Kaolinite, Dolomite, Plagioclase, Magnesite, Illite, Dawsonite, Gypsum, and Alunite.

The initial fluid composition as well as the mineral composition was taken from Table 1 of Moore et al. (2005). Surface area for all minerals was set to $100m^{-1}$. Table 6.6 lists the rate constants, activation energy and initial volume fractions used in the simulation. The initial fluid composition was set as follows: Al+++ was in equilibrium with Illite, Na+ had a total concentration of 0.018 mol/L, Ca++ was in equilibrium with Calcite, Mg++ was in equilibrium with Dolomite, pH was set to 7, K+ was in equilibrium with K-Feldspar, CO_2(aq) was in equilibrium with $ScCO_2$, SiO_2(aq) was in equilibrium with Quartz, SO_4-- was in equilibrium with Gypsum and Cl- was set to maintain charge balance.

Table 6.6 Mineral rate constants, activation energy and initial volume fraction.

Mineral	Rate constant (if <0, log of rate constant)	Activation energy	Initial volume fraction
Calcite	-5.81	23.5	0.01
K-Feldspar	-12.41d0	38	0.1275
Dolomite	-8.60	95.3	0.085
Kaolinite	-13.18	22.0	0
Plagioclase	-11.0	-	0.085
Magnesite	4.57e-10	-	0
Illite	1.6596e-13	-	0.1275
Quartz	1.e-14	-	0.415
Dawsonite	1.259d-9	-	0
Gypsum	-4.0	-	0
Alunite	-12.0	-	0

Figure 6.15 shows the CO_2 saturation distribution in the domain at different times and shows the movement of CO_2 from the injection well to the production well, as well as how CO_2 rises to the top of the domain due to buoyancy, with concomitant reservoir cooling (Figure 6.16). The acidification of the domain due to CO_2 can be seen in Figure 6.17, where the pH in the CO_2 path from the injection well to the production well decreases with time; the region around the production well becomes basic due to removal of CO_2. Additionally, along the flow path from injection to production well, quartz is precipitated as illustrated in Figure 6.18; plagioclase is precipitated (Figure 6.19) and Illite dissolves (Figure 6.20).

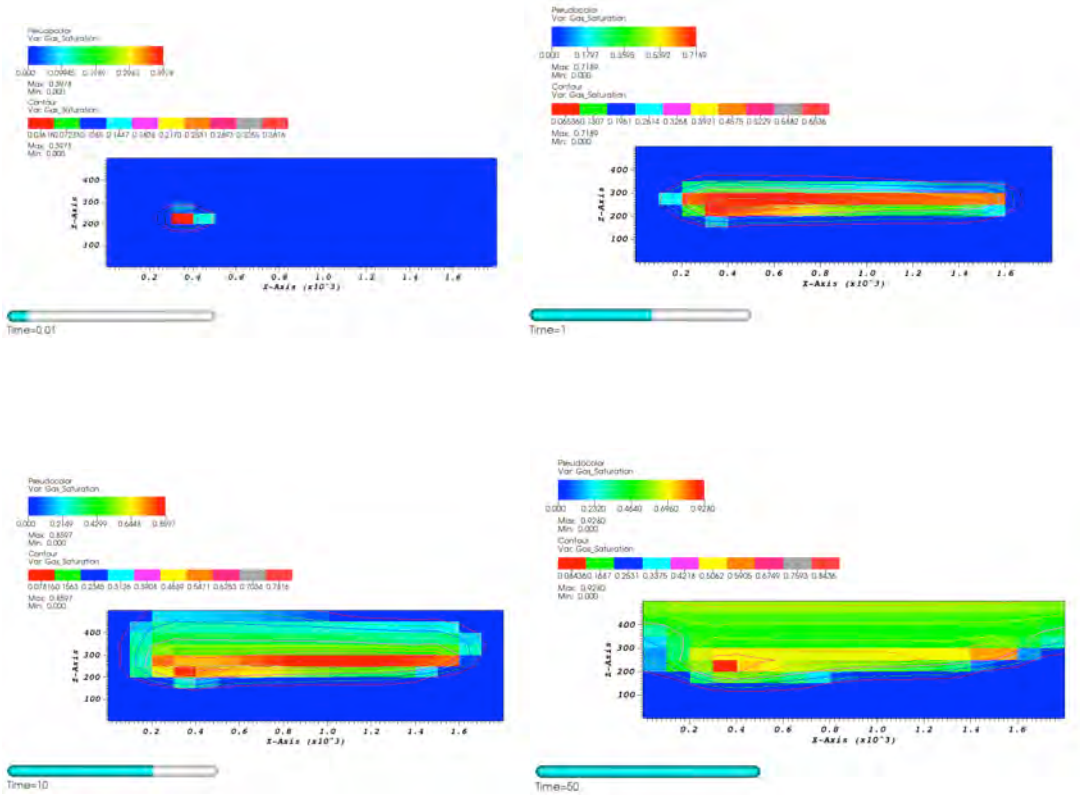

Figure 6.15. Simulated CO_2 saturation profiles at 0.01, 1, 10 and 50 years in the model cross-section at y = 250m.

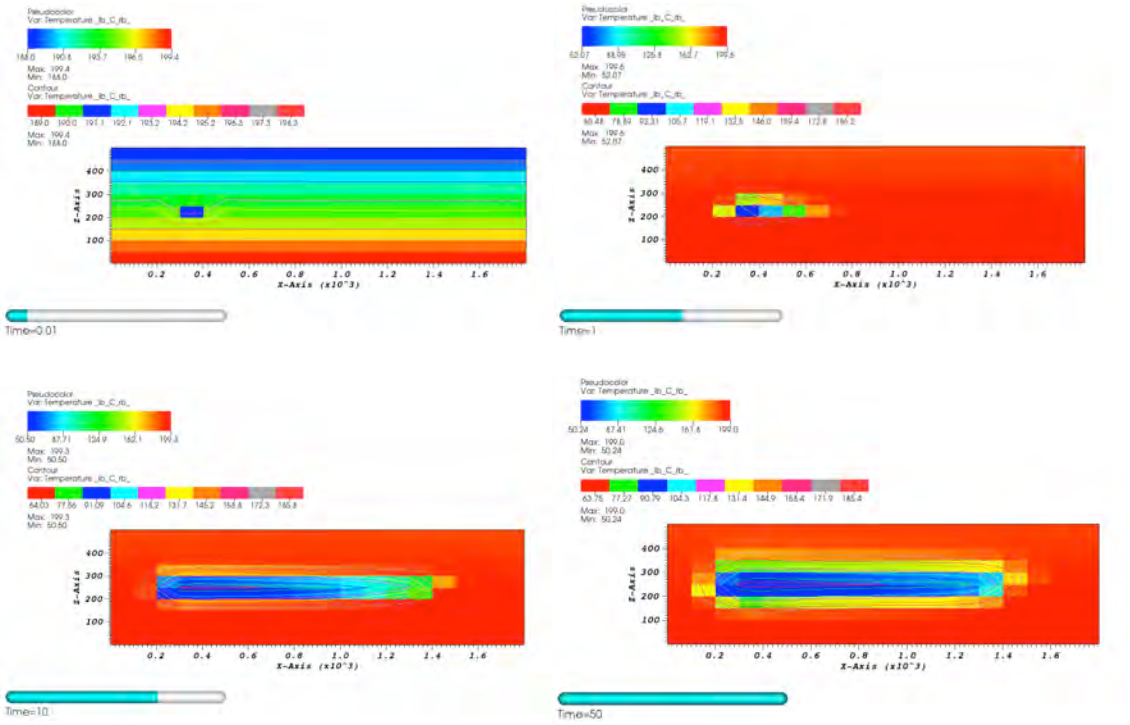

Figure 6.16. Simulated temperature in the domain at 0.01, 1, 10 and 50 years in the cross-section model at y = 250m.

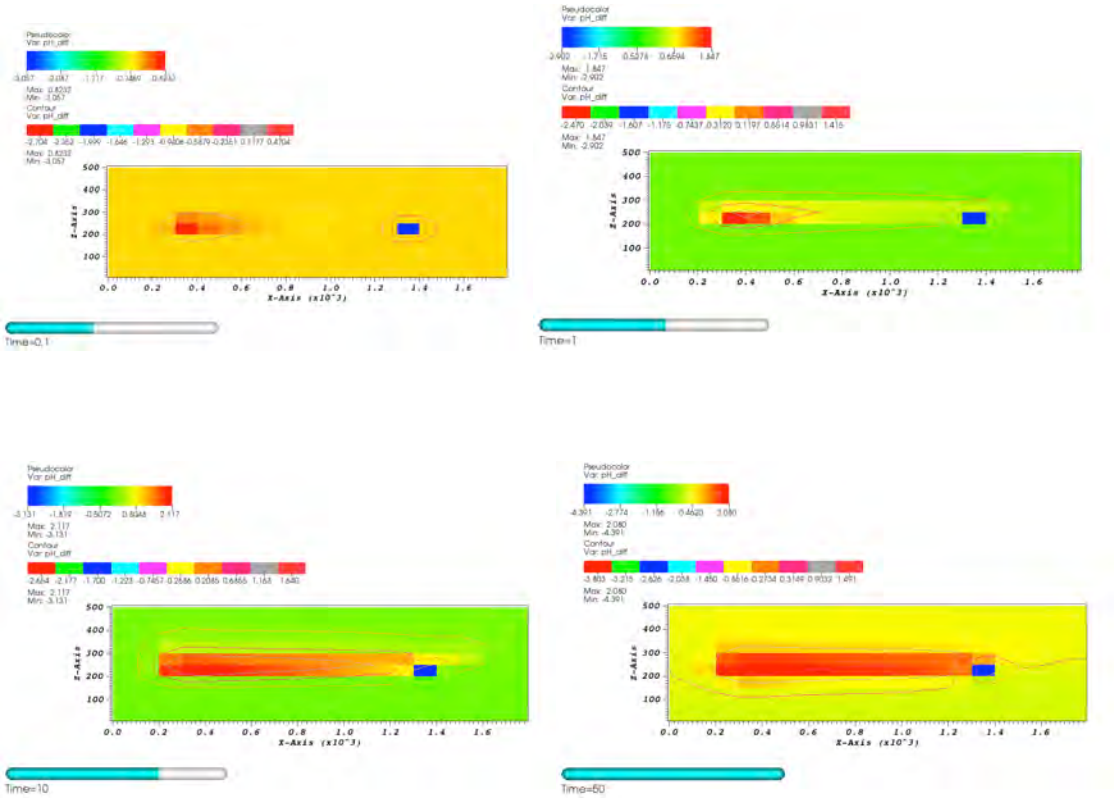

Figure 6.17. Simulated pH difference compared to t=0 at 0.1, 1, 10 and 50 years in the model cross-section at y = 250m.

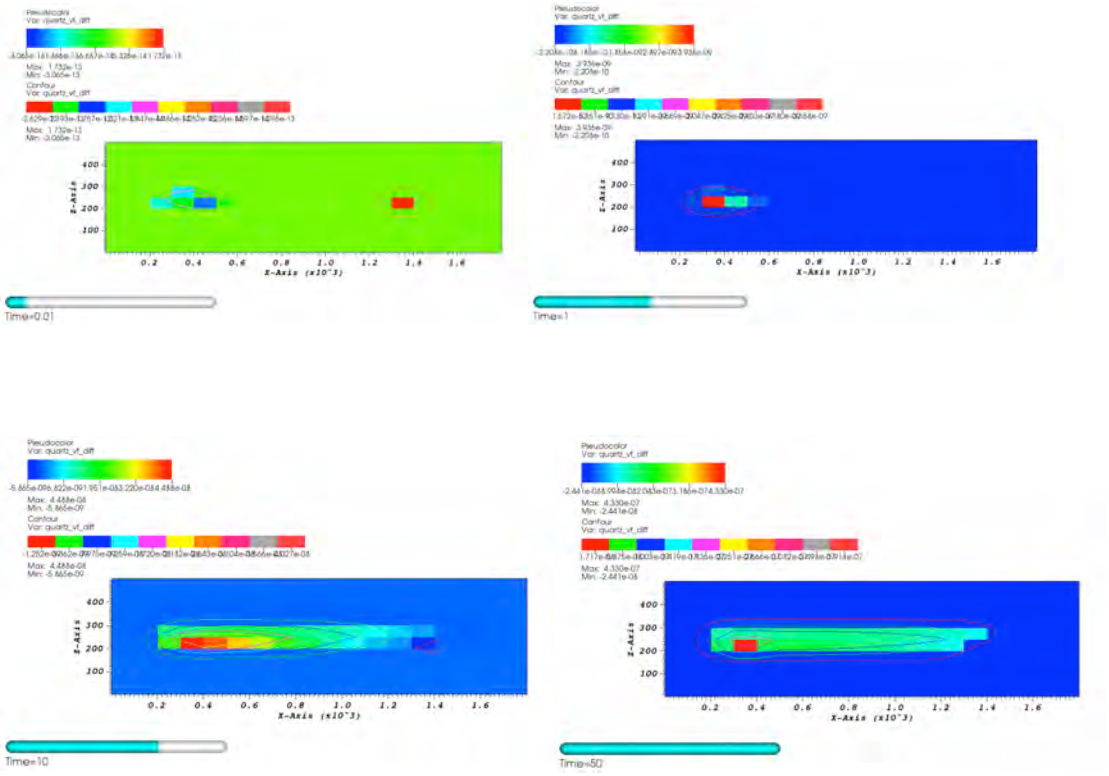

Figure 6.18. Simulated Quartz volume fraction difference compared to t=0 at 0.01, 1, 10 and 50 years in the model cross-section at y = 250m.

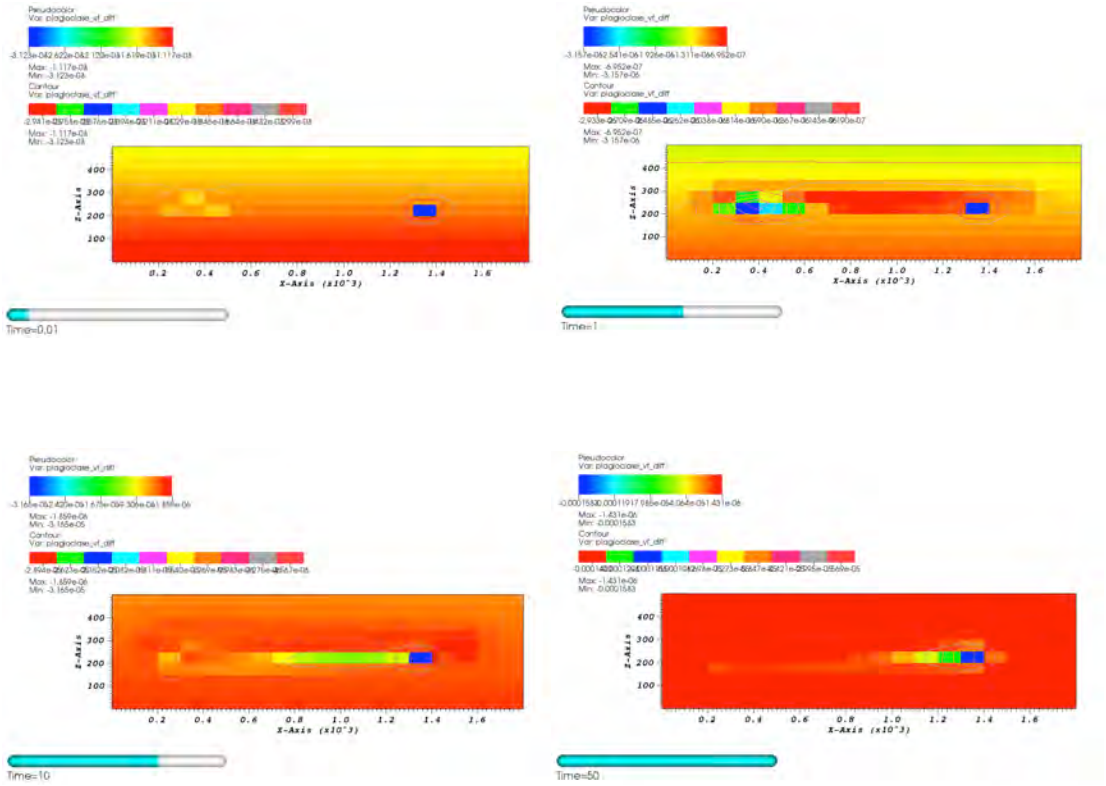

Figure 6.19. Simulated Plagioclase volume fraction difference compared to t=0 profiles at 0.01, 1, 10 and 50 years in the model cross-section at y = 250m.

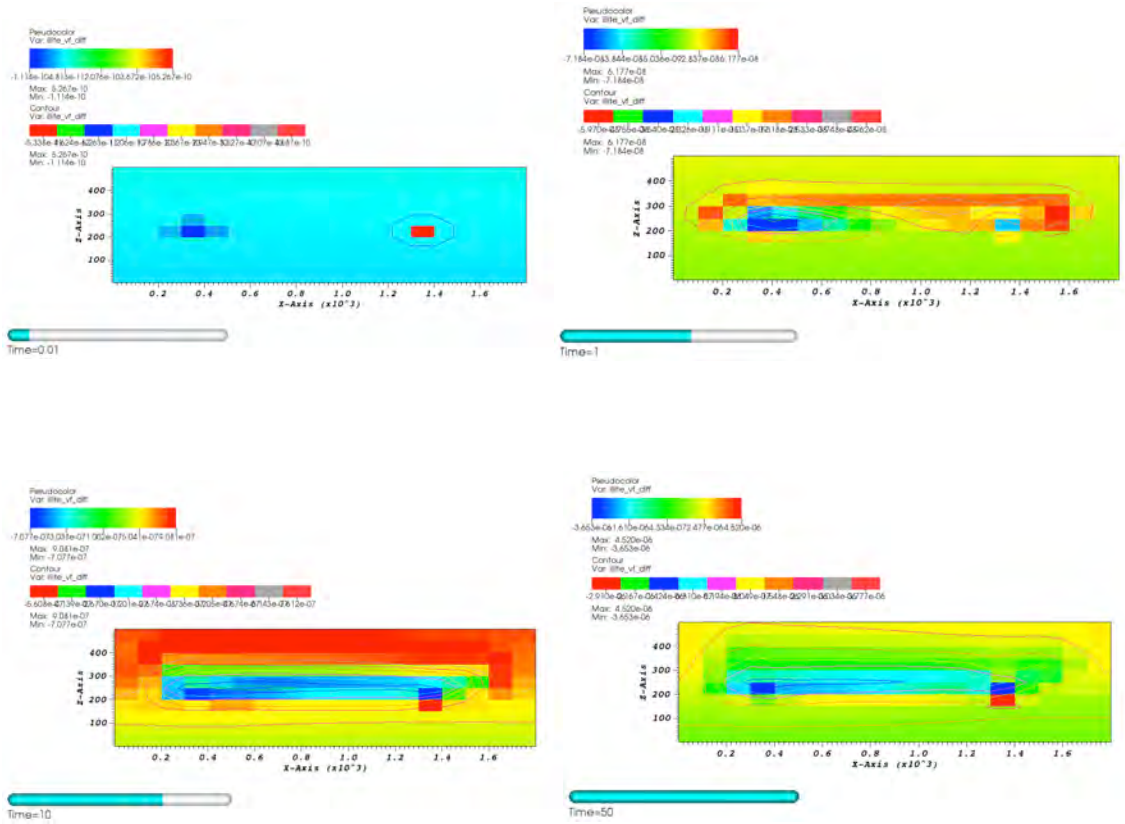

Figure 6.20. Simulated Illite volume fraction difference compared to t=0 at 0.01, 1, 10 and 50 years in the model cross-section at y = 250m.

Figure 6.21 shows the amount of CO_2 that is sequestered in this system with time, suggesting that up to 7 Mt can be sequestered simultaneously along with energy production (peak of 40MW) over a period of 50 years. The CO_2 that is sequestered dissolves in brine over time, while some remains in the supercritical phase and the remaining aqueous CO_2 reacts with existing minerals.

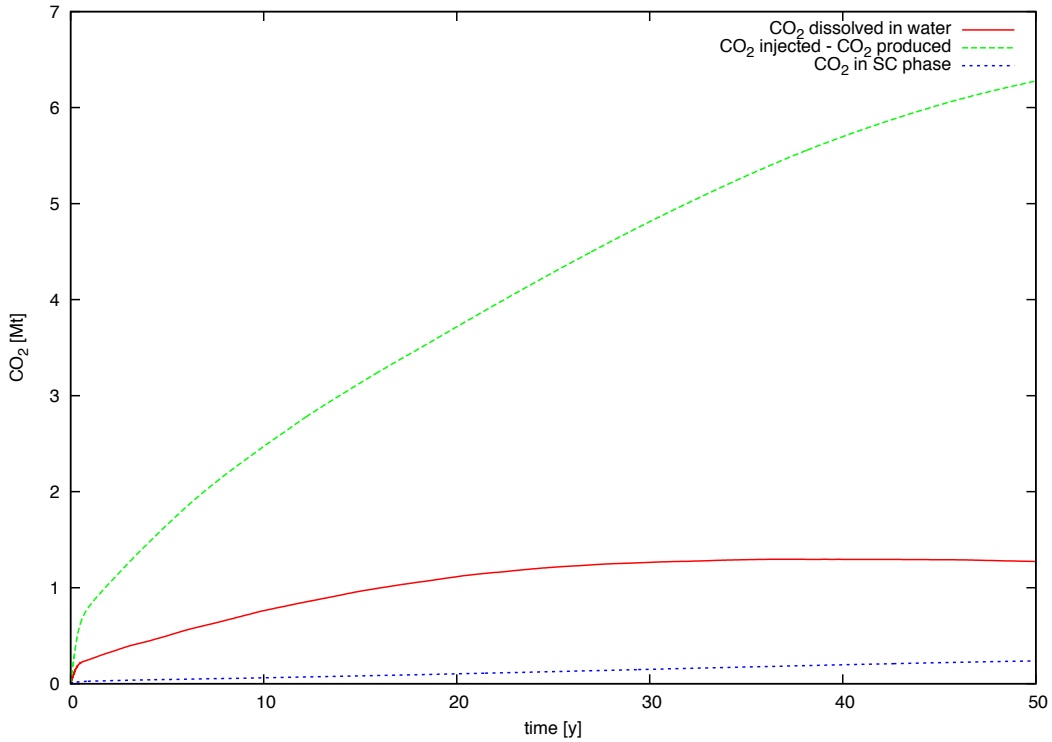

Figure 6.21. Amount of CO_2 injected minus CO_2 produced, calculated as the amount that is permanently sequestered. The amount of CO_2 that is dissolved in water and the amount of CO_2 that remains in the supercritical phase are also shown.

7. Investigate Mineral Precipitation in EGS Surface Facilities

During geothermal energy extraction, some dissolved minerals may precipitate because of temperature and/or pressure drops in the extraction wells and surface facilities (e.g., heat exchangers). In this section, we use a simple 1-D model to analyze the possible extent of mineral and saline precipitation in the production wells and surface heat exchangers.

We set up a 1-D vertical model to represent the geothermal heat pump system. The total depth of the 1-D model is set as 2000 m with each grid sized at 50 m. The heat exchanger is located at the surface and the production well is at the depth of 2000 m. A Dirichlet condition (constant pressure) was assigned to the top and bottom of the model. The initial pressure and temperature are set as hydrostatic pressure and 200 ^{o}C, respectively. To drive the aqueous-gas phase flow of water-CO_2 mixture from the production well to the heat exchanger, the pressure at the production well is set at an initial pressure of 5 bars. The inlet temperature of the heat exchanger is set at 50 ^{o}C. The initial aqueous solutions are obtained from previous geochemical simulations (described in Section 6.3.2). We employed the TOUGHREACT simulator to perform the 1-D simulation for a simulated period of 30 years, to evaluate the full history of pressure and temperature changes, and resulting possible extent of mineral precipitation from production wells to the surface heat exchangers.

Figure 7.1 plots the pressure and temperature changes over time in the production well and the surface heat exchanger. The pressure and temperature almost remain constant at the production well. The temperature at the surface heat exchanger decreases gradually over 30 years from 200 ^{o}C to 163 ^{o}C. This is due to heat extraction at the heat exchanger. Such changes of temperature could lead to the mineral and saline precipitation. Figure 7.2 shows the salt mass fraction (X_{NaCl}) and changes of mineral abundances for quartz over time at the production well

and the surface heat exchanger. Results shown in Figure 7.2 suggest that the values of salt mass fraction at both production well and heat exchanger maintain a constant level over time. No halite is precipitated in these simulations. A small amount of quartz is precipitated at 13.5 years of simulation in the heat exchanger. The quartz precipitation continuously increases through the end of the 30-year simulations. No simulated mineral precipitation was observed at the production well throughout the simulation time. Mineral precipitation at the heat exchanger could decrease the efficiency of heat extraction.

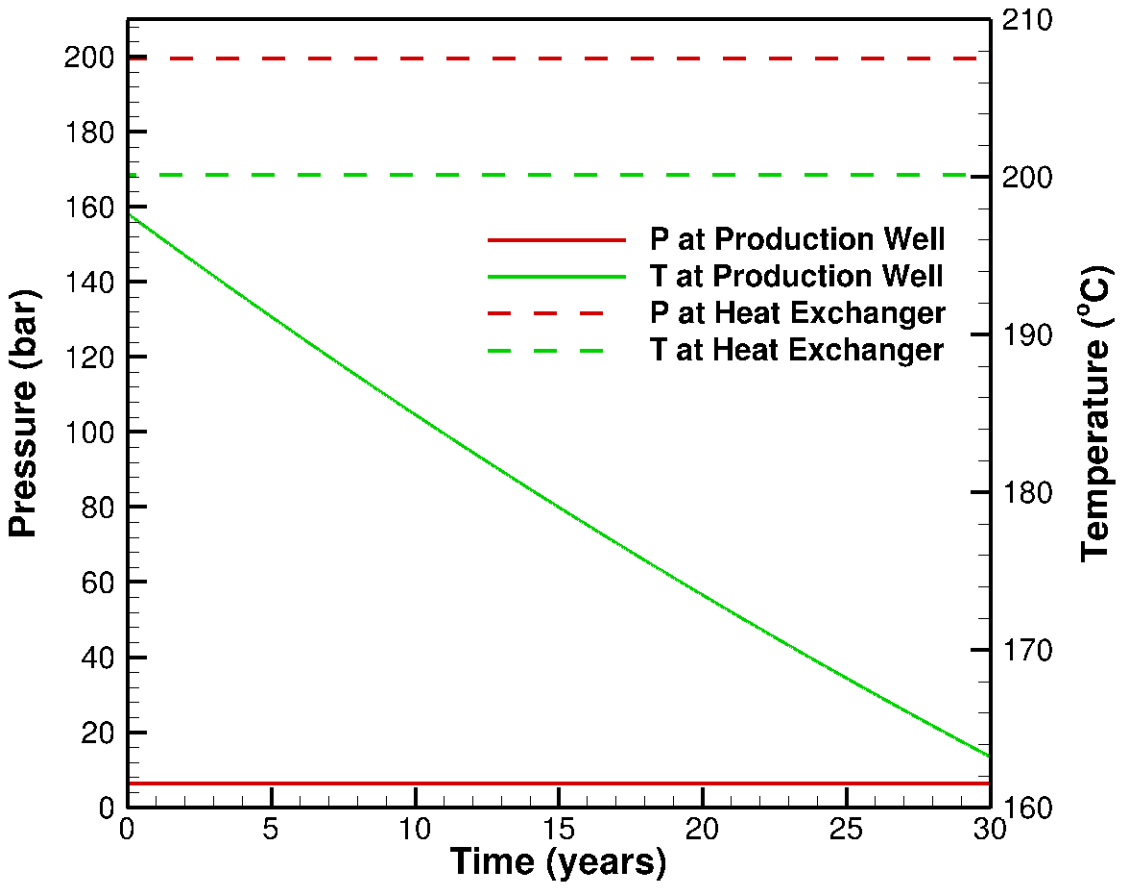

Figure 7.1. Simulated pressure and temperature over time at the production well and surface heat exchanger.

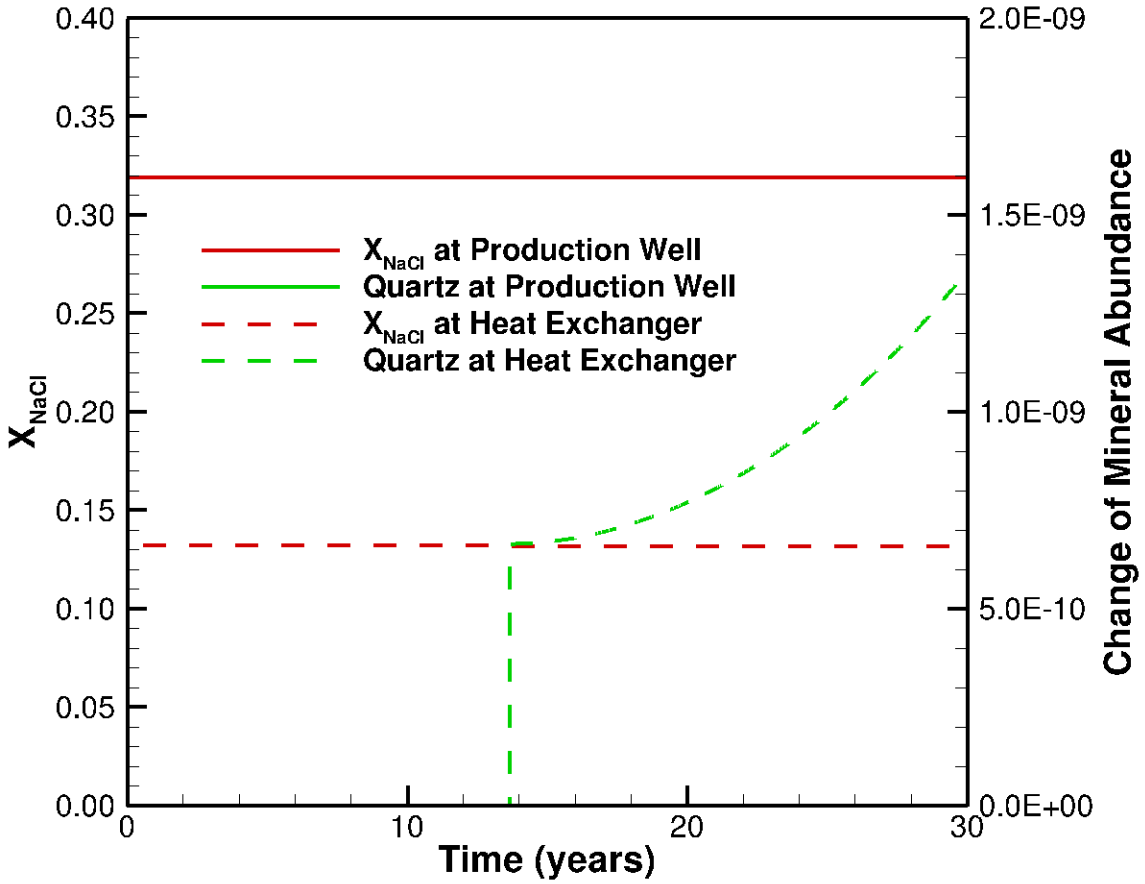

Figure 7.2. Simulated salt mass fraction (X_{NaCl}) and change of mineral abundance (in volume fraction) for quartz over time at the production well and surface heat exchanger.

8. Summary and Conclusions

8.1. Salient Conclusions of Experimental Results

Experimental results establish reactions in systems containing multi-component water-granite ± epidote ± $scCO_2$ at typical granite-hosted geothermal conditions of 250 °C and 25-45 MPa. At high water/rock ratios and relatively high silica activities, initial reactant minerals altered to illite ± smectite ± zeolite. Feldspar and epidote were the most reactive minerals. Reaction progress was incomplete, but meaningfully modeled with activity-activity diagrams. An integrated data analysis and comparison between experimental results, theoretical results, and natural systems helps define the implications of the study in the context of commercial geothermal operations and carbon sequestration projects. Results and implications follow.

1) Activity-activity diagrams provide a mechanism for determining the path towards and extent of equilibrium within each experiment. Fluid-rock interactions do not achieve the predicted equilibrium states.
2) Smectite, not carbonate, precipitates in experimental systems after injection of $scCO_2$.
3) With the exception of smectite, the secondary minerals in our experiments coincide with those found in natural systems and corroborate metasomatic processes in fluid-dominated systems. Experimental illite and smectite occurrences and morphologies indicate that temperature may not always dictate their stability and that clays can form directly from solution.
4) Experiments have relatively high silica activities as mediated by the Ostwald step rule. Prediction of metastable chalcedony in our experiments validates high temperature, metastable silica phases as sometimes observed in natural systems and commercial geothermal operations. This observation confirms incomplete reaction progress.

5) Results validate observations from natural systems such as acid alteration of felsic systems, the buffering capacity of granitic rocks, metastable argillic mineralization in zoned veins, and temperature/CO_2 conditions for tungsten ore formation.
6) Experimental smectite is observed and sometimes predicted thermodynamically at temperatures >180-220 °C. At these temperatures, however, smectite is not observed in natural systems. This variance may result from kinetics, extent of thermodynamic equilibrium, incomplete thermodynamic data, water:rock ratio and/or silica activity.
7) Stable or metastable clay precipitation is likely in commercial, granite-hosted geothermal systems. Illite may be the dominant clay in water-based geothermal operations (i.e., traditional operations), whereas smectite may be the dominant clay in CO_2-based geothermal operations (i.e., EGS or CPG). Subsequent porosity and permeability changes need to be well understood and addressed to optimize system functionality.
8) Carbonate formation, as desired for carbon sequestration projects (traditional, EGS, or CPG), may require extended periods of time to overcome kinetic barriers. Although the mineral trapping mechanisms may be slow, dissolution trapping of carbon species is fast (days), and is a reasonable mechanism for sequestration in these systems.
9) Parameters such as reaction progress, water:rock ratio, and silica activity may have significant effect on the aqueous geochemistry and mineralogy as observed or predicted in experimental, theoretical, or natural systems. These are not new concepts, but they are often overlooked in experimental studies. We should be mindful to consider them and how we apply experimental or theoretical results to natural systems or applied problems.
10) Within the broad area depicted for waters sampled from geothermal fields, however, calcium/proton and magnesium/proton activity in our experiments appear to be controlled by

metastable smectities as opposed to chlorite. This relationship suggests that aspects of field geochemistry (e.g., calcium/proton and magnesium/proton activity) in geothermal and hydrothermal systems are controlled by alteration minerals assemblages as opposed to primary granite minerals.

8.2. Salient Conclusions of Simulation Results

Proposed and executed code modification included implementation of a new (developed by this project team) database into the PFLOTRAN and TOUGHREACT codes, and massively parallel implementation of multiple-continuum features into the PFLOTRAN code to facilitate simulation of heat transfer and reactive transport in fractured porous media. Specific code modification work completed includes:

1) A new thermodynamics database for elevated pressure and temperature; results of associated simulations suggest that proper simulation of high pressure and temperature produces significantly different mineral dissolution and precipitation results compared to those associated with the original (standard) database.
2) A new dual-continuum model for both heat transfer as well as for reactive transport was coded and added to PFLOTRAN. For the case of reactive transport we started with single component scenario.
3) Benchmark tests were performed to ensure that the dual-continuum formulation was implemented correctly.
4) Parallel scalability was analyzed for the dual-continuum formulation to test the performance of the algorithms developed and applied.
5) Using the dual-continuum formulation implemented in PFLOTRAN, simulations were performed for an EGS model domain and the results were compared to dual-continuum

results from TOUGH2. The comparison was encouraging with minor differences due to differences in how the algorithms were implemented.

6) To check for proper convergence of solutions, a grid refinement study was performed. The net power production was not affected much by grid refinement, although temperature and pressure values were affected.

A total of 12 batch experiments were simulated, with the selections of water-granite ± epidote ± Calcite ± Chlorite ± $scCO_2$. We coupled a parameter estimation tool (iTOUGH2-PEST) with TOUGHREACT to mimic the batch experiments for calibration of mineral kinetic rate constants and reactive surface area against major cation concentrations. The following conclusions can be drawn based on the calibration results:

1) Overall, the simulated major cation concentrations for the experiments without CO_2 injection have better agreement with measured values than simulations of experiments with CO_2 injection.
2) The calibrated kinetic rate constants are 5 to 180 times larger than literature values of K-feldspar and the calibrated reactive surface area are also 2 to 5 times larger than the BET measured values for K-feldspar. This is due to the mineral surface area being measured based on unreacted powders by BET after experiments completed. A longer reaction period may be necessary for batch experiments to provide more effective calibration of mineral reactive surface areas and kinetic parameters.
3) Simulated pH values for calibrations generally exhibit good agreement with measured values, indicating that such calibration of mineral kinetic rate constants and reactive surface areas may improve batch simulations for high pressure and temperature conditions. Calibrated

kinetic parameters can also be used for related geochemical simulations in EGS reservoirs of elevated temperature.

The general objective of the model simulations executed here was to assess the application of CO_2 as a working fluid in EGS reservoirs, and to investigate its effects on energy extraction, geochemical reaction with rocks, carbon sequestration, and risk assessment. We designed 2-D and 3-D numerical models with generic 2-spot well patterns to evaluate the performance of several attributes of EGS reservoirs, including energy extraction, geological CO_2 sequestration, and risk of CO_2 leakage. We compared flow, heat and chemical reaction results for CO_2 as a working fluid with results for water as a working fluid. We also set up a field-scale model to evaluate EGS conditions and implications for the St. John's Dome CO_2-EGS research site, and to evaluate the effects of CO_2 as a working fluid on flow, heat extraction, geochemical processes of CO_2-rock-fluid interaction, and carbon sequestration at field scale.

The following conclusions are drawn based on these specific simulation results:

1) The net heat extraction and mass flow production rate for $scCO_2$ as a working fluid were much larger compared to water as a working fluid, indicating $scCO_2$ as a working fluid may enhance EGS heat extraction;
2) Pressure drops between injection and production wells have significant impacts on net heat extraction, mass flow rate and temperature. The effects of initial salinity on heat extraction are significant at the early stages of simulation and are very little after 4 years of CO_2 injection, in general.

3) Simulated CO_2 saturation contours indicate that CO_2 breakthrough in caprock may constitute a significant risk of CO_2 leakage, at least for the specific case of the St. John Dome CO_2-EGS research site.
4) Simulated aqueous CO_2 at the upper- and lower-lying layers is greater than that in the injection/production layer, which induces lower pH values and more dissolution and precipitation of minerals in the upper- and lower-lying layers of the system.
5) Precipitation of carbonate minerals in the upper-lying layers suggests favorable CO_2 storage (with respect to mineral trapping) in EGS reservoirs.

8.3. Comparison of Actual Accomplishments with the Goals and Objectives of the Project

The original specific goals and objectives of the project include the following, and underneath each heading are detailed the actual results.

1) Objective/goal: to improve thermodynamic databases to include wider temperature and pressure ranges than those currently available in existing simulators for application to geothermal reservoirs. Actual accomplishment: The newly developed thermodynamic database for elevated temperature / pressure and its implementation into the PFLOTRAN and TOUGHREACT models included wider temperature and pressure ranges appropriate for simulation analysis of EGS reservoirs.

2) Objective/goal: to determine applicable chemical reactions between water, rock, and $scCO_2$ through thermodynamics analyses. Actual accomplishment: we extended our new database to include chemical equilibrium constants for the wider temperature and pressure range. We selected mineral and aqueous species common to EGS reservoirs listed (see Table 3.1), and gathered and compared possible mineral and aqueous reactions from the SUPCRT92 and EQ3/6 databases.

3) Objective/goal: to estimate respective kinetic rates of chemical reactions. Actual accomplishment: a total of 12 batch experiments with the selections of water-granite ± epidote ± Calcite ± Chlorite ± $scCO_2$ were conducted. We then used a parameter estimation tool (iTOUGH2-PEST) with TOUGHREACT to replicate and interpret these batch experiments for calibration of mineral kinetic rate constants and reactive surface areas against major cation concentrations.

4) Objective/goal: to evaluate water/brine displacement by $scCO_2$, water recharge, geochemical reaction processes and effects on EGS reservoirs by lab- and field-scale numerical simulations. Actual accomplishment: Both 2-D and 3-D conceptual and field-scale models simulations were developed and used to assess application of CO_2 as a working fluid in EGS reservoirs, including geochemical reaction with reservoir strata and associated impacts.

5) Objective/goal: to investigate mineral precipitation in EGS surface facilities. Actual accomplishment: A generalized simulation was conducted to evaluate possible mineral and saline precipitation and associated effects on production wells and EGS surface facilities.

6) Objective/goal: to assess CO_2 leakage risk and the possibility of concurrent geothermal energy extraction and carbon sequestration. Actual accomplishment: Both 2-D and 3-D conceptual and field-scale models simulations were developed and used to assess application of CO_2 as a working fluid in EGS reservoirs, including net potential carbon sequestration and assessment of associated risks.

7) Objective/goal: to investigate the possibility of using $scCO_2$ as an acidization agent in EGS reservoirs. Actual accomplishment: Both 2-D and 3-D conceptual and field-scale models simulations were developed and used to assess application of CO_2 as a working fluid in EGS reservoirs, including use of that CO_2 as an acidization agent.

.In summary, the accomplishments of this project including the database, batch experiments, and modeling simulations met the original goals and objectives of the project.

8.4. Brief Summary of Project Activities

The project team developed an advanced chemical kinetic model for evaluating important processes in EGS reservoirs, such as mineral precipitation and dissolution at elevated temperature and pressure, and for evaluating impacts on EGS surface facilities of related chemical processes. We assembled a new database for better-calibrated simulation of water/brine/ rock/CO_2 interactions in EGS reservoirs. This database utilizes existing kinetic and other chemical data, and we updated those data to reflect corrections for elevated temperature and pressure conditions of EGS reservoirs. We designed and deployed an aggressive laboratory experimental/testing program to produce new (original) data. The experimental data are tailored for an "archetype" granite, representative of a typical host rock of EGS reservoirs, and "archetype" reservoir brines. We also evaluated aqueous geochemistry and mineralogical relationships in water-granite ± CO_2, water-epidote-granite ± CO_2, water-chlorite-granite ± CO_2, water-calcite-granite ± CO_2, and water-epidote-calcite-chlorite-granite ± CO_2 systems at 250°C and 25-45 MPa based on the new experimental data. Granite, epidote-granite, calcite-granite, and chlorite-granite experiments provide a baseline understanding of fluid-rock interactions in fresh rock and altered rock, respectively. The epidote-granite, calcite-granite, and chlorite-granite experiments specifically simulate fluid-rock interactions in EGS reservoirs stimulated by fracturing along pre-existing zones of weakness (i.e., epidote and/or calcite veins) and in pervasively altered granitic rocks (i.e., chlorite and/or epidote alteration). We conducted core-scale and EGS-reservoir scale reactive-transport simulations by implementing the databases in modified versions of the TOUGHREACT and PFLOTRAN codes. A dual-continuum feature for

fracture flow and reactive transport was also added to the PFLOTRAN model. Then, we conducted batch simulations to mimic the experimental data for calibration of kinetic rate constants and reactive surface area of minerals using a publicly-available coupled parameter estimation tool (iTOUGH2-PEST) with the TOUGHREACT code. We also designed and developed simplified numerical simulations of a "generalized" EGS reservoir (e.g., 2-spot and 5-spot well patterns) to explore the possible effects of $scCO_2$ interactions with EGS reservoir rocks, which include the investigation of suitable conditions for CO_2 as a working fluid in EGS reservoirs or $CO_2^{\text{EGS-Working Fluid}}$, optimization of geothermal heat extraction efficiency for $CO_2^{\text{EGS-Working Fluid}}$, and assessment of CO_2 leakage risk and possibility of concurrent carbon sequestration. We developed a field-scale model to emulate approximate conditions of St. John's Dome CO_2-EGS site, and to evaluate the effects of CO_2 as a working fluid on system flow, heat extraction, geochemical processes of CO_2-rock-fluid interaction, and possible carbon sequestration at that field scale. Finally, we conducted a simplified 1-D simulation to investigate mineral and saline precipitation on the production wells and EGS surface facilities.

9. References

Abercrombie H. J., Hutcheon I. E., Bloch J. D. and de Caritat, P. (1994) Silica activity and the smectite-illite reaction. *Geology* **22**, 539-542.

Anderson, G.M., Castet, S., Schott, J., and Mesmer, R.E. (1991) The density model for estimations of thermodynamic parameters of reactions at high temperatures and pressure. *Geochemical et Geochemical et Cosmochimica Acta*, **55**, 1769-1779.

André L., Audigane P., Azaroual M. and Menjoz A. (2007) Numerical modeling of fluid-rock chemical interactions at the supercritical CO_2-liquid interface during CO_2 injection into a

carbonate reservoir, the Dogger aquifer (Paris Basin, France). *Energy Conversion & Management* **48**, 1782-1797.

Azaroual M. and Fouillac C. (1997) Experimental study and modelling of granite-distilled water interactions at 180 °C and 14 bars. *Appl. Geochem.* **12**, 55-73.

Baker E. J., Burgess J. E., Brukin A. R. and Monhemius A. J. (1985) Leaching of Carnmenellis granite in brines at 300° and 350°C. In *High Heat Production (HHP) Granites,*

Baldeyrou A., Vidal O. and Fritz, B. (2003) Experimental study of phase transformations in a thermal gradient: application to the Soultz-sous-Forêts granite (France). *C. R. Geoscience* **335**, 371-380.

Beaufort D., Papapanagiotou P., Fujimoto K., Patrier P. and Kasai K. (1995) High temperature smectites in active geothermal systems. In *Water-Rock Interaction* (eds. Y. K. Kharaka and O. V. Chudaev). A. A. Balkema, Rotterdam, Netherlands. pp. 493-496.

Benson S. and Cook P. (2005) Underground geological storage. In *IPCC Special Report on Carbon Dioxide Capture and Storage*. Intergovernmental Panel on Climate Change, Interlaken, Switzerland. pp. 5.1-5.134 (Chapter 5).

Best M. G. (1995) *Igneous and Metamorphic Petrology*. Blackwell Science, Cambridge, MA.

Bethke C. M. and Yeakel S. (2009) *The Geochemist's Workbench Release 8.0: Reaction Modeling Guide*. University of Illinois, Champaign, Illinois.

Bethke C. M., Vergo N. and Altaner S. P. (1986) Pathways of smectite illitization. *Clays Clay Min.* **34**, 125-135.

Bischoff J. L. and Rosenbauer R. J. (1996). The alteration of rhyolite in CO_2 charged water at 200 and 350ºC: The unreactivity of CO_2 at higher temperature. *Geochim. Cosmochim. Acta* **60**, 3859-3867.

Borgia A., Pruess K., Kneafsey T.J. Oldenburg C.M. and Pan L. (2012) Simulation of CO_2-EGS in a fractured reservoir with salt precipitation. In *Proceedings: Thirty-Seventh Workshop on Geothermal Reservoir Engineering.* Stanford University, Stanford, California.

Bourg A. C. M., Oustrière P. and Sureau J. F. (1985) Experimental investigation of clogging of fissures and pores in granite. *Mineral. Mag.* **49**, 223-231.

Brown D. (2000) A Hot Dry Rock geothermal energy concept utilizing supercritical CO_2 instead of water. In *Proceedings of the Twenty-Fifth Workshop on Geothermal Reservoir Engineering*. Stanford University, Palo Alto, CA. pp. 233-238.

Browne P. R. L. (1978) Hydrothermal alteration in active geothermal fields. *Annu. Rev. Earth Planet. Sci.* **6**: 279-250.

Browne P. R. L. and A. J. Ellis (1970) The Ohaki-Broadlands Hydrothermal Area, New Zealand: Mineralogy and related geochemistry. *Am. J. Sci.* **269**: 97-131.

Brunauer S., Emmett P.H. and Teller E. (1938) Adsorption of gases in multimolecular layers. *J. Am. Chem. Soc.* **60**, 309-319.

Bucher K. and Ingrid S. (2000) The Composition of Groundwater in the Continental Crystalline Crust. In *Hydrogeology of Crystalline Rocks* (eds. I. Stober and K. Bucher). Kluwer Academic Publishers: Dordrecth, Netherlands. p. 141-176.

Capuano R. M. and Cole D. R. (1982). Fluid-Mineral equilibria in a hydrothermal system, Roosevelt Hot Springs, Utah. *Geochim. Cosmochim. Acta* **46**, 1353-1364.

Charles R. W. (1978) Experimental geothermal loop: I, 295ºC study. Informal Report LA-7334-MS. Los Alamos National Laboratory, Los Alamos, NM.

Charles R. W. and Bayhurst G. K. (1983) Rock-fluid interactions in a temperature-gradient: Biotite granodiorite + H_2O. *J. Volcanol. Geotherm. Res.* **15**, 137-166.

Coblentz D. (2011). Quarterly Progress Report, Activities description: National risk Assessment Partnership. *AARRA Quarterly Report* FY2011, Q4, 6p.

Duan Z. H. and Sun R. (2003) An improved model calculation CO_2 solubility in pure water and aqueous NaCl solutions from 273 to 533 K and from 0 to 2000 bar. *Chem. Geol.* **193,** 257-271.

Duan Z. H., Sun R., Zhu C. and Chou I. (2006) An improved model for the calculation of CO_2 solubility in aqueous solutions containing Na^+, K^+, Ca^{2+}, Mg^{2+}, Cl^-, and SO_4^{2-}. *Mar. Chem.* **98**, 131-139.

Duan Z.H., Hu, J., Li D. and Mao S. (2008) Densities of the CO_2-H_2O and CO_2-H_2O-NaCl systems up to 647 K and 100 Mpa. *Energy & Fuels* **22(3)**, 1666-1674.

Ellis A. J. (1968) Natural hydrothermal systems and experimental hot-water/rock interaction: Reactions with NaCl solutions and trace metal extraction. *Geochim. Cosmochim. Acta* **32**, 1356-1363.

Ellis A. J. (1979) Explored geothermal systems. In *Geochemistry of Hydrothermal Ore Deposits* (ed. H. L. Barnes). John Wiley & Sons, New York. pp. 632-684.

Ellis A. J. and Mahon W. A. J. (1964) Natural hydrothermal systems and experimental hot-water/rock interactions. *Geochim. Cosmochim. Acta* **28**, 1323-1357.

Ellis A. J. and Mahon W. A. J. (1967) Natural hydrothermal systems and experimental hot water/rock interactions (Part II). *Geochim. Cosmochim. Acta* **31**, 519-538.

Fournier R. O. and Rowe J. J. (1966) Estimation of underground temperatures from the silica content of water from hot springs and wet-steam wells. *Am. J. Sci.* **264**, 685-697.

Fournier R. O. and Potter R. W. (1982) An equation correlating the solubility of quartz in water from 25 °C to 900 °C at pressures up to 10,000 bars. *Geochim. Cosmochim. Acta* **46**, 1969-1974.

Franck, E.U. (1956) Hochverdichteter Wasserdampf II, Ionendis-sociation von KCL in H_2O bis 750 ^{o}C. *Z. Phys. Chem.* **8**, 107-126.

Gianelli G., Mekuria N., Battaglia S., Chersicla, A., Garofalo, P., Ruggieri, G., Manganelli, M. and Gebregziabher, Z. (1998) Water-rock interaction and hydrothermal mineral equilibria in the Tendaho geothermal system. *J. Volcanol. Geotherm. Res.* **86**, 253-276.

Giggenbach W. F. (1984) Mass transfer in hydrothermal alteration systems – A conceptual approach. *Geochim. Cosmochim. Acta* **48**, 2693-2711.

Henley R. W. and Ellis A. J. (1983) Geothermal systems ancient and modern: A geochemical review. *Earth-Science Rev.* **19**, 1-50.

Hutcheon I., de Caritat P. and Abercrombie H. J. (1994) Clay minerals – Equilibrium modes and temperature indicators. In *Alteration and Alteration Processes Associated with Ore-forming Systems* (ed. D. R. Lentz). Geological Association of Canada, Waterloo, Ontario. pp. 43-67.

The International Association for the Properties of Water and System (IAPWS, 1998) Revised Release on the IAPS Formulation 1985 for the Viscosity of Ordinary Water Substance. London, England. 23p.

Inoue A. (1995) Formation of clay minerals in hydrothermal environments. In *Origin and Mineralogy of Clays: Clays and the Environment* (ed. B. Velde). Springer-Verlag, New York. pp. 245-329.

Inoue A., Utada M. and Wakita K. (1992) Smectite-to-illite conversion in natural hydrothermal systems. *Appl Clay Sci* **7**, 131-145.

Johnson J. W., Oelkers E. H. and Helgeson H. C. (1992) SUPCRT92: A software package for calculating the standard molal thermodynamic properties of minerals, gases, aqueous species, and reactions from 1 to 5000 bar and 0 to 1000°C. *Computers & Geosciences* **18(7)**, 899-947.

Kaszuba J. P., Viswanathan H. S. and Carey J. W. (2011) Relative stability and significance of dawsonite and aluminum minerals in geologic carbon sequestration. *Geophys. Res. Lett.* **38**, L08404.

Kacandes, G.H. and Grandstaff, D.E. (1989) Differences between geothermal and experimentally derived fluids: How well do hydrothermal experiments model the composition of geothermal reservoir fluids? *Geochimica et Cosmochimica Acta* **53(2)**, 343-358.

Langmuir D. (1997) *Aqueous Environmental Chemistry*. Prentice Hall, Upper Saddle River, NJ.

Lichtner P.C. and Kang Q. (2007) Upscaling pore-scale reactive transport equations using a multi-scale continuum formulation. *Water Resources Research* **43**: W12S15, doi:10.1029/2006WR005664.

Lin H., Fujii T., Takisawa R., Takahashi T. and Hashida T. (2008) Experimental evaluation of interactions in supercritical CO_2/water/rock minerals system under geologic CO_2 sequestration conditions. *J. Mater Sci* **43**, 2307-2315.

Liu L., Suto Y., Bignall G., Yamasaki N. and Hashida T. (2003) CO_2 injection to granite and sandstone in experimental rock/hot water systems. *Energy Convers. Manag.* **44**, 1399-1410.

Mahon W. A. J. (1966) Silica in hot water discharged from drillholes at Wairakei, New Zealand. *N. Z. J. Sci.* **9**, 135-144.

Marshall, W.L. and Franck, E.U. (1981) Ion product of water substance 0-1000 ^{o}C, 1-10000 bars, new international formulation and its background. *J. Phys. Chem. Ref. Data* **10(2)**, 295-304.

Massachusetts Institute of Technology (2006). *The future of geothermal energy: impact of enhanced geothermal systems (EGS) on the United States in the 21st century: An assessment.* Cambridge, MA.

McLin K. S., Moore J. N., Bowman J. R. and McCulloch J. E. (2012) Mineralogy and fluid inclusion gas chemistry of prodcution well mineral scale deposits at the Dixie Valley geothermal field, USA. *Geofluids* **Feb 22**, 1-12.

Milodowski A. E., Savage D., Bateman K. and Hughes C. R. (1989). The precipitation of solids from potential heat exchange fluids for use in a HDR geothermal system in granite. *Geothermics* **18**, 233-240.

Moore D. E., Lockner D. A. and Byerlee J. D. (1994) Reduction of permeability in granite at elevated temperatures. *Science* **265**, 1558-1561.

Moore D. E., Morrow C. A. and Byerlee J. D. (1983) Chemical reactions accompanying fluid flow through granite held in a temperature gradient. *Geochim. Cosmochim. Acta* **47**, 445-453.

Moore J., Adams M., Allis R., Lutz S. and Rauzi S. (2005) Mineralogical and geochemical consequences of the long-term presence of CO_2 in natural reservoirs: An example from the Springerville-St. John's Field, Arizona, and New Mexico, U.S.A. *Chemical Geology*, **217**, 365-385.

Morrow C. A., Lockner D. A., Moore D. E. and Byerlee J. D. (1981) Permeability of granite in a temperature gradient. *J. Geophys. Res.* **86**, 3002-3008.

Morrow C. A., Moore D. E. and Lockner D. A. (2001) Permeability reduction in granite under hydrothermal conditions. *J. Geophys. Res.* **106**, 30551-30560.

Naumov V. B., Dorofeev V. A. and Mironova O. F. (2011) Physicochemical parameters of the formation of hyrothermal deposits: A fluid inclusion study. I. Tin and tungsten deposits. *Geochem. Int.* **49**, 1002-1021.

Newell D. L., Kaszuba J. P., Viswanathan H. S., Pawar R. J. and Carpenter T. (2008) Significance of carbonate buffers in natural waters reacting with supercritical CO_2: Implications for monitoring, measuring and verification (MMV) of geologic carbon sequestration. *Geophys. Res. Lett.* **35**, L23403.

Nicholson K. (1993) *Geothermal Fluids: Chemistry and Exploration Techniques.* Springer-Verlag, New York.

Okamoto A., Saishu H., Hirano N. and Tsuchiya N. (2010) Mineralogical and textural variation of silica minerals in hydrothermal flow-through experiments: Implications for quartz vein formation. *Geochim. Cosmochim. Acta* **74**, 3692-3706.

Palandri J.L. Kharaka Y.K. (2004) A compilation of rate parameters of water-mineral interaction kinetics for application to geochemical modeling. *U.S. Geological Survey Open File Report 2004-1068*. Menlo Park, California.

Pruess K. (2005) ECO2N: A TOUGH2 fluid property module for mixtures of water, NACL, and CO_2. *Lawrence Berkeley National Laboratory Report LBNL-57952*. Berkeley, California.

Pruess K. (2006) Enhanced geothermal system (EGS) using CO_2 as working fluid – A novel approach for generating renewable energy with simultaneous sequestration of carbon. *Geothermics* **35,** 351-367.

Pruess K. (2007) Enhanced geothermal system (EGS): comparing water and CO_2 as heat transmission fluids. In *Proceedings: New Zealand Geothermal Workshop 2007*. Aukland, New Zealand, November 19-21.

Pruess K. (2008) On production behavior of enhanced geothermal systems with CO_2 as working fluid. *Energy Conversion & Management* **49**, 1446-1454.

Randolph J. B. and Saar M. O. (2011) Combining geothermal energy capture with geoogic carbon dioxide sequestration. *Geophys. Res. Lett.* **38**, L10401, doi: 10.1029/2011GL047265.

Rauzi S.L. (1999) Carbon dioxide in the St. John's – Springerville area, Apache County, Arizona. *Arizona Geological Survey Open-file Report 99-2*. Tucson, Arizona.

Reed M. H. (1979) Hydrothermal alteration and its relationship to ore fluid composition. In *Geochemistry of Hydrothermal Ore Deposits* (ed. H. L. Barnes). John Wiley & Sons, New York. pp. 303-365.

Rimstidt J. D. and Barnes H. L. (1980) The kinetics of silica-water reactions. *Geochim. Cosmochim. Acta* **44**, 1683-1699.

Rose A. W. and D. M. Burt (1979) Hydrothermal alteration. In *Geochemistry of Hydrothermal Ore Deposits* (ed. H. L. Barnes). John Wiley & Sons, New York. pp. 632-684.

Rosenbauer R. J., Koksalan T. and Palandri J. L. (2005) Experimental investigation of CO_2-brine-rock interactions at elevated temperature and pressure: Implicatios for CO_2 sequestration in deep-saline aquifers. *Fuel Process. Technol.* **86**, 1581-1597.

Savage D. (1986) Granite-water interactions at 100ºC, 50 MPa: An experimental study. *Chem. Geol.* **54**, 81-95.

Savage D. and Chapman N.A. (1982) Hydrothermal behavior of simulated waste-glass and waste-rock interactions under repository conditions. *Chem. Geol.* **36**, 59-86.

Savage D., Bateman K. and Richards H. G. (1992) Granite-water interactions in a flow-through experimental system with applications to the Hot Dry Rock geothermal system at Rosemanowes, Cornwall, U.K. *Appl. Geochem.* **7**, 223-241.

Savage D., Cave M. R. and Milodowski A. E. (1985) Interaction of meteoric groundwater with Garnmenellis granite at 250ºC and 50 MPa: an experimental study. In *High Heat Production (HHP) Granites, Hydrothermal Circulation and Ore Genesis* (ed. C. Halls). Institution of Mining and Metallurgy, London. pp. 315-328.

Savage D., Bateman K., Milodowski A. E. and Hughes C. R. (1993) An experimental evaluation of granite with streamwater, seawater and NaCl solutions at 200ºC. *J. Volcanol. Geotherm. Res.* **57**, 167-191.

Savage D., Cave M. R., Milodowski A. E. and George I. (1987) Hydrothermal alteration of granite by meteoric fluid: An example from the Carnmenellis Granite, United-Kingdom. *Contrib. Mineral. Petrol*. **96**: 391-405.

Seyfried, Jr., W. E. and Bischoff J. L. (1977) Hydrothermal transport of heavy metals by seawater: The role of seawater/basalt ratio. *Earth Planet. Sc. Lett.* **34**, 71-77.

Seyfried, Jr., W. E., Janecky D. R. and Berndt M. E. (1987) Rocking autoclaves for hydrothermal experiments, II. The flexible reaction-cell system. In *Hydrothermal Experimental Techniques* (eds. G. C. Ulmer and H. L. Barnes). John Wiley & Sons, New York. pp. 216-239.

Span R. and Wagner W. (1996) A New Equation of State for Carbon Dioxide Covering the Fluid Region from the Triple-Point Temperature to 1100 K at Pressures up to 800 MPa. *J. Phys. Chem. Ref. Data* **25(6)**, 1509-1596.

Spycher N., Pruess K. and Ennis-King J. (2003) CO_2-H_2O mixtures in the geological sequestration of CO_2. I. Assessment and calculation of mutual solubilities from 12 to 100 ^oC and up to 600 bar. *Geochimica et Cosmochimica Acta* **67(16)**, 3015-3031.

Spycher N. and Pruess K. (2010) A phase-partitioning model for CO_2-brine mixtures at elevated temperatures and pressures: Application to CO_2-Enhanced Geothermal Systems. *Transport in Porous Media* **82**, 173-196.

Steiner A. (1968) Clay minerals in hydrothermally altered rocks at Wairakei, New Zealand. *Cl. Cl. Mineral.* **16**: 193-213.

Stone C. (1979) An overview of the geothermal potential of the Springerville area, Arizona. *Arizona Geological Survey Open-file Report 79-2a*. Tucson, Arizona.

Stumm W. and Morgan J. J. (1996) *Aquatic Chemistry: Chemical Equlibria and Rates in Natural Waters*. John Wiley & Sons, New York.

Sun R. (2011) Personal email communication to Xiuyu Wang (University of Wyoming) regarding executable file for Duan & Sun, 2003. November 20.

Suto Y., Liu L., Yamasaki N. and Hashida T. (2007) Initial behavior of granite in response to injection of CO_2-saturated fluid. *Appl. Geochem.* **22**, 202-218.

Taylor, Jr., H. P. (1979) Oxygen and hydrogen isotope relationships in hydrothermal mineral deposits. In *Geochemistry of Hydrothermal Deposits* (ed. H. L. Barnes). John Wiley & Sons, New York. pp. 232-277.

Tsuchiya N. and Hirano N. (2007) Chemical reaction diversity of geofluids revealed by hydrothermal experiments under sub- and supercritical states. *Isl. Arc* **16**, 6-15.

Ueda A., Kato K., Oshumi T., Yajima T., Ito H., Kaieda H., Metcalfe R. and Takase H. (2005) Experimental studies of CO_2-rock interaction at elevated temperatures under hydrothermal conditions. *Geochem. J.* **39**, 417-425.

Vidal O., Baldeyrou A., Beaufort D., Fritz B., Geoffroy N., Lanson B. (2012) Experimental study of the stabiligy and phase relations of clays at high temperatures in a thermal gradient. *Clays Clay Min.* **60**, 200-225.

Wan Y. Xu T. and Pruess K. (2011) Impact of fluid-rock interactions on enhanced geothermal systems with CO_2 as heat transmission fluid. In *Proceedings: Thirty-Sixth Workshop on Geothermal Reservoir Engineering*. Stanford University, Stanford, California.

Wang Y. and Xu H. (2006) Geochemical chaos: Periodic and nonperiodic growth of mixed-layer phyllosilicates. *Geochim. Cosmochim. Acta* **70**, 1995-2005.

Whitney G. (1990) Role of water in the smectite-to-illite reaction. *Clays Clay Min.* **38**, 343-350.

Wigand M., Kaszuba J.P., Carey J.W. and Hollis W.K. (2009) Geochemical effects of CO_2 sequestration on fractured wellbore cement at the cement/caprock interface. *Chemical Geology* **265**, 122-133.

Wolery T.J. (1992) EQ3/6: Software package for geochemical modeling of aqueous systems: Package overview installation guide (version 8.0). *Lawrence Livemore National Laboratory Report UCRL-MA-110662 PT I*. Livemore, California.

Xu T., Sonnenthal E., Spycher N. and Pruess K. (2004) TOUGHREACT user's guide: A simulation program for non-isothermal multiphase reactive geochemical transport in

variably saturated geologic media. *Lawrence Berkeley National Laboratory Report LBNL-55460*. Berkeley, California.

Xu T., Sonnenthal E., Spycher N. and Pruess K. (2006) TOUGHREACT: a simulation program for non-isothermal multiphase reactive geochemical transport in variably saturated geologic media. *Computers & Geosciences* **32**, 145-165.

Xu T. Pruess K. and Apps J. (2008) Numerical studies of fluid-rock interactions in enhanced geothermal systems (EGS) with CO_2 as working fluid. In *Proceedings: Thirty-third Workshop on Geothermal Reservoir Engineering*. Stanford University, Stanford, California.

Xu, T., Spycher, N., Sonnenthal, E., Zhang, G., Zheng, L. and Pruess, K. (2011) TOUGHREACT version 2.0: A simulator for subsurface reactive transport under non-isothermal multiphase flow conditions. *Computers & Geosciences*, **37**, 763-774.

Yasuhara H., Kinoshita N., Ohfuji H., Lee D. S., Nakashima S. and Kishida K. (2011) Temporal alteration of fracture permeability in granite under hydrothermal conditions and its interpretation by coupled chemo-mechanical model. *Appl. Geochem.* **26,** 2074-2088.

10. Project Products under the Award

10.1. Project Publication to Date

Lo Ré, C., J. Kaszuba, J. Moore, and B.J. McPherson, 2014. Fluid-rock interactions in CO_2-saturated, granite-hosted geothermal systems: Implications for natural and engineered systems from geochemical experiments and models. Geochimica et Cosmochimica Acta, v. 141, 160-178.

Kelkar, S., K.C. Lewis, S. Karra, G. Zyvoloski, S. Rapaka, H. Viswanathan, P.K. Mishra, S. Chu, D. Coblentz, and R. Pawar, 2014. A simulator for modeling coupled thermo-hydro-mechanical processes in subsurface geological media. International Journal of Rock Mechanics and Mining Sciences, 70, 569-580.

Lewis, K.C., S. Karra, and S. Kelkar, 2013. A Model for tracking fronts of stress-induced

permeability enhancement. *Transport in Porous Media*, 99: 17-35.

Pan, F., B.J. McPherson, P.C. Lichtner, J.P. Kaszuba, C. Lo Ré, S. Karra, C. Lu, and T. Xu, 2013. Numerical evaluation of energy extraction, CO_2-rock interactions, and carbon sequestration in Enhanced Geothermal System (EGS) with supercritical CO_2 as a working fluid. Proceedings of Thirty-Eighth Workshop on Geothermal Reservoir Engineering, Stanford University, Stanford, California, February 11-13.

Lichtner, P.C., and S. Karra, 2013. Modeling multiscale-multiphase-multicomponent reactive flows in porous media: Application to CO_2 sequestration and Enhanced Geothermal Energy using PFLOTRAN, in book of Computational Models for CO_2 Sequestration and Compressed Air Energy Storage, Taylor & Francis/CRC press.

Pan, F., B.J. McPherson, P.C. Lichtner, S. Karra, C. Lo Ré, J.P. Kaszuba, C. Lu, and T. Xu, 2012. Numerical simulations of interactions between supercritical CO_2 and high-temperature fractured rocks in enhanced geothermal systems. Proceedings of Thirty-Seventh Workshop on Geothermal Reservoir Engineering, Stanford University, Stanford, California, January 30 – February 1.

Lo Ré, C., J. Kasuba, J. Moore, and B.J. McPherson, 2012. Supercritical CO_2 in a granite-hosted geothermal system: Experimental insights into multiphase fluid-rock interactions. Proceedings of Thirty-Seventh Workshop on Geothermal Reservoir Engineering, Stanford University, Stanford, California, January 30 – February 1.

Karra, S., and P. Lichtner. An Efficient Multiple Continuum Algorithm for Heat and Mass Transport. (in review).

Karra, S., and P. Lichtner, 2013. On the multiscale continuum modeling of non-isothermal flow and reactive transport in fractured porous media. USNCCM 13, Raleigh, North Carolina.

Pan, F., B.J. McPherson, P.C. Lichtner, J.P. Kaszuba, C. Lo Ré, S. Karra, C. Lu, and T. Xu, 2012. Geochemical simulation on CO_2-fluid-rock interactions in EGS reservoirs. American Geophysical Union (AGU) Fall Meeting, San Francisco, CA, H13G-1433.

Kaszuba, J.P., C. Lo Ré, J. Martin, B.J. McPherson, and J. Moore, 2012. Experimental insights into multiphase (H_2O-CO_2) fluid-rock interactions in geothermal systems: Eos, Transactions, v. 93, Fall Meeting Supplement, Abstract H11O-01.

Lo Ré, C., J.P. Kaszuba, J. Moore, and B.J. McPherson, 2012. Experimental insights into fluid-rock interactions in granite-hosted and CO_2-saturated geothermal systems: Goldschmidt 2012, June, Montreal, Canada.

10.2. Other Products

a. **New thermodynamic database at elevated temperature and pressure;**
b. **The geochemical and mineralogical related data from batch laboratory experiments;**
c. **Modified PFLOTRAN model with addition of dual-continuum feature, and modified TOUGHREACT model with the implementation of new thermodynamic database;**
d. **The modeling simulation data from the simulations and calibration of batch experiments, and heat, flow, geochemical simulations of CO_2-rock interactions in EGS reservoirs with conceptual and field-scale models.**

Acknowledgements

This project is supported by the Geothermal Technologies Program of the U.S. Department of Energy under contract NO. DE – EE0002766. We would like to thank John Muir,

and Alan Eastman at GreenFire Energy, Susan Petty, Yini Nordin, and Joe Iovenitti at AltaRock Energy, and Joe Moore at the University of Utah for their help with the discussions and information on the research in EGS reservoirs. We also thank Dr. Joe Moore at the University of Utah for the XRD analysis on the two rock samples in Springerville-St. John Dome.

Appendix A. Mineral and Aqueous Reactions Whose Reaction Equilibrium Constants have been Evaluated

The following list contains mineral species and reactions included in the SLOP07 dataset (provided by GEOPIG, Arizona State University), which contains more species and geochemical reactions than sprons96 dataset. The project team has gathered the reaction equilibrium constants of these reactions from SUPCRT92. All equilibrium constants have been regressed according to Equation (1) and (6d).

Part I. Mineral reactions

Akermanite

```
 1  4  0  1
-1.000 AKERMANITE  Ca2MgSi2O7
-6.000  H+          H(+)
 1.000  Mg+2        Mg(+2)
 2.000  Ca+2        Ca(+2)
 2.000  SiO2,aq     SiO2(0)
 3.000  H2O         H2O
```

Albite

```
 1  4  0  1
-1.000  ALBITE       Na(AlSi3)O8
-4.000  H+          H(+)
 1.000  Al+3        Al(+3)
 1.000  Na+         Na(+)
 3.000  SiO2,aq     SiO2(0)
 2.000  H2O         H2O
```

```
Albite_high
  1   4   0   1
  -1.000  ALBITE,HIGH         Na(AlSi3)O8
  -4.000  H+                  H(+)
   1.000  Al+3                Al(+3)
   1.000  Na+                 Na(+)
   3.000  SiO2,aq             SiO2(0)
   2.000  H2O                 H2O

Albite_low
  1   4   0   1
  -1.000  ALBITE,LOW          Na(AlSi3)O8
  -4.000  H+                  H(+)
   1.000  Al+3                Al(+3)
   1.000  Na+                 Na(+)
   3.000  SiO2,aq             SiO2(0)
   2.000  H2O                 H2O

Alunite
  1   4   0   1
  -1.000  ALUNITE       KAl3(OH)6(SO4)2
  -6.000  H+                  H(+)
   3.000  Al+3                Al(+3)
   1.000  K+                  K(+)
   2.000  SO4-2               SO4(-2)
   6.000  H2O                 H2O

Amesite,7A
  1   4   0   1
  -1.000  AMESITE,7A Mg2Al(AlSi)O5(OH)4
  -10.000  H+                 H(+)
   2.000  Al+3                Al(+3)
   2.000  Mg+2                Mg(+2)
   1.000  SiO2,aq             SiO2(0)
   7.000  H2O                 H2O

Analcime
  1   4   0   1
  -1.000  ANALCIME            NaAlSi2O6*H2O
  -4.000  H+                  H(+)
   1.000  Al+3                Al(+3)
   1.000  Na+                 Na(+)
   2.000  SiO2,aq             SiO2(0)
   3.000  H2O                 H2O

Analcime_dehy
  1   4   0   1
  -1.000  ANALCIME,DEHYDRATED
NaAlSi2O6
  -4.000  H+                  H(+)
   1.000  Al+3                Al(+3)
   1.000  Na+                 Na(+)
   2.000  SiO2,aq             SiO2(0)
   2.000  H2O                 H2O

Anorthite
  1   4   0   1
  -1.000  ANORTHITE           Ca(Al2Si2)O8
  -8.000  H+                  H(+)
   2.000  Al+3                Al(+3)
   1.000  Ca+2                Na(+)
   2.000  SiO2,aq             SiO2(0)
   4.000  H2O                 H2O

Andalusite
  1   3   0   1
  -1.000 ANDALUSITE Al2SiO5
  -6.000  H+                  H(+)
   2.000  Al+3                Al(+3)
   1.000  SiO2,aq             SiO2(0)
   3.000  H2O                 H2O

Annite
  1   5   0   1
  -1.000  ANNITE
KFe3(AlSi3)O10(OH)2
  -10.000  H+                 H(+)
   1.000  Al+3                Al(+3)
   3.000  Fe+2                Fe(+2)
   1.000  K+                  K(+)
   3.000  SiO2,aq             SiO2(0)
   6.000  H2O                 H2O

Artinite
  1   4   0   1
  -1.000 ARTINITE    Mg2(OH)2(CO3)*3H2O
  -3.000  H+                  H(+)
   2.000  Mg+2                Mg(+2)
   1.000  HCO3-                HCO3(-)
   5.000  H2O                   H2O

Ca-Al_Pyroxene
  1   4   0   1
  -1.000 CA-AL_PYROXENE CaAl(AlSi)O6
  -8.000  H+                  H(+)
   2.000  Al+3                Al(+3)
   1.000  Ca+2                Na(+)
   1.000  SiO2,aq             SiO2(0)
```

```
   4.000  H2O              H2O

 Calcite
   1   3   0   0
   -1.000  CALCITE           CaCO3
   -1.000  H+               H(+)
    1.000  Ca+2             Ca(+2)
    1.000  HCO3-            HCO3(-)

 Clinochlore_14A
  1   4   0   1
   -1.000  CLINOCHLORE,14A
Mg5Al(AlSi3)O10(OH)8
  -16.000  H+               H(+)
    2.000  Al+3             Al(+3)
    5.000  Mg+2             Mg(+2)
    3.000  SiO2,aq          SiO2(0)
   12.000  H2O              H2O

 Clinochlore-7A
  1   4   0   1
   -1.000  CLINOCHLORE,7A
Mg5Al(AlSi3)O10(OH)8
  -16.000  H+               H(+)
    2.000  Al+3             Al(+3)
    5.000  Mg+2             Mg(+2)
    3.000  SiO2,aq          SiO2(0)
   12.000  H2O              H2O

 Corundum
   1   2   0   1
   -1.000 CORUNDUM  Al2O3
   -6.000  H+               H(+)
    2.000  Al+3             Al(+3)
    3.000  H2O              H2O

 Dawsonite
   1   4   0   1
   -1.000 DAWSONITE   NaAlCO3(OH)2
   -3.000  H+               H(+)
    1.000  Al+3             Al(+3)
    1.000  Na+              Na(+)
    1.000  HCO3-           HCO3(-)
    2.000  H2O              H2O

 Dolomite
  1   4   0   0
   -1.000  DOLOMITE          CaMg(CO3)2
   -2.000  H+               H(+)
    1.000  Ca+2             Ca(+2)
    1.000  Mg+2             Mg(+2)
    2.000  HCO3-            HCO3(-1)

 Dolomite_dis
  1   4   0   0
   -1.000  DOLOMITE,DISORDERED
CaMg(CO3)2
   -2.000  H+               H(+)
    1.000  Ca+2             Ca(+2)
    1.000  Mg+2             Mg(+2)
    2.000  HCO3-            HCO3(-1)

 Dolomite_ord
  1   4   0   0
   -1.000  DOLOMITE,ORDERED
CaMg(CO3)2
   -2.000  H+               H(+)
    1.000  Ca+2             Ca(+2)
    1.000  Mg+2             Mg(+2)
    2.000  HCO3-            HCO3(-1)

 Enstatite
   1   3   0   1
   -1.000 ENSTATITE     MgSiO3
   -2.000  H+               H(+)
    1.000  Mg+2             Mg(+2)
    1.000  SiO2,aq          SiO2(0)
    1.000  H2O              H2O

 Epidote
  1   6   0   1
   -1.000  EPIDOTE
Ca2FeAl2Si3O12(OH)
  -13.000  H+               H(+)
    2.000  Al+3             Al(+3)
    1.000  Fe+3             Fe(+3)
    1.000  K+               K(+)
    2.000  Ca+2             Ca(+2)
    3.000  SiO2,aq           SiO2(0)
    7.000  H2O              H2O

 Epidote_ord
  1   6   0   1
   -1.000  EPIDOTE,ORDERED
Ca2FeAl2Si3O12(OH)
  -13.000  H+               H(+)
    2.000  Al+3             Al(+3)
    1.000  Fe+3             Fe(+3)
```

```
   1.000  K+              K(+)
   2.000  Ca+2            Ca(+2)
   3.000  SiO2,aq         SiO2(0)
   7.000  H2O             H2O

Halite
 1  2  0  0
  -1.000  HALITE          NaCl
   1.000  Na+             Na(+)
   1.000  Cl-            Cl(-)
Hematite
1  2  0  1
  -1.000 HEMATITE    Fe2O3
  -6.000  H+              H(+)
   2.000  Fe+3            Fe(+3)
   3.000  H2O             H2O

Kaolinite
 1  3  0  1
  -1.000  KAOLINITE       Al2Si2O5(OH)4
  -6.000  H+              H(+)
   2.000  Al+3            Al(+3)
   2.000  SiO2,aq         SiO2(0)
   5.000  H2O             H2O

k-feldspar
 1  4  0  1
  -1.000  K-FELDSPAR      K(AlSi3)O8
  -4.000  H+              H(+)
   1.000  Al+3            Al(+3)
   1.000  K+              K(+)
   3.000  SiO2,aq         SiO2(0)
   2.000  H2O             H2O

Larnite
1  3  0  1
  -1.000 LARNITE     Ca2SiO4
  -2.000  H+              H(+)
   2.000  Ca+2            Ca(+2)
   1.000  SiO2,aq         SiO2(0)
   2.000  H2O             H2O

Magnesite
 1  3  0  0
  -1.000  MAGNESITE       MgCO3
  -1.000  H+              H(+)
   1.000  Mg+2            Mg(+2)
   1.000  HCO3-           HCO3(-1)

Muscovite
 1  4  0  1
  -1.000  MUSCOVITE
KAl2(AlSi3)O10(OH)2
 -10.000  H+              H(+)
   3.000  Al+3            Al(+3)
   1.000  K+              K(+)
   3.000  SiO2,aq         SiO2(0)
   6.000  H2O             H2O

Phlogopite
 1  5  0  1
  -1.000  PHLOGOPITE
KMg3(AlSi3)O10(OH)2
 -10.000  H+              H(+)
   1.000  Al+3            Al(+3)
   1.000  K+              K(+)
   3.000  Mg+2            Mg(+2)
   3.000  SiO2,aq         SiO2(0)
   6.000  H2O             H2O

Pyrite
 1  4  0  1
  -1.000  PYRITE          FeS2
  -1.000  H2O             H2O
   1.000  Fe+2            Fe(+2)
   0.250  H+              H(+)
   0.250  SO4-2           SO4(-2)
   1.75   HS-             HS(-1)

Quartz
 1  1  0  0
  -1.000  QUARTZ          SiO2
   1.000  SiO2,aq         SiO2(0)

Siderite
 1  3  0  0
  -1.000  SIDERITE        FeCO3
  -1.000  H+              H(+)
   1.000  Fe+2            Fe(+2)
   1.000  HCO3-           HCO3(-1)
```

Part II. Aqueous Reactions

```
Al(OH)+2
 0  3  0  1
  -1.000  Al(OH)+2          Al(OH)(+2)
  -1.000  H+                H(+)
   1.000  Al+3              Al(+3)
   1.000  H2O               H2O

Al(OH)2+
 0  3  0  1
  -1.000  Al(OH)2+          Al(OH)2(+)
  -2.000  H+                H(+)
   1.000  Al+3              Al(+3)
   2.000  H2O               H2O

AlO2-
 0  3  0  1
  -1.000  AlO2-             AlO2(-)
  -4.000  H+                H(+)
   1.000  Al+3              Al(+3)
   2.000  H2O               H2O

CO2(aq)
 0  3  0  1
  -1.000  CO2,aq            CO2(aq)
  -1.000  H2O               H2O
   1.000  H+                H(+)
   1.000  HCO3-             HCO3(-)

CO3--
 0  3  0  0
  -1.000  CO3-2             CO3(-2)
  -1.000  H+                H(+)
   1.000  HCO3-             HCO3(-)

Ca(CO3)(aq)
 0  4  0  0
  -1.000  Ca(CO3),aq        Ca(CO3)(aq)
  -1.000  H+                H(+)
   1.000  Ca+2              Ca(+2)
   1.000  HCO3-             HCO3(-)

CaCl+
 0  3  0  0
  -1.000  CaCl+             CaCl(+)
   1.000  Ca+2              Ca(+2)
   1.000  Cl-               Cl(-)

CaCl2(aq)
 0  3  0  0
  -1.000  CaCl2,aq          CaCl2(aq)
   1.000  Ca+2              Ca(+2)
   2.000  Cl-               Cl(-)

Fe(OH)+
 0  3  0  1
  -1.000  Fe(OH)+           Fe(OH)(+)
  -1.000  H+                H(+)
   1.000  Fe+2              Fe(+2)
   1.000  H2O               H2O

Fe(OH)2+
 0  3  0  1
  -1.000  Fe(OH)2+          Fe(OH)2(+)
  -2.000  H+                H(+)
   1.000  Fe+3              Fe(+3)
   2.000  H2O               H2O

Fe(OH)+2
 0  3  0  1
  -1.000  Fe(OH)+2          Fe(OH)(+2)
  -1.000  H+                H(+)
   1.000  Fe+3              Fe(+3)
   1.000  H2O               H2O

HSO3-
 0  3  0  0
  -1.000  HSO3-             HSO3(-)
   1.000  H+                H(+)
   1.000  SO3-2             SO3(-2)

HSO4-
 0  3  0  0
  -1.000  HSO4-             HSO4(-)
   1.000  H+                H(+)
   1.000  SO4-2             SO4(-2)

KSO4-
 0  3  0  0
  -1.000  KSO4-             KSO4(-)
   1.000  K+                K(+)
   1.000  SO4-2             SO4(-2)

MgCO3(aq)
 0  4  0  0
  -1.000  Mg(CO3),aq        MgCO3(aq)
```

```
  -1.000  H+              H(+)
   1.000  HCO3-           HCO3(-)
   1.000  Mg+2            Mg(+2)

MgHCO3+
 0  3  0  0
  -1.000  MgHCO3+     MgHCO3(+)
   1.000  HCO3-           HCO3(-)
   1.000  Mg+2            Mg(+2)

MgCl+
 0  3  0  0
  -1.000  MgCl+           MgCl(+)
   1.000  Cl-            Cl(-)
   1.000  Mg+2            Mg(+2)

MgOH+
 0  3  0  0
  -1.000  MgOH+         MgOH(+)
   1.000  OH-            OH(-)
   1.000  Mg+2            Mg(+2)

NaCl(aq)
 0  3  0  0
  -1.000  NaCl,aq          NaCl(aq)
   1.000  Cl-            Cl(-)
   1.000  Na+             Na(+)

NaHSiO3(aq)
 0  4  0  1
  -1.000  NaHSiO3,aq         NaHSiO3(aq)
  -1.000  H+              H(+)
   1.000  H2O             H2O
   1.000  Na+             Na(+)
   1.000  SiO2,aq          SiO2(aq)

NaAlO2(aq)
 0  4  0  1
  -1.000  NaAlO2,aq         NaAlO2(aq)
  -4.000  H+              H(+)
   2.000  H2O             H2O
   1.000  Na+             Na(+)
   1.000  Al+3            Al(+3)

NaOH(aq)
 0  3  0  0
  -1.000  NaOH,aq        NaCl(aq)
   1.000  OH-            OH(-)
   1.000  Na+             Na(+)

OH-
 0  2  0  1
  -1.000  OH-             OH(-)
  -1.000  H+              H(+)
   1.000  H2O             H2O

SO2(aq)
 0  3  0  1
  -1.000  SO2,aq          SO2(aq)
  -1.000  H2O             H2O
   2.000  H+              H(+)
   1.000  SO3-2           SO3(-2)

Fe+++
 0  3  0  1
  -1.000  Fe+++           Fe(+3)
  -0.500  H2O             H2O
   1.000  Fe++            Fe(+2)
   0.250  O2(aq)          O2(aq)

HS-
 0  4  0  0
  -1.000  HS-             HS(-)
  -2.000  O2(aq)          O2(aq)
   1.000  H+              H(+)
   1.000  SO4-2           SO4(-2)

SO3-2
 0  3  0  0
  -1.000  SO3-2           SO3(-2)
  -0.500  O2(aq)          O2(aq)
   1.000  SO4-2           SO4(-2)
```

Part III. Gas dissolution

H2S(g)
0 2 1 0
-1.000 H2S(g) H2S(g)
1.000 H+ H(+)
1.000 HS- HS(-)

CO_2(g)
0 2 1 1
-1.000 CO_2(g) CO_2(g)
-1.000 H2O H2O
1.000 H+ H(+)
1.000 HCO3- HCO3(-)

N2(g)
0 2 2 1
-1.000 N2(g) N2(g)
-3.000 H2O H2O
1.500 O2(g) O2(g)
2.000 NH3,aq NH3(aq)

NO(g)
0 2 2 1
-1.000 NO(g) NO(g)
-0.250 O2(g) O2(g)
-0.500 H2O H2O
1.000 H+ H(+)
1.000 NO-2 NO(-2)

NO2(g)
0 2 2 1
-1.000 NO2(g) NO2(g)
-0.250 O2(g) O2(g)
-0.500 H2O H2O
1.000 H+ H(+)
1.000 NO3-3 NH3(-3)

O2(g)
0 1 1 0
-1.000 O2(g) O2(g)
-1.000 O2(aq) O2(aq)

Appendix B. Comparison of the new HPT geochemical database with EQ3/6 database

Table B1. List of species that have a min error(%) of greater than 10 between the HPT database and the EQ3/6 database.

Name	*Min Error (%)*	*Name*	*Min Error (%)*
Celadonite	12676.52181	2-Heptanone(aq)	32.359956
Heulandite	7725.232657	HfOH+++	27.74102
Stilbite	7410.486681	CdCl+	27.323407
Minnesotaite	5610.39228	CuF+	26.282311
Natrolite	4789.724887	2-Octanone(aq)	23.907072
Larnite	999.054095	U(For)++	22.573924
Bromellite	188.564299	PbOH+	19.526966
HCl(aq)	177.154748	Mn(Glyc)+	18.612866
2-Butanone(aq)	162.546067	NO(g)	17.733894
PbF2(aq)	100.664073	FeF++	17.516322
PbF+	100.414345	Mn(Lac)+	17.345049
AgF(aq)	100.278363	Ru(SO4)2-	17.155897
ZrOH+++	99.984489	CsI(aq)	16.996575
CuCl2(aq)	99.857949	Mn(For)+	16.7161
Aspartic_acid(aq)	87.09819	NaSO4-	15.145558
Tm++	86.873014	Goethite	14.245421
Dy++	86.295397	CdCl2(aq)	13.908101
Nd++	85.587225	AgNO3(aq)	13.501315
Ho++	84.926191	Cr++	13.183159
Pm++	84.807377	BeO2--	13.144791
Er++	84.306395	Ethylbenzene(aq)	12.644805
Pr++	84.059515	Boehmite	12.628545
Tb++	82.42569	ZnOH+	12.461953
La++	81.426803	MnCl+	12.427133
Ce++	81.374042	1-Propanol(aq)	12.269841
Gd++	81.186265	Mn(Prop)+	11.743582
Asparagine(aq)	80.867692	CdCl3-	11.73163
FeCl2(aq)	79.67104	Mn(But)+	11.684242
2-Pentanone(aq)	74.175053	KHSO4(aq)	11.383941
HIO3(aq)	63.560191	Mn(Pent)+	11.367208
KCl(aq)	53.572436	U(But)++	11.157428
HCoO2-	48.286243	RbI(aq)	11.126456
2-Hexanone(aq)	46.479818	U(Pent)++	11.004623
Ru++	40.633433	U(Prop)++	10.845942
MnF+	38.772868	U(For)2+	10.668485
Analcime	37.882398	AmH2PO4++	10.656702
HClO2(aq)	37.638089	1-Heptanol(aq)	10.382031
CaCl+	37.180462	Rhodochrosite	10.190354
		SnOH+	10.099086

Table B2. Error between EQ3/6 database logKs (at water saturation pressures) and HPT database logKs at 1200 bar.

Name	*Max Error (%)*	*Min Error (%)*
Natrolite	2056264.009	4796.298909
Huntite	846531.5357	11.23451
Stilbite	168735.4364	7462.266201
Heulandite	152852.1835	7751.69102
Celadonite	102698.2067	12687.43893
Minnesotaite	26123.88521	5619.630064
La(Pent)2+	10907.22044	0.010746
Bromellite	10792.33037	189.242234
NdCl3(aq)	7624.057138	28.604615
P2O7----	7385.26513	16.655308
YbCl++	6875.711225	0.826465
RbI(aq)	6596.28741	25.402353
Wairakite	4832.482504	1.411446
RbBr(aq)	4177.619861	0.799767
PrCl3(aq)	3353.446006	33.262021
Epidote	3317.744953	0.231207
FeCl++	3152.73215	9.592731
NdCl4-	3029.417134	4.465075
Boehmite	2425.968384	15.747015
EuCl4-	2336.491997	5.659671
NaF(aq)	2215.086131	2.681266
GdCl4-	2125.341471	5.125796
CeCl3(aq)	1960.427787	16.876027
Hydromagnesite	1928.214103	3.927526
AgF(aq)	1909.36982	100.194116
PrNO3++	1870.037386	0.862961
TbNO3++	1735.65105	0.614123
PrCl4-	1702.663312	10.83323
PrSO4+	1591.659225	1.542487
ZnCl3-	1486.972307	20.137403
LiCl(aq)	1440.537157	2.794146
CaCl+	1220.683183	5.307535
LaCl4-	1212.285012	10.979718
NO(g)	1166.865608	6.118292
TbCl4-	1107.347755	10.107295
Larnite	1107.134989	1000.085909
GdSO4+	1070.72834	0.384965

YbCl3(aq)	1044.845379	18.839967
Alabandite	1031.994634	28.656744
GdNO3++	1020.224672	0.571556
SmCl4-	1008.680102	4.783647
YbNO3++	945.11056	2.768409
Dolomite-ord	931.647079	22.63393
Dolomite	924.91617	22.337358
Alunite	911.04571	19.722328
LuCl4-	774.284969	2.833468
Hematite	733.80349	15.75418
DyCl4-	665.999321	7.706207
KHSO4(aq)	649.60627	28.714981
Rhodochrosite	635.483573	33.80774
Zoisite	620.682751	0.106992
Clinozoisite	608.768972	0.122808
CuCl2(aq)	601.280553	99.836151
Kalsilite	590.015562	0.214913
KBr(aq)	582.406782	3.737556
GdCl3(aq)	555.648877	28.328112
Azurite	544.55803	9.996729
Ethylacetate(aq)	540.795748	36.798776
Analcime	532.475773	3.303279
MnCl+	532.364155	27.248656
HNO3(aq)	528.237193	9.828304
LaCl3(aq)	524.483644	26.918189
CeSO4+	520.149793	3.71561
H2O(g)	498.942822	11.987747
TmCl4-	497.529219	6.569744
CeCl2+	483.215344	13.406177
YbCl4-	476.003315	2.810934
Diaspore	473.382343	10.037362
AgNO3(aq)	469.891778	42.763919
TmNO3++	464.609772	1.328503
Calcite	454.771926	21.281472
ErCl4-	439.225948	8.10871
Decanal(aq)	437.086325	16.104295
KCl(aq)	434.613033	69.448588
EuF3-	418.593912	23.481819
NH3(g)	417.717197	23.538663
SmCl3(aq)	416.867461	29.32948
EuNO3++	380.812159	0.146018

Corundum	344.446543	8.59026
ErCl3(aq)	339.397955	32.951716
Albite	339.007651	4.651906
CeCl4-	338.317872	20.949069
HoCl4-	334.992454	9.425245
Smithsonite	330.23337	23.435374
TmCl3(aq)	329.839805	33.001357
Aspartic_acid(aq)	325.364943	98.867363
CsI(aq)	319.563121	2.724229
FeCl+	305.977397	18.867867
LuCl3(aq)	305.376568	11.652603
NaI(aq)	305.213075	0.390684
SmNO3++	299.227091	0.044275
Cuprite	298.537519	13.975541
ZrOH+++	298.430815	99.912081
NaBr(aq)	298.1113	1.314155
LaNO3++	291.382083	1.487625
FeCl2(aq)	287.899424	20.972019
ErNO3++	287.512491	2.090785
CoCl+	270.141037	5.897786
Sillimanite	269.667036	1.337615
KI(aq)	267.5264	5.119502
2-Butanone(aq)	255.986562	151.152314
NdNO3++	253.636969	0.665098
CaCl2(aq)	252.751956	7.633507
BaF+	250.412626	4.941883
EuCl3(aq)	247.772052	29.621897
HoCl3(aq)	243.002112	31.821586
CsCl(aq)	241.291479	3.272493
TbCl3(aq)	240.32901	31.190656
DyCl3(aq)	234.540137	30.711147
SrCl+	233.362105	11.927333
1-Propyne(aq)	228.308744	28.200717
DyNO3++	223.995769	1.894056
NaCl(aq)	220.73149	0.332812
Laumontite	216.520198	0.152899
AlOH++	216.166386	7.355546
La++	215.158401	81.385806
Siderite	214.534608	16.11184
Eu(Pent)2+	210.603192	0.21625
Pm++	204.490816	84.755054

PrCl2+	204.476953	19.326373
Zn(Lac)+	202.363098	0.354781
RbCl(aq)	201.337028	0.311864
Strontianite	201.33082	31.360843
Tm++	200.557451	86.821577
Nd++	200.460657	85.525053
Dy++	200.381689	86.250915
Ho++	200.374233	84.878501
Er++	200.371232	84.254553
Ce++	200.350613	81.312538
Tb++	200.335452	82.383269
Gd++	200.185106	81.142964
Jadeite	198.086204	1.356963
NdCl2+	193.180491	16.80096
Dolomite-dis	193.117729	14.986762
Muscovite	192.576716	2.159182
Andalusite	191.696121	1.309419
Pr++	189.648886	84.00214
Tl+++	187.558557	12.433416
HCl(aq)	186.80749	92.515461
Malachite	178.378931	7.621606
Kyanite	176.165977	0.432187
Anorthite	175.029709	0.166454
LaCl2+	174.978574	16.383851
Gibbsite	172.217357	0.547927
Fe+++	170.512636	0.652775
HoNO3++	170.014684	0.218886
Aragonite	167.613802	17.099289
Margarite	167.288515	0.759432
MgCl+	163.150636	19.632541
EuF2(aq)	160.501685	16.055684
LuNO3++	158.875421	1.149167
TbCl2+	152.380922	18.813157
Lawsonite	150.949648	0.765339
GdCl2+	150.216425	15.891398
DyCl2+	146.999488	15.777814
EuF4--	146.769031	31.134429
PbF+	141.816771	100.385868
EuCl2+	141.368036	16.588617
HoCl2+	138.397437	16.032163
HoCl++	136.889864	2.001065

SmCl2+	132.969448	18.241673
Andradite	129.714595	3.712677
Magnetite	128.020388	6.704888
Prehnite	127.1876	0.212238
DyCl++	126.602271	3.000521
YbCl2+	126.546225	17.014507
TbCl++	126.277007	3.359857
2-Pentanone(aq)	126.273303	67.018865
Halite	125.604569	7.115529
K-Feldspar	125.094397	25.245521
ErCl2+	123.304108	16.859864
TmCl2+	122.551995	16.906529
EuF+	122.513805	15.188361
TmCl++	117.188579	0.879286
Laurite	115.817739	0.638452
Magnesite	114.60448	10.453455
HfOH+++	111.333361	99.796836
EuCl+	108.205237	8.986765
Nepheline	106.858612	0.547588
H4P2O7(aq)	104.699166	4.205053
Ru+++	104.676792	8.264841
PbF2(aq)	103.903534	100.604442
H2SeO3(aq)	102.487368	5.473475
AmH2PO4++	102.406299	14.626778
AmCO3+	102.393173	12.025991
AmF2+	102.075994	0.551239
Ru(SO4)2-	102.070911	23.423426
Ru++	102.058644	50.97627
Am(CO3)2-	101.747092	5.765266
Am(SO4)2-	101.705571	2.452529
HBrO(aq)	101.69855	3.705486
AmF++	101.508371	0.672421
HClO(aq)	101.474016	6.781925
RuCl6---	101.417762	27.826671
CuCl3--	101.300194	6.836852
RuCl5--	101.271494	15.146811
AmSO4+	101.266877	5.326552
CuCl2-	101.18475	5.161805
RuSO4+	101.103896	2.470575
RuCl4-	101.082113	9.461702
Goethite	100.945331	2.454487

CdCl2(aq)	100.907146	6.866929
RuCl++	100.878296	0.633943
HClO2(aq)	100.872014	49.619894
RuSO4(aq)	100.824766	2.826852
MgSO4(aq)	100.784742	8.287748
AmCl++	100.759794	0.360315
H3AsO4(aq)	100.708333	3.999214
Asparagine(aq)	100.672801	87.056625
CuF+	100.649731	23.95385
CdCl+	100.636178	28.205717
FeF+	100.609092	1.960641
ZnF+	100.579054	3.817377
HNO2(aq)	100.56751	0.253589
MnF+	100.546396	42.037575
HIO3(aq)	100.513422	24.945686
CuCl+	100.451602	13.504993
NaSO4-	100.428395	44.070476
AmNO3++	100.38536	1.181063
RuCl+	100.298409	12.002941
FeOH++	100.225949	6.128192
RuOH++	100.190297	16.644243
VOH++	100.138711	4.28539
CrOH++	99.999011	7.287287
U(Pent)++	99.955544	21.587929
U(For)++	99.899126	32.578364
AmOH++	99.776677	7.486353
U(But)++	99.761851	21.794402
U(Prop)++	99.743678	19.860067
U(For)2+	99.71392	17.911542
CuCl4--	99.578076	12.089774
YOH++	99.560408	3.91635
U(But)2+	99.541045	11.105771
U(Prop)2+	99.388325	9.838914
VOOH+	99.266833	7.351278
CuOH+	99.169106	6.155103
CoOH+	99.039403	1.536719
FeOH+	99.030532	4.782575
HAsO2(aq)	99.006699	1.076237
CdOH+	98.89571	3.459436
Spinel	98.884894	0.315257
MnOH+	98.866046	2.360792

PbOH+	98.776586	19.699855
CaOH+	98.675278	0.534456
BaOH+	98.618855	0.34669
SrOH+	98.608824	0.696648
Litharge	98.550966	0.582338
Ce++++	98.300622	1.663476
VO4---	98.256011	8.168093
ZnOH+	98.199213	12.604746
LiOH(aq)	98.06882	1.901106
KOH(aq)	97.969341	2.00819
LuCl2+	96.998065	6.881624
HCoO2-	96.085045	45.555542
CuO2--	94.479364	3.582095
Sylvite	94.108644	13.603327
CsBr(aq)	93.057795	8.869832
VO2+	92.146155	12.506789
NiCl+	92.143766	1.306708
Yb(Pent)2+	91.825695	0.106656
HS2O3-	90.678751	0.378212
GdCl++	90.345575	2.342071
Pb(Pent)+	89.21499	0.473722
2-Hexanone(aq)	86.909157	40.65256
Ca-Al_Pyroxene	86.405352	0.097902
SmCl++	83.12435	1.293631
HAlO2(aq)	74.095003	1.954629
EuCl++	70.358334	1.819314
Romarchite	70.077959	16.171852
Gd(Pent)2+	68.50824	0.781095
Rn(g)	67.766862	34.848132
AgCl4---	67.717818	19.301619
2-Heptanone(aq)	66.367436	27.211571
Annite	66.179949	1.618894
Paragonite	66.071017	1.480272
NdCl++	64.725263	3.200429
IO-	63.080308	17.891139
ErCl++	63.05429	0.666398
Ethylbenzene(aq)	62.068457	26.157317
LaCl++	61.448997	4.320928
CeClO4++	61.172714	3.064492
CdCl3-	57.306019	16.32728
PrCl++	56.171737	3.494059

Hg2++	55.803062	1.283001
IO4-	55.613847	8.542688
PrOH++	55.106605	5.222497
2-Octanone(aq)	54.036188	19.165578
LuCl++	53.918423	3.565924
Pb(Lac)+	53.428836	0.213553
CO2(g)*	52.504113	34.867706
TbOH++	51.767444	4.599474
Pb(Glyc)+	50.474238	9.260697
FeF++	50.430245	8.818452
Mn(Pent)2(aq)	48.319589	3.152443
PbCl4--	46.84826	30.017256
ZnCl2(aq)	46.66613	15.265088
YbOH++	45.585975	5.537301
Kaolinite	45.256975	3.840029
EuCl2(aq)	44.338653	12.038573
SrF+	43.218309	17.237112
Mn(Pent)+	42.975354	6.205348
EuCl4--	42.935138	12.959836
SmOH++	42.532686	5.012635
EuCl3-	41.009938	12.363363
Xe(g)	40.389159	33.136667
TbCO3+	40.281536	0.398858
TmOH++	39.975712	5.095289
LuOH++	39.897126	5.444161
ErOH++	39.256392	5.089876
NdOH++	39.247577	5.512263
Ferrosilite	37.545525	3.358109
GdOH++	37.522567	4.712009
HoOH++	37.481594	4.940317
HP2O7---	36.799133	13.892968
EuOH++	36.527791	4.81351
Mn(Lac)+	35.768352	10.071432
CH4(g)	35.315686	28.028648
1-Butyne(aq)	34.922689	16.854222
n-Butylbenzene(aq)	34.765539	11.714953
Pyrophyllite	34.491603	14.318816
DyOH++	34.157694	4.651038
Talc	32.296979	3.722406
UO2OH+	32.166259	0.371767
BaCl+	31.91367	1.320559

Phlogopite	31.296203	0.973613
Grossular	30.389362	0.240345
Kr(g)	30.148989	17.700811
CeBr++	30.047847	7.885837
RbF(aq)	29.885482	4.729959
Cd(Pent)2(aq)	29.788151	0.116196
Pargasite	29.52349	0.447664
n-Pentylbenzene(aq)	29.474949	8.955186
HVO4--	29.440774	1.249557
CeCl++	29.363657	6.11765
Mn(Glyc)+	29.356265	12.915047
Gd(Pent)++	29.070277	0.993167
Cu(Glyc)+	28.817521	0.749266
MnSO4(aq)	28.810591	10.332967
Acetamide(aq)	28.701153	17.916141
PrCO3+	28.583478	0.60362
Greenalite	28.148511	6.895111
Nonanal(aq)	26.135265	11.575931
PbCl3-	26.129168	7.508053
Zn(Lac)2(aq)	26.009657	0.033671
CeNO3++	25.66333	2.074915
PdO(aq)	25.617502	2.080784
IO3-	25.608175	1.396412
Pb(Pent)2(aq)	25.370844	0.362413
LaOH++	25.023228	4.018543
Eu(Lac)2(aq)	24.904125	1.168467
Eu(Glyc)+	24.473809	2.501601
YbCO3+	24.293433	0.208929
CaSO4(aq)	24.244208	0.980572
SmF4-	24.035137	1.211435
PrF4-	23.893369	1.284178
n-Heptylbenzene(aq)	23.769636	6.121795
NdF4-	23.747137	1.203647
Gehlenite	23.477471	0.003938
Cerussite	23.375705	14.091021
CsOH(aq)	23.261733	1.410626
O2(g)	23.239611	15.87563
O2(aq)*	23.239215	15.875715
Cu(Lac)+	22.948653	1.853357
TmCO3+	22.604179	0.994532
HoCO3+	22.388967	1.344028

LuCO3+	22.225146	0.541979
GdCO3+	22.197294	1.589579
Mn(But)+	22.164777	6.597805
SnOH+	22.072444	9.955381
n-Octylbenzene(aq)	21.985148	5.207029
LaF4-	21.929053	1.192726
Mn(Prop)+	21.922053	7.542573
ErCO3+	21.889475	1.057706
SmCO3+	21.848039	1.21799
Eu(Lac)+	21.644543	2.12473
Cr++	21.53286	9.004275
PbCl2(aq)	21.528028	3.451272
DyCO3+	21.499082	1.621452
EuCO3+	21.413961	1.479328
Tenorite	21.285145	2.939236
TbHCO3++	21.079235	1.429559
PrHCO3++	21.077902	1.1167
Nesquehonite	20.986466	4.955016
Anthophyllite	20.927593	2.490653
1-Heptanol(aq)	20.880761	13.062511
NdCO3+	20.873916	1.488728
Fayalite	20.619534	2.379563
1-Pentyne(aq)	20.422122	13.48958
TbSO4+	20.332164	3.064716
Mn(For)+	20.087797	16.54754
TbF4-	20.069072	1.207571
EuF4-	19.931657	1.252451
1-Hexanol(aq)	19.930437	11.645845
Anhydrite	19.776538	11.797697
Tremolite	19.768642	2.922539
AgCl3--	19.765607	7.592067
KSO4-	19.65547	1.811611
Cu(Pent)2(aq)	19.595646	0.080967
Mn(Lac)2(aq)	19.50201	4.331344
SO2(g)	19.479442	0.097164
CeF4-	19.45336	1.077076
Glutamic_acid(aq)	19.284653	8.299784
ErSO4+	19.263771	4.24861
GdF4-	19.092483	1.224928
YbF4-	19.060491	0.889716
Pb(Glyc)2(aq)	18.921147	13.399148

NdSO4+	18.9123	4.841843
PbCl+	18.872221	3.012039
PdCl4--	18.840637	4.234777
CaF+	18.58673	3.981603
PdCl2(aq)	18.458526	0.394423
Eu(For)++	18.434996	0.651109
1-Propanol(aq)	18.413468	10.654429
PrF3(aq)	18.362082	0.751506
ErF4-	18.320772	1.01564
TmF4-	18.284687	1.016389
YbSO4+	18.14252	2.629531
TmSO4+	17.984291	1.722955
LuSO4+	17.936358	2.504286
V+++	17.926224	0.618703
PdCl3-	17.919692	1.945761
Yb(For)++	17.901507	0.728405
HoF4-	17.801411	1.139401
SmF3(aq)	17.720894	0.661995
NdF3(aq)	17.618314	0.674833
HoSO4+	17.611225	0.978803
SmSO4+	17.527306	1.306408
HSO5-	17.462379	2.79594
UO2+	17.399583	4.152578
CeOH++	17.374935	5.146988
DySO4+	17.348607	0.41991
LuF4-	17.343123	0.839083
EuSO4+	17.323008	0.850792
DyF4-	17.318464	1.197101
PrO+	17.309426	2.532891
ZnCl+	17.189427	7.674141
MgF+	17.182055	3.364297
Uraninite	17.157272	4.708887
AgCl(aq)	17.151837	0.017173
HSO4-	17.148107	8.117106
BeO2--	17.091257	9.016615
1-Butanol(aq)	17.089773	3.883243
Br3-	17.074744	0.058535
LaF3(aq)	17.071427	1.070852
HF2-	17.045984	11.570031
LaCO3+	17.041473	0.527432
TbO+	16.964549	2.266368

1-Hexyne(aq)	16.761033	12.196391
MgOH+	16.507779	1.141412
TbF3(aq)	16.49221	0.740118
Eu(Pent)++	16.473263	0.46868
S5O6--	16.419222	2.545094
Glutaric_acid(aq)	16.367255	6.206607
Yb(Pent)++	16.362325	0.293868
Cd(Pent)+	16.224353	0.239342
Enstatite	16.167397	1.837054
EuF3(aq)	16.113818	0.699613
Eu(But)++	16.079015	1.72824
NaHSiO3(aq)	15.9773	0.450979
Yb(But)++	15.976215	1.484414
GdF3(aq)	15.911424	0.74638
HSeO4-	15.829248	3.837347
Celestite	15.795248	10.756059
Pb(Prop)+	15.749866	1.050785
YbF3(aq)	15.583599	0.426312
YbO+	15.544407	2.728973
Hedenbergite	15.467413	2.569192
CeF3(aq)	15.411946	1.726452
Fe(Lac)+	15.262551	1.087512
ErF3(aq)	15.248844	0.53693
TmF3(aq)	15.232445	0.534895
AgCl2-	15.197661	2.653104
HoF3(aq)	15.131938	0.631679
1-Heptyne(aq)	15.094967	11.528861
LuO+	15.052699	2.73147
Gd(For)++	15.006468	0.274338
Ni(Glyc)+	15.005105	0.701284
Cr+++	14.973097	2.862204
Sepiolite	14.948545	3.061417
DyF3(aq)	14.928084	0.703577
Anglesite	14.777257	9.488712
SmO+	14.773866	2.471736
LuF3(aq)	14.652635	0.395061
Gd(But)++	14.648	1.051494
TmO+	14.539924	2.516454
Pyrrhotite	14.509981	6.082235
CeIO3++	14.447114	0.301174
GdO+	14.442709	2.332865

ErO+	14.439726	2.517554
HoO+	14.371144	2.410361
Eu(Glyc)2(aq)	14.356231	1.130115
Octanal(aq)	14.306646	5.521032
1-Octyne(aq)	14.287496	11.153559
Glutamine(aq)	14.171746	9.682475
EuO+	14.006347	2.375731
La(Pent)++	13.981051	1.975072
Bunsenite	13.880259	2.205657
Fluorite	13.818389	5.910669
NdO+	13.814677	2.67642
DyO+	13.762991	2.312387
Antigorite	13.691321	1.911358
Diopside	13.679499	2.14888
La(But)++	13.654355	0.621807
Fe(Glyc)2(aq)	13.649636	9.535753
Cd(Lac)+	13.618903	0.576531
Zn(Pent)2(aq)	13.475172	0.401694
Eu(Prop)++	13.423179	1.384292
PrF2+	13.407156	0.606854
HCN(aq)	13.344688	3.516738
Pb(But)+	13.260347	1.212864
AsO2-	13.249887	0.436538
Eu(For)+	13.225145	1.459119
Ne(g)	13.188896	10.605571
CaCO3(aq)	13.157578	2.219708
Artinite	13.145336	0.976013
Zn(Glyc)+	13.121947	0.987789
Barite	13.035019	7.652895
Au+++	12.984972	7.649716
La(For)++	12.836908	0.84612
Mn(But)2(aq)	12.7835	2.85376
Chrysotile	12.685671	1.82876
SmHCO3++	12.650601	1.688964
HCrO4-	12.597258	5.510858
YbHCO3++	12.589634	1.892359
TmHCO3++	12.5291	1.773583
PrH2PO4++	12.526672	3.220529
PdCl+	12.520473	0.326275
Mn(Glyc)2(aq)	12.461118	4.761739
CeCO3+	12.456045	1.293142

ErHCO3++	12.452021	1.762304
Cd(Glyc)+	12.444346	0.305403
EuHCO3++	12.417677	1.723396
Eu(Pent)+	12.383008	0.913503
TbH2PO4++	12.348269	3.124694
HoHCO3++	12.341861	1.693255
SmF2+	12.298021	0.491576
LuHCO3++	12.285434	1.845533
Eu++	12.282386	0.669451
Gd(Prop)++	12.232722	0.635634
GdHCO3++	12.210078	1.579912
TbF2+	12.204729	0.56155
NdF2+	12.181135	0.54317
Mn(Prop)2(aq)	12.179552	3.163727
DyHCO3++	12.17776	1.569905
MgCO3(aq)	12.131613	0.999968
SO2(aq)	12.072621	9.231387
NdHCO3++	12.059199	1.302051
LaF2+	12.004597	0.834266
Fe(Glyc)+	11.967997	8.538657
Yb(Prop)++	11.966983	1.127899
Wurtzite	11.962937	3.945337
Ni(Lac)+	11.854374	0.01671
Cu(Pent)+	11.665871	1.627593
Glycine(aq)	11.659419	5.887711
Mn+++	11.64692	0.99194
GdF2+	11.632142	0.568322
Zn(Pent)+	11.610208	0.687685
EuF2+	11.601886	0.533863
HSO3-	11.562216	8.292675
YbH2PO4++	11.553192	2.911907
TmH2PO4++	11.546251	2.953338
SmH2PO4++	11.540731	3.010199
ErH2PO4++	11.499211	3.009366
Urea(aq)	11.474555	0.044036
SrCO3(aq)	11.474377	2.228152
LaHCO3++	11.463236	1.018782
LuH2PO4++	11.451586	2.869116
CO2(aq)	11.434043	4.973624
SiF6--	11.433312	2.83381
H3PO4(aq)	11.430125	6.390897

EuH2PO4++	11.402002	2.975551
HoH2PO4++	11.401067	2.998883
DyH2PO4++	11.390973	3.032959
Formate(aq)	11.359658	0.394028
GdH2PO4++	11.351669	2.90554
NdH2PO4++	11.323063	3.075433
1-Pentanol(aq)	11.313424	3.210518
YbF2+	11.21906	0.309727
H2VO4-	11.21158	4.837854
HoF2+	11.101349	0.473551
HF(aq)	11.067216	5.868292
LaH2PO4++	11.062448	2.832097
BO2-	11.047945	8.547518
TmF2+	11.018504	0.393767
ErF2+	11.004559	0.399686
DyF2+	11.002006	0.536336
PrF++	10.954783	0.504762
Ba(Pent)+	10.922713	0.572813
Methionine(aq)	10.89192	4.788923
LaO+	10.859992	1.956915
HAsO4--	10.818733	4.50848
BF4-	10.790322	4.87297
Forsterite	10.65258	1.414721
Sphalerite	10.588061	3.208248
LuF2+	10.585184	0.280905
HSeO3-	10.561909	5.070342
Mg(Lac)+	10.517003	1.583163
Cu(Glyc)2(aq)	10.484652	0.4358
CeF2+	10.416795	1.668652
2-Hydroxybutanoate	10.341889	0.674814
Fe(Pent)2(aq)	10.33856	0.056132
HSiO3-	10.328535	4.993898
SCN-	10.274173	0.810052
La(Prop)++	10.261963	1.184648
1-Octanol(aq)	10.130731	3.51503
Co(Pent)2(aq)	10.10211	0.224948
Manganosite	10.100136	2.935449
Cu(But)+	10.034935	0.319733
TbF++	9.963548	0.392072
Cu(Lac)2(aq)	9.83012	0.629472
CeO+	9.828085	2.680423

He(g)	9.745168	7.535691
Chlorargyrite	9.673234	0.455073
CeH2PO4++	9.643046	3.474896
Galena	9.525216	2.274961
H2PO4-	9.520904	5.223073
2-Hydroxypentanoate	9.404711	0.741081
H3P2O7-	9.30411	5.408449
TbO2H(aq)	9.262646	1.071317
Ni(Glyc)2(aq)	9.207942	0.139236
SmF++	9.180456	0.329511
Coesite	9.167213	1.68631
PrO2H(aq)	9.106391	1.320465
LuO2H(aq)	9.047109	1.215619
Eu(But)+	9.03429	0.511496
Eu(Prop)+	9.007946	0.804867
NdF++	8.9877	0.463129
YbO2H(aq)	8.985698	1.33144
Ni(Pent)+	8.980785	0.486471
GdF++	8.974206	0.388728
Yb(But)2+	8.97225	0.937164
BaCO3(aq)	8.95916	0.690825
EuO2H(aq)	8.9533	1.095889
Yb(For)2+	8.925482	0.054964
SmO2H(aq)	8.907958	1.193563
LaF++	8.901835	0.623763
Cd(But)+	8.899411	0.481863
Ni(But)+	8.86595	0.570497
Wollastonite	8.844418	2.591502
EuF++	8.843606	0.362383
Threonine(aq)	8.76222	4.107548
Eu(But)2+	8.728835	1.285241
Eu(For)2+	8.716639	0.10292
LaSO4+	8.714058	0.365677
Gd(But)2+	8.679033	1.088449
HoF++	8.644474	0.32516
YbF++	8.636342	0.185705
TmO2H(aq)	8.627759	1.174884
Mn(For)2(aq)	8.614516	7.015953
Chalcedony	8.587426	2.582441
DyF++	8.569903	0.370061
ErO2H(aq)	8.557156	1.218123

TmF++	8.51213	0.254495
ErF++	8.494421	0.258208
Ca(Lac)+	8.464666	0.839088
Ca(Pent)+	8.368683	1.120733
Monticellite	8.322589	1.75687
Cd(Prop)+	8.311155	0.278642
Akermanite	8.305971	1.994032
Fe(Lac)2(aq)	8.303502	0.404017
Sr(Pent)+	8.257578	1.309807
HoO2H(aq)	8.215917	1.173844
Heptanal(aq)	8.192009	3.078264
LuF++	8.173548	0.168835
Pb(For)+	8.171741	0.863165
Quartz	8.139168	2.356896
Cu(Prop)+	8.112968	0.585038
H2S(aq)	8.095081	2.706526
CO3--	8.057316	4.398447
CeHCO3++	8.044206	2.04493
Pyrite	8.04088	0.614225
Sr(Lac)+	7.988854	0.751941
Co(Glyc)+	7.980923	0.505956
Fe(Pent)+	7.943477	1.420062
DyO2H(aq)	7.929841	1.081356
Fe(But)+	7.915201	0.054444
H2P2O7--	7.849895	2.660627
Zn(Glyc)2(aq)	7.841447	0.44798
Chalcopyrite	7.809387	1.640671
Eu(But)2(aq)	7.800502	0.46938
BrO-	7.770262	3.739838
S2(g)	7.76973	0.275063
GdO2H(aq)	7.725014	1.183051
La(But)2+	7.654526	0.917491
Eu(Prop)2+	7.636584	0.817621
Gd(For)2+	7.624346	0.519932
Ni(Lac)2(aq)	7.583215	0.664133
Co(Lac)+	7.569625	0.240582
Ni(Pent)2(aq)	7.512371	0.296363
Cd(For)+	7.455154	0.14197
NdO2H(aq)	7.407099	1.399148
Alanine(aq)	7.368896	4.827234
Eu(For)2(aq)	7.364797	0.502509

Ca(Glyc)+	7.273421	0.124225
Sr(Glyc)+	7.234282	0.277682
n-Propylbenzene(aq)	7.15314	6.293378
Yb(Prop)2+	7.109781	0.545614
Gd(Prop)2+	7.099852	1.293023
Co(Pent)+	7.037143	0.790954
Mg(Glyc)+	6.984724	0.31788
Ca(Pent)2(aq)	6.97263	0.413733
H2S(g)	6.885681	0.423391
Cd(Lac)2(aq)	6.867476	0.476962
Methane(aq)	6.748083	0.063769
La(For)2+	6.722009	0.1534
CeF++	6.684464	0.481642
Pb(Lac)2(aq)	6.652799	0.759684
Zn(But)+	6.649325	1.158104
OH-	6.577676	2.473608
Cu+	6.455348	0.397385
CO(aq)	6.402985	0.969219
Cd(Glyc)2(aq)	6.397534	0.097758
Merwinite	6.381167	1.504111
Co(But)+	6.35394	0.428663
ClO-	6.317196	1.922444
Phenol(aq)	6.303655	5.273826
Ni(Prop)+	6.291898	0.314402
Covellite	6.272444	1.161997
LaO2H(aq)	6.266164	0.933295
Ni(For)+	6.218758	0.120205
Fe(Prop)+	6.187454	0.248882
Ba(Lac)+	6.181785	0.483554
Cu(For)+	6.169046	0.538322
NaOH(aq)	6.140759	0.468845
La(Prop)2+	6.084776	0.487796
Berndtite	6.03971	1.15168
1-Propene(aq)	6.014071	0.360835
1-Butene(aq)	5.996876	0.360907
Ag(CO3)2---	5.977312	4.723183
1-Pentene(aq)	5.925234	0.666746
Cr2O7--	5.87013	2.764081
Mg(Pent)2(aq)	5.842488	0.139229
1-Hexene(aq)	5.836051	0.835792
1-Octene(aq)	5.812781	1.012665

1-Heptene(aq)	5.807197	0.938824
Ba(Glyc)+	5.642838	1.386659
n-Hexane(aq)	5.634784	2.710715
AsO4---	5.61086	2.163006
Bornite	5.593421	0.937253
Hexanal(aq)	5.557371	2.141279
PO4---	5.530788	4.055088
Eu(Prop)2(aq)	5.487776	0.4729
Methanol(aq)	5.419339	0.108082
Co(Glyc)2(aq)	5.415657	0.14959
Mg(Lac)2(aq)	5.392725	0.235831
SeO4--	5.347485	2.234572
AlO2-	5.289392	0.360562
Na(Glyc)2-	5.258836	0.087294
Zn(Prop)+	5.252392	0.919537
Yb++	5.230109	0.720112
Fe(For)+	5.156982	0.503409
Mg(But)+	5.156186	0.329316
CeO2H(aq)	5.147797	1.36506
Periclase	5.137984	0.764552
Phenylalanine(aq)	5.125214	3.650885
Zincite	5.093356	2.586285
Mg(Pent)+	5.056018	0.521208
Co(Lac)2(aq)	5.0103	0.588582
Sr(Pent)2(aq)	4.995935	0.486179
Cu(But)2(aq)	4.973635	0.578002
Sr(But)+	4.92888	0.111495
Brucite	4.878223	0.489497
Ni(But)2(aq)	4.860783	0.304702
S4O6--	4.85647	0.580874
n-Hexylbenzene(aq)	4.744422	3.518514
Tryptophan(aq)	4.729822	4.314871
Ca(But)+	4.708645	0.122114
Ca(Lac)2(aq)	4.636824	0.297972
Mg(Glyc)2(aq)	4.566911	0.561475
Na(Lac)2-	4.552385	0.65756
Na(For)2-	4.465606	0.515969
Ba(For)+	4.453713	0.390053
Co+++	4.433683	0.146503
I3-	4.429188	0.560602
Ba(But)+	4.34503	0.629548

Mg(Prop)+	4.337716	0.13957
Cd(Prop)2(aq)	4.328737	0.017132
Sm++	4.303185	0.541477
K(Glyc)2-	4.295402	0.095663
Metacinnabar	4.257859	0.97586
Sr(Lac)2(aq)	4.254722	0.044037
Cu(Prop)2(aq)	4.248122	0.775457
Cd(But)2(aq)	4.24394	0.044099
HSe-	4.234276	0.220834
Ba(Prop)+	4.204451	0.465148
Ca(Glyc)2(aq)	4.192741	0.459576
Co(Prop)+	4.191695	0.19323
Chalcocite	4.180372	0.867851
Cinnabar	4.17417	0.882538
Zn(Prop)2(aq)	4.114474	0.313563
Zn(For)+	4.096364	0.126464
Sr(Prop)+	4.01949	0.281508
Fe(But)2(aq)	4.00691	0.563603
Sr(Glyc)2(aq)	3.984826	0.111209
Zn(But)2(aq)	3.953922	0.393839
Na(But)2-	3.88933	0.22455
Na(Prop)2-	3.884504	0.326862
Ca(Prop)+	3.856387	0.055361
Isoleucine(aq)	3.807749	2.334604
K(For)2-	3.79038	0.008776
Sr(For)+	3.755377	0.619507
Ni(Prop)2(aq)	3.726046	0.495177
Pentanal(aq)	3.59929	1.484933
Toluene(aq)	3.576541	1.082645
S4--	3.529305	0.125604
Cd(For)2(aq)	3.514996	0.186417
Mg(For)+	3.502068	0.037322
Ni(For)2(aq)	3.493867	0.281948
Acanthite	3.485004	0.324682
Pb(Prop)2(aq)	3.478228	0.295879
Na(Lac)(aq)	3.443038	1.571139
Co(But)2(aq)	3.437637	0.341014
ClO4-	3.420381	1.938568
K(Lac)(aq)	3.408958	1.657743
Na(Pent)2-	3.3806	0.079253
CO2(g)	3.333868	0.104351

K(Lac)2-	3.330517	0.620158
Fe(Prop)2(aq)	3.329884	0.578697
PrO2-	3.324852	1.051685
Ba(Pent)2(aq)	3.316593	0.477185
Co(For)+	3.312038	0.037966
U++++	3.310608	2.105171
Pb(But)2(aq)	3.285235	0.14628
Ca(For)+	3.161626	0.344203
Valine(aq)	3.145536	2.609164
Ba(Lac)2(aq)	3.127282	0.401264
CO(g)	3.126598	0.053975
Na(But)(aq)	3.125385	1.471678
Na(Pent)(aq)	3.123551	1.28019
Ba(Glyc)2(aq)	3.118633	1.405085
S5--	3.085342	0.085771
TbO2-	3.044546	0.908893
Ag++	2.984839	0.853229
K(Prop)2-	2.961356	0.273625
Mg(But)2(aq)	2.915334	0.436989
Cu(For)2(aq)	2.898771	0.123926
K(But)(aq)	2.895376	1.764213
K(Pent)(aq)	2.894085	1.768195
K(But)2-	2.83349	0.327373
n-Butane(aq)	2.824177	0.129857
Mg(Prop)2(aq)	2.741542	0.394281
Na(Glyc)(aq)	2.72195	1.739124
Co(Prop)2(aq)	2.703843	0.533
NH4+	2.626672	1.22973
Leucine(aq)	2.624955	1.530514
Tyrosine(aq)	2.542866	1.849024
YbO2-	2.539553	1.131832
Na(Prop)(aq)	2.521575	0.793326
GdO2-	2.493495	0.985165
Lime	2.44435	0.742603
Fe(For)2(aq)	2.436963	0.023626
SmO2-	2.436362	1.032831
K(Glyc)(aq)	2.414518	1.541071
S3--	2.409747	0.0249
Ca(But)2(aq)	2.399323	0.10334
Lactic_acid(aq)	2.391896	1.817673
HoO2-	2.365017	0.992892

Sr(But)2(aq)	2.360567	0.294857
MnO4-	2.356718	1.902698
TmO2-	2.329181	1.02395
n-Pentane(aq)	2.309031	0.088751
ErO2-	2.306593	1.027551
SO3--	2.30227	0.657286
NdO2-	2.285811	1.118893
EuO2-	2.266464	0.969744
S2O3--	2.265117	0.06761
K(Prop)(aq)	2.264599	1.139119
Butanal(aq)	2.23457	1.025881
DyO2-	2.223177	0.921387
LuO2-	2.197583	1.071167
Ca(Prop)2(aq)	2.191538	0.157829
Zn(For)2(aq)	2.189899	0.24053
Ba(But)2(aq)	2.145719	0.220431
Propane(aq)	2.141788	0.055656
S3O6--	2.140383	0.265004
HO2-	2.120207	0.569293
Sr(Prop)2(aq)	2.119062	0.037932
Sulfur	2.10088	0.476344
Benzene(aq)	2.069208	1.427827
Ba(For)2(aq)	2.059672	0.313868
BrO4-	2.042956	1.094585
Ba(Prop)2(aq)	2.036016	0.646719
ClO3-	1.973807	1.56895
n-Heptane(aq)	1.871461	0.039743
Adipic_acid(aq)	1.863842	1.424719
MnO4--	1.86324	0.083008
S2O4--	1.860342	0.119949
Mg(For)2(aq)	1.821028	0.070847
Co(For)2(aq)	1.759772	0.223028
n-Octane(aq)	1.742228	0.025144
U+++	1.700103	0.019299
Sr(For)2(aq)	1.656785	0.116609
2-Hydroxyhexanoate	1.619804	0.895139
LaO2-	1.600516	0.740452
K(For)(aq)	1.599362	0.072211
K(Pent)2-	1.570857	0.152754
Ca(For)2(aq)	1.528527	0.077066
Pb(For)2(aq)	1.525085	0.124004

CeO2-	1.493296	0.882518
Pimelic_acid(aq)	1.461711	1.024567
Acetic_acid(aq)	1.43451	0.035521
2-Hydroxyheptanoate	1.42924	0.834635
Na(For)(aq)	1.410693	0.133396
S2O8--	1.381602	0.911436
Cassiterite	1.364993	0.519444
Suberic_acid(aq)	1.311493	0.902716
2-Hydroxyoctanoate	1.294644	0.799153
BrO3-	1.225399	0.834895
Formic_acid(aq)	1.211382	0.398907
1-Pentanamine(aq)	1.20669	0.194366
Azelaic_acid(aq)	1.205937	0.816669
2-Hydroxynonanoate	1.199241	0.771429
1-Hexanamine(aq)	1.170795	0.164124
ClO2-	1.167101	0.097244
N2(aq)	1.163598	0.610564
1-Octanamine(aq)	1.158731	0.154359
Benzoic_acid(aq)	1.144979	0.700646
1-Heptanamine(aq)	1.143402	0.139642
2-Hydroxydecanoate	1.128005	0.753078
1-Butanamine(aq)	1.116783	0.199892
H2(g)	1.107119	0.726101
NO3-	1.024478	0.191766
CN-	1.011145	0.023961
1-Propanamine(aq)	1.005766	0.161889
Ethyne(aq)	1.000092	0.354339
NO2-	0.985419	0.382383
HS-	0.934572	0.021269
Propanoic_acid(aq)	0.919193	0.795891
Dodecanoic_acid(aq)	0.912982	0.612311
Undecanoic_acid(aq)	0.91032	0.614013
Decanoic_acid(aq)	0.907072	0.614001
Nonanoic_acid(aq)	0.902497	0.620183
Octanoic_acid(aq)	0.897348	0.624614
Heptanoic_acid(aq)	0.886779	0.618674
Hexanoic_acid(aq)	0.865342	0.628286
Pentanoic_acid(aq)	0.845629	0.642951
Ethane(aq)	0.80354	0.378532
Butanoic_acid(aq)	0.800165	0.668876
Succinic_acid(aq)	0.661456	0.483289

Ethanamine(aq)	0.645423	0.470083
H2(aq)	0.602981	0.267764
H2AsO3-	0.574162	0.424886
Oxalic_acid(aq)	0.559578	0.252426
Acetaldehyde(aq)	0.506707	0.083736
Acetone(aq)	0.500095	0.302881
S2--	0.496676	0.132226
Formaldehyde(aq)	0.463853	0.056649
Ethylene(aq)	0.365367	0.00633
S2O6--	0.349115	0.242248
S2O5--	0.335613	0.005834
Methanamine(aq)	0.332884	0.04856
Ethanol(aq)	0.308354	0.137183
Glycolic_acid(aq)	0.28587	0.027705
Malonic_acid(aq)	0.274676	0.089902
N2(g)	0.267707	0.059799

Appendix C. Compilation of Batch Experiments Conducted for Fluid-granite Systems.

Reference	Temperature (°C)	Pressure (Mpa)	Length (days)	Initial Solids	Aqueous Fluid[a]	Other Fluid[b]	Alteration
Ellis & Mahon, 1964	150-350	50	1-13	Rhyolite, dacite, andesite (chips)	Distilled water		Indiscernible with available equipment
Ellis & Mahon, 1967	400-600	100-150	14-150	Rhyolite, dacite, andesite (chips)	Distilled water		Indiscernible with available equipment (possible micas and zeolites?)
Savage & Chapman, 1982	100-200	50-60	≤ 87	Granodiorite (powder)	"Water"		Montmorillonite
Savage et al., 1986	100	50	203	Monzogranite (powder)	"Water"		Complex smectite
Baldeyrou et al., 2003	200-300	60	40	Composite granite (powder)	Distilled water		Mg-rich saponite, alkaline or Ca-rich clays, intermediate micas
Tsuchiya & Hirano, 2007	≤600	≤60	2	Granite (chip)	Distilled water		Not reviewed (fluid compositions only)
Ellis, 1968	350-500	150	21	Andesite (powder)	Distilled Water, 2m NaCl, 4m NaCl		400C: quartz and montmorillonite 450C: quartz, montmorillonite, and illite-montmorillonite 500C: quartz, montmorillonite, chlorite
Baker et al., 1985	300, 350	11.1-17.7	0.25-3.1	Granite (fine cuttings)	NaCl (2M), seawater, HCl + NaCl (0.1M, 0.25, 1M)		Not reviewed (fluid compositions only)
Savage et al., 1985	250	50	100	Granite (cuttings)	Na-HCO3-Cl (<120 mg/L)		Ca-rich smectite, Ca-Al-silicate (laumontite?), calcite, Ca-sulfate
Savage et al., 1987	80, 150, 250	50	200, 150, 100	Granite (cuttings)	Na-HCO3-Cl (<800 mg/L)		All temperatures: smectite, calcite 150C: laumontite 250C: wairakite, anhydrite
Milodowski et al., 1989	200	50	70	Granite (cuttings)	Na-Ca-HCO3-Cl (TDS <120 mg/L); Modified seawater		Synthetic groundwater, 2:1 W:R: smectite, illite, mixed clays, Ca-Al-silicate (laumontite?), silica Synthetic groundwater, 10:1 W:R: smectite, silica Seawater, 10:1 W:R: smectite anhydrite, magnesium hydroxide sulphate hydrate
Savage et al., 1993	200	50	≤ 80	Granite (cuttings)	Synthetic streamwater (0.008M), seawater (0.028 M) Synthetic NaCl solutions + Li-Rb-Cs		Streamwater: 2:1 W:R ratio: Ca-Al-silicate (laumonitite), series of clays from smectite to illite. 10:1 W:R ratio: aluminous-smectite. Seawater without granite: caminite (hydrous Mg-sulfate) and anhydrite. Seawater with granite:anhydrite, mixed-layer smectite-chlorite. NaCl solutions: Clay (illite-composition)
Bischoff & Rosenbauer, 1996	200, 350	50	84-124	Rhyodacite (powder)	Deionized water	CO_2	Poorly crystalline smectite.
Liu et al., 2003	100-350	Not specified	7	Granite (blocks)	Distilled water	CO_2	With CO_2: Al-silicate (and clay?)
Ueda et al., 2005	200	2-6	1-15	Granodiorite (chips)	Distilled water	CO_2 & N_2	Not reviewed (thermodynamic calculations only)
Suto et al., 2007	100-350	≤25	0.25-7	Granite (chips)	Distilled water	CO_2	With CO_2: Positive identification not possible: smectite, kaolinite, and/or K-aluminosilicate? Without CO_2: Positive identification not possible: Ca-aluminosilicate
Lin et al., 2008	100	10-15	2	Granite (chips)	"Water"	CO_2	$scCO_2/H_2O(g)$/rock: Ca-rich carbonate (calcite?) $CO_2/H_2O(l)$/rock: aluminosilicate (kaolinite?)

[a] Waters may or may not be degassed.
[b] No additional fliud used unless otherwise stated. Waters may or may not be in contact with atmosphere.

Appendix D. Compilation of Flow-through Experiments Conducted for Fluid-granite Systems.

Reference	Temperature (ºC)	Pressure (MPa)	Length (days)	Initial Solids	Aqueous Fluid[a]	Other Fluid[b]	Alteration
Charles, 1978	300	31.0-34.5	240	Granodiorite, disks	Distilled water		On granodiorite: Phillipsite, thomsonite, vermiculite Elsewhere in system: Wollastonite, silica
Summers et al., 1978	100-400	50	≤ 17	Granite, cylinders	"Water"		On granite: Sericite, Al-silicates Elsewhere in system: Orthoclase, plagioclase, silica, calcite
Morrow et al., 1981	200-310	30-60	6-32	Granite, cylinders	Distilled water		Silica, Ca-rich mineral (zeolite?)
Charles & Bayhurst, 1983	72, 119, 161, 209, 270, 310	33	60	Biotite granodiorite	Distilled water		72, 119C: Beidellite 161C: Stilbite or heulandite 209, 270, 310C: Thomsonite
Moore et al., 1983	80-300	30-60	7-21	Granite, cylinders	Distilled and deionized water		Silica and Ca-rich mineral (see Moorow et al., 1981), alteration of deuteric sericite
Azaroual & Fouillac, 1997	180	1.4	38	Granite, chips	Distilled water		Calcite and ferromagnesian saponite
Morrow et al., 2001 (Moore et al., 1994)	150-500	15	10-40	Granite, cores of intact, fractured, and gouged rock	Deionized water		All temperatures: Albite, K-spar, quartz, calcite, Ce-La coatings 150C: smectite, Ca-Al zeolite (laumonite?), pyrite, barite 250C: smectite, Ca-Al zeolite (wairakite?), K-mica, chlorite, sphalerite 400C: Ferrosilite, Ca zeolite (zonotlite?), grossular, titanite, epidote
Yasuhara et al., 2011	20-90	5-10	9-37	Granite, fractured core	Deionized water		Silica, calcite
Bourg et al., 1985	50-100	Not specified	12-56	Granite, fractured core and powders	Solution created by flow-through of distilled water through powdered granite		Not reviewed (thermodynamic calculations only)
Savage et al., 1992	60-100	30	5-17	Granite, cuttings, granulated	Streamwater (TDS <120 mg/l; Na-Ca-HCO_3-Cl)		Variable flow expeirments: slight evidence of precipitates, assumed to be smectite clay +/- calcite, +/- illite based on other studies (Savage et al., 1985, 1987 and Milodowski et al., 1989).
Okamoto et al., 2010	430	31	5-6	Granite, blocks	Si-solution and Al-Na-K solution created by dissolution of quartz and granite sands		Si-Solution+Granite: Opal-A, Opal-C, quartz Si-Al-Na-K-Solution+Granite: Opal-C, quartz, chalcedony, alkali feldspar

[a] Waters may or may not be degassed.
[b] No additional fliud used unless otherwise stated. Waters may or may not be in contact with atmosphere.